MICROMECHANICAL MODELING OF PRECIPITATED NITIHF SHAPE MEMORY ALLOYS

A Dissertation

by

JOBIN KOLLIYIL JOY

Submitted to the Office of Graduate and Professional Studies of
Texas A&M University
in partial fulfillment of the requirements for the degree of

DOCTOR OF PHILOSOPHY

Chair of Committee,	Dimitris C Lagoudas
Committee Members,	Amine Benzerga
	James G Boyd
	Raymundo Arroyave
Head of Department,	Ivett A. Leyva

May 2022

Major Subject: Aerospace Engineering

ABSTRACT

Aging heat treatments in high temperature NiTiHf shape memory alloys (SMAs) create nano-sized precipitates and modify their phase transformation behavior. Depending upon specific application requirements, the phase transformation behavior in the SMA may be tailored through performing appropriate aging heat treatments. However, identifying the correct heat-treatment for the desired modification in the phase transformation behavior can be time-consuming and may require costly experiments. Can micromechanical modeling speed up this process by predicting the microstructure to behavior linkage? What factors need to be considered to improve accuracy? What tools can improve the computation cost?

The modified phase transformation behavior with heat treatment is a result of the new microstructure. Micromechanics connects the microstructure of a material to its behavior and is useful in the context of NiTiHf SMAs for identifying desired microstructures, and thereby the heat treatments. We developed a full-field finite element based micromechanical modeling framework for modeling the microstructure-behavior linkage in precipitation hardened NiTiHf SMAs. Representative volume elements (RVEs) from 3D transmission electron microscopy based reconstructions of the material microstructure were used. With the new modeling framework, the NiTiHf SMA behaviors of different compositions and processing were analyzed. Consequently, compositional and processing effects affecting phase transformation in NiTiHf SMAs were identified.

The full-field micromechanical modeling can be computationally expensive, and the size of RVEs modeled can affect the prediction. Additional investigations were performed to develop faster tools of computation and to determine size RVEs. Fast Fourier Transform (FFT) based solution methodology, in the SMA micromechanical model, was found to improve computation time. Using the FFT, larger RVEs and multiple realizations were analyzed in the SMA micromechanical model and the RVE size statistics were studied. Consequently, for capturing RVE size statistics, we developed a new general formulation using principles of perturbation theory. The dispersion of individual RVE behaviors was formulated as perturbation from the ensemble average behavior,

and hence the ensemble statistics can be derived in terms of perturbations. The new RVE size methodology was demonstrated for SMA micromechanical model, and found to be capturing the RVE statistics in a wide range of precipitate volume fractions.

Further, we investigated the potential of data-based machine learning tools for faster predictions in new RVEs using full-field simulation data. The machine learning models were explored at three levels of complexity: (a) with precipitates, (b) without precipitates and (c) with anisotropy without precipitation. For (a) with precipitates, the RVEs were represented using 2-point statistics and reduced using principal component analysis and taken as input to a machine learning model to target as the effective response. The model predicted responses in new volume fraction RVEs and were compared with full-field simulation. In (b) without precipitates, we investigated the ability of a machine learning model to predict complex partial transformation responses. The machine learning model was built using experimental major actuation responses of a NiTiHf SMA, and its ability to interpolate the behavior to predict minor cycle responses was investigated. In (c) with material property anisotropy, the ability of a machine learning model to capture the anisotropy in single crystal SMA responses was investigated. Simulations from a crystal plasticity model were used for training, and the ability of the machine learning model to predict responses in new orientations was investigated.

A micromechanical modeling framework was successfully demonstrated for predicting the behavior of precipitation hardened NiTiHf SMAs. The computational cost of the modeling framework can be reduced by choosing RVE sizes corresponding to the desired accuracy based on an RVE statistics study. The speed of computation can be improved by using FFT based solution methodology. Faster estimations for new RVEs can be simulated using data-based machine learning methods.

DEDICATION

To my wife Neenu, and children, Gianna and Thomas,

Chachan, Ammachi, Chettayi, Chechi, Jibi and family.

ACKNOWLEDGMENTS

To become an Aggie is a dream of many. I am grateful that I chose Texas A&M University for my PhD studies. During the time as a grad student, I had many beautiful moments to cherish. I want to thank all who helped me in this journey.

I am grateful to Prof. Dimitris Lagoudas, my advisor, for accepting me into the SMART group. His guidance, love, and support were invaluable throughout my PhD journey. He encouraged my ideas and carefully walked me through the process of completely developing them. He allowed me to explore new horizons of data-based modeling and statistical aspects in micromechanical modeling and SMAs. Prof. Lagoudas insisted on explaining the statistical findings on RVEs with solid mathematical derivation and encouraged me. It was because of his persuasion that I came up with perturbation-based explanation for RVE statistics. He has taught me scientific thinking and the process of finding explanation. I greatly owe to Prof. Lagoudas for the progress I made in this dissertation. Apart from the support in research, Prof. Lagoudas and Prof. Magda Lagoudas, have been tremendously supportive to my family during the birth of our children and during the difficulties of the Pandemic.

I am grateful to Prof. Raymundo Arroyave, Prof. Amine Benzerga and Prof. James Boyd for agreeing to serve in my dissertation committee. Their guidance and support throughout this journey were invaluable. Prof. James Boyd helped me understand about shape memory alloys and active materials in general through the course Mechanics of Active Materials.

I acknowledge the DMREF team including Prof. Raymundo Arroyave, Prof. Ibrahim Karaman, Dr. Anjana Talapatra, Tejas Umale and Pejman Honarmandi for helping me understand the basic material science and specifically about NiTiHf SMA literature. Tejas spent time with me discussing the material science aspects of NiTiHf SMAs and educated me on the tension experiments on NiTiHf, which were crucial for their micromechanical modeling. Interactions with Shahin Boluki and Prof. Xiaoning Qian were helpful in understanding the basics of machine learning. The help

from Dexin Zhao and Prof. Kelvin Xie is also acknowledged. They provided the 3D TEM images and educated me on the microstructures, which were necessary in the development of the NiTiHf micromechanical model.

The FFT based homogenization techniques from Dr. Aitor Cruzado and Prof. Amine Benzerga were crucial for the RVE convergence study. With the computationally efficient FFT framework, the responses for SMAs were generated for a broad range of RVEs. The responses generated were helpful in further demonstrating the machine learning framework.

The guidance of Prof. Theocharis Baxevanis during my initial days of PhD were helpful. Prof. Baxevanis helped me settle into the SMART group and guided me into micromechanical modeling. Further, the guidance of Dr. Alexandros Solomou and his help on ABAQUS implementation were essential. Dr. Solomou helped me in coding and understanding SMA UMAT. I thank Dr. Anargyros Karakalas and Dr. Manish Vasoya for giving feedback on my writing.

I want to thank the entire SMART research group including Behrouz, Mahdi, Tianyang, Dimitris, Evi, Edwin, Sameer, Francis, Lei and Ralston for helping and supporting me at different times of my dissertation work. Behrouz encouraged me, and was there to help, especially with many rides and groceries before having a car. Tianyang and Ralston, you were there for me whenever I needed with lots of encouragement and love. You encouraged my writing and helped in proofreading. The writing tips from Tianyang and the writing retreat organized by Patrick Walgren were extremely helpful towards finishing the dissertation. The feedback from Chris Mabe on the grammar and writing in this dissertation was very helpful. Incorporating those comments improved my dissertation. I also thank the Aerospace Department for supporting me financially, especially during the Pandemic, with the special scholarship programs.

Help and support from my friends Harikrishnan, John and the whole Aggie Malayali community were much needed. My neighbors Emil and family gave a lot of encouragement support. My first year roommates Alwin, Naveen and Richards, you are my lifetime friends and support. Their help, support, and prayers are most appreciated. Spiritual support and prayers from Johnson, Chinnu and Manu were there whenever needed. The Jesus Youth community including Dr. Anup,

Rence, Dr. Surya, Michael, Thomson, and rest of the team for supported me mentally and spiritually. I am extremely thankful to the St Mary's Catholic center for their spiritual support throughout my journey. Their presence and activities were such a blessing and refreshment to my soul and mind.

The support from my own family is the greatest. My wife stood by me through it all and encouraged me whenever needed. My children Gianna and Thomas were a blissful stress breaker. I am extremely thankful to my parents for your sacrifices throughout my life, especially towards the end of PhD for coming to the USA and helping by taking care of the kids. I am thankful to my siblings Jibin, Joswin and Divya for your encouragements, especially Jibin for helping during the summer. I am thankful to my extended family including Vellichachan, Kunchachi, Sr. Elsamma, Sr. Mercy and the nun aunts who supported me through prayers and encouragement.

I am grateful to my in-laws, Amma, Appa and Neha for helping us with the kids and giving me room to concentrate during the dissertation. Amma and Neha helped us during delivery and during the difficult times of Pandemic. I am thankful to Jimmichen and family for the encouragements and love you gave us.

Most importantly, from the spiritual point, I have done this PhD only because my Lord and my Savior Jesus Christ provided for me. I acknowledge the guidance of the Holy Spirit, who filled me with the joy and patience during difficulties. I also thank for the intercession of Mother Mary and all the saints.

CONTRIBUTORS AND FUNDING SOURCES

Contributors

This work was supported by a dissertation committee consisting of Professor Dimitris C. Lagoudas , Professor Amine Benzerga and Professor James Boyd of the Department of Aerospace Engineering and Professor Raymundo Arroyave of the Department of Materials Science and Engineering.

Experimental NiTiHf behaviors in Chapter 2 were provided by Dr. Tejas Umale and Professor Ibrahim Karaman of the Department of Materials Science and Engineering. 3D reconstructions of precipitated NiTiHf SMAs in Chapter 2 were provided by Dexin Zhao and Professor Kelvin Xie of the Department of Materials Science and Engineering. The implementation of micromechanical model using ABAQUS UMAT was completed with help from Dr. Alexandros Solomou. The fast Fourier transform methodology for solving micromechanical model simulations for Chapter 3, Chapter 4 and Chapter 5 was provided by Dr. Aitor Cruzado and Professor Amine Benzerga. The actuation experiments of NiTiHf behaviors in Chapter 6 were conducted by Dr. Behrouz Haghgouyan. Single crystal model simulations in Chapter 7 were conducted by Dr. Pawan Chaugule and Professor Jean-Briac le Graverend. All other work conducted for the thesis was completed by the student independently.

Funding Sources

This work is supported by Designing Materials to Revolutionize and Engineer our Future (DMREF) Program under National Science Foundation (NSF) under the Award Number: 1534534. Evaluations of the thermo-mechanical behavior were carried out in the Texas A&M Supercomputing Facility.

NOMENCLATURE

AR	Aspect Ratio
BVP	Boundary Value Problem
CI	Confidence Interval
CP	Crystal Plasticity
C-TT	Composition-Transformation Temperatures
CV	Coefficient of variation
DOF	Degree of Freedom
DSC	Differential Scanning Calorimetry
EDM	Electrical discharge machining
FE	Finite Element
FEM	Finite Element Method
FFT	Fast Fourier Transform
FIB	Focused ion beam (FIB)
GP	Guinier–Preston
GPR	Gaussian Process Regression
HAADF	High-angle annular dark-field
HTSMA	High Temperature Shape Memory Alloy
ML	Machine Learning
MLE	Maximum Likelihood Estimation
MKS	Materials Knowledge System
MSE	Mean Squared Error
PC	Principle component

PCA	Principle component analysis
RVE	Representative volume element
RSE	Relative standard error
SEM	Scanning electron microscopy
SEM	Standard error of the mean
SHT	Solution Heat Treated
SMA	Shape Memory Alloy
SME	Shape Memory Effect
STEM	Scanning Transmission Electron Microscopy
TAMU	Texas A&M University
TEM	Transmission Electron Microscopy
TRIP	Transformation Induced Plasticity
TTs	Transformation Temperatures
VF	Volume Fraction
WQ	Water Quenched

TABLE OF CONTENTS

Page

LIST OF FIGURES

FIGURE Page

LIST OF TABLES

TABLE Page

1. INTRODUCTION

From ancient times, man has explored the natural world in search of new materials. Advanced scientific exploration made possible materials of even further impact, including active materials, or smart materials. These materials exhibit special properties in the presence of temperature change, pressure change, and electric or magnetic field. They have the ability to convert between different forms of energy, for example from thermal to mechanical, from electrical to mechanical, magnetic to mechanical, from acoustic to electric, etc. Examples of active materials are Shape Memory Alloys, Piezoelectric, Magneto-elastic, Electro-acoustic and Photo-elastic. With the modern scientific revolution, active materials became more and more useful and used in variety of engineering applications and to build new technology.

Shape Memory Alloys (SMAs) are active materials which can undergo a diffussionless solid-to-solid phase transformation from low temperature martensitic phase to high temperature austenitic phase induced by variations in temperature, stress or both [8]. Due to their ability to recover from high strains and transform against high stress, they are suitable for designing solid-state actuators of high work density [9, 10]. SMAs are used in many engineering applications: as actuators and morphing structures in aerospace engineering [11, 12, 13, 14, 15], as passive energy dissipators and vibration dissipators in civil engineering [16, 17, 18], and to design stents, micro-devices and implantable devices in biomedical engineering [19, 20, 21, 22, 23].

In the past, most applications relied upon heavy electric actuators, with multiple moving parts. But SMAs, when formed into solid state actuators, provide a powerful alternative, because of their innate capacity to cause actuation motion during phase transformation. While other active materials like piezo-electric materials can also be used as actuators, they are limited by their actuation energy density (power/volume), which limits their use for applications requiring high work output. SMAs, because of their high actuation energy density (10 MJ/m^3) can instead be used to design lighter weight actuators that are powerful enough for morphing wings on aircraft.

Depending on the application, SMAs are chosen for transformation properties fitting the oper-

ating temperature range. Among the various SMA materials known, the NiTi SMAs are commonly used because of their high strength, high transformation strain and lower permanent deformation during actuation. Despite possessing these desirable transformation characteristics, the NiTi SMAs cannot martensitically transform above 100°C. On the other hand, NiTiHf High Temperature Shape Memory Alloys (HTSMAs) can transform at temperatures higher than 100°C [24]. Depending on the composition of the alloying elements, they can exhibit shape memory behavior in a wide range of temperatures ($\sim$ -50°C to 500°C) [3, 25, 26, 27, 28, 29]. The lower material cost compared to other HTSMAs with precious metals, and ability to exhibit high actuation energy density, make NiTiHf SMAs a good choice to design robust and efficient high temperature solid-state actuator systems [24, 30, 31, 32, 33].

Recent discoveries show that aging heat treatments in NiTiHf SMAs lead to formation of nano-precipitates that modify the transformation temperatures and the recoverable strains [34]. As NiTiHf SMA material systems exhibit phase transformation in a wide temperature range, varying levels of precipitates can produce SMAs with a range of transformation properties. This is advantageous for designing SMA actuators, as the transformation behavior can be tuned by applying suitable heat treatments. In addition to modifying the transformation properties, the heat treatments in NiTiHf SMAs are also shown to improve the cyclic response, reducing the Transformation Induced Plasticity (TRIP) associated with repeated thermal cycling [35] and thus making heat treatment modifications desirable. Presently, the NiTiHf SMA material response is known only for limited compositions and aging paths due to the time and cost associated with testing. The SMA designing process can be accelerated with the help of computational models that can predict the actuation responses from the heat treatment modifications.

In this thesis work, the focus is to assist the development of new NiTiHf shape memory alloys through micromechanical modeling. The concepts developed here are general and could be useful in the developments of other material systems as well. This chapter is structured with a brief introduction to the shape memory alloy behavior including NiTiHf, the challenges in the micromechanical modeling development, the challenges and importance of size microstructure representations

in micromechanical modeling, and some developments in the data science modeling which can assist the micromechanics predictions. The introduction chapter will give a brief outline of key concepts, and subsequent chapters will develop these ideas further with details of the modeling.

1.1 Shape memory alloy (SMA) behavior

SMAs offer complex behaviors based on the different thermo-mechanical loading path the material undergoes [8]. A shape memory effect (SME) is observed when the SMAs in the twinned martensitic phase are deformed, unloaded and heated above austenite finish temperature, recovering the original shape by transforming back into its parent austenitic phase. Pseudoelastic behavior in SMAs is observed when stress is applied to material at austenitic temperatures, creating a stress-induced transformation to the martensitic state, whereupon unloading it transforms back to austenite and any strain is recovered. The SMAs loaded under constant stress, when taken through cyclic cooling and heating between the austenite and martensite phase, produce actuation response. Modeling these constant stress responses is important for designing SMA-based actuators for predicting the extent of actuation displacement. For the current work, the focus is only on modeling the actuation responses of SMAs.

1.1.1 SMA actuation response

An actuation loading path for SMA in a temperature-stress phase diagram and a typical strain – temperature response are shown in Figure 1.1. The path indicated by the blue dotted line from A to B and B to A in Figure 1.1 (a) represents the cooling and heating of the material in the presence of a fixed stress. The material transforms between the high temperature austenitic phase (A) and the low temperature martensitic phase (B) during the actuation loading path. A typical actuation response is shown in Figure 1.1 (b), and the two phases are described with the crystalline structure. The phase transformations produce a sudden expansion or contraction in the strain versus temperature response, which is captured using a transformation strain parameter (H) in the Lagoudas et al.[5] constitutive model for SMAs. The phase transformation ranges are described using transformation temperatures (TTs), which can be calculated from the response using the tangent lines approach

shown in Figure 1.1 (b).

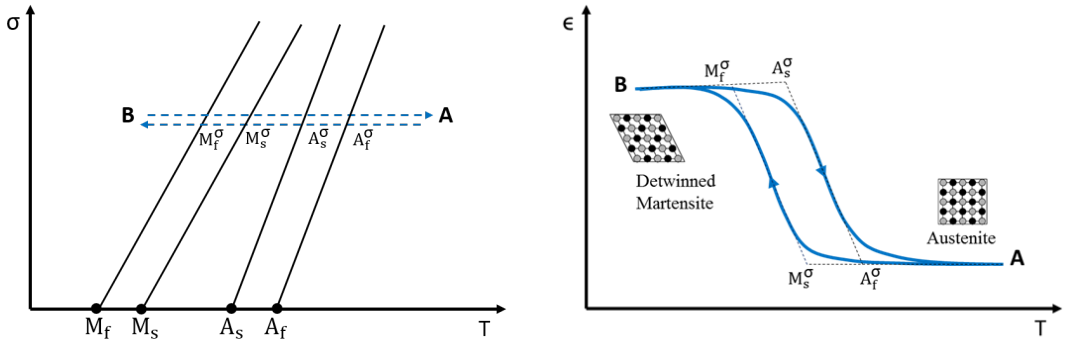

Figure 1.1: Actuation loading path and response: a) loading path shown on a typical phase diagram, and b) a representative strain - temperature response shown with the tangent line approach.

1.1.2 Shape memory alloys constitutive model

The constitutive model for SMAs used in this work is based on Boyd and Lagoudas' unified model for polycrystalline SMAs [36, 37, 38]. The evolution equations in the model are developed within the framework of continuum thermodynamics, and classical rate-independent small-strain flow theory is used. In this model, the Gibbs energy is used as the thermodynamic potential instead of Helmholtz free energy for modeling the thermomechanical loading path in the stress-temperature space. The form of Gibbs free energy G is given by Eq. (1.1) defined in terms of the independent state variables temperature T and stress $\boldsymbol{\sigma}$ and the state variables strain $\boldsymbol{\epsilon}$ and martensitic volume fraction ξ. The explicit form of the Gibbs free energy is given by Boyd and Lagoudas [36, 37], and Qidwai and Lagoudas [39].

$$\begin{aligned} G(\boldsymbol{\sigma}, T, \varepsilon^t, \xi) = & -\frac{1}{2\rho}\boldsymbol{\sigma} : \boldsymbol{S} : \boldsymbol{\sigma} - \frac{1}{\rho}\boldsymbol{\sigma} : [\boldsymbol{\alpha}(T - T_0) + \boldsymbol{\varepsilon}^t] \\ & + c\left[(T - T_0) - T \ln\left(\frac{T}{T_0}\right)\right] - s_0 T + u_0 + \frac{1}{\rho} f(\xi) \end{aligned} \tag{1.1}$$

where T_0 is the reference temperature, $\boldsymbol{S}$ is the fourth-order effective compliance tensor, $\boldsymbol{\alpha}$ is the second-order effective thermal expansion tensor, c is the effective specific heat, s_0 is the effective specific entropy at the reference state and u_0 is the effective specific internal energy at the reference state. The transformation hardening function is defined using the function $f(\xi)$ and will be defined subsequently.

The effective properties of the SMA material are expressed in terms of the properties of the pure phases (austenite and martensite) and the martensite volume fraction, ξ given by equations (1.2) -(1.6). Here, the rule of mixture is used to calculate the effective property in terms of the volume fraction of the pure phases.

$$\boldsymbol{S}(\xi) = \boldsymbol{S}^A + \xi\left(\boldsymbol{S}^M - \boldsymbol{S}^A\right) \tag{1.2}$$

$$\boldsymbol{\alpha}(\xi) = \boldsymbol{\alpha}^A + \xi\left(\boldsymbol{\alpha}^M - \boldsymbol{\alpha}^A\right) \tag{1.3}$$

$$c(\xi) = c^A + \xi\left(c^M - c^A\right) \tag{1.4}$$

$$s_0(\xi) = s_0^A + \xi\left(s_0^M - s_0^A\right) \tag{1.5}$$

$$u_0(\xi) = u_0^A + \xi\left(u_0^M - u_0^A\right) \tag{1.6}$$

An evolution equation for the transformation strain $\boldsymbol{\varepsilon}_{tr}$ is defined in terms of the changes in the martensitic volume fraction ξ, which is given as follows.

$$\begin{aligned} \dot{\boldsymbol{\varepsilon}}_{tr} &= \boldsymbol{\Lambda}\dot{\xi} \\ \boldsymbol{\Lambda} &= \begin{cases} \boldsymbol{\Lambda}^{fwd} & \text{if } \dot{\xi} > 0 \\ \boldsymbol{\Lambda}^{rev} & \text{if } \dot{\xi} < 0 \end{cases} \end{aligned} \tag{1.7}$$

where, the tensor $\boldsymbol{\Lambda}$, defines the direction of transformation strain. The components of the tensor $\boldsymbol{\Lambda}$ is defined by the following equations.

$$\boldsymbol{\Lambda}^{fwd} = \frac{3}{2}H^{cur}\frac{\boldsymbol{\sigma}'}{\overline{\sigma}'},\ \boldsymbol{\Lambda}^{rev} = \frac{\boldsymbol{\varepsilon}_{tr}^{rev}}{\overline{\varepsilon}_{tr}^{rev}}. \tag{1.8}$$

Where, H^{cur} is the transformation strain at complete transformation, $\overline{\sigma}' = \sqrt{\frac{3}{2}||\boldsymbol{\sigma}'||^2}$ is the Mises equivalent stress and $\boldsymbol{\sigma}' = \boldsymbol{\sigma} - \frac{1}{3}\text{tr}(\boldsymbol{\sigma})\mathbf{1}$ is the deviatoric stress tensor. The transformation strain at the reversal point is denoted by $\boldsymbol{\varepsilon}_{tr}^{rev}$ and the effective transformation strain at the reversal of the phase transformation is given by $\overline{\varepsilon}_{tr}^{rev} = \sqrt{\frac{2}{3}||\boldsymbol{\varepsilon}_{tr}^{rev}||^2}$. In both the above definitions, $||\cdot||^2$ denotes the inner product of the enclosed quantity. The transformation strain is oriented by the direction of the deviatoric stress in forward transformation, hence a J_2 form of the direction tensor is chosen. Whereas in reverse phase transformation, it is assumed that the average orientation of the martensite governs the direction.

For most SMAs, the maximum transformation strain at complete transformation H^{cur} is a function of stress. At high stress levels, a saturated value of maximum attainable transformation strain H^{sat} is reached. The value of H^{sat} depends on material system, processing conditions resulting from different crystallographic and morphological textures. To capture the evolution of H^{cur} with stress, an exponential function in terms of the H^{sat} given by Eq. (1.9) is used.

$$H^{cur}(\overline{\sigma}) = H^{sat}(1 - e^{-k\overline{\sigma}}) \tag{1.9}$$

where, k is the exponent that controls the rate of H^{cur} evolution. When transformation happens, the stress tensor should satisfy the transformation surface given in the Eq. 1.10.

$$\Phi = 0,\ \Phi = \begin{cases} \Phi^{fwd} = \pi^{fwd} - Y_0 \ \text{ for } \quad d\xi > 0, \\ \Phi^{rev} = -\pi^{rev} - Y_0 \ \text{ for } \quad d\xi < 0; \end{cases} \tag{1.10}$$

where, the π^{fwd} and π^{rev} are thermodynamic forces for forward and reverse phase transformation respectively, and Y_0 is the critical value of the thermodynamic force to allow phase transformation to initiate and continue. The π^{fwd} is given by the following equation Eq. (1.11).

$$\pi^{fwd} = \sigma_{ij}\Lambda_{ij}^{fwd} + \frac{1}{2}\Delta S_{ijkl}\sigma_{ij}\sigma_{kl} + \rho\Delta s_0 T - \rho\Delta u_0 - f^{fwd}, \tag{1.11}$$

where, f^{fwd} is given by

$$f^{fwd} = \frac{1}{2}\alpha_1[1 + \xi^{n1} - (1-\xi)^{n2}] + \alpha_3. \tag{1.12}$$

Similarly, the thermodynamic driving force π^{rev} is given by Eq. (1.13).

$$\pi^{rev} = \sigma_{ij}\Lambda^{rev}_{ij} + \frac{1}{2}\Delta S_{ijkl}\sigma_{ij}\sigma_{kl} + \rho\Delta s_0 T - \rho\Delta u_0 - f^{rev}, \tag{1.13}$$

and f^{rev} is given by

$$f^{rev} = \frac{1}{2}\alpha_2[1 + \xi^{n3} - (1-\xi)^{n4}] + \alpha_3. \tag{1.14}$$

The functions f^{fwd} and f^{rev} represent the hardening functions introduced for capturing the smooth phase transformation in the material. The symbol Δ is used in the expressions to denote the difference in property between the martensitic and the austenitic states for stiffness (in ΔS_{ijkl}), specific entropy (in Δs_0) and internal energy (in Δu_0). The variables α_i ($i = 1, 2, 3$) and n_i ($i = 1, 2, 3, 4$) are coefficients with real number values.

The model parameters in these constitutive relations must be calibrated based on experiments. These parameters include (i) stiffness properties of austenite and martensite (ii) parameters in the definition of current transformation strain $H^{cur}(\sigma)$ (iii) and six model parameters ($\rho\Delta s_0$, $\rho\Delta u_0$, α_1, α_2, α_3, Y_0) that characterize the transformation. These parameters are estimated from the properties that can be measured from the material behavior listed below. The commonly calibrated material parameters for the SMAs are stiffness properties of austenite and martensite (E^A, E^M), four transformation temperatures at zero load: martensitic start and finish (M_s, M_f) austenitic start and finish (A_s, A_f), phase-diagram forward and reverse transformation slopes (C^M, C^A), Poisson's ratio (ν^A, ν^M) and thermal expansion coefficients (α^A, α^M). The stiffness properties and thermal expansion coefficients are calculated directly the slopes of stress-strain variation and strain-temperature variation of the material. The phase-diagram shows the beginning and ending of forward and reverse phase transformation at different stress levels. The transformation temperatures and phase diagram slopes are estimated directly from the temperature-stress phase diagram of the SMA. More on the calibration and estimation of the model parameters can be found in [8].

1.2 Micromechanical modeling of materials

Micromechanics is one of the recent developments in the field of mechanics, and aims at applying the continuum level theories at the microscopic level in the material and predict the thermo-mechanical behavior of the material. The goal in micromechanics is to predict the behavior of the material by modeling its microstructure. Using continuum mechanics theories, the mechanics of the material is modeled from the microstructure. As the phenomena at the microscopic level is modeled, the macroscopic behavior is estimated as the average from the microscopic level. With the application of theories such as elasticity and plasticity on the material microstructure, the complex phenomena such as fatigue, fracture, material imperfections are studied.

Some key developments in the field of mechanics gave rise to the new field of micromechanics in the last 50 years. The earliest theories in continuum micromechanics are 'rule of mixtures in composites' by Voigt (1887) and Reuss (1929). These were simple equations that gave rough estimations of the property in the heterogeneous material with assumptions of uniform stress or strain and did not consider the micro-level mechanics and interaction between different heterogeneity inside the material. However, the beginning of the field of micromechanics in its present form may be traced to the Eshelby's work in 1957 [40] on the elastic field of an ellipsoidal inclusion. Eshelby developed an analytical solution for the elastic field around elliptical inclusion in an elastic infinite medium. With the Eshelby solution, estimation of effective material responses in heterogeneous materials with ellipsoidal inhomogeneities were made possible. Eshleby's solution worked well for dilute cases with low volume fraction. Further, the Mori-Tanka [41] approach extended the Eshelby's approach with better accuracy in the case of higher volume fractions. By the early 1980s, the micromechanics was fully developed into a subject area of its own. Several books like Mura (1986) [42], Nemat- Nasser and Hori (1993) [43], and Krajcinovic (1996) [44] published in the following years were useful for learning the techniques in micromechanics.

Through micromechanical modeling, one is able to predict the material behavior from its microstructure. By modeling the material at the microscopic level from the microstructure and upscaling its effects, the observable behavior of the material at the macroscopic level can be predicted.

The macroscopic response of the material is the result of cumulative effects from the mechanics of deformation at the microscopic level. The idea here is that the observable phenomenon of the material is directly related to the activity at the microscopic level and vice versa within the domain of continuum mechanics. Through micromechanical modeling, a direct correlation between the microstructure and the effective material response is developed. The micromechanics tools thus enable us to identify the phenomena happening at the microscopic level in relation to the phenomena at the macroscopic level and vise versa. This is very powerful to understand the material as a whole.

The methods developed in micromechanical modeling can be classified in two categories: mean-field approaches and full field approaches. The earlier developed analytical methods such as Eshelby's [40] and Mori-Tanka [41] fall into the category of mean-field approaches. The boundary value problem (BVP) based homogenization through finite element method (FEM) [45, 46, 47, 48, 49] and fast Fourier transform (FFT)[50, 51, 52, 53, 54, 55] methods fall into the category of full field approaches. In the mean-field approach, as the name suggests, the interactions inside the microstructure are modeled through average field (e.g. stress, strain) values. For e.g. in Eshelby's [40] and Mori-Tanka [41] methods, the interaction between the particles is captured through the average strain values in the surrounding matrix. Hence, for the mean-field approaches, the interactions in the microstructures can be modeled with analytical expressions of the average field variables. Whereas in the full field approaches, the focus is to model the field interactions close to the reality, taking into consideration the spatial variations in the microstructure. As the size of microstructure representation and grids size increase, the accuracy of the method increase the field modeled will be closer to the actual. Thus, in the context of full-field approaches, the size of Representative Volume Element (RVEs) [56] modeled is more relevant.

The full field approaches give certain advantages in the case of NiTiHf SMA modeling. The precipitates in the SMAs do not have perfect ellipsoidal shapes, and the full field approach enables the modeling of irregular geometry. With tools of reconstruction, the full 3D configuration of the microstructures in NiTiHf SMAs are available. The complexity of interaction between the

particles is increased with phase transformation, and the full field approaches enable to model these interactions more accurately. With the full field approaches, complex mechanisms such as diffusion and coherency can be easily modeled, and their effects can be isolated. The full field techniques come with better visualization capabilities, which helps to better understand the mechanics.

1.2.1 Challenges in the micromechanical modeling

The modeling of micromechanics of the materials has associated challenges. Some common challenges are the following.

- Understanding the mechanics at the micro-level is key to modeling the material. Often times, the mechanics at the material level can be different from the material's macroscopic behavior. Thus, constitutive models capturing the behavior at the material level is required.

- Determining Representative Volume Elements (RVEs) of the material can be a difficult task. Especially when the material microstructure is very small (e.g. nano-size precipitates in NiTiHf), it can often become very difficult to accurately determine the microstructure parameters such as the volume fraction.

- Estimation of material properties of the phases at the micro-level can be very difficult. Often times this is compromised by assuming the same properties as that at the macroscopic level.

In the case of NiTiHf SMAs, these challenges were resolved by development of new tools and with assumptions that explain their behavior. The challenges in NiTiHf include the modeling of the constitutive behavior of the participating phases in the material, generating the correct representation of their microstructures, estimation of appropriate RVE size and estimation of properties at the microstructure level. Using tools of 3D reconstruction (Chapter 2) the representations of the microstructures in NiTiHf were accurately determined. The constitutive behavior of the phases in the materials were modeled assuming macroscopic SMA behavior modeled with Lagoudas et al.[5] constitutive response in the phase transforming matrix and elastic response in the non-transforming [57] precipitates. The material properties at the microscopic level were resolved, assuming similar

properties to macroscopic SMA in the matrix. For the precipitate phase, the stiffness properties were estimated through inverse calculations taking into consideration the associated measurement uncertainties. The above developments are explained in detail in Chapter 2.

1.2.2 Size of Representative Volume Element in micromechanical modeling

In full-field micromechanical modeling, size of RVEs can affect the predictions of material behavior. Ideally it is good to model a very large volume of material in the RVE, however this will result in higher computational cost. The lower volume of RVEs can give uncertain predictions, as the representation is not converged. In this context, it is required to determine an optimal RVE with less uncertainty in the predictions and less computational cost. The optimal size of RVEs for giving predictions of the material behavior within a tolerance can be resolved through a statistical study, correlating RVE size to their uncertainty in estimations.

In the micromechanical models to predict the aged SMA response, the RVEs consist of a homogenized SMA matrix with randomly distributed precipitates [6, 58, 59]. Due to the high computational cost of the simulations, the statistical analysis in these studies [6, 58, 59] were limited to few particles. Thus, the modeling predictions may present dispersion in the effective response when the volume fraction of the precipitates, material properties or loading conditions are changed. In this context, it is important to estimate the converged RVE size to make predictions of the effective heat-treated response. In Chapter 4, the tools required to determine the optimum size of RVE is developed. Further, the convergence of the SMA behavior with RVE size is resolved with newly developed tools.

1.3 Data-based machine learning approaches in micromechanics

Data-based modeling is gaining popularity in nearly every field of research, including micromechanics, thanks to recent developments in data science. Because of the massive amounts of data that can be created, kept, and analyzed, data-driven models have been developed that can make faster predictions. Because computing costs associated with modeling large RVEs in the micromechanical modeling can become costly, data-based models can be developed using previously

generated data from micromechanical models. These faster models are useful in optimization and multiscale modeling, where many micromechanical model evaluations are necessary.

The way the input and targets are described is critical for the efficiency of data-based modeling. A preprocessing of input parameters to reduce their size can improve efficiency, as data-based models perform better when the inputs and targets are represented in a reduced in size form. The key input in the micromechanical modeling is the microstructure, which contains large amount of spatial information. Considering the microstructure with its full representation reduces the efficiency of data-based models. Hence, it is important to find ways to represent the microstructure using a minimum number of parameters without losing key information.

Spatial statistical techniques such as 2-point correlations are very useful for capturing the statistics in the microstructures and further reducing their representation. 2-point correlations are successfully used to describe microstructures of different size and morphology in many recent works [60, 61, 62, 63]. The advantage of using a 2-point spatial statistical representation is that it allows us to represent complex microstructures of various sizes and morphologies within the same framework of statistical representation[64]. The information at each grid in the 2-point statistic representation contains the same statistical information, irrespective of the geometrical complexity in the microstructures compared. This approach makes the comparison between different microstructures easier, and a simpler representation can be built using dimensionality reduction techniques.

Modern computational resources have made it easier to run numerous small-scale micromechanics simulations. This aids in the creation of a database that covers the design space, allowing for the development of robust data-based models covering all possible microstructures. The micromechanics community can now use some of these statistical methodologies more easily thanks to open source Python tools like 'PyMKS' developed at Georgia Tech [65]. RVEs of SMA microstructures can be represented using 2-point correlations with the help of PyMKS. Low-dimensional data-based ML models for the microstructure-property linkage are also possible using dimensionality reduction via principal component analysis (PCA) of statistical representations. The dimensionality of the model can be efficiently truncated according to the accuracy required

from PCA, and makes it possible to represent the microstructure with minimum number of variables in a data-based model.

Chapter 5 focuses on implementation of data based modeling for shape memory alloy micromechanical modeling. Simplified representations for RVEs with precipitated microstructures were created using 2-point statistics. Further, using neural network based machine learning, the predictions of phase transformation behaviors were trained and predictions were made. In Chapter 7, an attempt to extend the data based modeling for multiscale homogenization starting with a single crystal model is presented. Data-based modeling approach were used to capture the anisotropy in the single crystal responses. The responses in new orientations were predicted from the models and can be useful in a multiscale modeling approach accounting the grain level interactions.

1.3.1 Disadvantages in data based modeling

Some disadvantages in data based micromechanical modeling are listed:

- Data based modeling requires a considerable amount of data generation running the micromechanical modeling. This can be a difficulty when we need to modify the modeling approach or implement in a new material system.

- The data based modeling cannot give good predictions outside the domain in which they are trained compared to the physics based models. The physics based models, while computationally costly, can make realistic predictions within the constraints imposed by the physical laws. Whereas, the predictions from data based models outside the domain in which they are trained can be significantly erroneous, which users have to be aware of.

1.4 Data-driven modeling for partial transformation response

In designing SMA actuators and for developing control algorithms, faster and more accurate modeling of SMA behavior incorporating partial phase transformation are required [15]. There have been considerable efforts in phenomenological modeling of SMA actuation behaviors. The constitutive model developed by Lagoudas et al. [38] has successfully captured with good accuracy the major cyclic responses in the SMA polycrystals. The modeling attempts in the works in [66, 67,

68, 37] have modeled the minor cycle responses in the SMAs. Although physics based modeling is much more successful in producing new insights, accuracy can be compromised because of modeling assumptions. Oftentimes, the experimental data is fitted into the assumed model, not utilizing the full potential of information contained in them.

As data-based models are capable of adapting to the data, the full potential of information contained in them can be considered while making predictions. With the use of data driven machine learning models such as neural networks, faster and accurate models which can train directly from the experimental responses can be developed. Neural networks are capable of capturing complex behaviors and making faster predictions with less computational cost. Moreover, they can capture the hidden features specific to the experimental data, which may not be fully captured in the phenomenological modeling. The downside of depending on data driven techniques is that they can be inadequate to give new insights and cannot project those insights into another material behavior. Neural network based modeling has been successfully implemented in medical, material science, agriculture and finance fields to make predictions in real-time scenarios [69]. Relevant applications in material modeling include modeling Young's modulus [70] and strain responses [71]. Yet, for SMA responses, there have been few works using neural network based model for modeling SMA cyclic responses [72] and SMA wire actuation [73].

In Chapter 6, the neural network based modeling is implemented for the actuation transformation responses of a NiTiHf material. A neural network model was trained on the major cycle responses of the material at different stress levels. Predictions were made for major cycle responses at new stress levels and minor cycle responses in new temperature ranges. Comparisons show the presented approach captured the major cycle responses and the minor cycle responses close to the experimental cases that were available. Many complex minor cyclic responses were modeled for new loading paths using the trained neural network model. Although the predictions for these new paths look realistic, the accuracy of the predictions could not be verified because experimental behaviors were not available. To the best of the author's knowledge, this is the first attempt to use data based modeling to capture the partial transformation cycling in SMAs.

1.5 Research objectives

The primary goal of this work is to build a micromechanical modeling framework to predict the material response of heat treated NiTiHf alloys. Based on the challenges described in the micromechanical modeling so far, the subsequent objectives were identified with the goal of improving the micromechanical modeling framework. The tools developed in these objectives were focused on improving accuracy and making predictions faster. Further, with the data based models, the goal was to build tools that predict the behavior of NiTiHf SMAs in a faster manner and also extend to behaviors such as minor loop cycles. The objectives proposed in this work are summarized below.

- **Finite element based micromechanical modeling framework for Ni-Ti-Hf SMAs**

  In this objective, the focus is on building a finite element (FE) based micromechanical framework to capture the constitutive response of precipitation hardened NiTiHf SMAs. The RVEs used for the modeling are motivated from TEM images and effects of Ni and Hf depletion due to precipitation were taken into consideration. The predictive capability of the developed framework was assessed through comparing with experimental responses.

- **Fast Fourier Transform based solution in micromechanical modeling**

  The FFT based solution methodology can be useful in making faster prediction in micromechanical modeling. In this objective, the advantages of FFT based solution compared to FEA based solution is analyzed. The micromechanical model for SMAs was considered for comparison of these methodologies.

- **Determination of RVE size for convergence of effective strain response**

  The optimum size of Representative Volume Element (RVE) for the micromechanical framework has to be determined for accurate predictions using the model. In this objective, the focus is a systematic study of RVE size on microstructural RVEs in phase transforming Shape Memory Alloys (SMAs) with secondary non transforming precipitates. The dispersion of the strain behavior were quantified statistically, and new correlation relations were derived for predicting the RVE size.

- **Machine learning model for predicting SMA response from microstructures**

  Design optimization can be greatly speeded up with the help of machine learning tools that can interpolate the behavior in a faster manner in new microstructures. In this objective, the focus is building a machine learning model which can interpolate the precipitation hardened behavior in the RVEs. To assist multiscale modeling, a data based modeling is also demonstrated for single crystal behaviors.

- **Machine learning modeling for SMA response with minor loop predictions**

  In this objective, the goal is to build a data based model for NiTiHf SMA responses, that can make extensive predictions for the minor loop responses. The ability of the model is validated by implementation on experimental responses.

The subsequent chapters in this dissertation address these objectives.

2. MICROMECHANICAL MODELING OF HIGH TEMPERATURE SHAPE MEMORY ALLOYS WITH TEM RECONSTRUCTED MICROSTRUCTURES [1]

2.1 Introduction

Micromechanical modeling has been successfully used in the past to predict the SMA responses. The geometry and mechanical properties of the phases, the interaction between the phases, and bridging these small-scale individual phenomena to the imposed macroscopic loading conditions are key aspects in developing such micromechanical models. Many of the past works used orientation averaging techniques or mean field approaches such as the Mori-Tanaka approximation to model the SMA response in the presence of precipitates [75, 76, 77, 78, 79, 80, 81]. These methods were limited to capturing the effects of regular precipitate shapes and simple interactions. In recent years, Finite Element Analysis (FEA) based full-field modeling using the approach of Representative Volume Elements (RVEs) is found to be effective not only in capturing the effects of irregular shapes of precipitates but also capable of predicting the effects due to compositional variations in the NiTi SMA systems [58, 82, 49, 1, 59].

In the current work, an FEA based full-field micromechanical model is developed to predict the precipitation hardened NiTiHf SMA actuation response from the precipitate microstructure. RVEs of the SMA microstructure were generated in the following two ways: (1) 3-D reconstructions of the precipitates from TEM micrographs and (2) approximated ellipsoidal precipitates RVEs. Constructing RVEs from the TEM sample is an expensive process, but it gives the real 3-D microstructure, while constructing RVEs using ellipsoids is an approximated description but is less expensive. Using the approximated ellipsoidal method helps in studying the effects due to microstructural variations, as they are easy to generate. In both RVEs, the precipitates were modeled as non-transforming elastic material and surrounded by polycrystalline phase-transforming ma-

[1] Reprinted with permission from "Effects of microstructure and composition on constitutive response of high temperature shape memory alloys: micromechanical modeling using 3-D reconstructions with experimental validation.", Acta Materialia (2022): 117929 by Joy, Jobin K., Tejas Umale, Dexin Zhao, Alexandros Solomou, Kelvin Xie, Ibrahim Karaman, and Dimitris C. Lagoudas. [74].

trix. The matrix was modeled using the Lagoudas *et al.* [5] constitutive model, and the precipitates using isotropic elastic behavior. In the thermo-mechanical constitutive model of the matrix, the compositional effects were incorporated by considering the composition dependency of the phase transformation properties. The effects of residual stress arising from lattice mismatch and the difference in elastic properties between the phases were also accounted for.

The resulting FEA micromechanical model was then used to analyze the actuation behavior in aged NiTiHf samples for different heat treatments from the physics and modeling perspectives. The precipitation hardened responses of $\mathrm{Ni_{50.3}Ti_{29.7}Hf_{20}}$ SMA were modeled, and the behavior was analyzed in terms of the microstructure and composition changes. Estimation of composition effects, stiffness of the precipitate phase and material parameters of the matrix phase were carried out through calibration using the FEA model. The 3-D reconstructions studied in this work focus on shorter heat treatments and varying volume fractions compared to previous efforts [83, 84], where the focus was on very long heat treatments. This work presents the first modeling study on the actuation response of HTSMAs considering realistic 3-D microstructures. Knowledge of the real microstructures from the 3-D reconstructions helped to validate the methodology for ellipsoidal shaped RVEs. Experiments conducted on multiple samples of solutionized (unprecipitated) and heat treated $\mathrm{Ni_{50.3}Ti_{29.7}Hf_{20}}$ SMA were used to analyze the sample-to-sample variation. In addition, the ellipsoidal RVE methodology was used for modeling the heat treatment responses in two other SMAs available in the literature [4] with compositions $\mathrm{Ni_{50.3}Ti_{29.7}Hf_{20}}$ and $\mathrm{Ni_{50.3}Ti_{34.7}Hf_{15}}$, but with a different processing history. The comparison of simulations and experiments demonstrates that the proposed micromechanical model framework accurately predicts the precipitation hardened response and will be extremely useful in designing aging heat treatments in NiTiHf SMAs.

The chapter is structured as follows. Section 2.2 describes the microstructural observations from TEM study in NiTiHf in different heat treated samples. 3-D reconstructions of the microstructure, volume fraction estimation and the precipitate morphology are shown. Section 2.3 describes the experimental observation of actuation responses in precipitation-hardened NiTiHf

and discusses the mechanisms through which the precipitates can modify the actuation response. Section 2.4 discusses the key steps in the developed micromechanical model. Section 2.5 discusses the steps involved in building approximate RVEs with ellipsoidal precipitate shapes. Section 2.6 explains the calibration of model parameters from the experimental responses. Section 2.7 discusses the comparison of experiments and predictions. Section 2.8 summarizes the main conclusions from the work.

2.2 Microstructure in NiTiHf and 3-D reconstruction

An accurate description of the precipitate microstructure and measurements of the volume fraction of precipitates is needed in the micromechanical modeling. Regular TEM and scanning TEM (STEM) micrographs display only the 2-D projection of 3-D objects, and cannot give a complete picture of the shape of precipitates. The volume fraction of the precipitates, which is critical information required in the modeling, cannot be estimated accurately from the 2-D representations. To overcome these difficulties, 3-D reconstructions of the microstructures were generated. In this section, the procedure used for these reconstructions, the key observations and estimation of volume fraction are discussed.

2.2.1 Experimental procedure

Elemental Ni, Ti, and Hf (99.98%, 99.95% and 99.9% in purity, respectively) were used to fabricate a Ni-rich $Ni_{50.3}Ti_{29.7}Hf_{20}$ (at.%) SMA via vacuum induction melting. The material was then vacuum homogenized at 1050°C for 72 hours and air cooled. The ingot was hot forged to an R ratio of 2.35:1 followed by cooling in the air. The samples cut using wire electrical discharge machining (EDM) were then solution heat treated (SHT) at 900°C for 1 hour followed by water quenching. The samples were then heat treated at 550°C, 600°C and 650°C for 10 hours followed by air cooling to grow precipitates with various sizes and volume fractions. The TEM specimens from the bulk samples were mechanically polished using 1200-grid silicon carbide papers and punched into 3 mm TEM discs with a thickness around 100 μm. These discs were then twin-jet electropolished using a Tenupol-5 polishing system with a solution of 30% nitric acid in ethanol

at -30°C. High-angle annular dark-field scanning transmission electron microscopy (HAADF-STEM) micrographs were acquired near the perforation to characterize the precipitates using a FEI Tecnai G2 F20 Super-Twin FE TEM operating at 200 keV. 3-D models of precipitates were reconstructed from the HAADF-STEM images using TEM tomography. The micrographs were taken under different magnifications to ensure similar amounts of precipitates were captured in the view field. The tomographic tilt series were collected over 90° at 2° intervals. Image alignment and 3-D reconstruction were performed using open-source tomography platform Tomviz with a "weighted back projection" algorithm [85]. The detailed process is described in Levin *et al.* [86]. The reconstructed 3-D models were then imported into the Paraview software [87], where the visualization and analysis were performed.

2.2.2 Microstructure in 2-D HAADF-STEM

Precipitates of different sizes and number densities were observed in the heat-treated SMAs. The HAADF micrographs shown in Figure 2.1 were taken at the same magnification for direct comparison. In all samples, the precipitates appear to be brighter. Such contrast mainly comes from the higher Hf content in the precipitates than in the matrix. Figure 2.1(a) illuminates a high density of nano-precipitates with ~ 10 nm in size in the 550°C heat-treated NiTiHf. Increasing the heat treatment temperature to 600°C, the precipitates grow to ~ 30 nm in size with a decreasing number density (Figure 2.1(b)). Further, increasing the heat treatment temperature to 650 °C results in even larger precipitates (~ 150 nm long) and lower number density (Figure 2.1(c)). In contrast to the non-uniform precipitate distribution in NiTi [88] with differences at the grain interior and grain boundary, the precipitate distribution in NiTiHf were observed to be more uniform. The difference between NiTi and NiTiHf can be explained by their differences in precipitation kinetics. In NiTi, the precipitates form directly from the solute via heterogeneous nucleation on crystallographic defects, whereas in NiTiHf, the solute atoms form Guinier–Preston (GP) zones first and the GP zones then evolve into precipitates, which creates a more uniform distribution of precipitates.

TEM studies on the precipitates showed coherency between the precipitate and the austenite B2 matrix, with continuity of the atomic planes across the precipitate interfaces over large distances

more than 50 nm [34, 89]. The heat treatments $550°$C 10h and $600°$C 10h produce precipitates smaller than 50 nm, which can be assumed coherent with the matrix. Whereas, the heat treatment $650°$C 10h produce precipitates of 200 nm size that may lose some coherency. However, the extent of incoherency is difficult to be measured. Preliminary calculations performed by the authors indicates that a loss of coherency causing up to 20% loss of precipitate stiffness do not modify the responses significantly. Thus, in the modeling, a complete coherency was assumed owing to the better coherency properties in the h-phase precipitates.

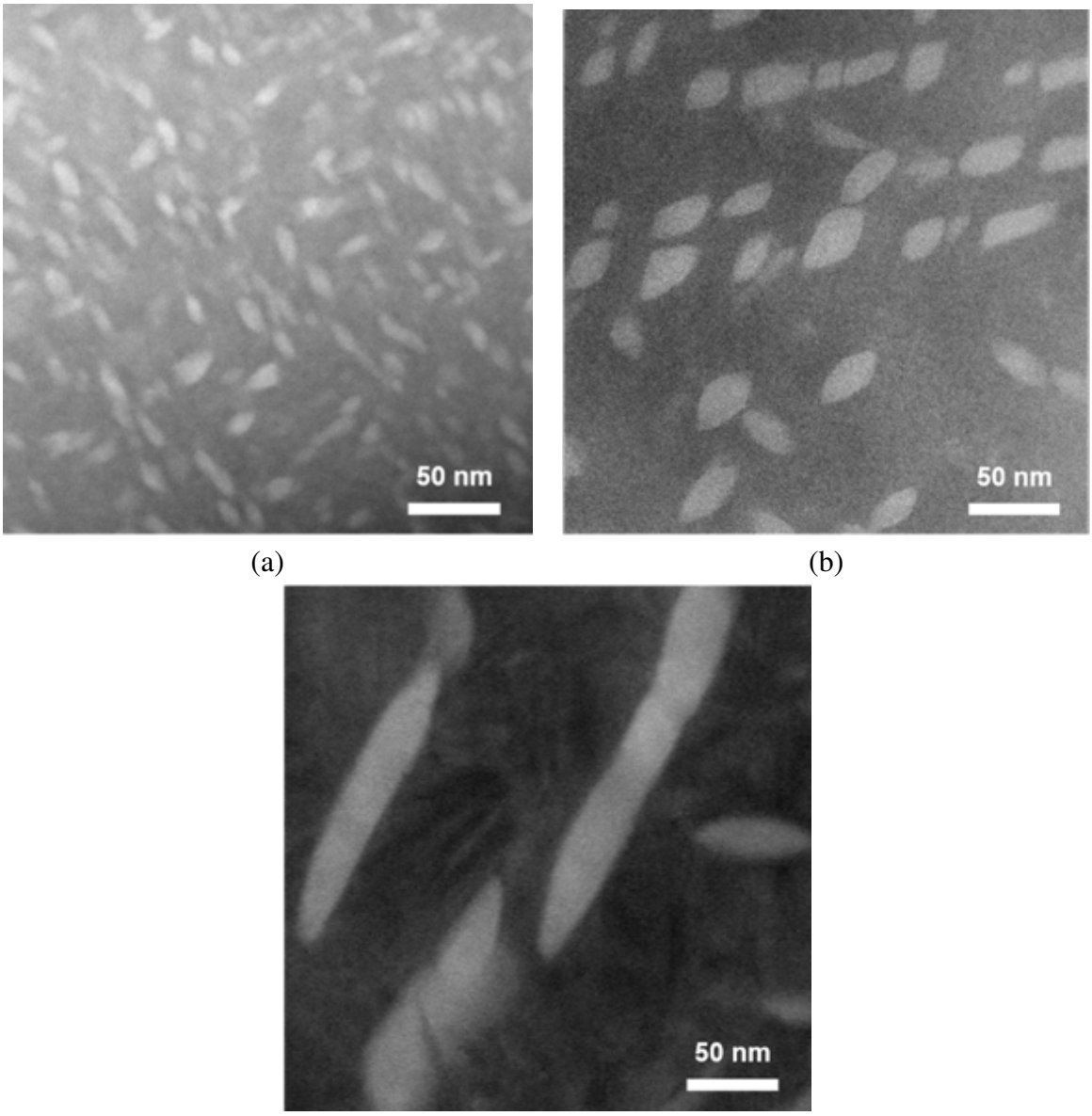

(a) (b)

(c)

Figure 2.1: HAADF-STEM images of $Ni_{50.3}Ti_{29.7}Hf_{20}$ heat treated at (a) 550°C for 10 h, (b) 600°C for 10 h and (c) 650°C for 10 h.

2.2.3 Microstructure in 3-D reconstructions

TEM-based tomography was used to extract the 3-D microstructural features of the precipitates. Figure 2.2 show the 3-D reconstruction of the microstructures in the 3 heat treatments studied. The precipitate volume fractions were calculated from the 3-D reconstruction as the ratio of grids in

the precipitate region to the total grids. The volume fractions were estimated to be $8.5 \pm 0.3\%$, $9.8 \pm 3\%$ and $12.9 \pm 2.5\%$ for the heat treatments at 550°C, 600°C, and 650°C respectively. The error bars reported were the spatial variation from four divisions of the whole volumes in the reconstruction. The increase in precipitate volume fraction from 550°C to 650°C indicates excess amount of solute atoms (Hf and Ni) in the matrix and the precipitation has not saturated. Morphology of individual precipitates was extracted from the 3-D reconstructions using cluster analysis in MATLAB software [90]. The selected precipitate shapes from each heat treatment are shown in Figure 2.3. The precipitate shapes were observed to be close to that of platelet or curved prolate ellipsoidal geometry.

Compared to other methods like Focused Ion Beam (FIB) Scanning Electron Microscopy (SEM) 3-D slice-and-view [88], the TEM-based tomography has advantages and disadvantages. FIB is not suitable for the current heat treatment cases in the NiTiHf SMA, especially in the lower aging temperature cases (e.g., 550°C) as the precipitates are too small (few nm in width and $\sim$20 nm in length) to be resolved in the SEM. Moreover, the smallest slicing thickness in FIB is 5 nm and many precipitates will only constitute one voxel, which is difficult to distinguish from the noise. When compared to the FIB-based 3-D slice and view approach, the TEM-based tomography method may contain "missing wedges" due to the physical limitation of how much the TEM holder can tilt, although this should not significantly affect the measurement accuracy. To assess the accuracy of the volume fraction estimates in the TEM-based tomography requires a standard sample with known precipitate volume fraction, which was not available. Nonetheless, the accuracy of the TEM-based volume fraction estimate can be assumed to be satisfactory, as it is a well-established technique based on the Radon transformation.

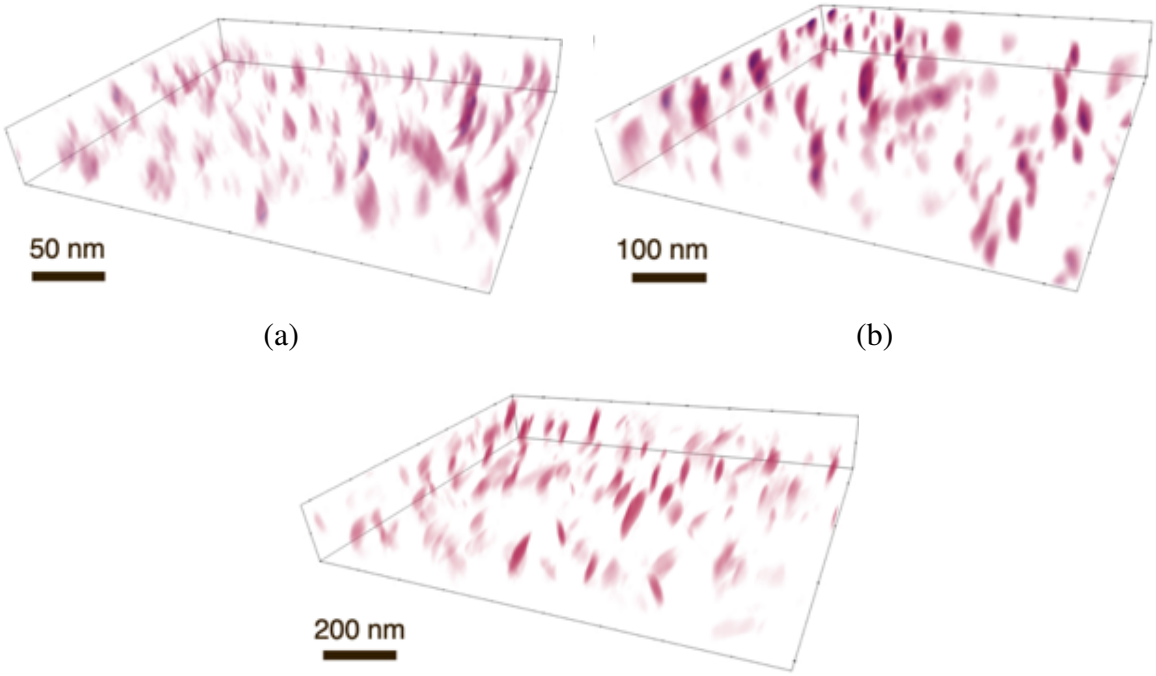

(a) (b)

(c)

Figure 2.2: 3-D reconstructions from HAADF-STEM images of $Ni_{50.3}Ti_{29.7}Hf_{20}$ with precipitation from different heat treatments: (a) 550°C for 10h, (b) 600°C for 10h, and 650°C for 10h.

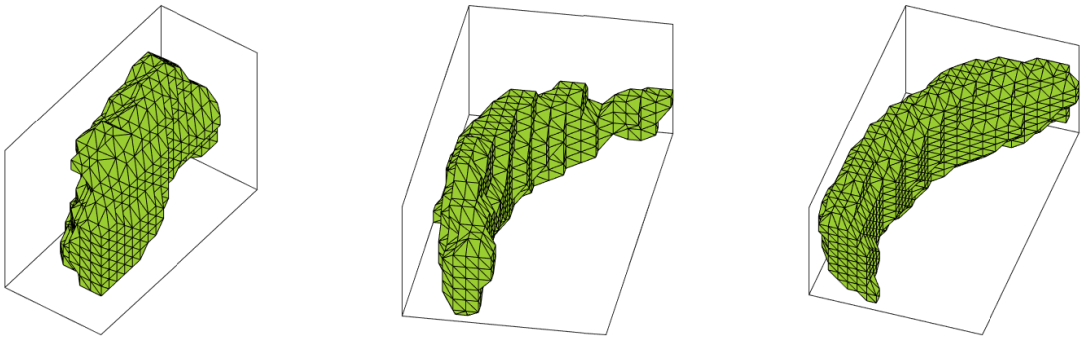

(a) Precipitate shapes in 550°C for 10 h.

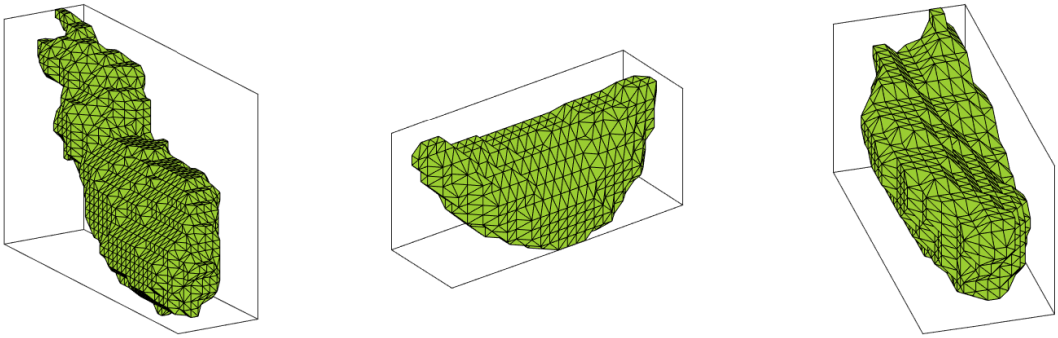

(b) Precipitate shapes in 600°C for 10 h.

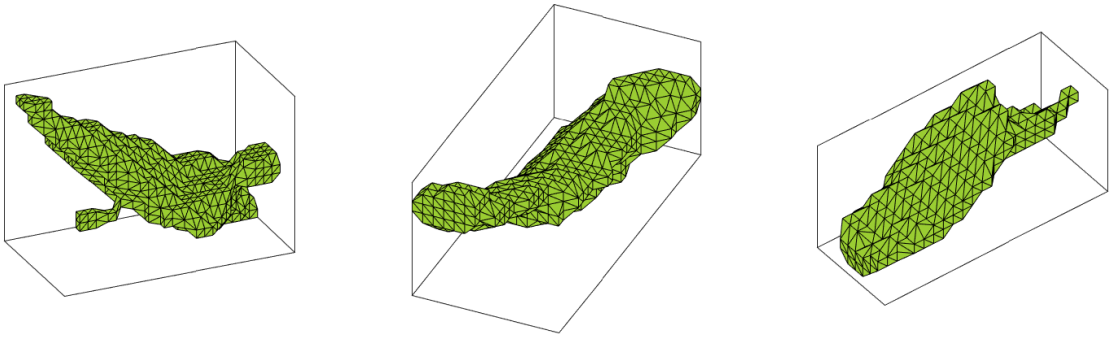

(c) Precipitate shapes in 650°C for 10 h.

Figure 2.3: Individual precipitate morphology extracted from the 3-D reconstructions of precipitation hardened $Ni_{50.3}Ti_{29.7}Hf_{20}$ SMAs.

2.3 Actuation response in precipitation hardened NiTiHf SMAs

The presence of precipitates in NiTiHf SMAs has been shown to change actuation behavior by modifying transformation temperatures, recoverable strain and reducing transformation induced plasticity [30, 91, 92, 93]. Yang *et al.* [83] measured the precipitate composition as $\mathrm{Ni_{53.62}Ti_{20.03}Hf_{26.35}}$ using atom probe tomography in $\mathrm{Ni_{50.3}Ti_{29.7}Hf_{20}}$ heat treated at 600°C for 815 hours. Since the precipitate phase has higher concentration of Ni and Hf, it results in a Ni-lean and Hf-lean matrix in the aged SMA compared to the solutionized as a result of atomic diffusion during precipitation. The h-phase precipitates maintain coherency with the matrix [34, 89]. All these aspects of the aged NiTiHf SMA can affect the phase transformation behavior.

The actuation responses in heat treated $\mathrm{Ni_{50.3}Ti_{29.7}Hf_{20}}$ SMAs were measured with the following experimental procedure. Dog-bone shaped tension samples with 1.5 mm x 3 mm x 8 mm gauge sections were cut from the $\mathrm{Ni_{50.3}Ti_{29.7}Hf_{20}}$ ingot using wire EDM and used for load-biased thermal cycling (actuation) experiments. The samples were subjected to solution heat treatment (SHT) at 900°C for 1h in argon and water quenched (WQ) to dissolve any possible secondary phases formed during fabrication. Further, the aging heat treatments were performed to create precipitation. Actuation experiments were performed on the solutionized and precipitation hardened samples to compare the change with precipitation.

In actuation experiments, the tension samples were loaded to different stress levels in the fully austenitic state and thermally cycled between ambient temperature and a temperature significantly above the austenite finish temperature. Two to three repetitions were performed using different samples to check the sample-to-sample variation. The experiments were carried out using a servo-hydraulic MTS test frame, where the specimens were conductively cooled by flowing liquid nitrogen through copper tubing wrapped around the grips and heated via resistive heating bands. The heating and cooling rates were 8-10°C $\mathrm{min^{-1}}$ and the sample temperature was measured using a K-type thermocouple attached directly to the samples' gauge section. The change in axial strain during the thermal cycles was recorded with an MTS high-temperature extensometer attached directly to the gauge section of the specimen.

Figure 2.4 shows the comparisons of tensile actuation responses in $Ni_{50.3}Ti_{29.7}Hf_{20}$ heat treated at 550°C, 600°C and 650°C for 10 hours. The comparisons show the phase transformation in the heat treated materials are happening at much higher temperatures than the solutionized material. Also, the maximum strain in these responses is increasing with the heat treatment from 550°C to 650°C (Figure 2.4 (a)-(c)). A higher strain is observed in the aged material response compared to the solutionized responses in the 600°C and 650°C cases. This trend is counterintuitive, as it is generally expected that the non transforming precipitates [57] in these precipitation hardened materials impede phase transformation. Similar increase in strain was reported in the work of Evirgen [4] on two NiTiHf compositions ($Ni_{50.3}Ti_{29.7}Hf_{20}$ and $Ni_{50.3}Ti_{34.7}Hf_{15}$) as well, which are discussed in the upcoming sections and in the results (section 2.7).

Higher transformation temperatures in the aged NiTi and NiTiHf have been well studied in the literature and are attributed to compositional changes in the matrix of the precipitation hardened material [82, 94, 95, 3]. While the increase in transformation strain in aged SMA has not been well studied, some similar trends of increasing transformation strain have been observed in NiTi. In the work of Kim and Miyazaki [96] on Ti-50.9at.%Ni SMAs, it was seen that transformation strain increased from non-precipitated to precipitated alloy (aging at 100°C to 200°C).

In the work of Hamilton *et al.* [97], it was seen that Ti–50.4 at.%Ni [0 0 1] single crystals produced higher strain in 550°C 1.5h aging compared to its solutionized response. This behavior is similar to what is seen in the NiTiHf, where increasing heat treatment gives higher transformation strain. To model the aged material response coherently with all these observed phenomenons, the following microstructural mechanisms were identified.

- The Ni-lean and Hf-lean matrix in the NiTiHf create higher transformation temperatures (TTs) in the matrix, which is reflected in phase transformation occurring at higher temperatures in the aged SMA (see Figure 2.4). In NiTiHf SMAs, the TTs are highly sensitive to composition and changes in the order of few percentages can shift the behavior in the order of 100°C [3, 98].

- As the precipitates are coherent with the matrix [34, 89], they create residual stress in the

matrix. Since the phase transformation is sensitive to stress, the residual stress can increase the TTs [99].

- The coherent non-transforming precipitates restrain the transformation in the surrounding matrix. Consequently, a higher driving force is required for complete transformation, which is reflected as a decrease in the forward transformation temperatures [100].

- In addition to the composition dependency of TTs, a dependency of transformation strain on composition is hypothesized. The Ni-lean and Hf-lean matrix creates higher transformation strain in the matrix. As a result, the competition of constraining effects of the precipitate and the increasing transformation strain in the matrix determines the increase or decrease of maximum strain in the aged SMA response compared to the solutionized response. More on the composition dependency of transformation strain and calibration is discussed in section 2.6.2.2.

These identified mechanisms are incorporated into the micromechanical model and are discussed further in the next section.

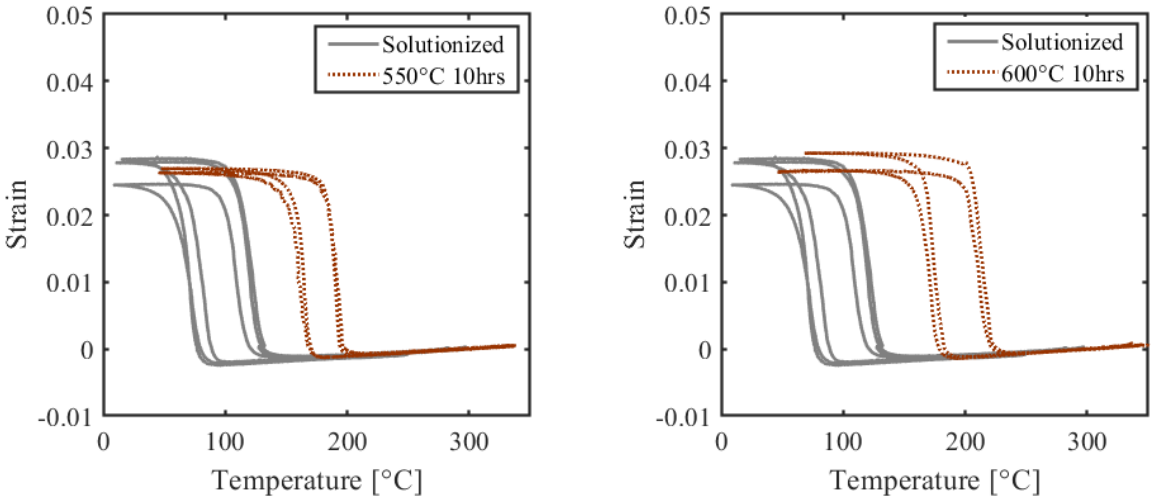

(a)

(b)

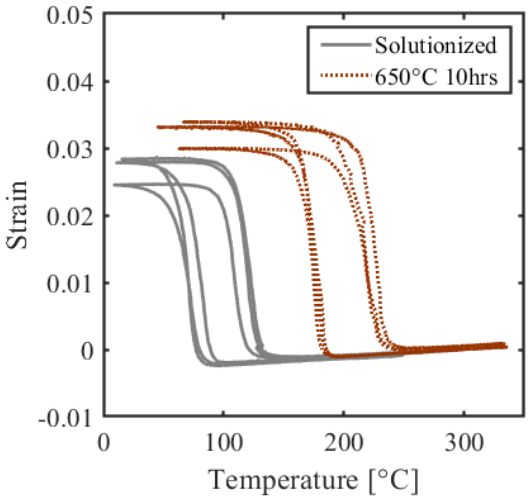

(c)

Figure 2.4: Comparison of thermomechanical behavior of $Ni_{50.3}Ti_{29.7}Hf_{20}$ heat treated at (a) 550°C, (b) 600°C and (c) 650°C for 10 hours at 200 MPa. The response from multiple samples demonstrates the samples-to-sample variation in the material behavior.

2.4 Micromechanical modeling using 3-D reconstructions

A finite element based micromechanical model was developed to model the actuation response in precipitation hardened NiTiHf SMAs. RVEs of the material microstructure extracted from the 3-D reconstructions were modeled with different constitutive behaviors in the precipitate and the matrix regions. The matrix was modeled as polycrystal phase transforming material and the precipitates as linear elastic material. The residual stress due to coherency and the composition change in the matrix due to diffusion were computed and used as inputs in the model. Finally, the actuation response was computed by applying boundary conditions on the RVE.

In the current modeling, a phenomenological approach for predicting the precipitation hardened polycrystal SMA response is used. In the actual material microstructure, the precipitates are present in single crystal grains within a polycrystal containing many grains, whereas in the current framework, the grain or grain level interactions are not modeled, but modeled as precipitates in an effective polycrystal matrix. Compared to a multiscale homogenization approach, the authors assume that accuracy is not compromised in the phenomenological approach towards predicting the effective precipitation hardened polycrystal SMA response. The authors compared the effective stiffness value for a precipitation-hardened polycrystal solved with two approaches: 1) as a multiscale homogenization problem with 200 grains and 2) as a phenomenological homogenization approach with precipitates in the effective polycrystal matrix. The properties were chosen such that they reflect the tangent stiffness in phase transformation. The two methods gave close predictions of effective stiffness (see Appendix A) in agreement with the assumption in the phenomenological approach.

The main steps in the developed micromechanical model are: 1) generating RVEs, 2) modeling the matrix phase and precipitate phase, 3) Characterizing matrix composition, 4) solving for internal stresses, and 5) solving the RVE boundary value problem to predict the actuation. Figure 2.5 shows a summary of the simulation process, where the RVEs are created using the TEM 3-D reconstructions, and the actuation behavior is solved using FEA. The SMA actuator responses were predicted in the ABAQUS software [101] with the application of thermomechanical boundary

conditions. Steps in the micromechanical model are discussed in the following subsections.

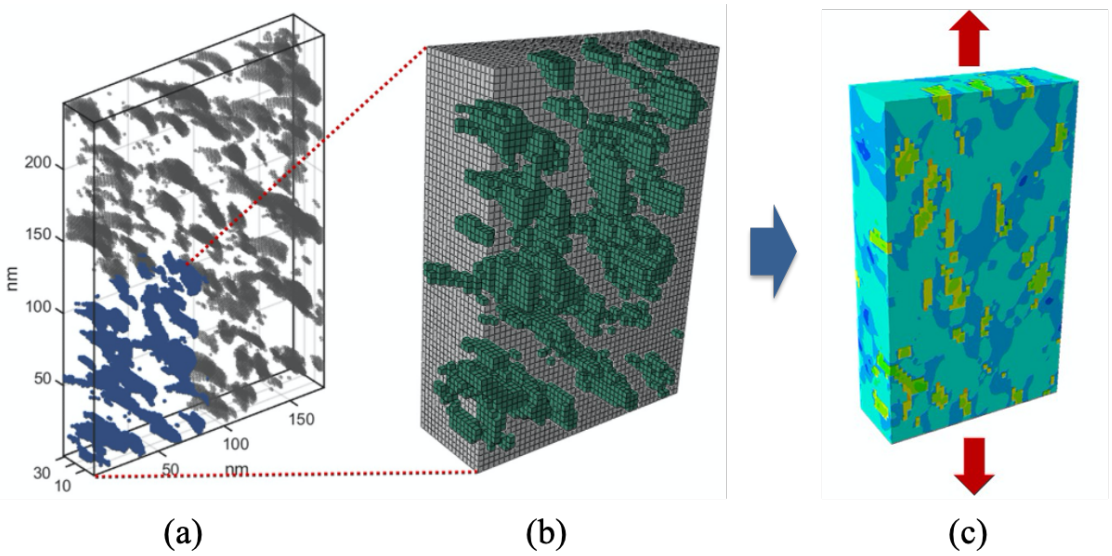

Figure 2.5: Micromechanical modeling showing the RVE creation from the 3-D reconstruction and FEA simulation to solve the effective response. (a) The full 3-D reconstruction, (b) one of the four RVEs taken from the reconstruction and (c) FEA simulation of the RVE along an in-plane loading direction.

2.4.1 RVE generation

The RVEs were created from the TEM microstructure representations explained in section 2.2. Figure 2.5 shows a RVE extracted from the complete microstructure in the 550°C for 10h heat treatment case. The pixel representation of the 3-D reconstructions were imported as structured voxel mesh. The precipitate regions were identified and assigned the precipitate properties, and the remaining region was assigned to be the phase transforming matrix. From each 3-D reconstruction of the heat treatment case, four smaller RVEs were created. The multiple realization simulated how the microstructural variation affects the effective response.

2.4.2 Matrix and precipitate material models

The phase transforming matrix was modeled using the polycrystalline constitutive model of Lagoudas *et al.* [5]. The constitutive model was implemented using the User Material (UMAT) subroutine feature in ABAQUS software [101]. The precipitates were modeled as linear elastic with isotropic stiffness properties, and implemented using the default material model in ABAQUS. The phase transformation properties of the matrix and precipitate stiffness were obtained through calibration. More on the calibration is explained in section 2.6.

2.4.3 Composition of the phase transforming matrix

The composition profiles in the matrix are the result of the Fickian diffusion during precipitation. These profiles will not change significantly during thermal cycling, as the kinetics of diffusion is very low at the thermal cycling temperatures. If one has to solve for the full field diffusion in NiTiHf alloys, Appendix B summarizes the rate equations that should be modeled. Because of the complexity of solving diffusion, in the current modeling, the composition profiles were approximated by the average composition of the matrix. In reality, there are gradients around the precipitates and can have an effect on the phase transformation, which is neglected for the current modeling. The average composition of the matrix (C_m) was calculated in terms of the volume fraction of precipitates (VF) and the solutionized material composition (C_0) using the following atomic balance equation.

$$C_m = \frac{C_0 - VF * C_p}{1 - VF}, \tag{2.1}$$

where, C_P is the composition of the precipitate which can be taken as $\mathrm{Ni}_{53.62}\mathrm{Ti}_{20.03}\mathrm{Hf}_{26.35}$ based on the measurements of Yang *et al.* [83]. Equation (2.1) represents a set of three equations on Ni, Ti and Hf contents as the atomic balance is separately satisfied in each element for the same volume fraction. In each TEM based RVE modeled, the average matrix composition was calculated from the corresponding measured volume fraction in the RVE.

2.4.4 Residual stress calculations

The internal stresses in the material are created from two sources: the lattice misfit between the phases and the misfit in the elastic stiffness between the phases. The internal stress from the lattice misfit is resulted during precipitation and remains constant during loading, so are termed as residual stress. The internal stress due to elastic stiffness evolves during the loading and phase transformation, and are accounted inherent in the finite element model. The residual stress distribution due to the lattice misfit between the precipitate and the matrix phases was solved by applying an equivalent eigenstrain on the precipitates. This was solved as a problem using the idea that a difference in thermal expansion coefficients in the matrix and precipitate can simulate eigenstrain in a pure thermal loading. A difference in the thermal expansion coefficients corresponding to the eigenstrain value was applied to the two phases, and a corresponding pure thermal heating step was used to solve the residual stress distributions. This was done using FEA in ABAQUS software, and the solution of residual stress distribution was introduced as an initial condition in the overall solution process. For the current work, the eigenstrain in the precipitates was calculated to be 0.01 hydrostatic strain based on the 1% lattice misfit between the two phases [89]. Here, only the hydrostatic components were considered, assuming a similarity with NiTi eigenstrain[102].

2.4.5 Solving the thermo-mechanical response from the RVEs

The actuation responses of the aged NiTiHf SMAs were simulated by applying temperature and stress boundary conditions on the RVEs according to the actuation loading path (Figure **??**(a)). A constant stress corresponding to the actuation was applied on the RVE in the loading direction. The heating-cooling thermal environments were simulated by changing the temperature boundary condition for the entire volume. In addition, the periodic boundary conditions were applied on the faces of the RVEs to avoid the boundary effect and to predict pure bulk constitutive behavior. The RVE deformation was solved through FEA using implicit formulation in the ABAQUS FEA software [101]. The effective response was calculated from the volume average in the RVE. The responses were calculated along two in-plane loading directions in the TEM microstructure to

capture the variability. The through-the-thickness loading was not included, as there might be thickness effect due to the comparable size of precipitate to thickness. Actuation responses for three different stress levels (100 MPa, 200 MPa and 300 MPa) were simulated.

2.5 Modeling with ellipsoidal RVEs

As the TEM reconstructions (section 2.2) show that the precipitate shapes are closer to curved prolate ellipsoid, a less expensive modeling methodology with RVEs of ellipsoidal shape is proposed. As an alternative to volume fraction estimation from the 3-D reconstruction, here the volume fraction is estimated from shifts in differential scanning calorimetry (DSC) measurements of the precipitated SMA using composition-transformation temperatures (C-TT) relations. The ellipsoidal precipitate shapes are approximated from the 2-D TEM instead of using the 3-D reconstructions. These steps are discussed in the following subsections.

2.5.1 Estimation of matrix composition and volume fraction from calorimetric measurements

The matrix composition in the aged material was estimated comparing its DSC based TTs with C-TT relations, and the volume fraction was computed from the matrix composition utilizing atomic balance (Eq. 2.1). First, the transformation temperatures of the aged SMA in the stress-free state were calculated from peaks in forward and reverse transformations from their DSC responses [3]. Because DSC measurements are performed in a stress-free material, the effects of stress concentration can be expected to be minimal, and the transformation peaks are mostly dictated by the matrix transformation. With this assumption, the TTs of the precipitation-hardened SMAs can be correlated to its matrix phase composition, as only the matrix is phase transforming. Hence, using the C-TT relations, the average matrix composition is determined to be the one which give TTs closer to those measured. Figure 2.6(a) shows an example of estimating average composition in the modeling of precipitation-hardened NiTi SMAs [82], where, C_0 is the composition before precipitation and C_M is the average composition in the matrix after precipitation.

For NiTiHf SMAs, the C-TT relations based on the extensive DSC measurements conducted

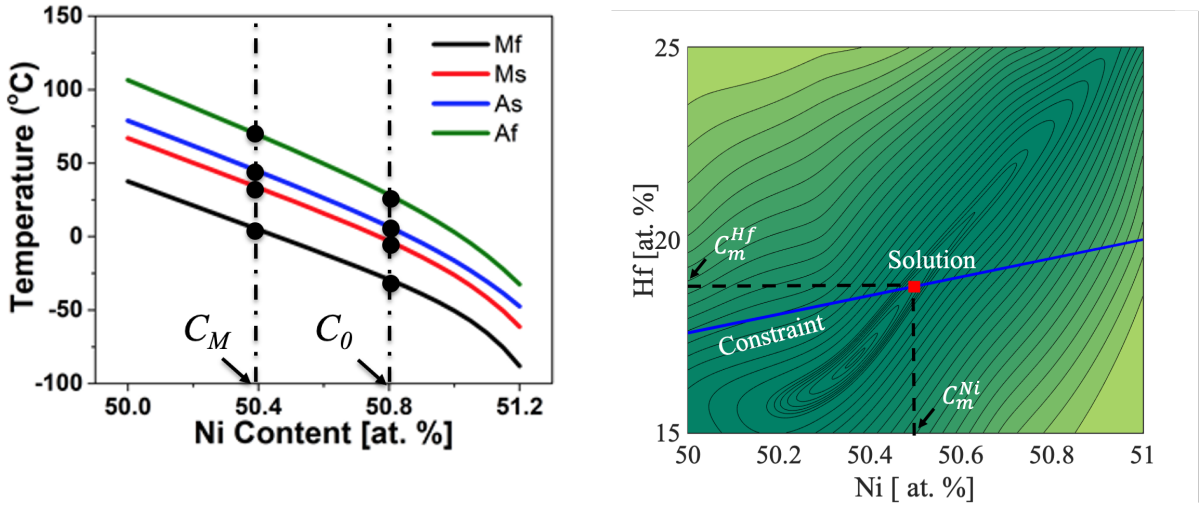

(a) Composition estimation in NiTi (b) Composition estimation in NiTiHf

Figure 2.6: Figure showing the estimation of the average matrix composition from TTs using C-TT relations in (a) NiTi SMA [1, 2] and (b) NiTiHf SMA. In NiTiHf, a constrained optimization on mean squared error (MSE) gave better estimations.

by Umale *et al.* [3] were used. The 2-D Thin-Plate Smoothing Splines in MATLAB software [90] were used for fitting and interpolation. Figure 2.7 shows the variation of M_s with composition in NiTiHf SMAs in the work of Umale *et al.* [3]. For a given M_s measured, one can identify many Ni and Hf values that would result in the same value (see Figure 2.7) as opposed to a single Ni composition in the case of binary NiTi SMAs. Therefore, we used all four transformation temperatures to find the best composition that would fit the DSC measured TTs. For this, a constraint optimization on the C-TT relations (summarized in Equation 2.2) was used, where the constraint ensured atomic balance for Ni and Hf. The mean squared error (MSE) between the measured TTs in the aged material (M_s^{ag}, M_f^{ag}, A_s^{ag} and A_f^{ag}) and the values from the C-TT relations are minimized to find the optimum value of composition. The whole process is summarized as:

$$\begin{aligned} \left[C_m^{Ni}, C_m^{Hf}\right] &= \min_{C^{Ni}, C^{Hf}} \left(\frac{1}{4} \sum_{TT=M_s,M_f,A_s,A_f} \left(TT^{ag} - TT^{CTT}(C^{Ni}, C^{Hf})\right)^2 \right) \\ \text{s.t.} \left(\frac{C_0^{Ni} - C^{Ni}}{C_P^{Ni} - C^{Ni}}\right) &= \left(\frac{C_0^{Hf} - C^{Hf}}{C_P^{Hf} - C^{Hf}}\right) \end{aligned} \tag{2.2}$$

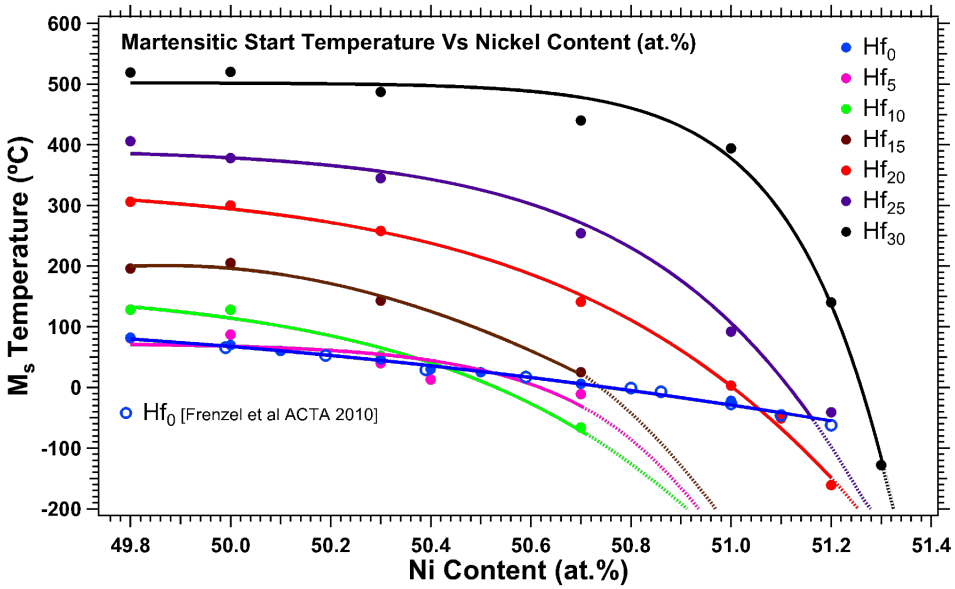

Figure 2.7: Variation of martensitic start temperature (M_s) with Ni and Hf composition in NiTiHf SMAs. Reprinted from Umale *et al.* [3], Copyright 2019, with permission from Elsevier.

where, C_m is the matrix composition, C_0 is the solutionized material composition, C_P is the precipitate composition, and the $'TT'$ refer to the four TTs. The superscripts $'Ni'$ and $'Hf'$ refer to the specific components, and the superscripts $'ag'$ and $'CTT'$ refer to the values measured for the aged SMA and values from the C-TT relations, respectively. The constraint equation makes sure the atomic balance is satisfied in both Ni and Hf for the same volume fraction. An example of the minimization problem for 600°C 10h is summarized in the MSE contour plot shown in Figure 2.6(b), where the solution is the optimum from the constrained minimization. The optimization problem (equation 2.2) was solved for all heat treatments. The results are summarized in Table 2.1 and compared with values measured in the 3-D reconstructions (section 2.2.3). For the two lower heat treatments, the volume fraction estimation is close to the measured value, but considerably different in the 650°C 10h heat treatment. One of the reasons for this discrepancy is that the precipitate composition is assumed to be constant in the current estimation, despite the fact that it is known to be a function of the initial composition and heating conditions[89]. For example, the calculation with a precipitate composition $\mathrm{Ni_{52.9}Ti_{18.6}Hf_{28.5}}$ [89] for 650°C 10h gives a volume fraction of 14.1 % which is much closer to the 3-D measured value. However, as with the current

literature, the variation of precipitate composition with heat treatments is not known accurately, hence $Ni_{53.62}Ti_{20.03}Hf_{26.35}$ [83] is used.

2.5.2 Shape of precipitates from 2-D TEMs

The aspect ratio (AR) required for creating ellipsoidal RVEs was estimated from the 2-D TEM images (Figure 2.1) by selecting points of precipitate boundary and fitting an ellipse using fit_ellipse [103] tool. The schematic in Figure 2.8 (a) show the calculation performed for the 650°C 10h sample. The values obtained for different heat treatments are summarized in Table 2.1. The values of aspect ratios from 3-D reconstruction precipitate morphology by fitting ellipsoids (see Figure 2.8 (c)) are also compared in Table 2.1. The single AR values obtained using 2-D TEM images are close to the larger AR in the 3-D shapes. The second AR estimations in the 3-D shapes are close to 1.5, which means the shapes are in fact significantly tri-axial ellipsoidal, whereas in the 2-D TEM based modeling they are assumed to be spheroids with 2 equal axes.

Table 2.1: Summary of volume fractions (VF) calculated from TTs versus from 3-D microstructures in $Ni_{50.3}Ti_{29.7}Hf_{20}$[A] heat treatment cases. The aspect ratios (AR) of precipitates estimated from 2-D images and 3-D reconstructions are compared with confidence interval (CI).

Heat treatment	**Calculated VF**	**3-D TEM VF**	**2-D TEM AR** $AR\pm$(95% CI)	**3-D morphology ARs** $(AR_1, AR_2)\pm$(95% CI)
550°C for 10 h	7.2%	8.5%	2.4 ± 0.5	$(3.1, 1.5) \pm (1.6, 0.8)$
600°C for 10 h	9.2%	9.8%	2.2 ± 0.3	$(2.5, 1.5) \pm (1.2, 0.6)$
650°C for 10 h	9.7%	12.9%	4.2 ± 2.2	$(3.2, 1.8) \pm (1.6, 0.8)$

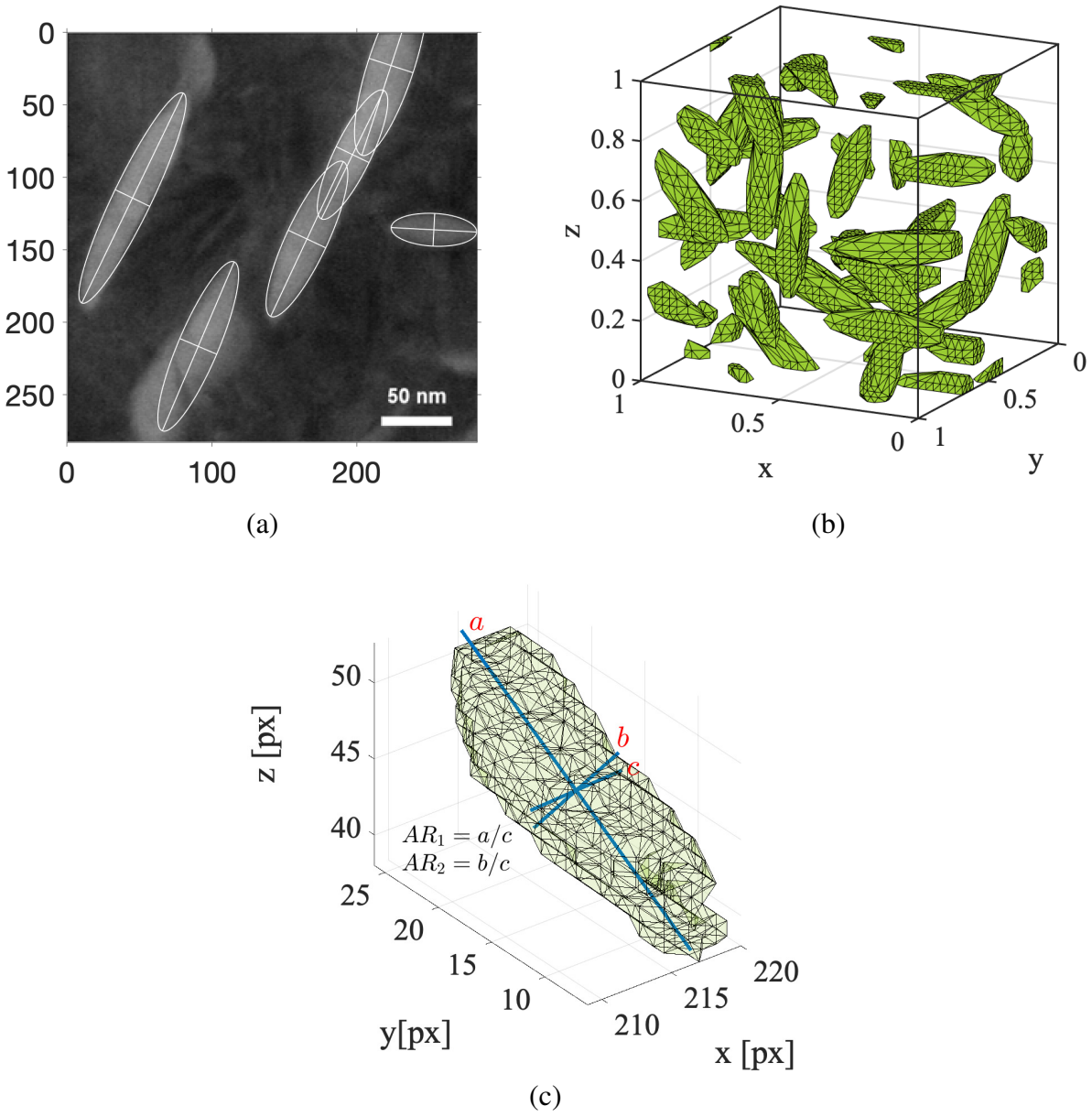

Figure 2.8: (a) Calculation of aspect ratio from TEM image in 650°C 10h sample. (b) An RVE with periodic boundary conditions generated for 650°C 10h case with 30 particles.(c) Measuring 2 aspect ratios from 3-D reconstruction of an individual precipitate in 650°C 10h case.

2.5.3 Generating ellipsoidal RVEs and simulation of behavior

The RVEs of the material were constructed with the calculated volume fraction and aspect ratio (Sections 2.5.1 and 2.5.2). Based on the volume fraction and the number of particles to be mod-

eled, the geometrical dimensions of the individual ellipsoidal particles were determined. Inside the RVE, the ellipsoidal particles were placed at random positions and random orientation. The particles intersecting the faces of the RVE are repeated at the opposite faces to create periodicity and be consistent with periodic boundary conditions. By choosing the random orientations, the cumulative effect from many precipitate orientations in a polycrystal is assumed to be simulated. Measuring the texture of polycrystalline NiTiHf high temperature SMAs is challenging, since heating the sample to the austenitic state requires specialized facilities. Because of this limitation, the crystallographic texture was modeled to be random in the current work. Although within a grain, precipitates can have preferred orientations [104, 105], as the grains can be oriented in many directions, the polycrystal will have precipitates in several orientations. The position and orientation of precipitates were determined using a script, which also ensured their periodicity at the faces. A minimum distance of $1/4$ major axis length between the precipitates ensured there were no overlapping particles or particles that were too close to one another. Fig 2.8 (b) shows an RVE generated corresponding to the 650°C 10h sample from the TEM in Fig 2.8 (a).

The steps followed after the RVE creation were the same as described in sections 2.4 and are not repeated here. The material behavior was predicted from the RVEs by applying periodic boundary conditions and thermo-mechanical loading corresponding to actuation.

2.6 Estimation of material parameters

The material parameters in the micromechanical model were obtained from available experimental measurements and through calibration with the model.

2.6.1 Solutionized material composition

In the tension samples of solutionized NiTiHf SMA, the nominal composition was given as $\mathrm{Ni}_{50.3}\mathrm{Ti}_{29.7}\mathrm{Hf}_{20}$ by the manufacturer. However, this may not be the actual composition of the material due to the losses during processing, as described in detail in [106]. While EDX and WDS were two available techniques to measure the composition of the alloy, due to the high sensitivity of TTs to composition in NiTiHf SMAs, the uncertainty in these techniques were considerable

from the modeling perspective. Hence, the compositions were estimated from the C-TT relations using the method described in section 2.5.1, ensuring the compositions were consistent with the DSC data used in estimating matrix transformation temperatures. For the alloy $\mathrm{Ni_{50.3}Ti_{29.7}Hf_{20}}$, the estimated composition of the material (C_0) was $\mathrm{Ni_{50.78}Ti_{29.74}Hf_{19.48}}$.

2.6.2 Properties of the phase transforming matrix

The material parameters in the constitutive model [5] for the matrix which includes TTs (M_s, M_f, A_s, A_f), phase-diagram slopes (C^A, C^M), stiffness properties (E^A, E^M), Poisson's ratio (ν^A, ν^M), thermal expansion coefficients (α^A, α^M) and parameters to describe transformation strain variation with stress (H^{max}, k), were determined as follows.

2.6.2.1 Transformation temperatures of the matrix

The TTs for the matrix were calculated from the composition of the matrix (section 2.4.3) using the C-TT relations (section 2.5.1). For RVEs from 3-D reconstruction, the matrix composition were calculated from their measured VF using Equation 2.1. Hence, in TEM RVEs, the dispersion in the VF from different realizations were reflected in the estimations of TTs and consequently in the effective response, while in the ellipsoid RVEs, the matrix compositions were calculated from DSCs (section 2.5.1) and had fixed value.

2.6.2.2 Composition effects on transformation strain and its calibration

The externally measured transformation strain in an SMA can be influenced by its composition, texture, and grain size [107, 106]. Regarding the composition effect, the Hf and Ni content can modify the externally measured transformation strain by affecting twin modes and ease of detwinning. The crystallographic calculations in NiTiHf single crystals [107] shows that the Hf content increases the transformation strain. In the same study [107], crystallographic calculations for polycrystal $\mathrm{Ni_{50.5}Ti_{36.2}Hf_{13.3}}$ and $\mathrm{Ni_{51.2}Ti_{23.4}Hf_{25.4}}$ SMAs show, by increasing Ni (by 0.7%) and Hf (by 12%) content, the transformation strain is decreased (from 4% to 7%). This shows that the Ni content has higher sensitivity, and increasing Ni content reduces the externally measured transformation strain. The differences in texture in SMAs can be caused by a difference in their

processing history, and can affect the transformation strain. When comparing the transformation behavior in solutionized SMAs, the composition and textural effects will be the dominant effects and the grain size effect might be negligible.

In Figure 2.9 (a), a comparison of experimentally measured transformation strain versus applied load variation in three different solutionized NiTiHf SMAs is shown. Here, the material $\mathrm{Ni}_{50.3}\mathrm{Ti}_{29.7}\mathrm{Hf}_{20}$ [A] represents the alloy presented in the current work (sections 2.2 and 2.3), which was acquired from the company ATI. The materials $\mathrm{Ni}_{50.3}\mathrm{Ti}_{29.7}\mathrm{Hf}_{20}$ [B1] and $\mathrm{Ni}_{50.3}\mathrm{Ti}_{34.7}\mathrm{Hf}_{15}$ [B2] represent alloys manufactured in a NASA facility, and the response data is taken from the work of Evirgen [4]. The key difference between [A] and [B] is their processing history. The material [A] was manufactured through a hot forging process, whereas the materials [B1] and [B2] were manufactured through a hot extrusion process. Because of differences in processing, there can be differences in their grain textures, although the composition is the same (in [A] and [B1]). As the two compositions [B1] and [B2] have the same processing history, the texture effects may be negligible, and the difference seen in their externally measured strain can be rationalized solely due to the composition effect. While [A] might be expected to have a lower externally measured transformation strain based solely on composition effect, similar to [B1], the reason for the unexpected difference may be due to the texture effect, i.e., the austenite texture. Because of facilities limitations for measuring the austenite texture, a study on texture was not performed.

The evolution of maximum current transformation strain ($H^{cur}(\sigma)$) with stress can be modeled using an exponential function (shown in Figure 2.9 (a)) in terms of maximum attainable transformation strain (H^{max}) and an exponent parameter (k). In Figure 2.9 (a), this variation with stress is fitted to the experimental values in [A], [B1] and [B2], which are shown with the dashed lines. For the three materials, the H^{max} was fixed ($= 0.075$) and the value of the exponent k was varied, which provided fits with goodness > 0.94. In these measurements, the $H^{cur}(\sigma)$ does not approach saturation before the samples fail in tension at stresses above 400 MPa, so any variation in H^{max} could not be verified. Hence, the strain variations were captured solely through variation in k while assuming fixed H^{max}. The $H^{cur}(\sigma)$ variation in $\mathrm{Ni}_{50.3}\mathrm{Ti}_{29.7}\mathrm{Hf}_{20}[A]$ was verified from responses in

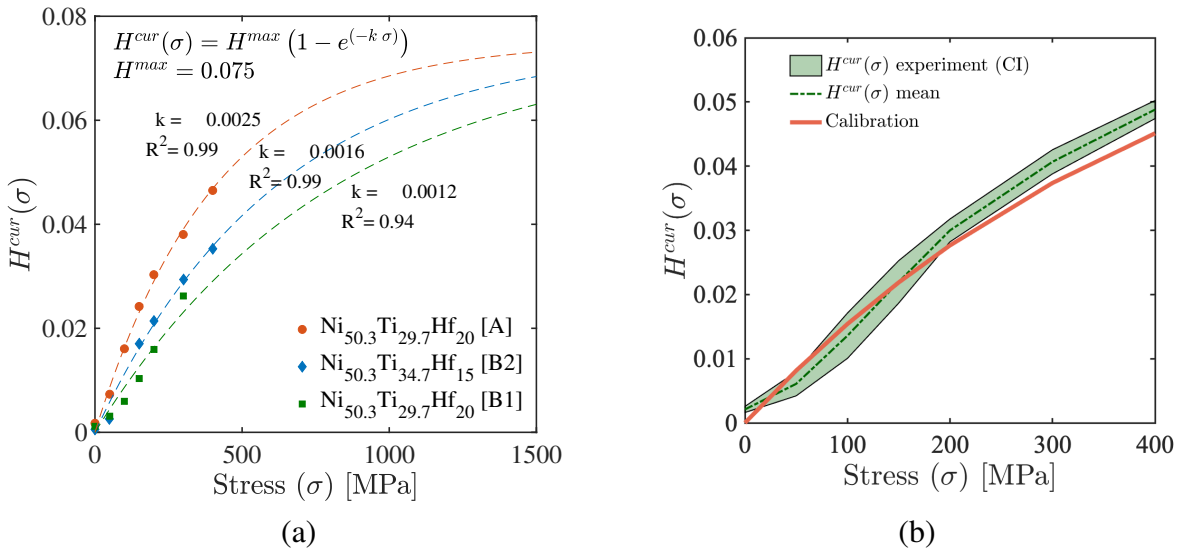

Figure 2.9: (a) Experimentally measured stress (σ) dependency of the maximum current transformation strain ($H^{cur}(\sigma)$) in three different solutionized NiTiHf SMAs. (b) Confidence interval (CI) of $H^{cur}(\sigma)$ versus σ generated from experiments performed on four samples of solutionized $Ni_{50.3}Ti_{29.7}Hf_{20}[A]$. The exponential model for the evolution is fitted to the experimental variation.

four samples, and a comparison of the confidence interval (CI) to the fit is shown in Figure 2.9(b). The sample-to-sample variation was observed to be less, and the fit matches well with the $H^{cur}(\sigma)$ values generated from measurements on multiple samples.

In addition to the stress variation of transformation strain, the composition variation of transformation strain should be accounted as this is significant in the precipitation hardened behavior (section 2.3). Figure 2.10 shows a comparison of actuation response predictions in material [A] when the composition effects on transformation strain were not considered in the modeling. Shifts in experimental curves of solutionized sample versus aged sample show clearly how the compositional changes affect both transformation strain and transformation temperature. In the modeling predictions compared in Figure 2.10, the composition effect on transformation temperatures, which was well documented (Figure 2.7), was included, whereas the $H^{cur}(\sigma)$ was assumed to be the same as the solutionized. The resulting predictions provide for much lower transformation strain compared to the experimental measurements. The difference also increases with volume fraction between heat treatments at $550°$C and at $650°$C. This increasing difference is due to the

increasing k parameter in the matrix with the Ni-lean composition, which should be accounted for in the modeling. Moreover, in Figure 2.10, for the same volume fraction, the predictions of ellipsoidal RVEs match well with that of TEM reconstruction RVEs, which shows that the effect of volume fraction through composition is the dominating factor over the geometrical topology.

With the knowledge that the parameter k and Ni composition are inversely related, k for additional Ni compositions were calibrated from the heat-treated responses using the micromechanical model simulations. Figure 2.11 shows the variation of k obtained for the three alloys, where the values obtained from the solutionized experiments ('Expt.') and values from the aged response ('Calibration') are correlated with Ni composition. For [A], two heat treatment response (550°C 10h and 650° 10h at 300 MPa) were used in the calibration and a spline interpolation was used. For [B1], one heat treatment response (550°C 3h at 300 MPa) was used for calibration with linear interpolation. Similarly, for [B2], one heat treatment response (600°C 10h at 300 MPa) was used for calibration with linear interpolation. The higher values in the [A] alloy compared to the ([B1] and [B2]) alloys can be explained as the result of differences in texture due to different processing history. Compared to [A], the alloys [B1] and [B2] give closer values, probably due to similar texture in both. As the variation of k in a wide range of composition was captured, the matrix can now be modeled with composition effects on transformation strain.

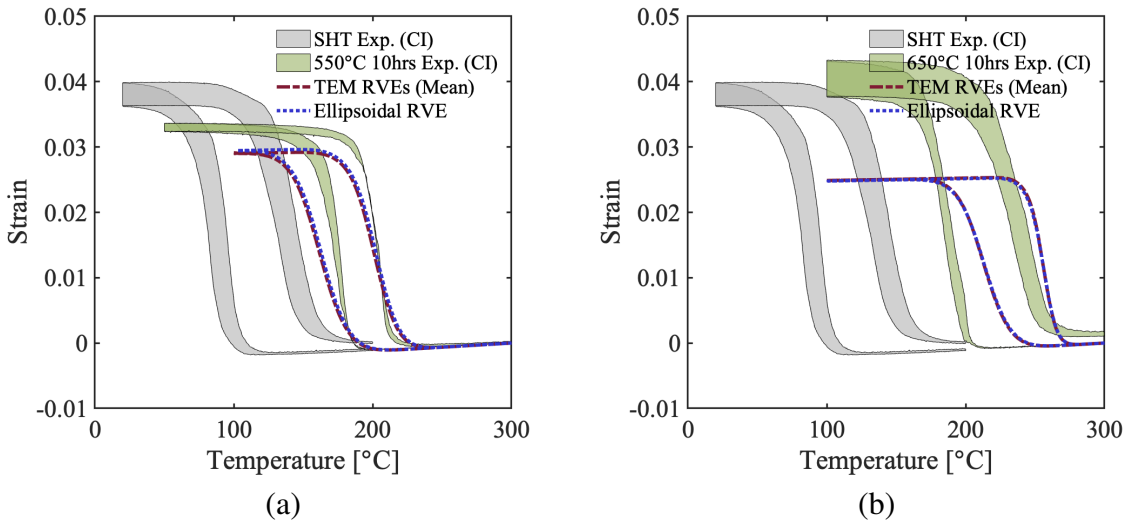

Figure 2.10: Comparison of micromechanical prediction for actuation response at 300 MPa using a TEM RVE neglecting the compositional effects of k in precipitation hardened $\mathrm{Ni}_{50.3}\mathrm{Ti}_{29.7}\mathrm{Hf}_{20}$[A] heat treated at (a) $550°$C for 10h and (b) $650°$C for 10h. Prediction from an ellipsoidal RVE with same volume fraction is shown. For the TEM case, the mean value from the two in-plane loading directions is shown.

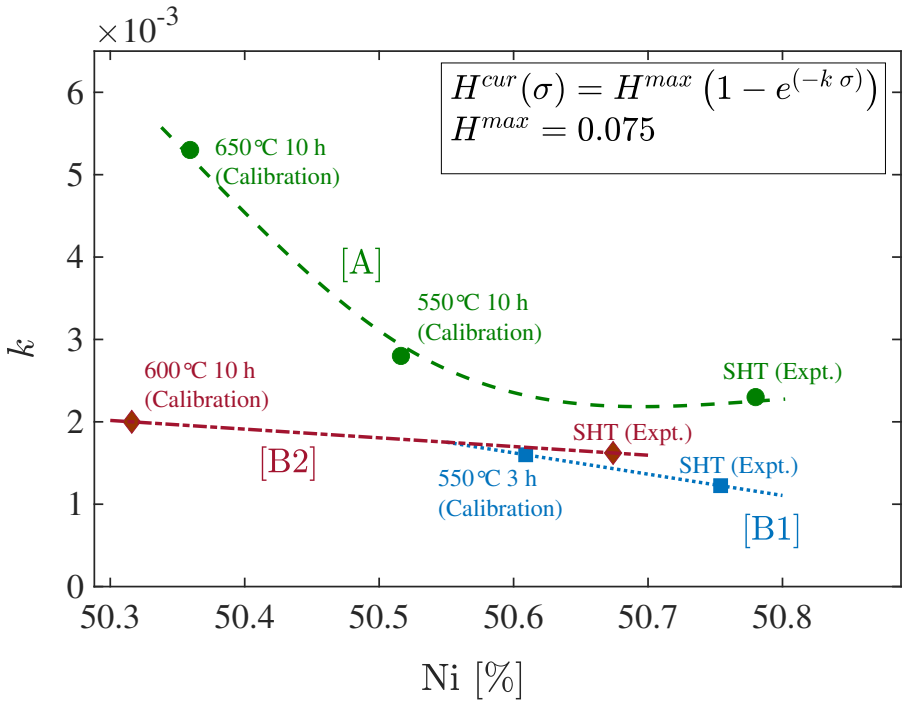

Figure 2.11: Variation of exponent k in solutionized NiTiHf alloys with Ni composition for three different alloys, where [A] (alloy in this work) and ([B1], [B2]) ([4]) have different processing parameters. The curves were developed using points from experimental measurements (Expt.) and values estimated through calibration with the micromechanical model.

2.6.2.3 Calibration of remaining properties

The properties such as: phase-diagram slopes (C^A, C^M), stiffness (E^A, E^M), Poisson's ratio (ν^A, ν^M) and thermal expansion coefficients (α^A, α^M) were assumed to be constant with composition. The values for these parameters were obtained from calibration of solutionized SMA actuation response with the Lagoudas et al. constitutive model following the standard methodology in [5]. Table 2.2 shows the summary of the calibrated values in the phase diagram and other parameters in the model.

Figure 2.12 shows a comparison of the experimental and the calibrated model phase diagrams for the solutionized $\mathrm{Ni_{50.3}Ti_{29.7}Hf_{20}}$ SMA, where the transformation temperatures at each stress level were estimated from the actuation responses using the tangent approach (section 2.3). For the experimental phase diagram in Figure 2.12, the discrepancy between different samples of $\mathrm{Ni_{50.3}Ti_{29.7}Hf_{20}}$ is shown as a confidence interval of one standard deviation. As the nonlinear variation in the phase diagram of NiTiHf could not be captured exactly in the SMA constitutive model, the phase diagram curves were approximated in the modeling with the solid curves illustrated in Figure 2.12. In Figure 2.13, comparison of experimental and the calibrated constitutive model responses in solutionized $\mathrm{Ni_{50.3}Ti_{29.7}Hf_{20}}$ SMA for 200 MPa and 300 MPa is shown, where the CI is used to represent variation from four different samples. The experiment curves and the calibrated model curves have a matching response, indicating the parameters to be appropriately estimated.

Following are some of the intrinsic assumptions that have been made in this estimation of parameters.

1. The grain morphology of the solutionized SMA and the precipitation-hardened SMA samples were assumed to be the same. Although the grain boundaries can grow during aging, this change in grain morphology is usually minimal, since the growth kinetics at aging temperatures ($500^\circ C - 700^\circ C$) are much slower than that at the solutionizing temperature ($\approx 1000^\circ C$). With this assumption, the changes in the matrix properties due to grain morphology changes in the aging were disregarded.

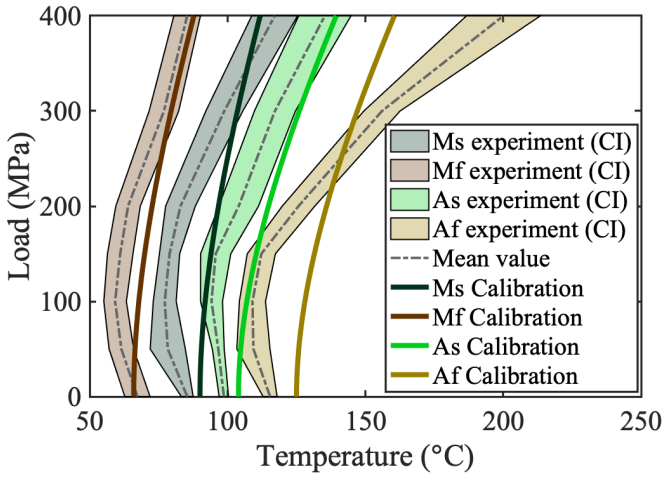

Figure 2.12: The temperature-stress phase diagram for $Ni_{50.3}Ti_{29.7}Hf_{20}$[A] developed from experimental responses in four samples presented with confidence interval (CI). The phase diagram from the calibration of Lagoudas *et al.* [5] constitutive model is compared.

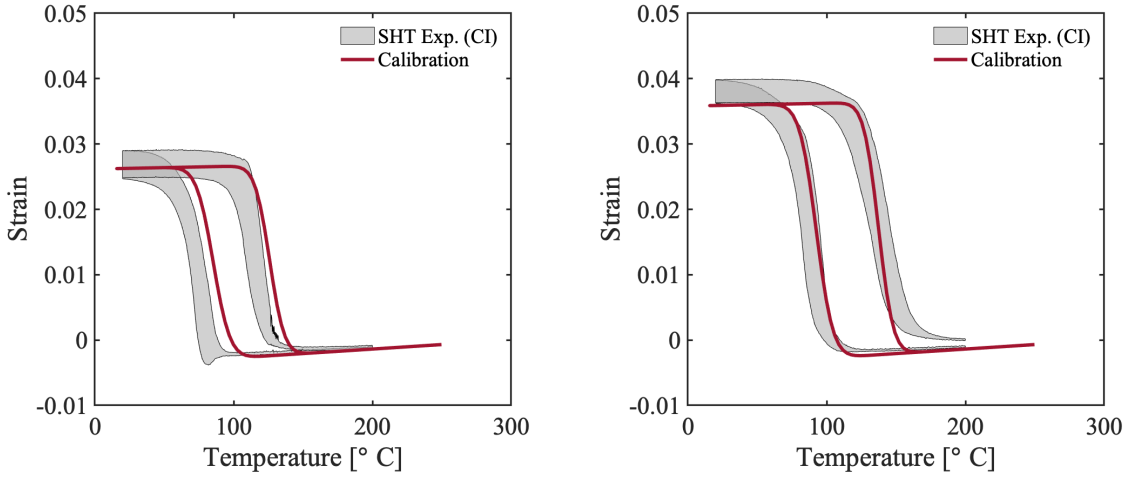

(a) Load = 200 MPa (b) Load = 300 MPa

Figure 2.13: Comparison of the Lagoudas *et al.* [5] model responses to the experimental responses for the solutionized $Ni_{50.3}Ti_{29.7}Hf_{20}$[A] at (a) 200 MPa and (b) 300 MPa.

Table 2.2: SMA properties obtained for solutionized $\mathrm{Ni}_{50.3}\mathrm{Ti}_{29.7}\mathrm{Hf}_{20}$[A] through calibration of experimental responses using Lagoudas *et al.* [5] constitutive model.

Material parameter	**Value**
E_A	79 GPa
E_M	83 GPa
α^A	$1.38 * 10^{-5}$
α^M	$4.34 * 10^{-6}$
$v^A = v^M$	0.4
H^{max}	0.075
$k[MPa^{-1}]$	0.00267
C_A	8 MPa/K
C_M	13 MPa/K
$n_1 = n... = n_4$	0.1

2. It was shown in the previous sections that the matrix composition changes with volume fraction. By assuming fixed model parameters after different aging heat treatments, the influence of composition changes on these properties were disregarded.

2.6.3 Estimation of precipitate phase stiffness

The precipitate phase is expected to be stiffer than the solutionized phase, so the aged SMA will be stiffer than the solutionized SMA. As the RVEs of the aged SMAs were known from the TEM reconstructions, the precipitate stiffness could be calibrated from the higher stiffness values in the aged samples, assuming matrix stiffness to be the same as in the solutionized. The micromechanical model was used to calibrate the precipitate stiffness from the austenite stiffness values of the solutionized and three heat-treated SMA samples. Experimental stress-strain values above 300°C, where the material is expected to be fully in the austenite phase, were used to estimate the austenite stiffness values. These values are summarized in Table 2.3 with the mean and bounds reflecting standard deviation of sample-to-sample discrepancy from several samples (3-4).

With the solutionized material stiffness (E_{sht}) in the matrix, the effective stiffness of the RVEs were estimated in the micromechanical model for different precipitate stiffness (E_P) values. Considering the uncertainty from multiple samples, the precipitate stiffness was estimated using maxi-

mum likelihood estimation (MLE), which allowed accounting for these uncertainties in the estimation. The following equations summarize the likelihood function($\mathcal{L}$) estimation for the precipitate stiffness (E_P).

$$\begin{aligned} \mathcal{L}(E_P) &= \prod_{Ag=1,2,3} \mathcal{L}\left(E_P|Ag\right), \\ \mathcal{L}\left(E_P|Ag\right) &= \int_{-\infty}^{\infty} \mathcal{L}\left(E_P|E_{Ag}\right) \mathcal{L}\left(E_{Ag}\right) dE_{Ag}, \end{aligned} \tag{2.3}$$

where, $Ag = 1, 2, 3$ represents the three aging conditions corresponding to $550°$C, $600°$C and $650°$C respectively, and E_{Ag} corresponds to the austenite stiffness of the aged SMA. $\mathcal{L}\left(E_P|E_{Ag}\right)$ represents the likelihood of E_P in the model for a fixed E_{Ag} when accounting for the uncertainty in the solutionized stiffness ($\mathcal{L}\left(E_{sht}\right)$) and its propagation in the model for estimating the E_{Ag}. The likelihood functions $\mathcal{L}\left(E_{sht}\right)$ and $\mathcal{L}\left(E_{Ag}\right)$ were assumed to have Gaussian distributions and were calculated from the experiments using the mean and standard deviation reported in Table 2.3. The analysis gave E_P to be 95 ± 26 GPa based on the MLE, and this value was used in the further analysis. Table 2.3 also compares the estimations from MLE with the experiments. The calibrated stiffness in the $550°$C case is close to the experimental value owing to its higher precision across samples. The $600°$C and $650°$C cases, because they had lower precision across samples, contributed less to the calibration of E_P. In conclusion, better precision measurements contribute more to the maximum likelihood estimation, while observations with substantial uncertainties contribute less. More discussion related to the stiffness estimations is presented in Appendix C.

Table 2.3: Austenite phase stiffness values for different heat treatments in $\mathrm{Ni_{50.3}Ti_{29.7}Hf_{20}}$[A] and their estimated values from the finite element micromechanical model.

Material aging	**Experimental Young's modulus (GPa)**	**Value from E_P estimation (GPa)**
Solutionized	79.6 ± 2.4	-
$550°$C for 10 h	80.8 ± 1.8	80.6 ± 2.1
$600°$C for 10 h	82.2 ± 2.7	80.8 ± 2.1
$650°$C for 10 h	84.4 ± 4.1	81.3 ± 2.0

2.7 Results and discussion

The developed micromechanical modeling framework was used to model the precipitation hardened responses in $Ni_{50.3}Ti_{29.7}Hf_{20}$ [A], $Ni_{50.3}Ti_{29.7}Hf_{20}$ [B1] and $Ni_{50.3}Ti_{34.7}Hf_{15}$ [B2] SMAs for different heat treatment conditions. For aged [A] SMAs the modeling was performed using TEM reconstruction RVEs (section 2.4) and ellipsoidal RVEs (section 2.5). For [B1] and [B2] SMAs, the precipitation hardened responses were modeled using the ellipsoidal RVEs and comparisons were made with experimental responses available in the literature [4].

2.7.1 Predictions of responses in precipitation hardened $Ni_{50.3}Ti_{29.7}Hf_{20}$ [A] SMA

Figures 2.14, 2.15 and 2.16 show predictions of actuation responses in [A] for heat treatment conditions $550°$C 10h, $600°$C 10h and $650°$C 10h respectively. The experimental responses of solutionized (SHT) and heat treated SMAs are shown along with the modeling. Because of the sample-to-sample variation, the experimental responses are presented with confidence intervals (CIs) of 1 standard deviation accounting for differences from many samples (3 for SHT, 2 for $550°$C, 2 for $600°$C and 3 for $650°$C). The predicted responses from four TEM RVEs are also shown with confidence interval(CI) with their mean response. For the predictions from the ellipsoidal RVE, a single response is shown, since there was little variation between different realizations.

Depending upon on the extent of spatial variation of volume fraction in the 3-D TEM reconstruction, the predictions using the four TEM RVEs gave wider confidence regions in the responses. In $550°$C, we see 3-D reconstruction to be uniform with little spatial variation of volume fraction ($8.5 \pm 0.3\%$), and the predictions also showed tight confidence intervals, whereas in $600°$C, the TEM RVEs responses gave wider CI, mainly due to the higher spatial variation of volume fraction ($9.8 \pm 3\%$). At $650°$C as well, the responses from TEM RVEs had wider confidence interval because of the higher spatial variation in the volume fraction ($12.9 \pm 2.5\%$). The irregular transformation shapes in the mean response shown in the Figure 2.15 are only an artifact from the spread of responses in different realizations. Also, the peaks in the confidence interval for the case of $600°$C at 300 MPa and $650°$C are produced when there is large scatter along temperatures, which

can also be seen in [108].

In the comparisons shown (Figures 2.14-2.16), an increase in transformation strain with increasing precipitation was observed in the three aging conditions. In the $550°$C heat treatment compared to the solutionized, the responses give comparable strain at lower stresses (100 MPa and 200 MPa) and lower strain at high stress (300 MPa), while in the $600°$C heat treatment, strain values are higher at lower stresses (100 MPa,200 MPa) and comparable at high stress (300 MPa) to the solutionized responses. In the $650°$ heat treatment, higher strain values were seen compared to the solutionized SMA at all stress levels. This increasing behavior on strain with precipitation is explained using the compositional effects on transformation strain (section 2.6.2.2). As the extent of precipitation increased from $550°$C to $650°$ heat treatment, the transformation strain ($H^{cur}(\sigma)$) in the matrix increased due to the composition effect, and this resulted in the observed gradual increase of strain in these heat treatments. With the composition effect on transformation strains accounted for, the model is able to predict the rise in transformation. Although the heat treatment $600°$C was not used in the calibration, the close prediction of strain values validates the composition variation in Figure 2.11. This shows the ability of the developed micromechanical model to predict the transformation strain in new heat treatments.

The temperature ranges of transformation predicted in the responses of TEM RVEs and ellipsoidal RVEs are close to the experimental measurements (see Figures 2.14-2.16). The Ellipsoidal RVEs gave slightly lower temperature range compared to the TEM RVEs due to the lower volume fraction estimations in the methodology (see table 2.4). As the volume fraction of precipitates increases, the matrix becomes more Ni-lean and the transformation temperatures increase with the Ni-lean matrix. The good agreement between the predictions from micromechanical modeling with experimental measurements shows that the method of microstructure reconstruction from TEM images provides volume fraction values in the realistic range. The ellipsoidal RVE methodology produced comparable predictions for all heat treatments and stress levels, which indicates it is a good methodology for RVEs in new materials and also gives volume fractions in a realistic range.

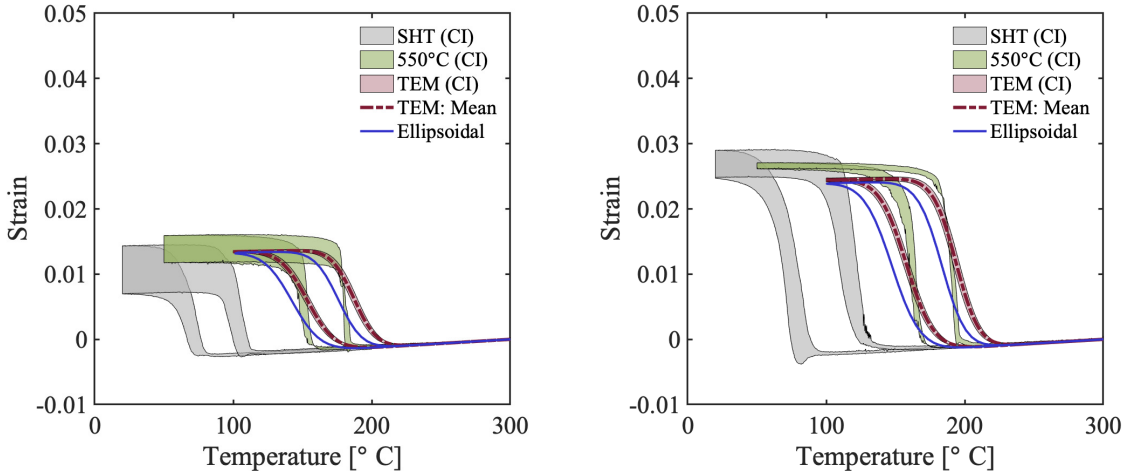

(a) Load = 100 MPa

(b) Load = 200 MPa

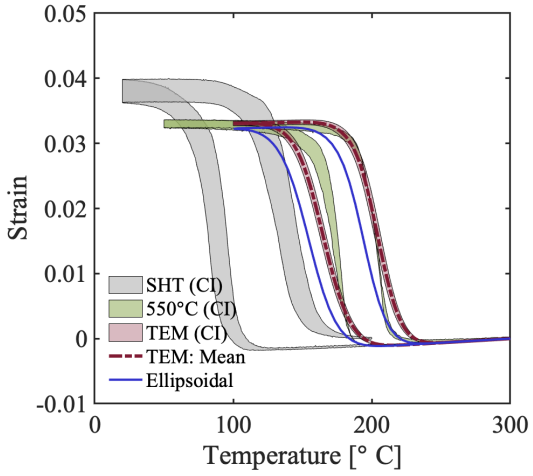

(c)Load = 300 MPa

Figure 2.14: Comparison of predictions to experimental responses in $Ni_{50.3}Ti_{29.7}Hf_{20}$ [A] aged at 550°C for 10h. The experimental responses of solutionized material (SHT) and the heat treated material (550°C) from different samples are presented with confidence interval (CI). The predictions from four TEM RVEs are presented with CI and prediction from ellipsoidal RVE is compared.

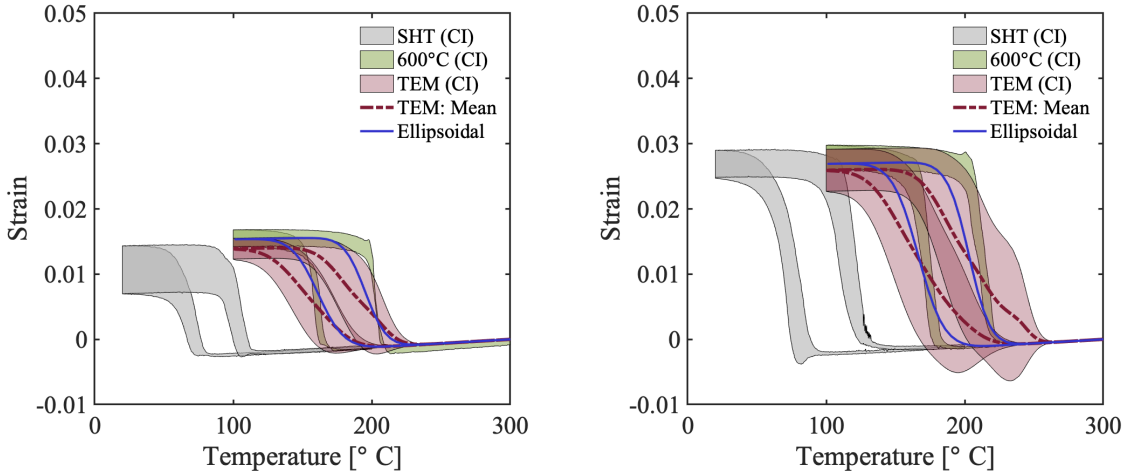

(a) Load = 100 MPa

(b) Load = 200 MPa

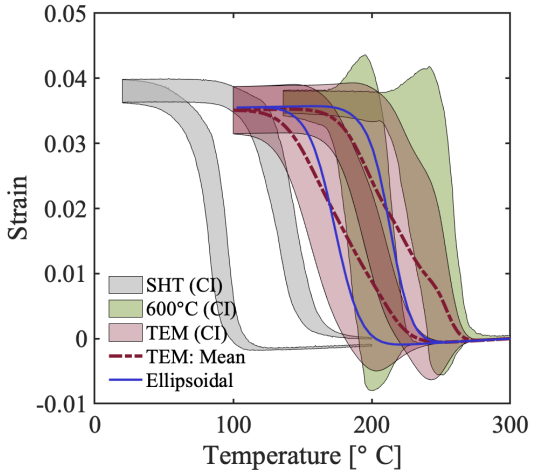

(c) Load = 300 MPa

Figure 2.15: Comparison of predictions to experimental responses for $Ni_{50.3}Ti_{29.7}Hf_{20}$ [A] aged at 600°C for 10h. The experimental responses of solutionized material (SHT) and the heat treated material (600°C) from different samples are presented with confidence interval (CI). The predictions from four TEM RVEs are presented with CI and prediction from ellipsoidal RVE is compared.

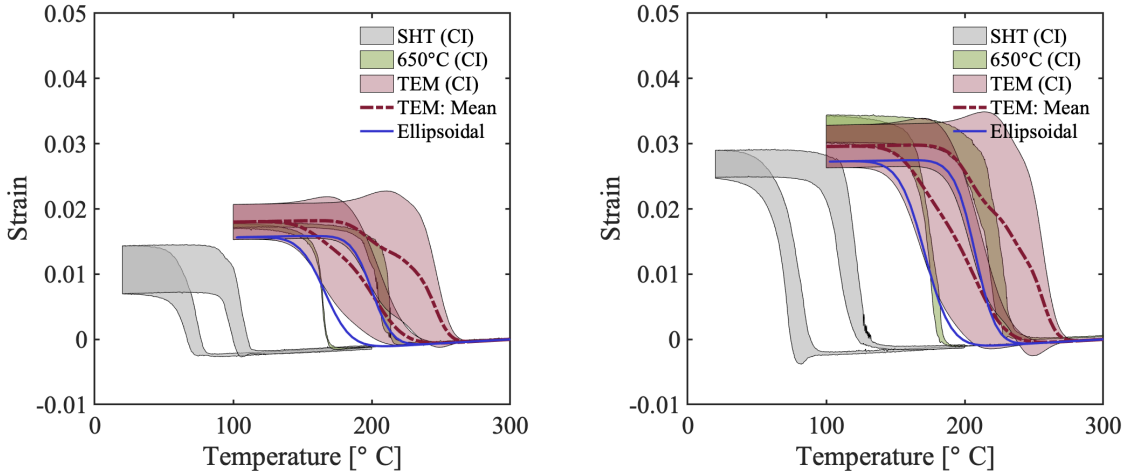

(a) Load = 100 MPa

(b) Load = 200 MPa

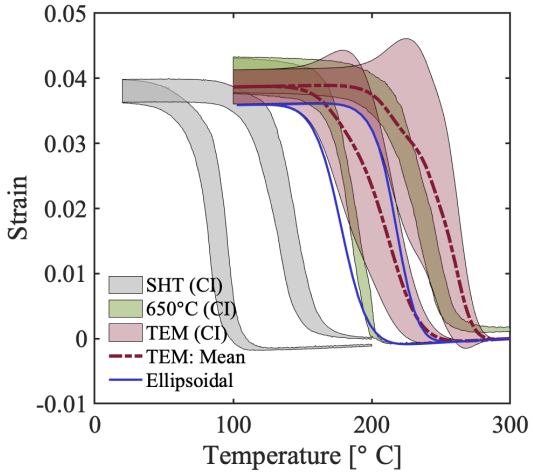

(c) Load = 300 MPa

Figure 2.16: Comparison of predictions to experimental responses for $Ni_{50.3}Ti_{29.7}Hf_{20}$ [A] aged at 650°C for 10h. The experimental responses of solutionized material (SHT) and the heat treated material (650°C) from different samples are presented with confidence interval (CI). The predictions from four TEM RVEs are presented with CI and prediction from ellipsoidal RVE is compared.

2.7.2 Prediction in SMAs with different processing parameters

The developed micromechanical modeling framework was implemented to study the HTSMAs with a different processing history. The RVE based on ellipsoidal methodology (section 2.5) was used for modeling the precipitation hardened responses in $Ni_{50.3}Ti_{34.7}Hf_{15}$[B2] and $Ni_{50.3}Ti_{29.7}Hf_{20}$[B1] SMAs from the work by Evirgen [4]. The summary of the estimated composition, volume fraction and aspect ratios is given in Table 2.4. The variation of k with composition from Figure 2.11 was used. The additional material parameters for the SMA matrix were assumed to be the same as Table 2.2. Responses of material [B2] in two heat treatment conditions (550°C 3h and 600°C 10h) were modeled. Similarly, for material [B1], two heat treatment (500°C 48h and 550°C 3h) responses were modeled.

Figure 2.17 and Figure 2.18 show the actuation response comparisons in [B2] and [B1] respectively. The response at 200 MPa and 300 MPa were predicted using the micromechanical model for different heat treatment cases, and are compared with experimental responses of solutionized and aged SMAs. The heat treatment cases 550°C for 3h in [B2] and 500°C for 48h in [B1] were not used in the calibration, but predicted well with the developed model. The comparisons (Figure 2.17(a) and (b), Figure 2.18 (a) and (b)) show that the model is able to predict the strain values and the temperatures of transformation close to the experiments in these new heat treatments.

In the aged [B2] SMAs experiments (Figure 2.17), a higher value of maximum strain is observed in 550°C for 3h and a lower value in 600°C for 10h in comparison with the solutionized. The lower strain in 600°C for 10h in comparison to the solutionized contrasts with the behaviors seen in the aged [A] SMAs, where higher strain was observed compared to the solutionized with increase in precipitation. Looking into the k variation for [B2] SMAs (Figure 2.11), we see a lower gradient with decreasing composition, which indicates a less dominant composition effect of transformation strain in this alloy. Hence, it can be concluded that in 600°C 10h heat treatment, the constraining effects of precipitates because of a higher volume fraction ($= 0.107$) dominates over the composition effect resulting in a lower strain, while in 550°C for 3h, the composition effects dominated and resulted in a higher strain than the solutionized response. The micromechanical

modeling is able to capture the trend in the modeling.

In the two heat treatments (500°C 48h, 550°C 3h) in [B1] SMA, we see higher strains in both heat treatments compared to the solutionized response. This can be explained by the competing effects of composition change and precipitation hardening. The volume fraction estimation in these heat treatments are ≈ 4.5 % (see Table 2.4), which can be considered to be lower. When examining the composition effect in [B1], it has a stronger gradient of k versus composition than [B2], indicating a stronger composition effect (see Figure 2.11). The higher transformation strain in the presented heat treatments of [B1] can be attributed to the stronger composition effect, which dominates over the constraining effect from precipitates. The modeling successfully captured these higher strains through accounting to the compositing variation of k.

Table 2.4: Summary of volume fraction (VF) and aspect ratio (AR) estimations in precipitation hardened $\mathrm{Ni_{50.3}Ti_{34.7}Hf_{15}}$[B2] and $\mathrm{Ni_{50.3}Ti_{29.7}Hf_{20}}$[B1] SMAs.

SHT material & calculated composition	**Heat treatment**	**Aged material** [Ms Mf As Af]	**Calculated VF**	**AR**
$\mathrm{Ni_{50.3}Ti_{34.7}Hf_{15}}$[B2]	550°C for 3h	[46 37 91 102]	0.038	3 ± 0.5
$(\mathrm{Ni}-50.67, \mathrm{Hf}-15)$	600°C for 10h	[109 65 113 170]	0.107	5 ± 0.5
$\mathrm{Ni_{50.3}Ti_{29.7}Hf_{20}}$[B1]	500°C for 48h	[150 130 162 177]	0.045	2.5 ± 0.5
$(\mathrm{Ni}-50.75, \mathrm{Hf}-20)$	550°C for 3h	[155 128 160 181]	0.047	2.7 ± 0.5

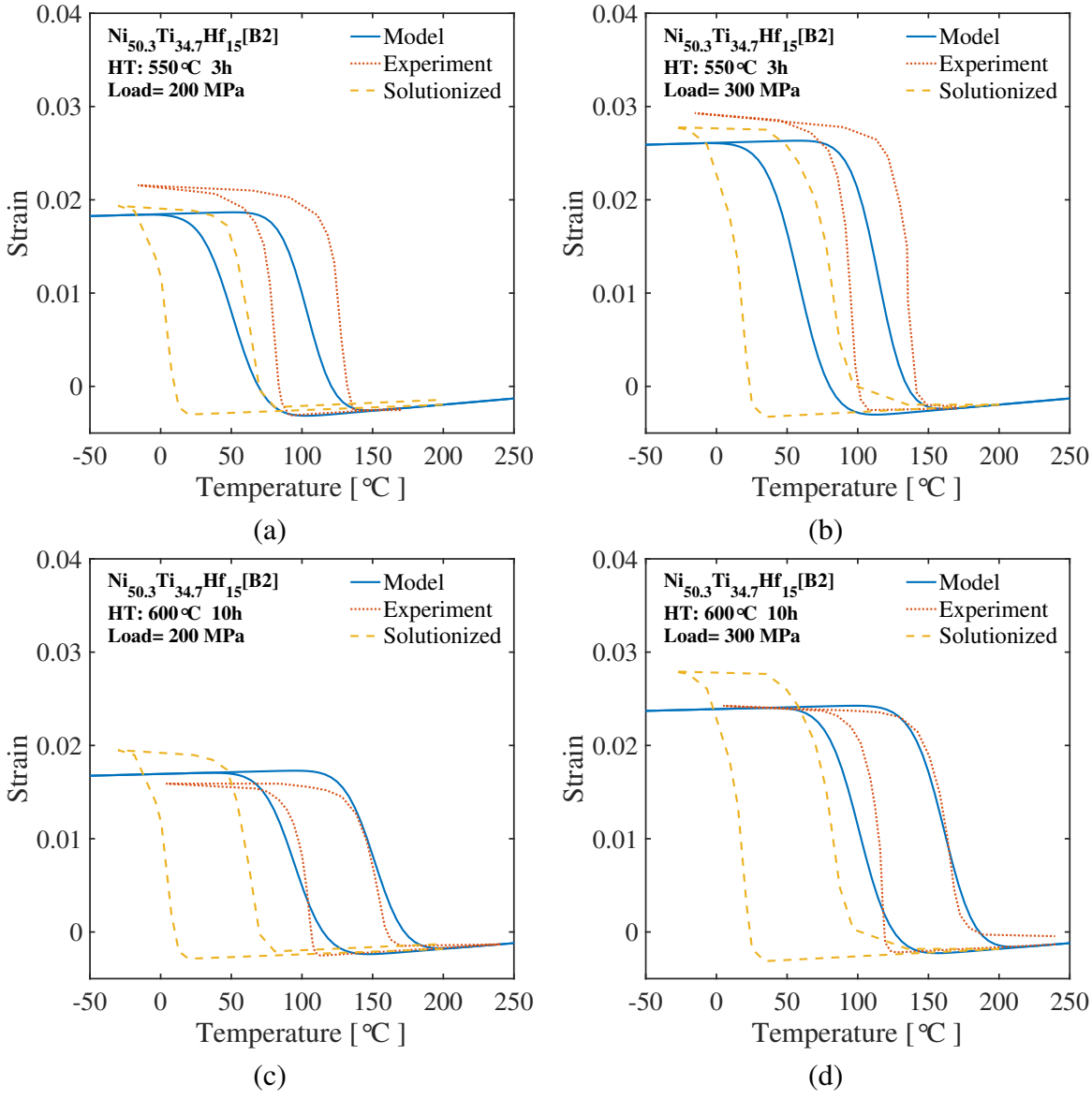

Figure 2.17: Model and experimental responses for two heat treatments in $Ni_{50.3}Ti_{34.7}Hf_{15}$[B2] are compared. (a) and (b) show comparison in 550°C for 3h responses at 200 MPa and 300 MPa, (c) and (d) show comparison in 600°C for 10h responses at 200 MPa and 300 MPa.

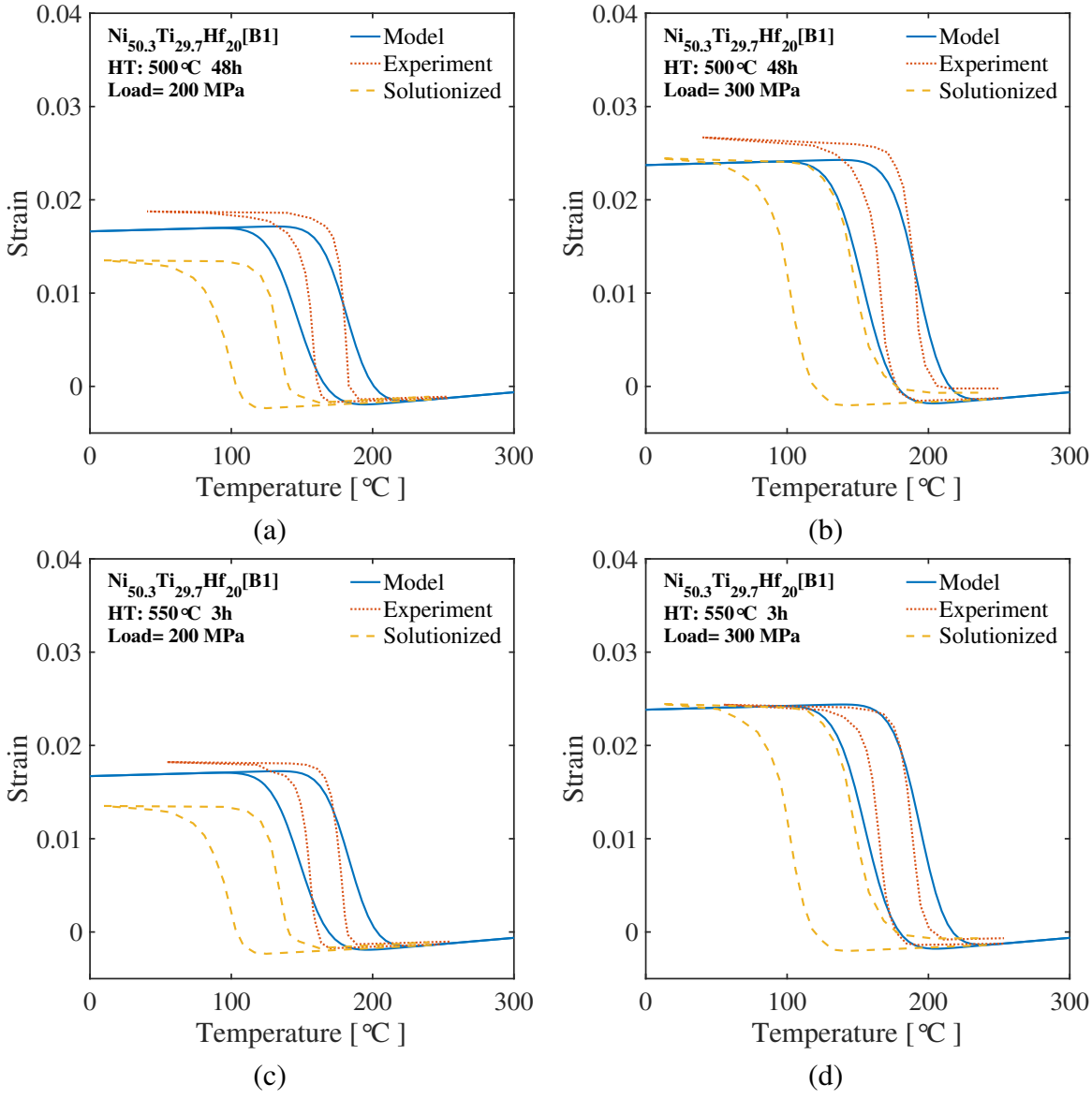

Figure 2.18: Model and experimental responses for two heat treatments in $\mathrm{Ni_{50.3}Ti_{29.7}Hf_{20}[B1]}$ are compared. (a) and (b) show comparison in 500°C for 48h responses at 200 MPa and 300 MPa, (c) and (d) show comparison in 550°C for 3h responses at 200 MPa and 300 MPa.

2.8 Conclusions

This paper presents a study on the phase transformation behavior of precipitation-hardened NiTiHf SMAs, focusing on their micromechanical modeling. The aged NiTiHf SMAs produced higher transformation strain with precipitation, which was counterintuitive, as the non-transforming precipitates would have reduced the phase transformation. Further, investigating the responses of NiTiHf SMAs with different compositions and processing, it was observed that the extent of transformation at given stress depends on composition and processing. The higher strain behavior in the precipitation hardened SMAs can be explained by the changing of transformation strain in their matrix with composition.

A finite element based micromechanical model was developed for the precipitation hardened NiTiHf SMAs taking into consideration the composition effects in their matrix phase transformation. Two methods of RVE generation were considered: 1) RVEs based on TEM reconstructions of the aged SMAs and 2) ellipsoidal RVEs with an estimated volume fraction. The modeling framework was implemented to model behavior in NiTiHf SMAs from two different processing methods. The predictions demonstrated good comparison for temperature range of transformation and maximum strain to the experiments. To the best of the authors' knowledge, the present work constitutes the first study of the prediction of the actuation response of high temperature SMAs by considering realistic microstructures in the model.

Following are some key results from the developed micromechanical model.

1. The volume fraction in the microstructure was found to be the dominant factor over the exact details of microstructural topology in predicting the behavior.

2. Accounting for the composition dependency of transformation strain in the modeling was necessary to capture the increasing strain values in the precipitation-hardened NiTiHf SMA behavior. The model predicted significantly lesser values of strain when the composition dependency was not accounted for.

3. Upon incorporating the dependency of the transformation strain on compositional content

in the matrix, the model predicts the behavior in accordance with the experimental observations.

4. The less expensive methodology of RVE generation based on approximated ellipsoidal predicts the behavior with good agreement with predictions from the RVEs generated based on TEM reconstructions. This provides a rigorous computational framework for heuristic studies in exploring the sensitivity of the behavior as a function of several microstructural and compositional parameters.

5. The resulting model was employed to study the effects due to processing history on the constitutive behavior of these alloys.

The key implication of this work is that the resulting framework will be useful in optimizing the heat treatment processes to get desired microstructures. As a result, it will be useful in the faster and systematic heat treatment designing in NiTiHf HTSMAs for a specific application.

3. FAST FOURIER TRANSFORM BASED HOMOGENIZATION: APPLICATION FOR PRECIPITATION HARDENED SHAPE MEMORY ALLOYS

3.1 Introduction

SMAs are unique active materials that have the ability to recover from large deformations through a reversible, diffussionless solid-to-solid phase transformation. The phase transformation between the participating phases, martensite at low temperatures and austenite at high temperatures, results in recoverable transformation strain during temperature changes in the transformation range. Due to their unique thermo-mechanical behavior and the ability to produce high stress when constrained, they are suitable for making compact actuators which use thermal energy to perform mechanical work [109]. Compared to other similar active materials, SMAs have higher actuation energy density, and thus are suitable for applications requiring higher work output. Because of their unique material behavior, the SMAs have been studied extensively for their mechanical, failure and constitutive responses [109, 110, 111, 112].

Heat treatment or aging in NiTi SMAs produce Ni_4Ti_3 precipitates with non-transforming behavior. Experimental studies [113, 114, 115] have shown that these precipitates significantly influence the transformation properties and thus also the actuation behavior of the resulting heterogeneous SMA. A careful heat treatment can modify transformation properties of the SMAs and the actuation behavior in a desired manner, providing an innovative way to modify an available NiTi-based SMA to suit a particular application requirement. To speed up this design process, we need computational models capable of accurately predicting the new material response of the heterogeneous SMA [1].

Micromechanical homogenization is key to estimating the effective properties and behavior of heterogeneous materials. In the context of modeling complex microstructures with non-linear material behaviors, the use of full field based computational homogenization techniques is required. Traditionally, the boundary value problem (BVP) for the homogenization was solved through Fi-

nite Element Methods (FEM) [45, 46, 47, 48, 49]. In the past two decades, more efficient spectral methods based on Fast Fourier transform (FFT)[50, 51, 52, 53, 54, 55] have emerged.

A micromechanical homogenization model to predict the aged SMA response has been proposed by several authors [6, 58, 59], where the RVEs consist of homogenized SMA matrix with randomly distributed precipitates. These methods used FEM based homogenization to solve for the precipitated RVE behavior. Due to their high computational cost, the previous FEM based analyses [6, 58, 59] were limited to smaller representative volume containing few particles. It is relevant in this context to look into the effectiveness of the FFT homogenization method as compared to the FEA techniques used in the previous model.

Recently, Cruzado *et al.*[116] developed an FFT homogenization framework for micromechanical modeling of SMAs. The developed FFT homogenization was shown to have advantage over FEA homogenization when using voxel based discretization in both [116]. Since previous FEA micromechanics frameworks for SMAs [6, 58, 59, 1] use geometrically conforming mesh and accurately capture the precipitate geometry compared to the voxel restricted FFT method, in this study, the performance of the FFT voxel based homogenization and the FEA conforming mesh based homogenization are compared. A study to extract different aspects of convergence of FFT and FEA methods are analyzed, and the focus is towards determining the effective SMA response accurately.

In addition to the convergence of the solving techniques, the RVE representations of the material must converge in terms of the volume modeled. Higher sized RVEs are needed to predict the effective response accurately, especially when the precipitate volume fraction is higher, causing higher dispersion between realizations. FFT homogenization[116] allows analysis of bigger RVE sizes (i.e. higher number of particles) in a wider range of volume fractions. With the help of a FFT based homogenization framework [116], a statistical study of the RVE size convergence has also been performed. While in the current work, the dispersion and the RVE size is analyzed in the context of NiTi SMAs, the work is applicable for other material systems including SMAs like Ni-Ti-Hf because of similar modeling methodology[59].

3.2 Modeling precipitation hardened SMAs

Secondary heat treatments in the temperature ranges $\sim 300°C - 500°C$ on NiTi SMAs result in non transforming Ni_4Ti_3 precipitates that can modify the behavior of the SMA [117, 118, 119]. The precipitation modifies the actuation behavior of NiTi SMAs through mechanical and compositional modifications in the microstructure. More on actuation behavior of SMAs can be read in section 1.1.1. In this section, precipitation hardened behavior and the key mechanisms affecting the SMA behavior are summarized. The micromechanical modeling is targeted at capturing the interactions in the microstructure that affect phase transformation. Two homogenization frameworks were compared: FFT based homogenization and FEA based homogenization. The details of the micromechanical homogenization frameworks considered are presented in detail.

3.2.1 Material behavior and effect of precipitation

As the precipitates do not transform, they act to restrict phase transformation in the surrounding matrix. This results in a lower amount of transformation strain in the effective response of the precipitated SMA. The extent of precipitation in the NiTi SMAs is dependent on the initial composition and the heat treatment temperature. With higher temperature and longer duration of heat treatment, higher volume fraction and larger sized precipitates may be produced. The shapes of the precipitates formed are observed to be ellipsoid and coherent with the surrounding matrix [102].

Figure 3.1(a) shows the TEM image of precipitates in $Ni_{50.8}Ti$ aged at 500°C for 24 h. The non-transforming precipitates are formed in different orientations inside the phase transforming matrix. A precipitation of 4.2 % volume fraction (VF) is estimated in this heat treatment [6]. The effect of these precipitates on the actuation response can be seen in the comparison in Figure 3.1(b), where the experimental responses at 200 MPa in the precipitated SMA is compared to the response of the unprecipitated (solutionized) SMA. With the precipitates, the actuation response of the aged SMA has lower strain than that produced by the solutionized SMA. There is also a shift in temperature range where the transformation is happening. The temperature change can be primarily attributed

to composition changes in the matrix caused by elemental diffusion during precipitation [118].

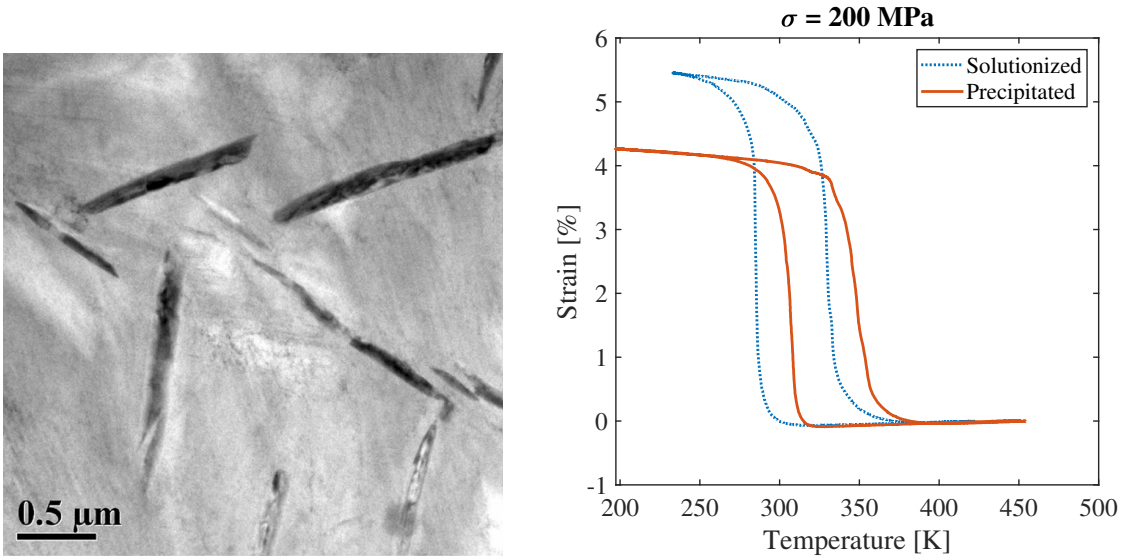

(a) (b)

Figure 3.1: Effect of aging heat treatment in $Ni_{50.8}Ti$ SMA. (a) TEM microstructure of $Ni_{50.8}Ti$ aged at 500°C for 24h [Reprinted by permission from Springer, Cox et al. [6], Copyright (2017)]. (b) A comparison plot showing the effect of precipitation on the actuation response of the alloy compared to the solutionized SMA response [6].

A list of mechanisms through which the precipitated may modify the actuation response is summarized below.

1. The coherent non-transforming precipitates restrain the transformation in the surrounding matrix. Therefore, a higher driving force is required to finish the transformation [100].

2. The precipitation is associated with Fickian diffusion, creating composition gradients in the surrounding matrix. This has considerable effect on the transformation temperatures, which are very sensitive to composition [2].

For the current study, only the mechanical effects of precipitates are modeled. The effects of composition change due to diffusion are not considered. The material properties used for the mi-

cromechanical modeling of precipitated SMA behavior are listed in Table 3.1. The SMA matrix properties (SMA-1) considered are calibrated from $Ni_{50.8}Ti$ SMA responses [6]. The phase transformation constitutive model proposed by Lagoudas *et al.* [38] is used for this purpose. The elastic properties [6] used for modeling the behavior of precipitates are also listed in Table 3.1.

Table 3.1: Material properties used for matrix and precipitate in the NiTi micromechanical model.

SMA Matrix		**Precipitate**	
Parameter	Value	Parameter	Value
E_A	68 GPa	E	107 GPa
E_M	43 GPa	v	0.3
$v^A = v^M$	0.33		
H^{max}	0.055		
$k[MPa^{-1}]$	0.0206		
C_A	6.4 MPa/K		
C_M	21.7 MPa/K		
$n_1 = n... = n_4$	1		
Ms, Mf, As, Af	280 K,266 K,290 K,307 K		

3.2.2 FFT based homogenization [1]

A FFT based homogenization framework is used to obtain the thermo-mechanical behavior of precipitated SMAs. For modeling aged Ni_4Ti_3 SMAs, periodic RVEs containing dispersed precipitates in phase transforming matrix are considered. The RVEs are created with randomly arranged ellipsoid, shaped precipitates, and geometric periodicity is ensured at the faces. Representations of the RVEs for two different volume fractions are shown in Figure 3.2. The domain is discretized using a regular grid in $\mathbb{R}^3$ with N_x=N_y=N_z denoting the number of grid points along each principal direction. A convergence analysis is carried out to determine the number of grid points necessary for convergence, which is presented in 3.4.2. The constitutive response of the SMA matrix is modeled with the thermodynamically consistent formulation developed by Lagoudas *et al.*[38], and the

[1] Adapted with permission from "Representative volume size in micromechanical modeling of precipitated SMAs." by Joy, J. K., Cruzado, A., Solomou, A., Benzerga, A. A., & Lagoudas, D. C., 2019, March, Smart Structures and NDE for Energy Systems and Industry 4.0 (Vol. 10973, pp. 76-85). SPIE.

precipitates are modeled with isotropic linear elastic behavior.

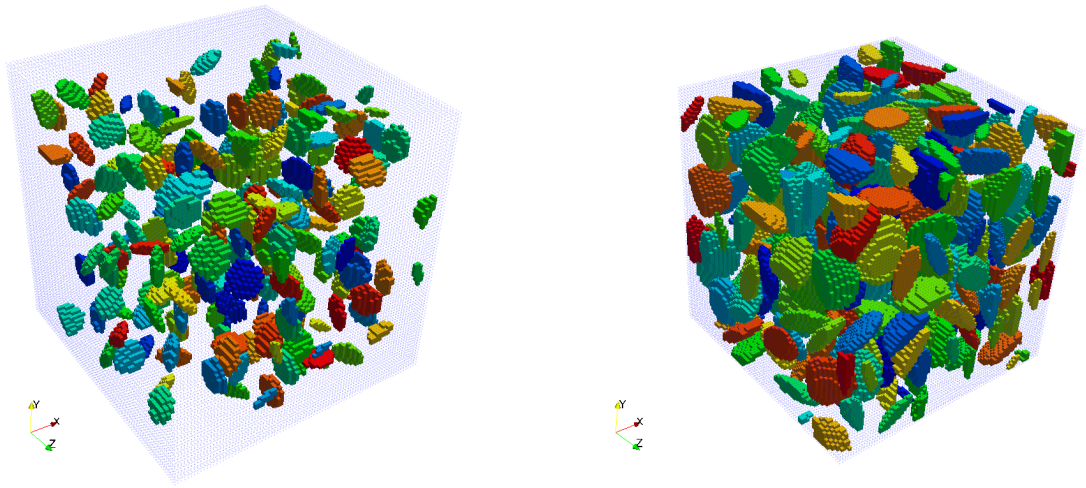

(a) (b)

Figure 3.2: A representation of the RVEs considered. RVEs for different volume fractions (VF) (a) 4.2% and (b) 20% (b) are shown. The precipitates are modeled as ellipsoid geometry with aspect ratio of 4, having random arrangement and orientation. The periodicity is ensured at the boundaries.

The effective actuation response described in section 3.2.1 is considered in this work. Refer to section 1.1.1 for more on the actuation response and corresponding thermo-mechanical loading path. The material is first uni-axially loaded at a constant temperature where the material is in the fully austenite phase, according to $\boldsymbol{\Sigma} = \Sigma_{zz}(\boldsymbol{e}_z \otimes \boldsymbol{e}_z)$ with an overall axial stress of Σ_{zz} . The material initially in the austenite state transforms to martensite upon cooling and transforms back to original austenite phase upon heating. The full actuation responses are computed by simulations of the RVE taken through the thermo-mechanical loading path. The heating and cooling is simulated by incremental temperature changes for the whole RVE.

The microstructural based homogenization is performed through FFTMAD code [55], extended for the SMA thermomechanical behavior by Cruzado *et al.* [116]. The method is briefly described here for completeness. The model is based on the variational FFT formulation [54]

within the framework of FFT based Galerkin methods [120]. Considering periodic boundary conditions, the linear momentum is imposed through a weak form of the stress equilibrium and the compatibility via the convolution integral of a linear projection operator. The standard Galerkin procedure is now adopted to solve the problem. First the domain is discretized using a regular grid, i.e. $N_x \times N_y \times N_z$. The local fields are then approximated by interpolation of the value of the fields at the center of the voxels using trigonometric polynomials. Finally, expressing the convolution operation in the Fourier space while evaluating the volume integral using the trapezoidal rule, a discrete expression for the linear momentum balance is obtained:

$$\mathcal{F}^{-1}\Big\{\Big\{\hat{\mathbb{G}}\Big\} : \mathcal{F}\Big\{\boldsymbol{\sigma}\left[\{\tilde{\boldsymbol{\varepsilon}}\}\right]\Big\}\Big\} = -\mathcal{F}^{-1}\Big\{\Big\{\hat{\mathbb{G}}\Big\} : \mathcal{F}\Big\{\boldsymbol{\sigma}\left[\{\boldsymbol{E}\}\right]\Big\}\Big\}, \tag{3.1}$$

where $\boldsymbol{E}$ denotes the volume-averaged strain, $\tilde{\boldsymbol{\varepsilon}}$ the unknown periodic fluctuation strain field and $\boldsymbol{\sigma}$ the Cauchy stress. $\mathcal{F}$ and $\mathcal{F}^{-1}$ represent the direct and inverse discrete Fourier transforms, respectively, and the notations $[-]$, $\{-\}$ are respectively for local and assembled matrices. $\hat{\mathbb{G}}$ is the Fourier transform representation of the projection operator, which in component form is expressed as [121]:

$$\hat{G}_{pqrs}(\boldsymbol{k}) = \frac{1}{2}\frac{k_p\delta_{qr}k_s + k_p\delta_{qs}k_r + k_q\delta_{pr}k_s + k_q\delta_{ps}k_r}{||\boldsymbol{k}||^2} - \frac{k_pk_qk_rk_s}{||\boldsymbol{k}||^4}, \tag{3.2}$$

with $\hat{G}_{pqrs}(\mathbf{0}) = 0$. Here, δ_{pq} is the Kronecker delta and $\boldsymbol{k}$ is a point in Fourier space representing scaled discrete frequencies, i.e., $k_{v=x,y,z} \in [-N_v/2, N_v/2]/L_v$, with L being the side length of the RVE.

Note that the non-linearity of the algebraic linear system of equations derived from Eq. 3.1 originates only from the constitutive model. This can be solved efficiently in the Newton-Krylov subspace [54] using the conjugate gradient iterative solver. Linearizing the stress about the strain $\boldsymbol{\varepsilon}$ in Eq. 3.1 and expressing the unknown strain fluctuation for the Newton iteration $(i+1)$ as

$\{\tilde{\boldsymbol{\varepsilon}}\}^{i+1} = \{\tilde{\boldsymbol{\varepsilon}}\}^{i} + \{\Delta\tilde{\boldsymbol{\varepsilon}}\}^{i+1}$, being $\Delta\tilde{\boldsymbol{\varepsilon}}$ the fluctuation strain increment, it leads to:

$$\mathcal{F}^{-1}\left\{\left\{\hat{\mathbb{G}}\right\} : \mathcal{F}\left\{\left\{\mathbb{K}\right\}^{i} : \left\{\Delta\tilde{\boldsymbol{\varepsilon}}\right\}^{i+1}\right\}\right\} = -\mathcal{F}^{-1}\left\{\left\{\hat{\mathbb{G}}\right\} : \mathcal{F}\left\{\boldsymbol{\sigma}\left[\{\boldsymbol{\varepsilon}\}^{i}\right]\right\}\right\}, \tag{3.3}$$

where $\mathbb{K}$ is the (consistent or continuum) tangent stiffness. This formulation however is only valid for predefined strain control problems where, for time increment n, the total strain at the beginning of each newton iteration can be expressed as $\boldsymbol{\varepsilon}^{i} = \boldsymbol{E}_n + \tilde{\boldsymbol{\varepsilon}}^{i}$. However, the thermo-mechanical loading conditions involved in phase transforming materials leads to stress-free eigen-strains resulting from unconstrained thermo-elastic expansion and phase transformation. This can be solved through the stress-control algorithm for thermo-mechanical problems described in detail in Cruzado *et al.* [116]. After achieving the convergence of Newton iterations in Eq. 3.3, the total local strain should be corrected according to:

$$\boldsymbol{\varepsilon}^{j+1}(\boldsymbol{x}, T^n) = \boldsymbol{\varepsilon}^{j}(\boldsymbol{x}, T^n) + \left\langle \mathbb{K}^{j}(\boldsymbol{x}, T^n)\right\rangle^{-1}\left(\boldsymbol{\Sigma}^0 - \left\langle \boldsymbol{\sigma}^{j}(\boldsymbol{x}, T^n)\right\rangle\right), \tag{3.4}$$

where $\boldsymbol{\Sigma}^0$ is the initial imposed constant stress and j refers to the current stress control correction iteration. Note that now the constitutive model depends on temperature T at increment n. After each correction, a new Newton iteration must be performed until stress equilibrium is satisfied when the imposed macroscopic stress $\boldsymbol{\Sigma}^0$ is equal to the average of the local stress field $\langle \boldsymbol{\sigma}^{j+1}(\mathbf{x}, T^n)\rangle$, within some tolerance.

3.2.3 FEA based homogenization

An FEA based homogenization is implemented in ABAQUS FEA software to solve for the effective SMA response from the RVEs. The matrix is modeled using the constitutive model by Lagoudas *et al.* [38] and implemented using the ABAQUS user material subroutine. The precipitates are modeled as linear elastic material with isotropic property, using the elastic model in the ABAQUS. The RVEs of the material were discretized using conforming mesh (C3D4) in ABAQUS with different seeding parameters. The periodic boundary conditions were applied on

the faces of the RVEs to avoid the boundary effect and to predict pure bulk constitutive behavior. A stress (= 200 MPa) was applied on the RVE along the loading direction at temperature 380 K and maintained constant throughout the thermal cycle. The cooling and heating (to 250 K and back to 380 K) on the RVEs were simulated by changing the temperature boundary conditions on the RVE. The RVE deformation was solved through FEA using implicit formulation using direct solver in the ABAQUS FEA software [101]. The effective response of the RVE was obtained using the volume average of strain in the whole RVE. Figure 3.3 shows the RVE of the material modeled and the stress distribution around the precipitates solved with the implementation.

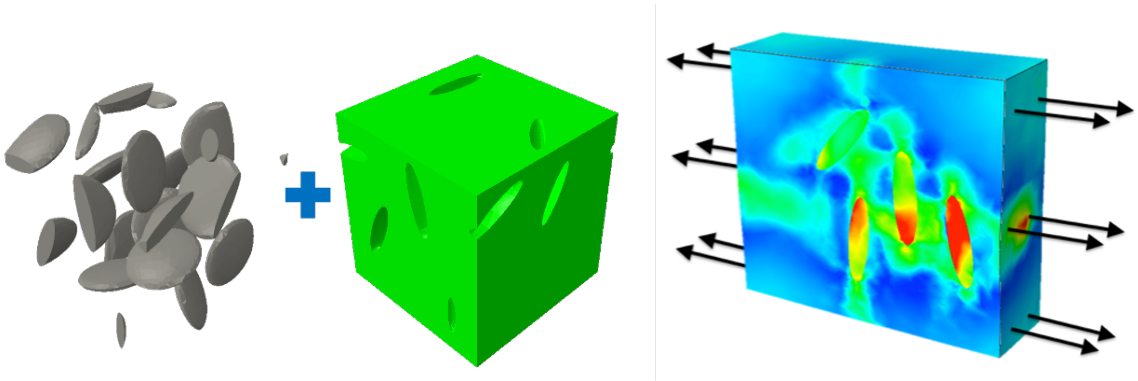

(a) (b)

Figure 3.3: Figure showing the FEM based modeling for RVE response. (a) RVE used in the modeling shown separated as the precipitate and matrix phase (b) Loading on the RVE to solve for the effective response.

3.3 Methodologies

With the two homogenization methodologies (FFT and FEA), it is important to look into their performance towards solving the converged SMA homogenized response. The first part of the study presents a comparison of convergence on the two methodologies. As the FEA can be implemented with different mesh types, the performance in conforming and non-conforming mesh types are analyzed. In the second part of the study, we look into convergence of the response with size

of the RVE. This is performed with the goal of developing statistical relations that can be used in future studies using the micromechanical model for SMAs.

3.3.1 Comparison of convergence in methods

In the context of comparison of computational homogenization methods, it is important to define terms such as 'evolution', 'convergence', 'accuracy' and 'solution time'. Evolution of solution in each method is studied in terms of the degree of freedom (DOF) it needs to solve. Thus, the convergence of the methods are analyzed in terms of the DOF. A solution is said to be 'converged' when it achieves a certain 'convergence criterion' for a number of DOF, and satisfy the same criterion for any greater number of DOF. The 'value of convergence' in a solution is defined as the value of the 'convergence criterion' for the specific solution.

The 'convergence criterion' is defined with two different approaches in the presented study. In the first approach, it is the amount of difference between the current solution and the available highest DOF solution solved using the same method. This criterion is summarized in Eq. 3.5, where $E(T)$ is the strain at temperature T and the subscript $'Ref'$ denotes the highest DOF solution taken as reference. For the second approach, the convergence criterion evaluates the rate of improvement in the solution with DOF. The second approach is summarized in Eq. 3.6, where the solution of two adjacent evaluations denoted by 'i' and '$(i+1)$' are compared and Df denotes the DOF in each evaluation.

$$\overline{|E(T) - E_{Ref}(T)|} = \frac{\oint_{cycle} |(E(T) - E_{Ref}(T))\, dT|}{\oint_{cycle} |dT|} \tag{3.5}$$

$$\frac{\overline{|E_{i+1}(T) - E_i(T)|}}{(Df_{i+1} - Df_i)} = \frac{\oint_{cycle} |(E_{i+1}(T) - E_i(T))\, dT|}{(Df_{i+1} - Df_i) \oint_{cycle} |dT|} \tag{3.6}$$

In the two convergence criterion presented, the 'value of convergence' is defined taking the average of the whole response. One drawback here is that it does not give a good estimation of how a specific strain value in the response is evolving with DOF, hence it may not represent the convergence of a specific strain value in the response. Another approach that should be looked

into is the evolution of a specific strain value in the response. For the SMA actuation response, the evolution of the maximum strain at the end of cooling is worth exploring further.

In the absence of close-form solution, it is difficult to define the accuracy of solutions. It is not guaranteed that all methods converge to the close-form solution. The numerical error in the method may dominate, and the method can converge to a different solution than the close-form solution. With an assumption that all methods converge to a same solution, we might be able to develop a definition for accuracy. The method which achieves 'convergence criterion' solving for the fewest DOF is defined as the most accurate among the methods satisfying the above assumption. The 'value of accuracy' according to this definition will be simply the 'value of convergence' assuming the solution has met the convergence criterion. This definition for accuracy is different from the traditional approach where the close-from solutions are available, but it allows us to compare the accuracy of the methods within the current solution framework.

The determination of which is the faster method can be made in terms of the time taken to solve converged solutions. The method which gives the solution in the least time for the same accuracy is then considered to be faster. When calculating the time for solution, each method is solved in the same computational environment. The CPU time taken for the solutions is compared and the speed is defined with this time.

These definitions were used to examine the FFT and FEA homogenization methods. The convergence was analyzed for different mesh types. The RVE used for comparing has a volume fraction of 4.2% , 15 particles, and an aspect ratio of 4. SMA actuation responses with Σ_{zz} =200 MPa were investigated, with cooling and heating between 250 K and 380 K.

For the FEA homogenization model, conforming tetrahedral linear (C3D4) and quadratic (C3D10M), and non-conforming voxel (C3D8) meshes were analyzed. For the FFT method, only the non-conforming voxel mesh was analyzed, as the formulation is specific to the voxel mesh. The details of the meshes considered are listed in Table 3.2. The conforming meshes are identified by the seed size used. The non-conforming meshes are identified by their discretization size. Figure 3.4 shows examples of the conforming meshes used in the FEA model, where only the precipitates are

shown. In Figure 3.5, examples of non-conforming voxel meshes used in the study are shown.

Table 3.2: Mesh size of cases considered in the FEA versus FFT comparison study.

FEA			**FFT**
Linear (C3D4)	Quadratic (C3D10M)	Voxel (C3D8)	Voxel
Seed size =	Seed size =	size N=	size N=
0.25	0.25	11	11
0.2	0.2	21	21
0.125	0.125	31	31
0.1	0.1	41	41
0.0625	0.05	51	51
0.05	0.04	61	61
0.04			
0.03125			
0.025			

The value of convergence for different meshes was studied using Eq. 3.5 and Eq. 3.6, where the DOF is the key varying parameter. In the FEA method, the DOF is obtained by multiplying the total number of integration points by three, corresponding to the three displacement degree of freedom. In the FFT method, the total number of DOF is obtained by multiplying the total number of nodes with nine, corresponding to the nine strain components solved at each node. The DOF in FFT and FEA methods for different meshes are compared in Table 3.3.

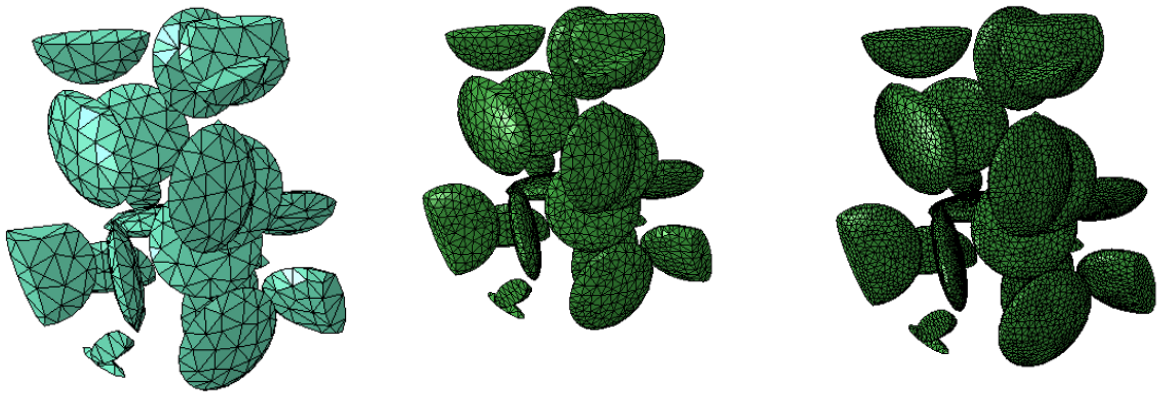

(a) (b) (c)

Figure 3.4: Figure showing the conforming mesh in the FEM model with different seeding sizes (a) seeding size = 0.1, (b) seeding size = .04 and (c) seeding size = 0.025.

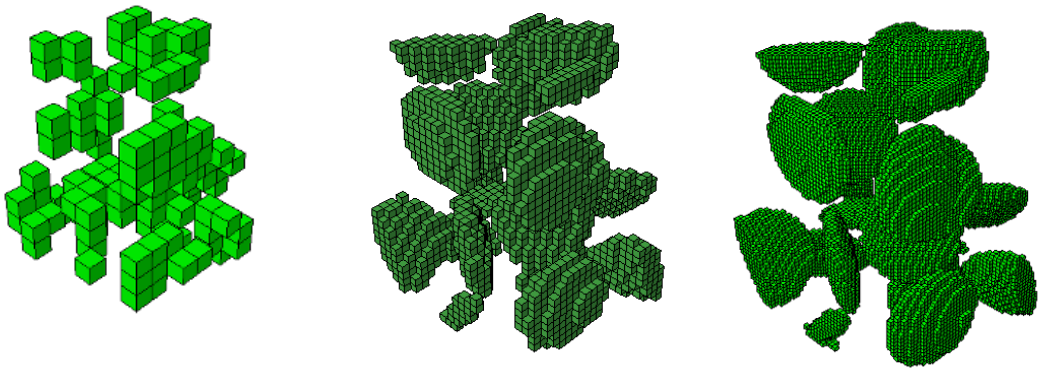

(a) (b) (c)

Figure 3.5: Figure showing the structural meshes in the FFT model with different discretization. Each side is discretized into (a) 11 (b) 31 and (c) 61.

Table 3.3: DOF for each mesh size considered in the FEA versus FFT comparison study.

FEA						**FFT**	
Linear (C3D4)		Quadratic (C3D10M)		Voxel (C3D8)		Voxel	
Seed size	DOF	Seed size	DOF	Size (N)	DOF	Size (N)	DOF
0.25	2058	0.25	16155	11	4002	11	11979
0.2	2964	0.2	23496	21	27792	21	83349
0.125	7824	0.125	62430	31	89382	31	268119
0.1	13425	0.1	107592	41	206772	41	620289
0.0625	38352	0.05	537423	51	397962	51	1193859
0.05	66921	0.04	868347	61	680952	61	2042829
0.04	108063						
0.03125	197478						
0.025	321591						

3.3.2 RVE convergence analysis [2]

Previous studies on RVE sizes [58] for micromechanical modeling were limited by smaller volume fractions and few number of particles, which was not extensive enough to build statistical relationship. In the current study, convergence of the SMA RVE is analyzed for a wider range of microstructures. The convergence of the RVEs was evaluated for accuracy in determining the homogenized response. The list of factors that may determine the convergence of the effective homogenized response based on the RVEs size is summarized below.

1. Volume fraction of the particle increases the dispersion in the homogenized response between RVE realizations. With volume fraction, the mechanical interactions at the microstructure increase, consequently the microstructure difference between RVE realizations is reflected much more in the homogenized response.

2. The number of precipitates modeled influences the convergence in the effective response. RVEs with a larger number of precipitates are more representative of the material and can give accurate predictions.

3. With many RVE realization simulations, the ensemble averaged behavior has higher accuracy. Smaller RVEs require many more realizations than larger RVEs to obtain the same convergence of the ensemble average.

To address the different aspects of RVE convergence, a systematic statistical analysis of RVEs was carried out. RVEs of the precipitated SMAs were created for different volume fractions of precipitates, and the effective actuation responses were simulated. The effective responses were solved using the FFT homogenization framework described in section 3.2.2.

The RVE convergence study was performed in the following sequence. With a spatial convergence analysis on the FFT grid discretization, the grid size required for simulating RVEs were

[2] Adapted with permission from "Representative volume size in micromechanical modeling of precipitated SMAs." by Joy, J. K., Cruzado, A., Solomou, A., Benzerga, A. A., & Lagoudas, D. C., 2019, March, Smart Structures and NDE for Energy Systems and Industry 4.0 (Vol. 10973, pp. 76-85). SPIE.

determined as a function of the RVE size. Further, for volume fractions 7%, 10%, 15% and 20%, the variation of the effective response was analyzed for different RVE size by changing the number of particles. Multiple realizations were created for the same size of RVE to understand the dispersion of the effective property.

The dispersion from different realizations were compared using Coefficient of Variation (CV) denoted as $\hat{D}$ in the maximum strain in the response. From RVEs with a given number of precipitates (P), the coefficient of variation is defined as:

$$\hat{D}_{E_{zz}}(\mathrm{P}) = \frac{\sigma[E_{max}(\mathrm{P})]}{\mu[E_{max}(\mathrm{P})]}, \tag{3.7}$$

where μ and σ are the mean and the standard deviation is obtained for the different number of realizations. E_{max} is the maximum effective strain during the actuation cycle in the loading direction for a given number of particles P. For the current work, CV was calculated from 10 realizations in each case (VF, P).

A converged effective response may be achieved from a large sized RVE with fewer number of realizations or from a smaller RVE with many realizations. Larger RVEs are more representative of the material microstructures. However, solving larger RVEs requires more computational power. Nevertheless, modeling using small RVEs is not an accurate methodology, as it may represent the material inadequately, and some mechanical interactions will not be captured in the small RVEs. A superior methodology is to choose an adequate size for the RVEs with multiple realizations. This must be done optimally, considering the accuracy requirement and available computational power. For this, we require the knowledge of the dispersion for different RVE sizes. Building statistical relations of the dispersion of RVE properties will help in optimizing the RVE size and number of realizations required for a desired accuracy in the prediction.

3.4 Results and Discussion

The FFT and FEA based homogenization techniques were used to simulate the behavior of an RVE using different mesh sizes. The convergence of the two homogenization methods were

studied with different mesh types. The FFT method was analyzed for voxel mesh type for different sizes of discretization. The FEA method of solution in the ABAQUS FEA solver was analyzed for conforming smooth meshes and non-conforming voxel mesh. For different seeding sizes, the conforming smooth mesh performance was investigated.

Further, the convergence of RVE for effective actuation response was analyzed using the FFT homogenization method. The RVE dispersion of the response at volume fractions VF$= 10, 15, 20\%$ was quantified for size of particles P$= 3, 6, 9, 12, 15, 30, 60, 90$ analyzing solutions from multiple ($= 10$) RVE realizations. The dispersion of the maximum strain in the responses was analyzed in terms of coefficient of variation ($\hat{D}$) (section 3.3.2). Further, their convergence regarding RVE size (P) was studied for different VF. Simple statistical correlations on the dispersion of the effective responses were derived for different volume fractions.

3.4.1 Performance comparison of FFT and FEA based homogenization

The comparison of the responses showed that as the mesh size increased, the responses converged towards the response with the highest mesh size. Figure 3.6 (a)-(d) shows the comparison of the responses from the four methods (FFT (voxel), FEA (C3D4), FEA (C3D10M) and FEA (voxel)) studied in the work. The different methods differ in the extent of closeness of responses with increasing mesh size. As the size of the mesh increases, the responses converge to the finest discretization used in each method.

A comparison from the finest mesh responses from different methods show converging solutions. Figure 3.7 shows a comparison of the most converged responses from different methods studied. The responses from linear (C3D4) and quadratic (C3D10M) meshes in FEA match well with voxel mesh solution in the FFT method. However, the voxel mesh solution from the FEA has a different solution from the other method solutions. Here, the FFT method gives a matching response from the non-conforming mesh modeling to the conforming mesh modeling in the FEA method, while FEA method could not achieve the same from the same non-conforming mesh. This motivates us to investigate further the evolution, convergence, accuracy of the different solving methods and meshing approaches.

The convergence of the approaches was analyzed using the criterion defined in Eq. 3.5. Figure 3.8 shows the evolution of the convergence value with DOF, where an exponentially decaying kind of variation of convergence value with DOF is seen. The conforming mesh approach in the FEA and FFT voxel approach converge in the same order, whereas the FEA voxel mesh has much lesser convergence compared to the other three. The convergence criterion ($< 10^{-4}$) is shown, and the intersection between the variation and the criterion marks the DOF where the convergence is met. Based on this criterion, the accuracy of the methods can be ordered according to the definition in section 3.3.1. The methods can be ordered in the decreasing accuracy as: FEA C3D4 $>$ FFT voxel $>$ FEA C3D10M $>>$ FEA voxel.

Further, the convergence of the approaches were analyzed using the second convergence criterion defined in Eq. 3.6. Figure 3.9 shows the evolution of the convergence value with DOF. The comparison here gives a similar message as the previous convergence analysis. The conforming mesh approaches in FEA and FFT voxel converge with a same order of accuracy. The FEA voxel mesh gave the least rate of convergence among the four. Based on the definition of accuracy for the convergence criterion ($< 10^{-4}$), the order of accuracy can be defined as: FEA C3D10M $\sim$ FFT voxel $>$ FEA C3D8 $>>$ FEA voxel. If the value for convergence criterion is increased, the accuracy order can change. Thus, from the two analyses of convergence, for a reasonably fine mesh it can be concluded that the accuracy can be determined as FEA C3D4 $\sim$ FFT voxel $\sim$ FEA C3D10M $>>$ FEA voxel.

Computation time in the FFT and FEA methods was calculated. Table 3.4 shows the comparison of the time for solution in FEA (C3D4) and FFT (voxel). These times are for computation with one CPU, without any parallel computing. A case with close DOF from the two can be assumed to be of the same accuracy in accordance with the observations in the previous convergence analyses. Based on time, it can be concluded that the FFT method achieves convergence at least four times faster than the FEA C3D4 method. However, a conclusion regarding the speed of the FFT method compared to FEA cannot be made solely on this analysis. This is because in the current study, both methods use different solvers, since FFT uses an iterative solving method and FEA uses a direct

solving method. To have a proper comparison, the same analysis should be using the same kind of solver in both methods. This is a future work to consider.

Table 3.4: Comparison of FFT versus FEA solution time for the selected RVE.

	FEA			**FFT**		
Case	C3D4 Size=	No of Eqns.	Time (s)	Eqvnt. (N)	No of Eqns.	Time (s)
1	0.1	13425	2379	12	15552	632
2	0.0625	38352	8852	17	44217	2544
3	0.05	66921	18370	20	72000	2976
4	0.04	108063	44049	23	109503	6918

An analysis of the evolution of maximum strain (E_{MAX})in the responses with DOF was performed. Figure 3.10 (a)-(d) shows the variation of the maximum strain (E_{MAX}) with degree of freedom (DOF) solved from the four approaches. Qualitatively, these variations are converging to an asymptotic value. A similar kind of evolution is observed in the FFT (voxel) and FEA (C3D4) methods, with a minimum and then converges to asymptotic values. For the FEA (voxel) and FEA (C3D10M) methods, the evolution is monotonic to their asymptotic value. A rational function fitting is used to capture the evolution, and further used to estimate the asymptotic values.

The estimation of the asymptotic values indicates that the methods are converging to close values of maximum strain within a bound. Close values with $\approx 0.15\%$ relative difference are obtained between linear FEA (C3D4) and FFT (voxel) methods. The values in quadratic (C3D10M) $\approx 0.52\%$ and voxel $\approx 1.5\%$ have higher relative difference from FFT and linear method estimates. While these values are close, estimates show that the methods can converge only within a bound. These asymptotic values might get closer with a higher number of DOF solutions, but the difference may not be fully eliminated.

A comparison of the E_{MAX} evolution from all cases is shown in Figure 3.11, which makes it easier to understand the differences in their asymptotic convergence. The x-axis is shown in log-scale to depict the convergence of all orders of DOF. Among the four cases, FEA (C3D4) is

seen to give values closer to its asymptotic value with the least DOF. If we analyze the methods for the least DOF to give a solution closer (< 0.0005) to their asymptotic value, the required value of DOF in FEA (C3D4)$<$ FFT (voxel) $<$ FEA (C3D10M) $<$ FEA (voxel). This means the accuracy of methods follow the order FEA (C3D4)$>$ FFT (voxel) $>$ FEA (C3D10M) $>$ FEA (voxel). If we look for closeness of evolution among the different methods, FEA (C3D4) and FFT (voxel) evolve closer to each other but not to the same asymptotic value. The quadratic (C3D10M) shows much less convergence rate in spite of the observations from previous analyses, where the quadratic showed almost the same order of convergence. As before, the FEA voxel mesh solution showed poor convergence and gave the asymptotic value with a larger difference.

In summary, the following conclusions can be drawn from the presented convergence study. The analysis using average convergence criterion showed that the three methods FFT (voxel), FEA (C3D4) and FEA (C3D10M) have a closer level of convergence and accuracy compared to the FEA (voxel) method, which has lower convergence and accuracy. The convergence study for the maximum strain value showed that FFT (voxel) and FEA linear have close asymptotic solutions. Further, the rate of convergence and accuracy was determined to be FEA (C3D4)$>$ FFT (voxel) $>$ FEA (C3D10M) $>$ FEA (voxel). Since the FFT (voxel) and FEA (C3D4) produce close convergence, accuracy and asymptotic values, their CPU solving time were compared for the same DOF. The comparison showed that the FFT (voxel) method solves at least four times faster than the FEA (C3D4) considering that both use different solvers. Hence, it is justifiable to continue the RVE analysis using the FFT method given its good accuracy and less computation time.

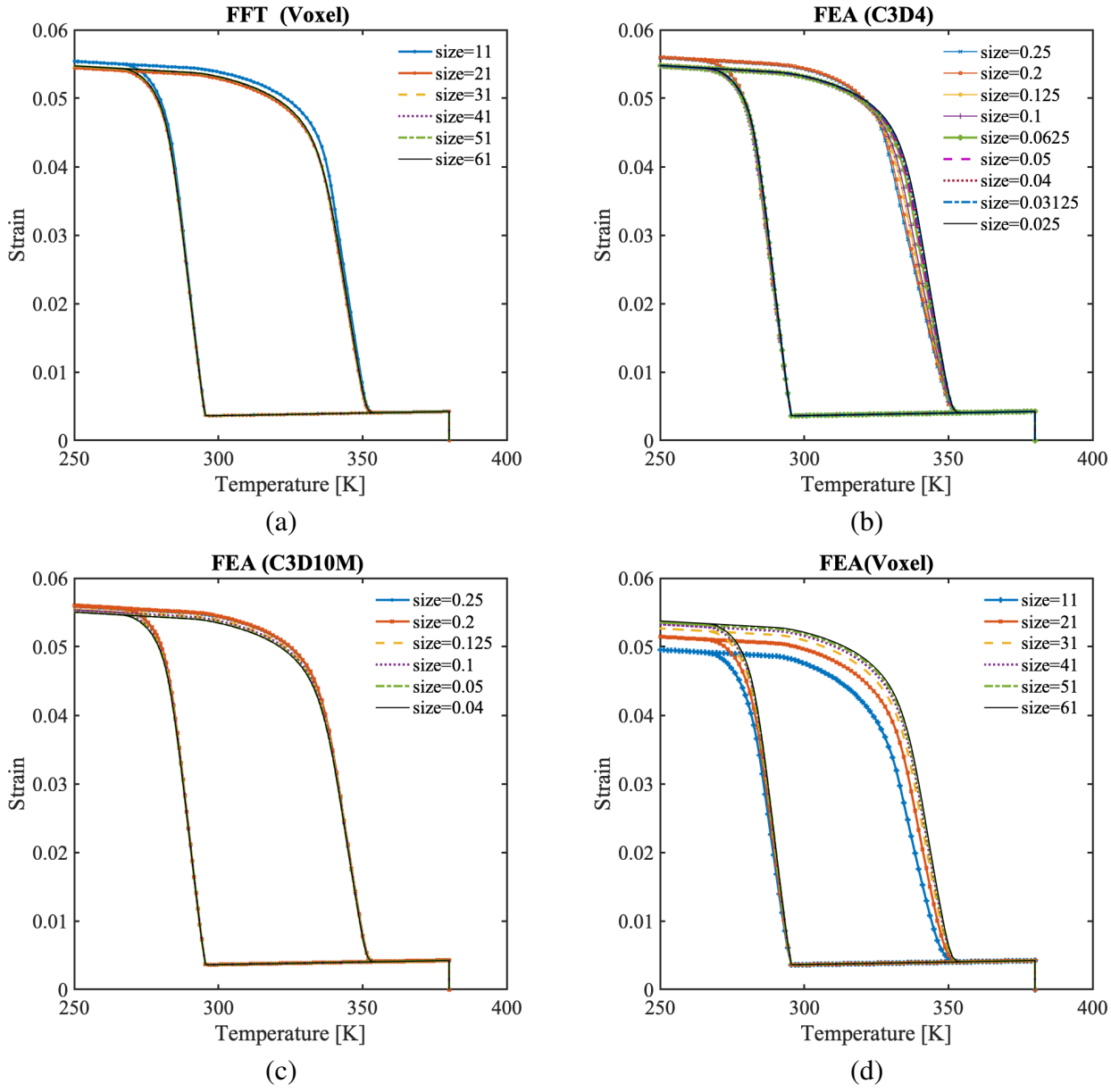

Figure 3.6: Figures indicate full response convergence to the finest mesh case with increasing mesh size. Responses in (a) FFT (voxel) (b) FEA (C3D4) (c) FEA (C3D10M) and (d) FEA (voxel) cases shown

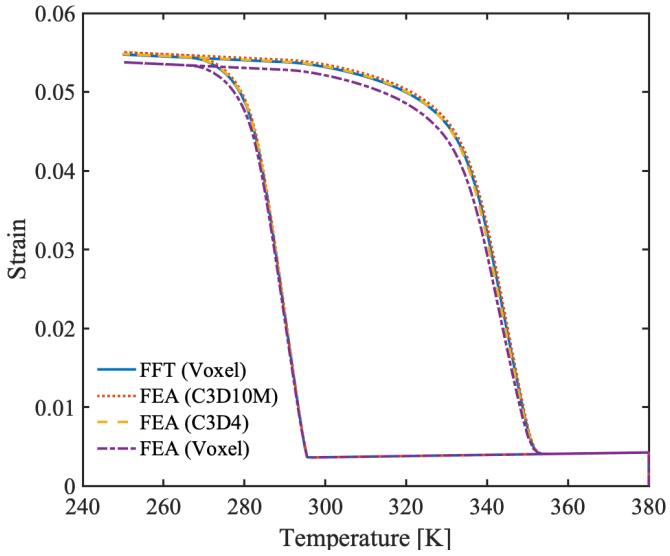

Figure 3.7: Comparison of responses from most converged cases in FFT and FEM homogenization techniques. FFT (N=61) and FEM using C3D10M (seed size = 0.04), C3D4 (seed size = 0.025) and Voxel (N=61) are compared.

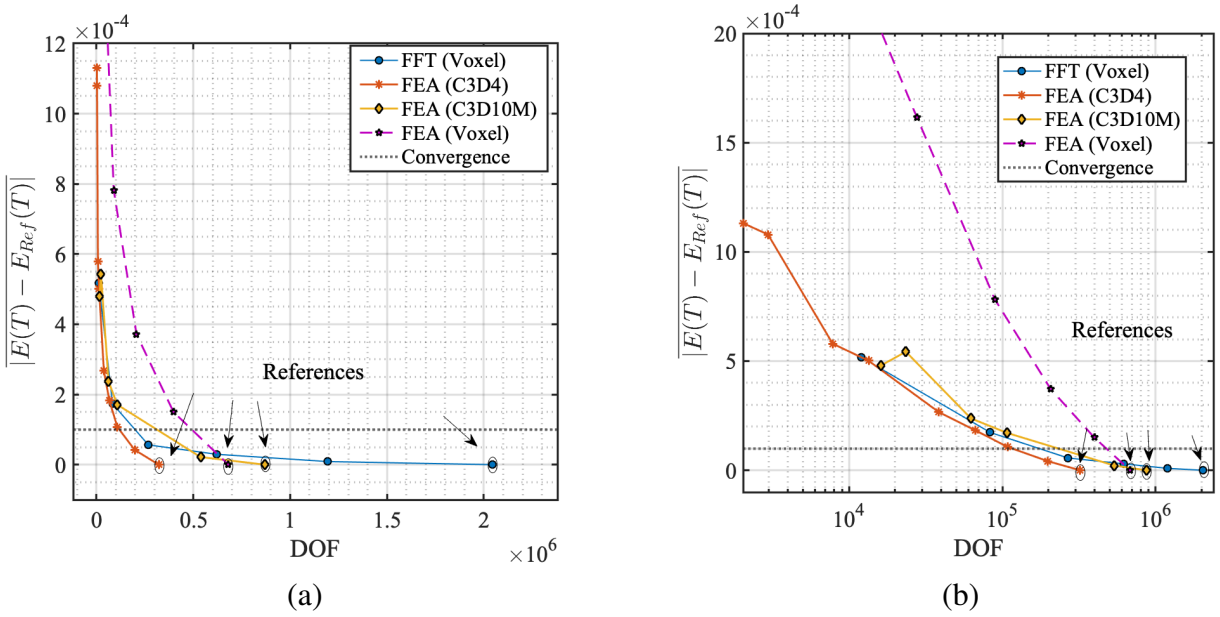

Figure 3.8: Evolution of convergence criterion in Eq. (3.5) with DOF in FFT and FEM homogenization for different types of meshes. The comparison shown in (a) linear scale and (b) log scale for x-axis.

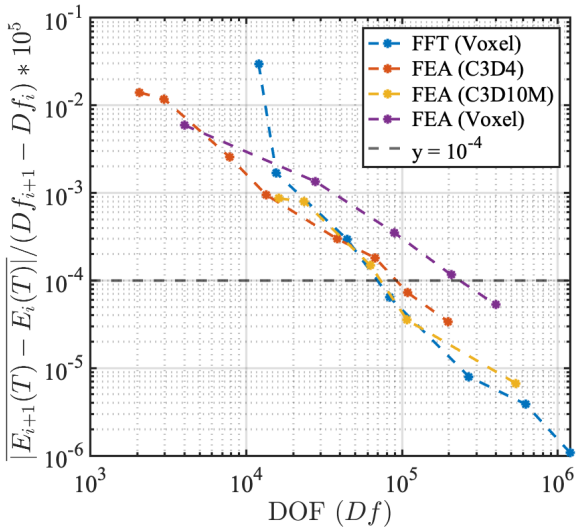

Figure 3.9: Evolution of convergence criterion in Eq. (3.6) with DOF in FFT and FEM homogenization for different types of meshes. The comparison is shown in log-log plot.

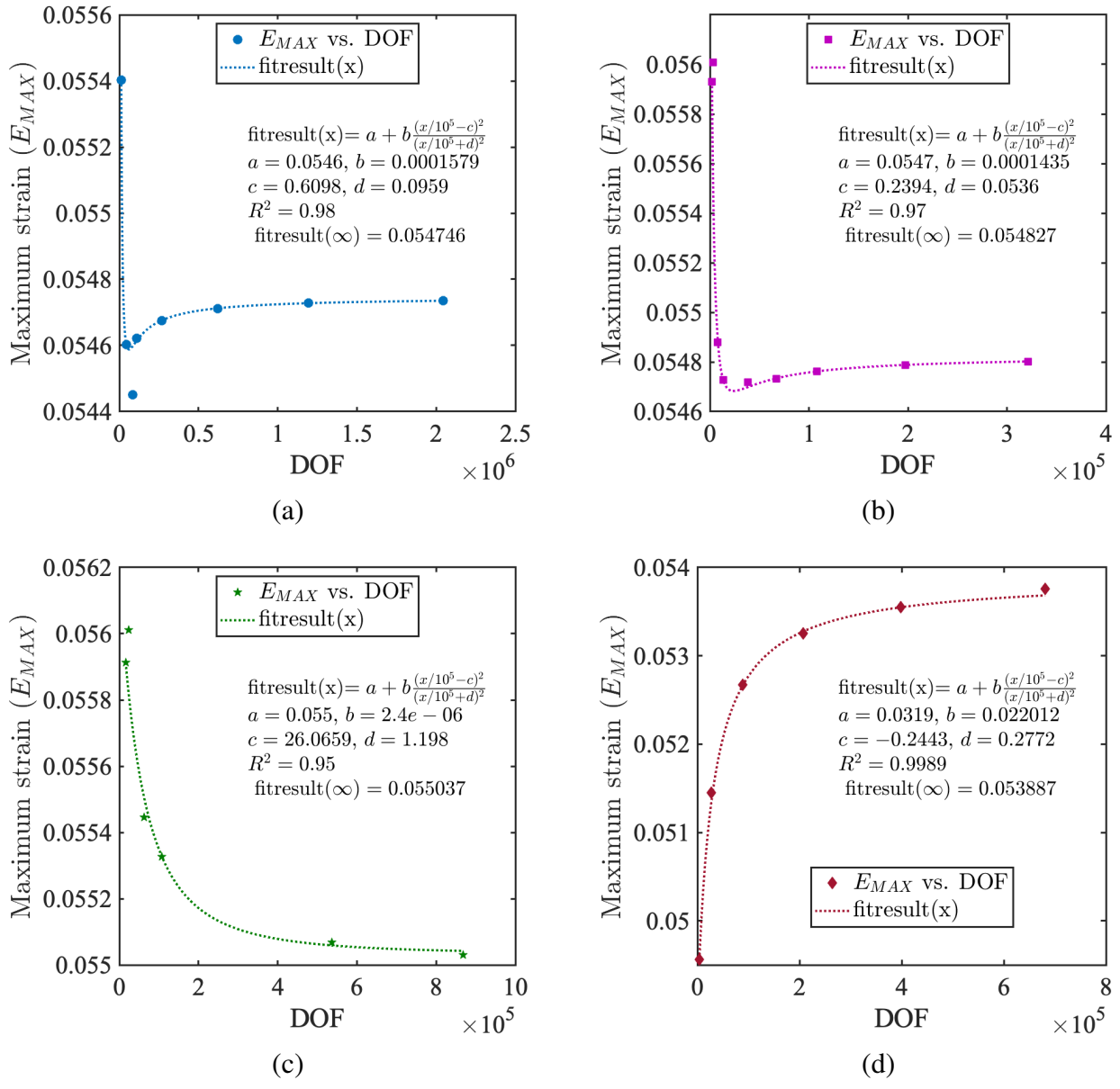

Figure 3.10: Comparison of convergence of maximum strain (E_{max}) in the responses against degree of freedom (DOF) solved in (a) FFT (Voxel) (b) FEA (C3D4) (c) FEA (C3D10M) and (d) FEA (Voxel). An equation is used to fit the convergence, and the value at ∞ is predicted using the equation. The details of the fit and goodness of fit are presented.

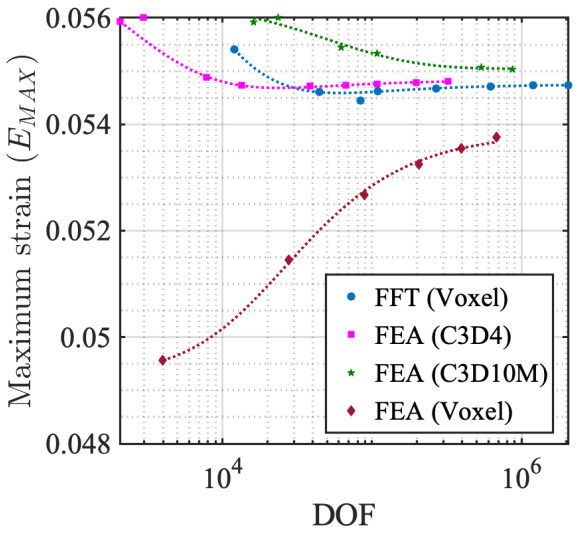

Figure 3.11: Comparison of convergence of maximum strain (E_{max}) versus DOF from all the cases is shown together. Values and fit are compared, and the x-axis is plotted in log-scale.

3.4.2 FFT grid convergence analysis [3]

An FFT grid convergence study was carried out to decide the discretization required for modeling the RVEs of different sizes. For this, we considered 5 different discretizations, N=11^3, 21^3, 31^3, 51^3 and 91^3 i.e. $N_x = N_y = N_z$. The study was performed for the highest volume fraction analyzed in this work, 20% and for 4 RVE sizes P=15, 30, 60 and 90.

Figure 3.12 (a) shows the variation of relative error versus grid size. The relative errors are calculated between two successive grid discretizations, and are defined for the maximum strain (E_{max}) in the response. In Figure 3.12 (a), the convergence of error in different RVE sizes (P = 15,30,60,90) is analyzed. Larger RVEs (P = 60, 90) converge more slowly compared to the smaller RVEs (P=15, 30). To have a preset accuracy in all RVEs solved, an accepted error limit of 1%[7, 122] is taken as reference, which is represented using the dashed line in Figure 3.12 (a).

The optimal value of grid size is calculated for each RVE size P from the Figure 3.12 (a) by interpolating for the error limit. The optimal grid points are normalized with respect to P and are plotted versus P in Figure 3.12 (b). As can be seen, the optimal number of grid points per particle decrease with increasing the size of RVE and are bounded in the plot shown. For the current study, to ensure all simulation within the error limit, the optimal number of grid points per particle is taken to be 3000. This will ensure the desired accuracy for all RVEs considered in the study.

[3] Adapted with permission from "Representative volume size in micromechanical modeling of precipitated SMAs." by Joy, J. K., Cruzado, A., Solomou, A., Benzerga, A. A., & Lagoudas, D. C., 2019, March, Smart Structures and NDE for Energy Systems and Industry 4.0 (Vol. 10973, pp. 76-85). SPIE.

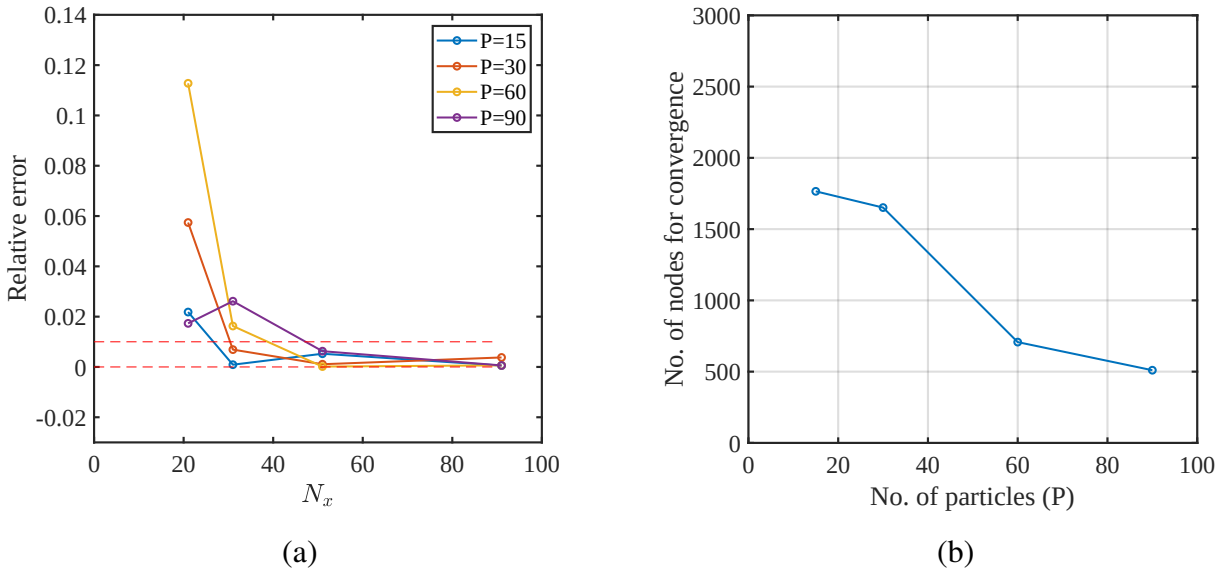

Figure 3.12: Convergence study done on voxel mesh using the FFT based solution technique at VF=20% for different numbers of particles. a) Plot showing the relative error in the maximum strain between two successive grid sizes is compared versus grid size, where, the total number of grid points is $N = N_x^3$. The acceptable tolerance of convergence is marked with the red dashed line. b) The number of nodes per particle for the optimal grid is plotted versus the number of particles.

3.4.3 RVE convergence study [4]

Let us first look at the effect of volume fraction on the convergence of RVEs. Figure 3.13 compares actuation responses from the SMA RVEs with two different volume fractions with varying number of particles (P =1, 15, 30, 60, 90). A low volume fraction (4.2%) case (Figure 3.13(a)) and a high volume fraction (20%) case in (Figure 3.13(b)) are shown. For 4.2% RVEs, there is small variation in the actuation response with increasing P. The response is accurately captured even with an RVE of 1 particle. In the case of high volume fraction (20%) RVEs, there is a considerable variation with changing P, and the response cannot be captured with an RVE of 1 particle.

The comparisons in Figure 3.13 indicate the effect of increasing mechanical interaction at

[4]Modified with permission from "Representative volume size in micromechanical modeling of precipitated SMAs." by Joy, J. K., Cruzado, A., Solomou, A., Benzerga, A. A., & Lagoudas, D. C., 2019, March, Smart Structures and NDE for Energy Systems and Industry 4.0 (Vol. 10973, pp. 76-85). SPIE.

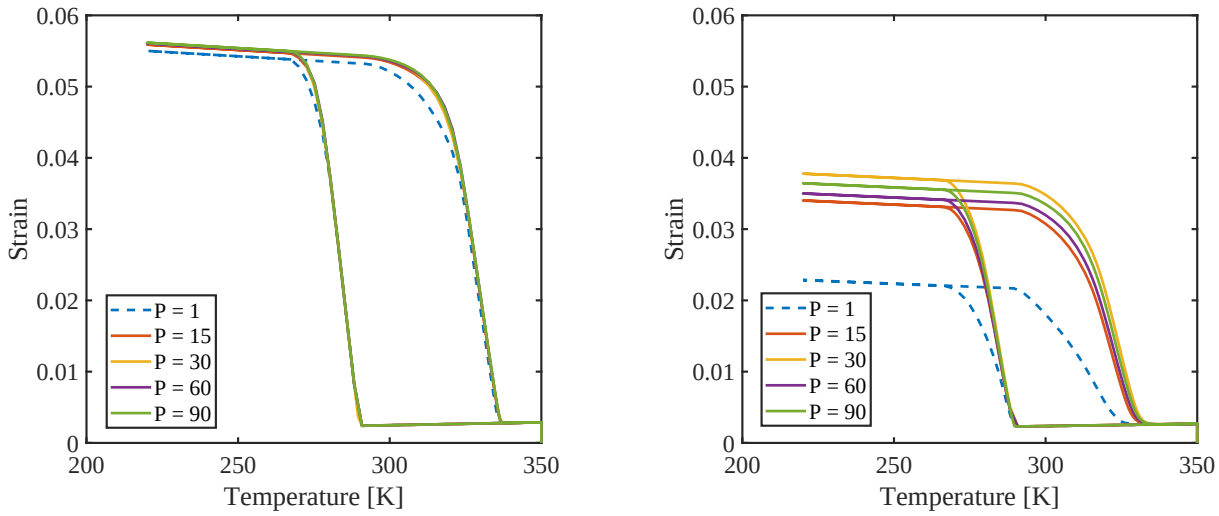

(a) Volume fraction = 4.2%

(b) Volume fraction = 20%

Figure 3.13: Effect of number of particles in the RVEs on the convergence of SMA actuation response. a) At low volume fraction, the number of particles has less effect on the response. b) At high volume fraction, more number of particles are required to capture accurately the material response

higher volume fraction. At lower volume fraction, the interaction between the particles is negligible, and the response can be captured well using smaller RVEs (even 1 P). However, at high volume fraction, the complex interactions between the particles is critical in determining the effective response. Hence, larger RVEs with higher number of particles are required for accurate prediction of responses. These comparisons provided motivation for a systematic study of the convergence of RVE sizes with different volume fractions and many realizations.

This systematic study on the RVE convergence was carried out with RVEs of varying number of precipitates (P = 3, 6, 9, 12, 15, 30, 60, 90). For each number of precipitates, 10 realizations were performed to simulate the dispersion in the responses. Figure 3.14 (a) shows the responses simulated from 10 RVE realizations for volume fraction (VF) 20% at P = 15. Maximum dispersion is seen with the completed phase transformation at lower temperatures ($T = 220$ K), where the strain is maximum, and the material is in the martensite. Hence, in further analyzes, the strain at the

end of cooling ($T = 220$ K) in the whole strain-temperature response is considered for quantifying the dispersion.

In Figure 3.14 (b), the maximum strain from many realizations is plotted versus number of particles modeled. Each point in the comparison represents the maximum strain value from a different RVE realization. The summary from many realizations show that the dispersion decreases with the increasing number of particles in the RVE. The ensemble average value of these values is calculated for each RVE size (P) and compared in the same plot (shown in red color). The average value has higher convergence compared to individual realizations, and more or less the same with increasing RVE size. Though the dispersion of calculated properties is higher for lower sized RVEs, their average value from many realizations gives higher convergence.

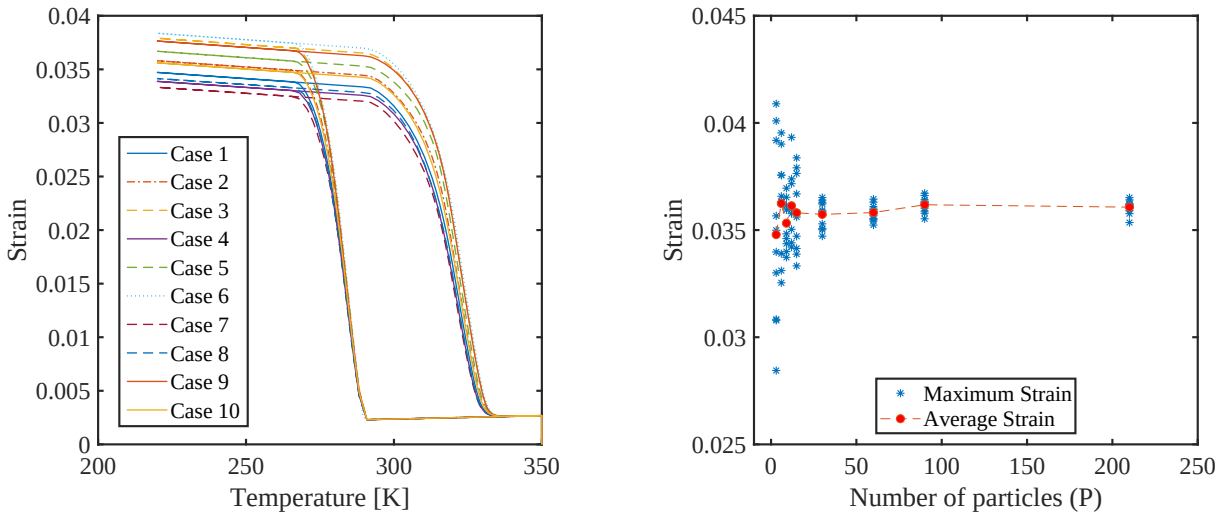

(a) (b)

Figure 3.14: The effective response simulated from the RVEs at VF=20%. a) Material response from 10 RVE realizations with number of particles (P)=15 are compared. b) Plot showing the maximum strain from many realizations at different P. The average value at each P is compared.

With lesser number of particles, the RVEs will not be representative of the microstructure and has higher scatter between realizations. Bigger RVE size increases the computational cost and may

not be preferred. Whereas, the average response from multiple realizations at different RVE size is closer to the converged response, as concluded from the results in Figure 3.14 (b). A good scenario for predictions will be to use an optimum RVE size and adequate number of realizations, making sure the required accuracy and minimum computation power. To use this scenario in optimal manner, prior knowledge on the variation of the dispersion at the different RVE size is required. In the next analysis, some statistical aspects of the RVE size convergence are looked into.

The statistics of dispersion of the response for different volume fractions (7%, 10%, 15% and 20%) and RVE size (P = 3, 6, 9, 12, 15, 30, 60, 90) were carried out. Coefficient of variation (CV) defined in equation 3.7 was used following the methodology in section 3.3.2. Figure 3.15 shows the variation of CV with RVE size (P) with changing volume fraction microstructures. As the volume fraction increases, higher CV represents higher dispersion between the realizations. This is anticipated since higher volume fraction of particles requires larger RVEs to capture all the mechanical interaction between the particles. With increasing size of the RVEs, the CV asymptotically converges to zero, as can be seen in Figure 3.15 (a). Figure 3.15 (b) shows that this decay is close to linear in the log-log plot and may be captured with a linear curve fit. The obtained fits from Figure 3.15 (b) are summarized in Table 3.5 with coefficients of the power function of the form: $\hat{D}_{E_{zz}}(\mathrm{P}) = a\,\mathrm{P}^b$.

Table 3.5: Details of fit capturing the variation of $\hat{D}_{E_{zz}}(\mathrm{P})$ for different volume fractions. Fit used: $\hat{D}_{E_{zz}}(\mathrm{P}) = a\,\mathrm{P}^b$.

VF (%)	a	b
7	0.057	-0.545
10	0.103	-0.653
15	0.139	-0.629
20	0.243	-0.726

The CV values which quantify the dispersion with RVEs can be used for statistical estimations. It can be used to estimate the uncertainty in the estimations and to calculate number of realizations

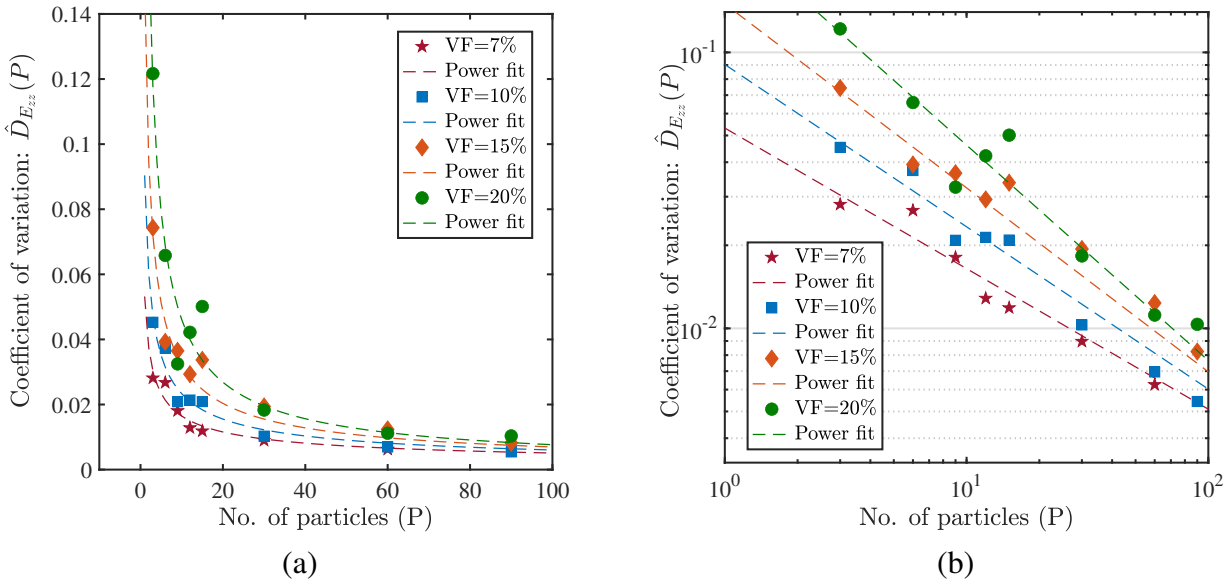

Figure 3.15: Coefficient of variation (CV) with number of particles compared for volume fractions 7%, 10%, 15% and 20%. a) As the number of particles in the RVE increases, the CV decreases exponentially. b) CV vs No. of particles plotted in log-log plot. The variation of CV is fitted with linear relations in the log-log plot.

for desired accuracy. From the sampling theory, the relative standard error (RSE) of the average responses can be defined in terms of the CV ($\hat{D}$) and the number of realizations (N_P) used as:

$$RSE = \frac{\hat{D}_{E_{zz}}(\mathrm{P})}{\sqrt{N_P}}, \tag{3.8}$$

The CV is useful to calculate the number of realizations required at each RVE size, as proposed in Kanit *et al.* [7]. The number of realizations (N_P) required for a given RSE is given as:

$$N_P = \left(\frac{\hat{D}_{E_{zz}}(\mathrm{P})}{RSE} \right)^2. \tag{3.9}$$

Estimation of number of realizations (N_P) in different RVEs for getting RSE values less than 0.01 were calculated using Eq. 3.9. The values of CV were estimated using the fits in Table 3.5. The estimated number of realizations (N_P) for RSE $<$0.01 for different volume fractions are sum-

marized in Table 3.6. It can be seen that the N_P increases with volume fraction and decreases with size of RVE P. As reasoned earlier, the higher volume fractions increase the mechanical interactions. Hence, require larger RVE size or higher number of realizations to get accuracy. Conversely, in the lower volume fraction microstructures, lower RVE size and number of realizations can give good estimations. In further statistics study, the number of realizations considered is listed in Table 3.5 as 'N_P considered'. Among the VFs, VF $= 20\%$ require the highest number of realizations. Hence, the 'N_P considered' were taken to be greater VF $= 20\%$ values.

Table 3.6: Number of realizations calculated for SE$= 0.01$ for different VF and P.

Size of RVE	**No of realizations required**				N_P considered
(P)	VF=7%	VF=10%	VF=15%	VF=20%	
3	10	26	49	120	120
6	5	11	21	44	50
9	3	7	13	25	30
12	3	5	9	17	20
15	2	4	7	12	20
30	1	2	3	5	10
60	1	1	2	2	10
90	1	1	1	1	10

3.5 Conclusions

A comparative study on the convergence of four methods FFT (voxel), FEA (C3D4), FEA (C3D10M) FEA (voxel) was performed for solving the homogenized from SMA micromechanical model. The analysis using average convergence criterion showed that the three methods FFT (voxel), FEA (C3D4) and FEA (C3D10M) have closer convergence and accuracy compared to the FEA (voxel) method. A convergence study for the maximum strain value showed that FFT (voxel) and FEA linear have close asymptotic solutions compared to FEA (C3D10M) and FEA (voxel). The rate of convergence and accuracy in the maximum strain value was deduced as FEA (C3D4)$>$ FFT (voxel) $>$ FEA (C3D10M) $>$ FEA (voxel). As the FFT (voxel) and FEA (C3D4) give same

performance, their CPU solving time were compared. The FFT (voxel) method solves at least four times faster than the FEA (C3D4) given both uses different solvers.

Determining the converged RVEs is critical in determining the effective properties of precipitated SMAs using micromechanical modeling. An inaccurate RVE can give considerable error in the predictions, as all the mechanical interactions may not be captured. The size of RVEs and number of realizations are important towards accurate prediction of material properties. A systematic study on the convergence of precipitated SMA RVEs is implemented. The effect of size of RVEs is carried out changing the number of precipitates and analyzing the variation in the effective response. Study at different volume fraction showed that larger RVEs are required to capture the response at higher volume fractions. The average response from many realizations at different RVE size showed less variation. The dispersion of the response for higher volume fractions are analyzed with many realizations. Results showed that the dispersion with RVE sizes can be correlated with simple relations and can be used with statistical interpretations for accurate predictions and efficient use of computational power.

4. MICROMECHANICAL AND STATISTICAL DETERMINATION OF THE RVE SIZE WITH LOCAL VARIATION OF VOLUME FRACTION AND SHAPE OF HETEROGENEITIES: APPLICATION TO SHAPE MEMORY ALLOYS

4.1 Introduction

Micromechanical homogenization is key to estimating the effective properties and behavior of heterogeneous materials. In the context of modeling complex microstructures with non-linear material behaviors, the use of full field based computational homogenization techniques is required. Traditionally, the Boundary Value Problem (BVP) for the homogenization was solved through Finite Element Methods (FEM) [45, 46, 47, 48, 49]. In the past two decades, however, more efficient spectral methods based on Fast Fourier Transform (FFT)[50, 51, 52, 53, 54, 55] have emerged. In both methodologies, it is critical to know the acceptable size of the modeling domain, as it must be large enough to account for the whole material with sufficient number of inclusions, independent of the boundary conditions [123]. In other words, it is necessary to define the size of the Representative Volume Element (RVE).

Common approaches for determining RVE size rely on convergence of the effective property in a set of RVE realizations with volume size [124, 125, 126, 46, 127, 6, 128, 129]. The RVE size is defined with a specific convergence criteria on the mean and standard deviation of the desired property in the set of RVE realizations. In [126, 46, 129], the RVE is defined once the mean and standard deviation have converged within a given tolerance. In [128], the ratio between the standard deviation and the mean quantity value is used to decide the convergence. In [124], the size of the RVE is defined such that the response will not deviate more than a certain percentage from the response of a 'true' infinite value considering the Student's t-distribution. In [130], the RVE size is defined based on the Chi-square criterion. In [46, 131], the RVE size is defined when the relative error between consecutive volume sizes is less than a specific defined error. In [132], the coefficient of variation is used for the converged criterion. All these methods require

identifying the RVE size each time the microstructure is different (i.e. shape, size, volume fraction of grain/precipitate/phase/particle).

A more advanced statistical approach was proposed by Kanit *et al.* [7] in which the RVE size was determined in terms of several statistical quantities (i.e. point variance and integral range). This formulation was first demonstrated for the elastic and thermal properties of composite materials [7, 133] and further extended to nonlinear behavior in polycrystalline materials [134]. The parameters necessary to accurately build the Kanit *et al.* [7] formulation are based on an initial sampling that requires many realizations and variability in the microstructure parameters for different RVE sizes. To reduce this initial sampling, it was proposed to include the uncertainty quantification of variance and mean in the integral range, and a sampling strategy to reduce the number of realizations [135]. An alternative method was proposed [136, 137] in which by using a single realization/simulation of a large RVE, and creating non overlapping subdivisions, statistical quantities can be determined.

It is well known that the volume fraction of heterogeneities (i.e.: precipitates, voids) [7, 130, 138, 137] and shape [124] influence the RVE size. One of the drawbacks in the statistical approach developed by Kanit *et al.* [7] is that it requires the use of new fitting parameters each time the volume fraction changes. As shown in [137], the integral range in the Kanit *et al.* [7] formulation has a non-linear dependency with respect to the volume fraction. To advance in this further, a formulation that accounts for the nonlinear dependency in the RVE statistics is desired. A higher order formulation for the RVE size is attempted in this work to account for the effects of geometrical parameters (shape, size, volume fraction and arrangement of the heterogeneities), and its performance is studied for precipitated Shape Memory Alloys (SMAs) responses.

With the help of the FFT based homogenization framework [116] presented in chapter 3, in this chapter the aim is to analyze the statistics of RVE size convergence. The performance of the new higher order relation will be analyzed for modeling the statistics for non-linear SMAs responses. The good performance shown by FFT homogenization for predicting non-linear SMA behavior [116] allows for analyzing bigger RVE sizes (i.e. more number of particles) in a wider range of

volume fractions. Although in the current work, the dispersion and the RVE size is analyzed in the context of NiTi SMAs, the work is applicable for other material systems, including SMAs like Ni-Ti-Hf because of similar modeling methodology[59].

The chapter is organized as follows. Section 4.2 presents a brief description of the FFT based micromechanical homogenization model for precipitated SMAs. In section 4.3 the derivation of the statistical-micromechanical model for RVE size determination is shown. Finally, section 4.3 addresses the precision of the proposed model compared with existing statistical models, as well as the validation of the RVE size for a specific accuracy in the studied quantity.

4.2 Micromechanical model for precipitation hardened SMAs

Micromechanical model for actuation behavior of precipitation hardened NiTi SMAs is considered in the presented statistical study. For better understanding of actuation behavior studied in this chapter, refer to section 1.1.1. The presence of precipitates modifies the actuation behavior of SMAs considerably. The details of the precipitation mechanism that affects the SMA behavior and the micromechanical model for SMAs can be referred in section 3.2. A brief summary of the micromechanical model considered for generation of results in this chapter is presented in the following discussion.

Out of the many mechanisms through which the precipitates influence effective behavior, only the mechanical effects of precipitates are considered in the current work. The effects of composition change from diffusion were not included. The material properties used for the micromechanical modeling of precipitated SMA behavior are listed in Table 4.1. Two sets of SMA matrix properties were considered: SMA-1 and SMA-2, which were calibrated from $Ni_{50.8}$Ti SMA and $Ni_{51.3}$Ti SMA experimental responses [6] respectively. The phase transformation constitutive model proposed by Lagoudas *et al.* [38] is used for this purpose. The elastic properties [6] used for modeling the behavior of precipitates are also shown.

Table 4.1: Material properties used for matrix and precipitate.

SMA Matrix			**Precipitate**	
Parameter	SMA-1	SMA-2	Parameter	Value
E_A	68 GPa	68 GPa	E	107 GPa
E_M	43 GPa	43 GPa	v	0.3
$v^A = v^M$	0.33	0.33		
H^{max}	0.055	0.044		
$k[MPa^{-1}]$	0.0206	0.01		
C_A	6.4 MPa/K	5 MPa/K		
C_M	21.7 MPa/K	5 MPa/K		
$n_1 = n... = n_4$	1	1		
(Ms, Mf, As, Af) [K]	(280, 266, 290, 307)	(211, 181, 226, 242)		

4.2.1 FFT based homogenization

The FFT based homogenization framework presented in chapter 3 is used to obtain the thermo-mechanical behavior of precipitated SMAs. To this end, periodic RVEs containing dispersed Ni_4Ti_3 precipitates in a shape memory alloy matrix are considered. The RVEs are created with randomly arranged ellipsoidal shaped precipitates, and geometric periodicity is ensured at the faces. The domain is discretized using a regular grid in $\mathbb{R}^3$ with N_x=N_y=N_z denoting the number of grid points along each principal direction. The constitutive response of the SMA matrix is captured with the thermodynamically consistent formulation developed by Lagoudas *et al.*[38], and the precipitates are modeled with linear elastic and isotropic behavior.

The effective isobaric thermal response described in section 4.2 is considered in this work. Under this condition, the material was first uniaxially loaded according to: $\boldsymbol{\Sigma} = \Sigma_{zz}(\boldsymbol{e}_z \otimes \boldsymbol{e}_z)$ with an overall axial stress of $\Sigma_{zz} = 300\,\text{MPa}$ at a constant nominal temperature of $T = 350\,\text{K}$, and then was cooled to $T = 220\,\text{K}$, and heated back to $T = 350\,\text{K}$. The SMA RVE is in the austenite state initially and transforms to martensite with cooling to 220 K.

4.3 Statistical and micromechanical description of RVE size

4.3.1 Dispersion of the effective property and representative volume

There have been numerous attempts in the literature to quantify the statistics for the effective property computed from the representative volume. In these works, the correlation between the variation of the effective property from different representative volume and the local variation of the property within the volume is of interest. One of such early attempt is by Lantuéjoul in geostatics, concerning the ergodic stationary random function $Z(x)$, where the variance of the average $\overline{Z}$ over volume V represented by $D^2_{\overline{Z}}(V)$ is correlated to the local variance or the point variance D^2_Z in the following relation [139],

$$D^2_{\overline{Z}}(V) = D^2_Z \frac{A_3}{V}, \tag{4.1}$$

where the constant A_3 is defined as the integral range [139, 7] of the random function $Z(x)$. Lantuéjoul [139] further proposed that in cases where the integral range is infinite, the V in the Eq. (4.1) may be replaced by V^α (with $\alpha \neq 1$) to capture a slower decrease of the variance $D^2_{\overline{Z}}(V)$ with the size of subdomains (V). In these works of Lantuéjoul, the homogenized properties of interest $\overline{Z}(V)$ were calculated directly from the subdomains as the average of the local value $Z(x)$, while in the micromechanical homogenization problems, finding the effective response involves solving governing differential equations, nonlinear constitutive responses and assumption of periodicity. Because of this, the random fields of interest (e.g. strain field, elastic moduli) may not follow the Lantuéjoul [139] formulation and assumptions like ergodicity. Further correlation studies in mechanics have tried to circumvent this issue with different modifications on the Lantuéjoul [139] formulation.

In the work by Kanit *et al.* [7], which is one of the recognized works in the quantification of RVE size in mechanics, a modified relation with power law is proposed. The argument behind modifying the equations of Lantuéjoul was that the elastic moduli are in general not additive compared to the cases in Lantuéjoul's work, where the property of interest was simply the average

inside the volume. The relation proposed by Kanit *et al.* [7] is the following:

$$D^2_{\overline{Z}}(V) = D^2_Z \left(\frac{A_3}{V} \right)^{\alpha}, \tag{4.2}$$

where α is the exponential, which could be determined from the study of variance. One significant drawback in the Kanit *et al.* [7] relation is that both α and A_3 change significantly for different volume fractions, and thus the model cannot be generalized. The following section aims to develop a statistical correlation for the effective strain response independent of the volume fraction and geometry of the heterogeneity.

4.3.2 Statistics of effective strain through perturbations

The variation of the effective response comes primarily from the microstructural variation between RVE realizations. In the micromechanical model of NiTi SMAs studied in this work, the RVEs are composed of ellipsoidal precipitates placed at random positions and in random orientations inside a cube volume. As the microstructural changes between the RVE realizations follow a specific description, the variation of the effective response can also be described accordingly. Because of the microstructural variations inside the RVEs, the variation of effective behavior in the RVEs can be described in the following assumptions:

1. As the precipitates are chosen with random orientation without any preferred orientation, the ensemble average behavior from infinite RVE realization must be isotropic.

2. The behavior in a particular RVE may be described as a perturbed behavior from the isotropic average behavior.

Two different type of perturbations were considered: 1) isotropic perturbation and 2) anisotropic perturbation. The isotropic perturbation is such that the magnitude of the ensemble average behavior is perturbed. Further, the anisotropic perturbation with direction preference results in the overall anisotropic behavior in the RVE. Since the preferred orientation in a particular RVE can be in any direction, a rotation is added to the perturbations. Appendix D explains the thought process

involved in the perturbation based description for RVE realizations.

4.3.2.1 Definition of the effective strain in a particular RVE through perturbations

The effective strain from an RVE at a particular loading state in a nonlinear response may be described using a compliance matrix as the following:

$$\boldsymbol{E}_{\mathrm{RVE}} = \mathbb{S}_{\mathrm{RVE}} : \boldsymbol{\Sigma}, \tag{4.3}$$

where $\boldsymbol{E}_{\mathrm{RVE}}$ is the effective strain state in the RVE and $\mathbb{S}_{\mathrm{RVE}}$ is the compliance matrix to describe $\boldsymbol{E}$ in terms of the applied stress state $\boldsymbol{\Sigma}$. The compliance $\mathbb{S}_{\mathrm{RVE}}$ is described in terms of the average compliance $\mathbb{S}_{\mathrm{Avg}}$, perturbations ($\delta$, $\mathbb{Z}$) and rotation ($\mathbf{R}$) as in the following:

$$\mathbb{S}_{\mathrm{RVE}} = \mathbf{R} \cdot \mathbf{R} \cdot (1+\delta)\left(\mathbb{S}_{\mathrm{Avg}} + \mathbb{S}_{\mathrm{Avg}} \odot \mathbb{Z}\right) \cdot \mathbf{R}^T \cdot \mathbf{R}^T, \tag{4.4}$$

where δ is the isotropic perturbation, $\mathbb{Z}$ is the anisotropic perturbation and $\mathbf{R}$ is the rotation corresponding to the RVE. The δ is a scalar and $\mathbb{Z}$ is a tensor of the same dimension as $\mathbb{S}_{\mathrm{Avg}}$. The operation '$\odot$' represents the element-wise multiplication or Hadamard product of two matrices. The perturbation δ has a mean of 0 and standard deviation D_δ, and $\mathbb{Z}$ has a mean of 0 and standard deviation $\mathbb{D}_{\mathbb{Z}}$. By introducing Eq. (4.4) in Eq. (4.3) and deriving the variance, the variation of the effective strain ($\mathbf{D}_E$) can be written in terms of D_δ and $\mathbb{D}_{\mathbb{Z}}$.

From Eq. (4.3) and Eq. (4.4), the effective strain in the RVE is written as the following.

$$\begin{aligned}
\boldsymbol{E}_{\mathrm{RVE}} &= \mathbf{R} \cdot \mathbf{R} \cdot (1+\delta)(\mathbb{S}_{\mathrm{Avg}} + \mathbb{S}_{\mathrm{Avg}} \odot \mathbb{Z}) \cdot \mathbf{R}^T \cdot \mathbf{R}^T : \boldsymbol{\Sigma} \\
&= (1+\delta)\left(\mathbf{R} \cdot \mathbf{R} \cdot \mathbb{S}_{\mathrm{Avg}} \cdot \mathbf{R}^T \cdot \mathbf{R}^T + \mathbf{R} \cdot \mathbf{R} \cdot (\mathbb{S}_{\mathrm{Avg}} \odot \mathbb{Z}) \cdot \mathbf{R}^T \cdot \mathbf{R}^T\right) : \boldsymbol{\Sigma} \\
&= (1+\delta)\left(\mathbb{S}_{\mathrm{Avg}} + \mathbf{R} \cdot \mathbf{R} \cdot (\mathbb{S}_{\mathrm{Avg}} \odot \mathbb{Z}) \cdot \mathbf{R}^T \cdot \mathbf{R}^T\right) : \boldsymbol{\Sigma}
\end{aligned} \tag{4.5}$$

Once the effective strain in a particular RVE is described, the variation can be derived by averaging over all the possible RVEs. The ensemble average of strain over all possibilities ($\overline{\boldsymbol{E}}_{\mathrm{RVE}}$) is obtained

as the average over all the perturbations and rotations through the following steps:

$$
\begin{aligned}
\overline{\boldsymbol{E}}_{\mathrm{RVE}} &= \left\langle (1+\delta)\left(\mathbb{S}_{\mathrm{Avg}} + \mathbf{R}\cdot\mathbf{R}\cdot(\mathbb{S}_{\mathrm{Avg}}\odot\mathbb{Z})\cdot\mathbf{R}^T\cdot\mathbf{R}^T\right) : \boldsymbol{\Sigma}\right\rangle_{\delta\mathbb{Z}R} \\
&= (1+\overline{\delta})\left(\mathbb{S}_{\mathrm{Avg}} + \left\langle \mathbf{R}\cdot\mathbf{R}\cdot(\mathbb{S}_{\mathrm{Avg}}\odot\overline{\mathbb{Z}})\cdot\mathbf{R}^T\cdot\mathbf{R}^T\right\rangle_R\right) : \boldsymbol{\Sigma} \\
&= (1+0)\left(\mathbb{S}_{\mathrm{Avg}} + \left\langle \mathbf{R}\cdot\mathbf{R}\cdot(\mathbb{S}_{\mathrm{Avg}}\odot 0)\cdot\mathbf{R}^T\cdot\mathbf{R}^T\right\rangle_R\right) : \boldsymbol{\Sigma} \\
&= (\mathbb{S}_{\mathrm{Avg}} + 0) : \boldsymbol{\Sigma} \\
&= \mathbb{S}_{\mathrm{Avg}} : \boldsymbol{\Sigma}
\end{aligned}
\tag{4.6}
$$

where, the operation $\langle - \rangle_{\delta\mathbb{Z}R}$ is used to represent the ensemble average over perturbations (δ and $\mathbb{Z}$) and rotation (R). The symbols in the subscript represent the domains in which the average is taken. Now, the variance of strain is solved from the description as the following:

$$
\begin{aligned}
\mathbf{D}_E^{\odot 2}(V) &= \left\langle (\boldsymbol{E}_{\mathrm{RVE}} - \overline{\boldsymbol{E}}_{\mathrm{RVE}})^{\odot 2}\right\rangle_{\delta\mathbb{Z}R} \\
&= \left\langle \left(\delta\mathbb{S}_{\mathrm{Avg}} : \boldsymbol{\Sigma} + (1+\delta)\mathbf{R}\cdot\mathbf{R}\cdot(\mathbb{S}_{\mathrm{Avg}}\odot\mathbb{Z})\cdot\mathbf{R}^T\cdot\mathbf{R}^T : \boldsymbol{\Sigma}\right)^{\odot 2}\right\rangle_{\delta\mathbb{Z}R}
\end{aligned}
\tag{4.7}
$$

Eq. (4.7) is written in the index notation and expanded in Eq.4.8 and Eq.4.9. Here the indices (a, b, c, d, i, j, k, l, m, n, o, p, r, s, u, v, x, y, A, B, C, D, E, F, G, H, M, N, O, P) take the values $(1, 2, 3)$ representing 3 Cartesian coordinates. The repeated index follows the Einstein summation convention. We define variables δ^a_{bc} and variable $\delta^{(mnop)}_{(abcd),(efgh)}$ to be used in the summation

$$
\delta^a_{bc} = \begin{cases} 1 & \text{if } (a=b=c) \\ 0 & \text{Otherwise} \end{cases}, \delta^{mnop}_{abcd,efgh} = \begin{cases} 1 & \text{if } [m,n,o,p]=[a,b,c,d]=[e,f,g,h] \\ 0 & \text{Otherwise} \end{cases}.
$$

$$
\begin{aligned}
D^2_{E_{ij}}(V) &= \left\langle \left(\delta(S_{Avg})_{ijkl}\sigma_{kl} + (1+\delta)R_{im}R_{jn}R_{ko}R_{lp}\delta^{mnop}_{MNOP,efgh}(S_{Avg})_{MNOP}Z_{efgh}\sigma_{kl}\right)^2 \right\rangle_{\delta ZR} \\
&= \delta^i_{ux}\delta^j_{vy}\left\langle \left(\delta(S_{Avg})_{uvkl}\sigma_{kl} + (1+\delta)R_{um}R_{vn}R_{ko}R_{lp}\delta^{mnop}_{MNOP,efgh}(S_{Avg})_{MNOP}Z_{efgh}\sigma_{kl}\right) * \right. \\
&\qquad \left. \left(\delta(S_{Avg})_{xyrs}\sigma_{rs} + (1+\delta)R_{xa}R_{yb}R_{rc}R_{sd}\delta^{abcd}_{ABCD,EFGH}(S_{Avg})_{ABCD}Z_{EFGH}\sigma_{rs}\right) \right\rangle_{\delta ZR}
\end{aligned}
\tag{4.8}
$$

Expanding Eq. (4.8) further gives

$$
\begin{aligned}
D^2_{E_{ij}}(V) = \delta^i_{ux}\delta^j_{vy}\Big\langle & \delta^2(S_{Avg})_{uvkl}\sigma_{kl}(S_{Avg})_{xyrs}\sigma_{rs} + \\
& \left(1+2\delta+\delta^2\right)R_{um}R_{vn}R_{ko}R_{lp}R_{xa}R_{yb}R_{rc}R_{sd}\delta^{mnop}_{MNOP,efgh}\delta^{abcd}_{ABCD,EFGH}(S_{Avg})_{MNOP}(S_{Avg})_{ABCD}Z_{efgh}Z_{E} \\
& (\delta+\delta^2)R_{ua}R_{vb}R_{rc}R_{sd}\delta^{abcd}_{ABCD,EFGH}(S_{Avg})_{ABCD}Z_{EFGH}\sigma_{rs}(S_{Avg})_{uvkl}\sigma_{kl} + \\
& (\delta+\delta^2)R_{xm}R_{yn}R_{ko}R_{lp}\delta^{mnop}_{MNOP,efgh}(S_{Avg})_{MNOP}Z_{efgh}\sigma_{kl}(S_{Avg})_{xyrs}\sigma_{rs}\Big\rangle_{\delta ZR} \\
& \equiv A2 + (B0+B1+B2) + (C1+C2) + (D1+D2).
\end{aligned}
\tag{4.9}
$$

The following relations hold as the average of the perturbations δ and Z_{mnop} are zero and have standard deviation (D):

$$
\langle\delta\rangle_{\delta Z} = 0, \qquad \langle\delta Z_{mnop}\rangle_{\delta Z} = 0, \qquad \langle\delta Z_{mnop}Z_{abcd}\rangle_{\delta Z} = 0, \tag{4.10}
$$

$$
\langle Z_{mnop}\rangle_{\delta Z} = 0, \qquad \langle\delta^2 Z_{mnop}\rangle_{\delta Z} = 0, \qquad \langle\delta^2\rangle_{\delta Z} = D^2_\delta \tag{4.11}
$$

$$
\langle Z_{mnop}Z_{abcd}\rangle_{\delta Z} = \begin{cases} D^2_{Z_{mnop}} & \text{if } [m,n,o,p] = [a,b,c,d] \\ 0 & \text{Otherwise} \end{cases} \quad \text{and} \tag{4.12}
$$

$$\langle \delta^2 Z_{mnop} Z_{abcd} \rangle_{\delta Z} = \begin{cases} D_\delta^2 D_{Z_{mnop}}^2 & \text{if } [m,n,o,p] = [a,b,c,d] \\ 0 & \text{Otherwise} \end{cases}. \tag{4.13}$$

Eq. (4.9) is simplified using the above relations. As a result, only the terms $A2$, $B0$, $B2$ are non-zero. In addition, the extra indices $a, b, c, d, u, v, x, y, A, B, C, D, E, F, G, H$ are removed using the definition of δ^a_{bc}, $\delta^{mnop}_{abcd,efgh}$, and the constraints from Eq. (4.12) and Eq. (4.13). The following equation follows the Einstein summation convention:

$$\begin{aligned} D^2_{E_{ij}}(V) =& D^2_\delta \left((S_{Avg})_{ijkl}\sigma_{kl}\right)^2 + \left\langle R^2_{im} R^2_{jn} R_{ko} R_{lp} R_{ro} R_{sp} \delta^{mnop}_{MNOP,efgh} (S_{Avg})^2_{MNOP} D^2_{Z_{efgh}} \sigma_{kl}\sigma_{rs} \right\rangle_R \\ &+ D^2_\delta \left\langle R^2_{im} R^2_{jn} R_{ko} R_{lp} R_{ro} R_{sp} \delta^{mnop}_{MNOP,efgh} (S_{Avg})^2_{MNOP} D^2_{Z_{efgh}} \sigma_{kl}\sigma_{rs} \right\rangle_R, \end{aligned} \tag{4.14}$$

Representing, $\left\langle R^2_{im} R^2_{jn} R_{ko} R_{lp} R_{ro} R_{sp} \delta^{mnop}_{MNOP,efgh} (S_{Avg})^2_{MNOP} D^2_{Z_{efgh}} \sigma_{kl}\sigma_{rs} \right\rangle_R$ as: $H_{ijmnop} D^2_{Z_{mnop}}$, Eq. (4.14) is in the following form.

$$D^2_{E_{ij}}(V) = D^2_\delta \left((S_{Avg})_{ijkl}\sigma_{kl}\right)^2 + D^2_{Z_{mnop}} H_{ijmnop} + D^2_\delta D^2_{Z_{mnop}} H_{ijmnop}. \tag{4.15}$$

Normalizing with mean value $\overline{E}^2_{ij} = \left((S_{Avg})_{ijkl}\sigma_{kl}\right)^2$, Eq. (4.15) is written in terms of coefficient of variation ($\hat{D}$):

$$\begin{aligned} \hat{D}^2_{E_{ij}}(V) = \frac{D^2_{E_{ij}}(V)}{\overline{E}^2_{ij}} &= \frac{D^2_\delta \left((S_{Avg})_{ijkl}\sigma_{kl}\right)^2}{\overline{E}^2_{ij}} + \frac{D^2_{Z_{mnop}} H_{ijmnop}}{\overline{E}^2_{ij}} + \frac{D^2_\delta D^2_{Z_{mnop}} H_{ijmnop}}{\overline{E}^2_{ij}} \\ &= D^2_\delta + D^2_{Z_{mnop}} \left(\frac{H_{ijmnop}}{\overline{E}^2_{ij}}\right) + D^2_\delta D^2_{Z_{mnop}} \left(\frac{H_{ijmnop}}{\overline{E}^2_{ij}}\right) \\ &= D^2_\delta + D^2_{Z_{mnop}} A_{ijmnop} + D^2_\delta D^2_{Z_{mnop}} A_{ijmnop}, \end{aligned} \tag{4.16}$$

where, $A_{ijmnop} = \left(\frac{H_{ijmnop}}{\overline{E}^2_{ij}}\right)$.

Let us assume both the isotropic and anisotropic perturbations are directly proportional to the

variation of the local strain. Assuming the following relations hold true for fixed strain component ε_{ij} (i.e. fixed i and j):

$$\begin{aligned} D_{\delta}^{2} &= a_{ij}^{2}(V)\hat{D}_{\varepsilon_{ij}}^{2} \\ D_{Z_{mnop}}^{2} &= b_{ijmnop}^{2}(V)\hat{D}_{\varepsilon_{ij}}^{2}, \end{aligned} \tag{4.17}$$

where the variation of the local strain inside the RVE is denoted by the term $\hat{D}_{\varepsilon_{ij}}^{2}$. Now, the variation of effective strain from Eq. (4.16) can be simplified as the following:

$$\begin{aligned} \hat{D}_{E_{ij}}^{2}(V) &= a_{ij}^{2}(V)\hat{D}_{\varepsilon_{ij}}^{2} + b_{ijmnop}^{2}(V)A_{ijmnop}\hat{D}_{\varepsilon_{ij}}^{2} + a_{ij}^{2}(V)b_{ijmnop}^{2}(V)A_{ijmnop}\hat{D}_{\varepsilon_{ij}}^{4} \\ &= \left(a_{ij}^{2}(V) + b_{ijmnop}^{2}(V)A_{ijmnop}\right)\hat{D}_{\varepsilon_{ij}}^{2} + a_{ij}^{2}(V)b_{ijmnop}^{2}(V)A_{ijmnop}\hat{D}_{\varepsilon_{ij}}^{4} \\ &= M_{ij}(V)\hat{D}_{\varepsilon_{ij}}^{2} + N_{ij}(V)\hat{D}_{\varepsilon_{ij}}^{4}, \end{aligned} \tag{4.18}$$

where $M_{ij}(V)$ and $N_{ij}(V)$ are constants that are functions of the RVE volume V. Eq. (4.18) presents a simple relation for the variation of the average strain at a fixed V in terms of the local dispersion of the strain within the RVE.

Following the derivation, the coefficient of variation (CV notated as $\hat{D}$) of the effective strain component E_{ij} is related to the CV of strain inside the RVE ε_{ij} through Eq. (4.19). Note that Eq. (4.19) is defined for fixed i and j and no summation shall be assumed for the repeated indices.

$$\hat{D}_{E_{ij}}^{2}(V) = M_{ij}(V)\hat{D}_{\varepsilon_{ij}}^{2} + N_{ij}(V)\hat{D}_{\varepsilon_{ij}}^{4} \tag{4.19}$$

Where $\hat{D}_{E_{ij}}(V)$ is the CV of the ensemble with volume V defined as $\hat{D}_{E_{ij}}(V) = D_{E_{ij}}(V)/\overline{E}_{ij}$ with $\overline{E}_{ij}$ as the ensemble average. $\hat{D}_{\varepsilon_{ij}}$ is the point-CV of ε_{ij} within the volume defined as $\hat{D}_{\varepsilon_{ij}} = D_{\varepsilon_{ij}}/\overline{\varepsilon}_{ij}$. $M_{ij}(V)$ and $N_{ij}(V)$ are constants that change with the volume of the RVE V. The effect of changes in the volume fraction of the microstructure are captured with the changes in the $\hat{D}_{\varepsilon_{ij}}$. As the terms in Eq. (4.19) are a function of V, it needs to be simplified further.

To generalize the relation in Eq. (4.19) for any volume, we assume the correlation of Lantuéjoul

(Eq. (4.1)) holds true for a fixed microstructure (i.e. fixed $\hat{D}_{\varepsilon_{ij}}$) across changing volume.

$$\hat{D}^2_{E_{ij}}(V) = \hat{D}^2_{\varepsilon_{ij}} \frac{A_3}{V}. \tag{4.20}$$

Replacing Eq. (4.20) for a fixed V_0, writing down the ratio $\hat{D}^2_{E_{ij}}(V)/\hat{D}^2_{E_{ij}}(V_0)$ and rearranging, the following expression is obtained:

$$\hat{D}^2_{E_{ij}}(V) = \hat{D}^2_{E_{ij}}(V_0) \frac{V_0}{V}. \tag{4.21}$$

Now replacing $\hat{D}^2_{E_{ij}}(V_0)$ by Eq. (4.19) leads to:

$$\hat{D}^2_{E_{ij}}(V) = \left(M_{ij}(V_0)\hat{D}^2_{\varepsilon_{ij}} + N_{ij}(V_0)\hat{D}^4_{\varepsilon_{ij}} \right) \frac{V_0}{V}. \tag{4.22}$$

In this work, we assume that the number of precipitates (P) are a good representation of the volume V of the microstructure, and thus Eq. (4.22) leads to,

$$\hat{D}^2_{E_{ij}}(P) = \frac{A_{ij}}{P}\hat{D}^2_{\varepsilon_{ij}} + \frac{B_{ij}}{P}\hat{D}^4_{\varepsilon_{ij}}, \tag{4.23}$$

where $A_{ij} = V_0 M_{ij}(V_0)$ and $B_{ij} = V_0 N_{ij}(V_0)$. The new relation Eq. (4.23) has 2$^{\text{nd}}$ order terms in $\hat{D}^2_{\varepsilon_{ij}}$ compared to the Lantuéjoul [139] and Kanit *et al.* [7] relations in Eq. (4.1) and Eq. (4.2), where only the 1$^{\text{st}}$ order effects in $\hat{D}^2_{\varepsilon_{ij}}$ are included. Note that from Eq. (4.23) it is possible to recover Lantuéjoul (Eq. (4.1)) by dropping the 2$^{\text{nd}}$ order term. The new relation in Eq. (4.23) is expected to capture better the variation due to changes in the microstructure, since the higher order effects are included.

If instead of using Lantuéjoul approximation, the Kanit *et al.* [7] approximation in Eq. (4.2) is used, the modified relation will be given by Eq. (4.24), which can be referred for simplicity as 2$^{\text{nd}}$ order Kanit *et al.* relation:

$$\hat{D}^2_{E_{ij}}(P) = \frac{A_{ij}}{P^\alpha}\hat{D}^2_{\varepsilon_{ij}} + \frac{B_{ij}}{P^\alpha}\hat{D}^4_{\varepsilon_{ij}}. \tag{4.24}$$

From the sampling theory, the size of a RVE (P) can now be directly related to the relative error (η) of the effective response, according to:

$$\eta = \frac{z_s \, \hat{D}_{E_{ij}}(P)}{\sqrt{n}}, \tag{4.25}$$

where n represents the number of realizations and 'z_s' is the z-score. Finally, the required RVE size (P_{req}) for a specified η, and number of realizations n, are obtained by replacing Eq. (4.23) or Eq. (4.24) in Eq.(4.25) as:

$$P_{req} = \frac{z_s^2 \left(A_{ij} \hat{D}^2_{\varepsilon_{ij}} + B_{ij} \hat{D}^4_{\varepsilon_{ij}} \right)}{n\eta^2} \quad \text{or} \quad P_{req} = \left(\frac{z_s^2 \left(A_{ij} \hat{D}^2_{\varepsilon_{ij}} + B_{ij} \hat{D}^4_{\varepsilon_{ij}} \right)}{n\eta^2} \right)^{1/\alpha}. \tag{4.26}$$

Note that for the specific case where $A_{ij} << B_{ij}$, the P_{req} can be approximated as

$$P_{req} = \frac{z_s^2 B_{ij} \hat{D}^4_{\varepsilon_{ij}}}{n\eta^2} \quad \text{or} \quad P_{req} = \left(\frac{z_s^2 B_{ij} \hat{D}^4_{\varepsilon_{ij}}}{n\eta^2} \right)^{1/\alpha}. \tag{4.27}$$

4.4 Results and discussion

A set of FFT simulations varying the RVE size with number of particles (3, 6, 9, 12, 15, 30, 60 and 90), volume fractions (7%, 10%, 15% and 20%) and aspect ratio (AR) of precipitates (4 and $1/4$) were carried out. Realizations of the RVE for fixed geometric parameters (P, VF and AR) were created with different random position and orientation for the particles. Two SMA properties for the phase transforming matrix, SMA-1 and SMA-2 in Table 4.1, were studied. For each RVE size, the number of realizations were chosen such that the relative standard error of the average is less than 1% (refer to section 3.4.3 and Table 3.6). Spatial convergence was found for 3000 FFT grid points per particle, following the grid convergence analysis presented in section 3.4.2. The dispersion of the effective response was studied at two points in the actuation response (Figure 1.1 in section 1.1.1). Point 'A' refers to the purely elastic strain at the end of loading , and 'B' refers to the end of transformation strain at the end of the cooling. The results obtained at point 'B' were

labeled 'SMA-1' or 'SMA-2' depending on the material and the results at point 'A' were labeled 'Elastic.'

For each RVE case (i.e. fixed VF, AR and P), the ensemble average $\overline{E}_{zz}$ and standard deviation ($D_{E_{zz}}(P)$) were calculated at point 'A' and point 'B'. Further, the coefficient of variation ($\hat{D}_{E_{zz}}(P)$) was obtained as $\hat{D}_{E_{zz}}(P) = D_{E_{zz}}(P)/\overline{E}_{zz}$. Similarly, from the strain distribution (ε_{zz}) inside the RVEs, the point-variation ($D_{\varepsilon_{zz}}$) and point-CV ($\hat{D}_{\varepsilon_{zz}}$) at loading point 'A' and 'B' were obtained. Further ensemble average values of $\hat{D}_{\varepsilon_{zz}}$ from the realizations were used in the analysis. The correlation between the macroscopic dispersion $\hat{D}_{E_{zz}}(P)$ and the microscopic dispersion $\hat{D}_{\varepsilon_{zz}}$ were analyzed for the different models shown in Table 4.2. These models were categorized as 1st order relations or 2nd order, and are listed in Table 4.2 according to the increasing number of parameter and accuracy of the model.

Table 4.2: Summary of relations for quantifying the strain dispersion.

Cases	Equation format	From	Type
Lantuéjoul	$\hat{D}^2_{E_{zz}}(P) = \hat{D}^2_{\varepsilon_{zz}} A/P$	Eq. (4.1)	1st order
Kanit *et al.*	$\hat{D}^2_{E_{zz}}(P) = \hat{D}^2_{\varepsilon_{zz}} A/P^{\alpha}$	Eq. (4.2)	1st order
Case 1	$\hat{D}^2_{E_{zz}}(P) = (B\hat{D}^4_{\varepsilon_{zz}})/P$	Eq. (4.23) for $A << B$	2nd order
Case 2	$\hat{D}^2_{E_{zz}}(P) = (A\hat{D}^2_{\varepsilon_{zz}} + B\hat{D}^4_{\varepsilon_{zz}})/P$	Eq. (4.23)	2nd order
Case 3	$\hat{D}^2_{E_{zz}}(P) = (B\hat{D}^4_{\varepsilon_{zz}})/P^{\alpha}$	Eq. (4.24) for $A << B$	2nd order
Case 4	$\hat{D}^2_{E_{zz}}(P) = (A\hat{D}^2_{\varepsilon_{zz}} + B\hat{D}^4_{\varepsilon_{zz}})/P^{\alpha}$	Eq. (4.24)	2nd order

The point coefficient of variance $\hat{D}_{\varepsilon_{zz}}$ is a key variable in the statistical relations proposed in Table 4.2. An examination on the values of $\hat{D}_{\varepsilon_{zz}}$ was performed. Figure 4.1 shows the values of $\hat{D}_{\varepsilon_{zz}}$ for different RVEs, which are compared for different number of precipitates (P) and volume fractions. In sub-plots (a), (b) and (c) of Figure 4.1 this comparison is made for different SMA properties (SMA-1 and SMA-2) and shape of precipitates ($AR = 4$ and $AR = 1/4$). At each P,

the values from different RVE realizations show the scatter of $\hat{D}_{\varepsilon_{zz}}$ values between realizations. Between different volume fractions, $\hat{D}_{\varepsilon_{zz}}$ values show considerable difference, while within the same VF and microstructure, changing the RVE size doesn't change their value noticeably. The comparison indicates that $\hat{D}_{\varepsilon_{zz}}$ is more or less constant for a specific microstructure and SMA property with changing volume of the RVE. With this observation, the relations proposed in Table 4.2 can be applied, taking $\hat{D}_{\varepsilon_{zz}}$ to be constant in a particular microstructure.

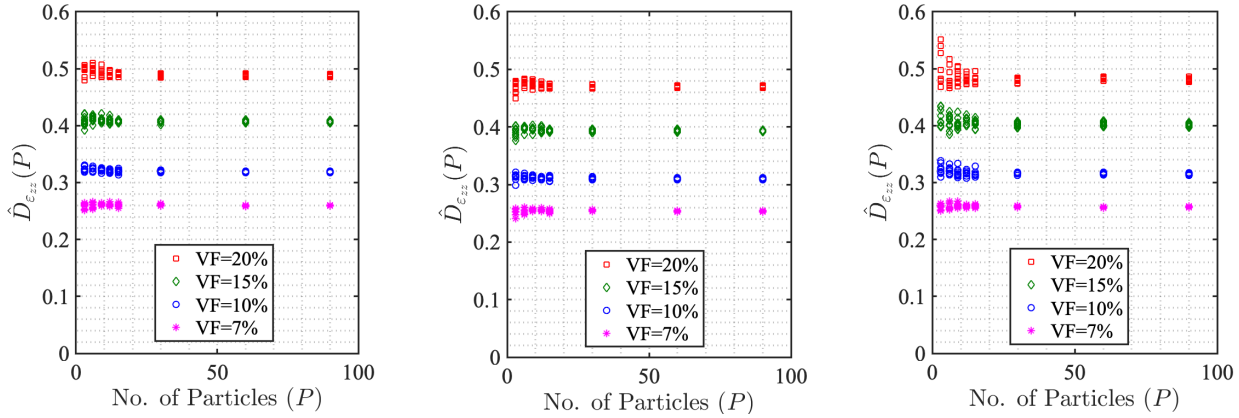

(a) Matrix: SMA-1, $AR = 1/4$ (b) Matrix: SMA-2, $AR = 1/4$ (c) Matrix: SMA-2, $AR = 4$

Figure 4.1: The convergence of $\hat{D}_{\varepsilon_{zz}}$ within the RVEs is compared for cases with different number of precipitates (3, 6, 9, 12, 15, 30, 60, 90), volume fraction, shape of precipitates and material properties. In (a) the properties of the matrix is SMA-1 and AR of precipitates is $1/4$. In (b) and (c), the matrix has properties of SMA-2 and AR is varied.

The performance of the Kanit *et al.* [7] approximation (Eq. (4.2)), which assumes 1st order correlation between $D_{E_{zz}}(P)$ and point-variation $D_{\varepsilon_{zz}}$ was analyzed. By linearizing Eq. (4.2) and rearranging, the following expression is obtained.

$$\log\left(\frac{D_Z^2(V)}{D_Z^2}\right) = \log(A_3^\alpha) - \alpha\log(V), \tag{4.28}$$

where $-\alpha$ is the slope and $log(A_3^\alpha)$ the intercept. Considering $Z = \varepsilon_{zz}$ and V as number of

precipitates P, the dispersion of strain values is fitted for the relation. The comparisons obtained for the material behavior 'Elastic,' 'SMA-1' and 'SMA-2' are shown in Figure 4.2 (a-c). With a goodness of fit (R^2) in the range of $(0.72 - 0.79)$, this relation is shown to be inadequate for capturing the influence of different volume fractions and aspect ratios. This is consistent with the non-linear dependency between the integral range and the volume fraction shown in the Kanit *et al.* [7] relation and described in detail in [137].

Before investigating the performance of the 2nd order relations, it is helpful to analyze the 2nd order effects in a fixed RVE size P. For fixed P, the 2nd order relation given by Eq. (4.23) can be written as: $\hat{D}^2_{E_{zz}}(P) = A\hat{D}^2_{\varepsilon_{zz}} + B\hat{D}^4_{\varepsilon_{zz}}$ with constants A and B. A quadratic relation of the form $Ax + Bx^2$ in $\hat{D}^2_{\varepsilon_{zz}}$ is obtained, in contrast to the linear relation assumed in Lantuéjoul [139] or Kanit *et al.* [7] formulations (Section 4.3.1). This quadratic variation is analyzed in Figure 4.3 for $P = 3$ comparing $\hat{D}^2_{E_{zz}}(P)$ versus $\hat{D}^2_{\varepsilon_{zz}}$ for different volume fractions (7%, 10%, 15% and 20%) and aspect ratios (4 and 1/4) for (a) elastic (b) SMA-1 and (c) SMA-2 properties in the matrix. Figure 4.3 ((b) and (c)) shows the good approximation of the proposed model in capturing the influence of both the volume fraction and aspect ratio derived from the non-linear behavior of SMA-1 and SMA-2. In contrast, the elastic case shown in Figure 4.3 (a) is moderately correlated with the quadratic model. Although a detailed discussion on this matter will be performed later in the chapter, this reduction in accuracy comes from the ability of the model to predict the influence of precipitate aspect ratios. Comparing the proposed 2^{nd} order model with the first order Lantuéjoul model, it is possible to derive that the integral range (A_3 in Eq. (4.1)) for the 2nd order model has the form of $A_3 = A + B\hat{D}^2_{\varepsilon_{zz}}$, and thus it presents a nonlinear dependency with respect to ($\hat{D}_{\varepsilon_{zz}}$).

One can further simplify Eq. (4.23) assuming a purely 2nd order relation based on $A << B$ in Figure 4.3. A pure 2nd order form of Eq. (4.23) is given by Eq. (4.29) by taking the square root and dividing both sides by $\sqrt{P}$:

$$\frac{\hat{D}_{E_{zz}}(P)}{\sqrt{P}} = \sqrt{B_{zz}} \left(\frac{\hat{D}_{\varepsilon_{zz}}}{\sqrt{P}} \right)^2 \tag{4.29}$$

In its logarithmic form, Eq. (4.29) can be written as:

$$\log\left(\frac{\hat{D}_{E_{zz}}(P)}{\sqrt{P}}\right) = 2\log\left(\frac{\hat{D}_{\varepsilon_{zz}}}{\sqrt{P}}\right) + c, \tag{4.30}$$

where c is a constant related as $c = log\left(\sqrt{B_{zz}}\right)$. The peculiarity of Eq. (4.30) is that it relates the same term $\hat{D}_Z/\sqrt{P}$ obtained from macroscopic variance to the microscopic variance. The term is of the same form as the standard error of the mean (SEM$= D/\sqrt{n}$), where n is the number of samples. Hence, on comparison, an RVE realization with P number of precipitates can be seen as a sample set with P number of samples.

Now, the performance of the 2nd order correlation in Eq. (4.23) for the new approximation proposed in Eq. (4.30) is tested again for the elastic, SMA-1 and SMA-2 behaviour in Figure 4.4. The resulting fitting parameters show that $A << B$, indicating a predominantly 2nd order correlation and consistent with the analysis performed on a fixed RVE size. Further, Figure 4.5, shows the performance of the purely 2nd order correlation of Eq. (4.30) by removing the linear term A. The Performance of both models in Figure 4.4 and Figure 4.5 is almost the same. The goodness of the fit corroborates the better approximation of the second order model with respect to the first order model shown in Figure 4.2. The lower accuracy of the second order model in predicting the pure elastic behavior will be analyzed next by an independent analyses on different aspect ratios.

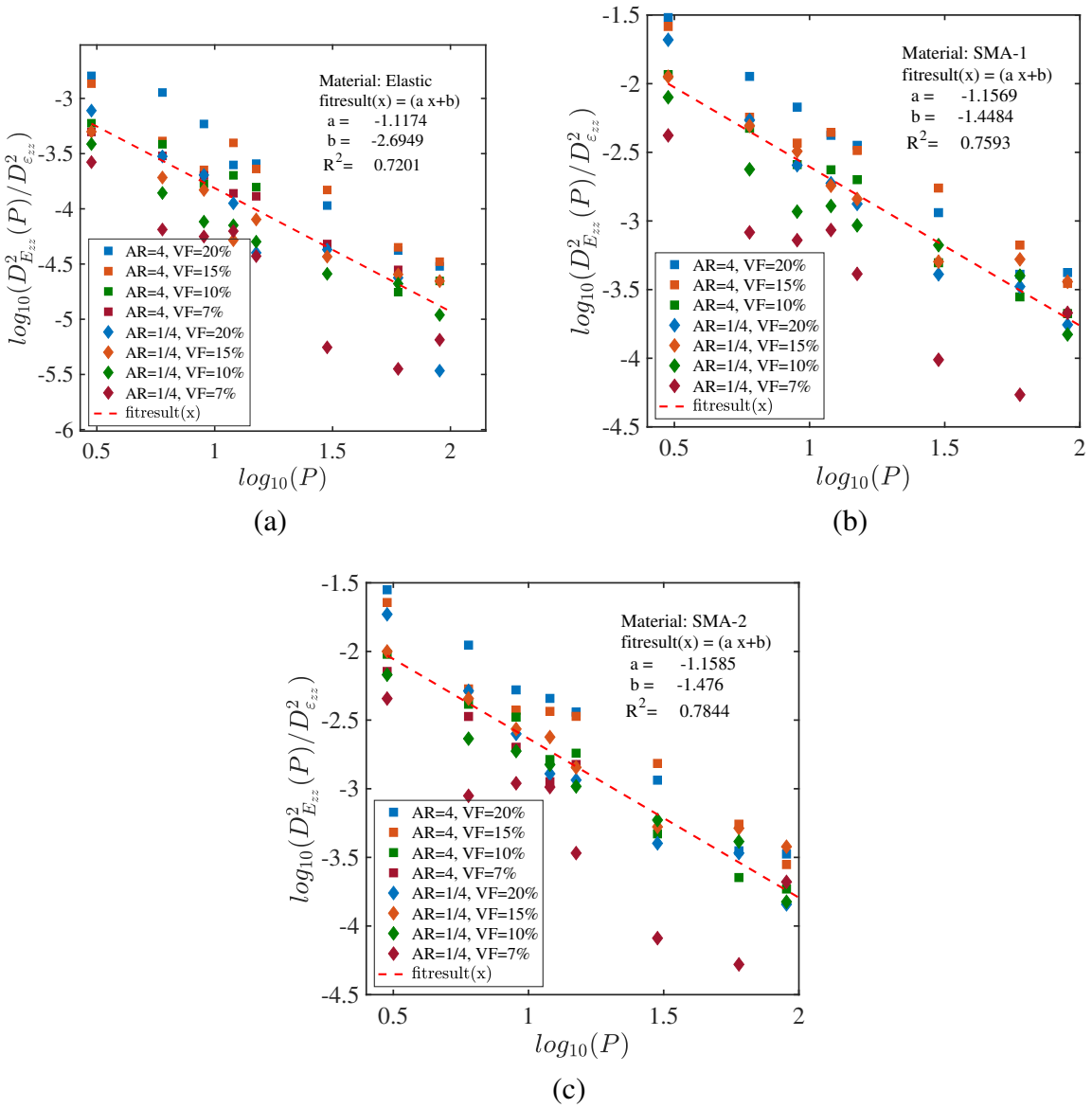

Figure 4.2: Quantifying the strain variation in the SMA response using 1st order Kanit *et al.* [7] formulation for (a) Elastic (b) SMA-1 (c) SMA-2 properties in the matrix. The $D^2_{\overline{Z}}(V)/D^2_Z \mid Z = \varepsilon_{zz}$ term is compared against P (3, 6, 9, 12, 15, 30, 60, 90) for different volume fractions (7%, 10%, 15% and 20%) and AR$= (4, 1/4)$ precipitates at $\sigma = 300$MPa in a log-log plot. The data in each case is fitted with Eq. (4.28); the coefficients and goodness of fit R^2 are shown.

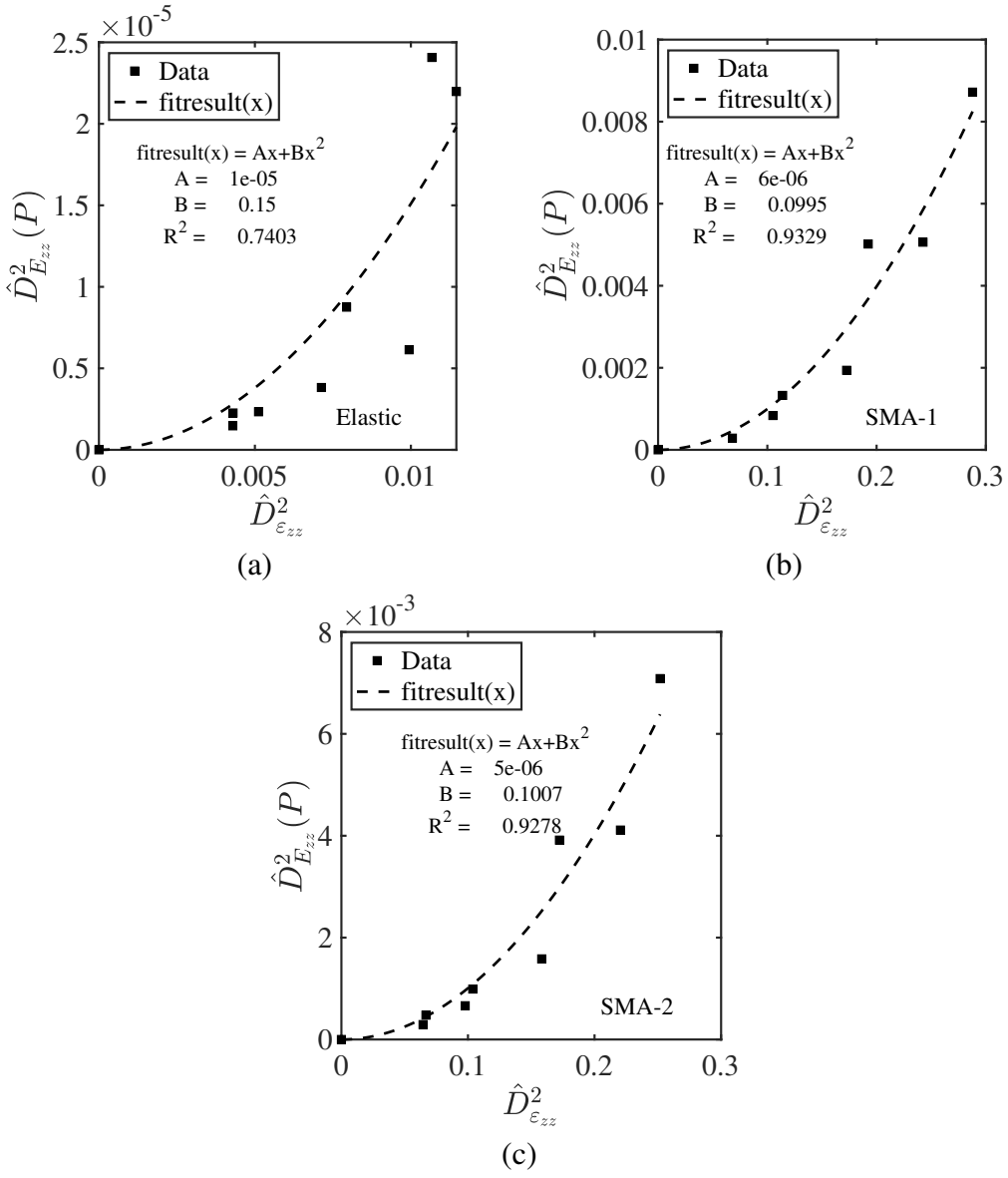

Figure 4.3: Variation of $\hat{D}^2_{E_{ij}}(P)$ versus $\hat{D}^2_{\varepsilon_{zz}}$ with $P = 3$ for different volume fractions (7%, 10%, 15% and 20%) and aspect ratios (4 and 1/4). Variation in the case of different material properties was studied: (a) Elastic (b) SMA-1 and (c) SMA-2 property in the matrix.

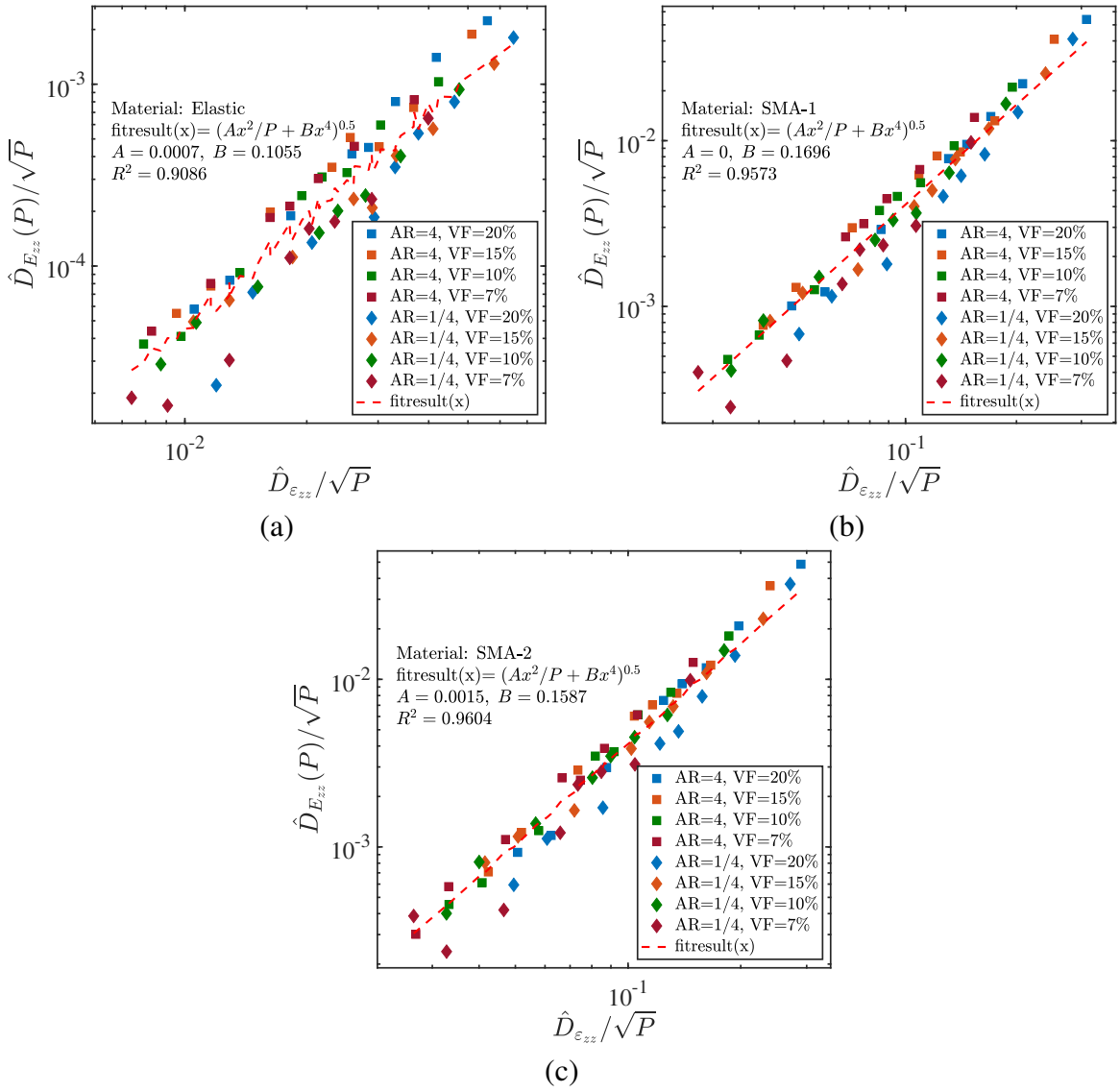

Figure 4.4: Quantifying the strain variation in the SMA response using 2nd order formulation [Case 2: $\hat{D}^2_{E_{zz}}(P) = (A\hat{D}^2_{\varepsilon_{zz}} + B\hat{D}^4_{\varepsilon_{zz}})/P$] for (a) Elastic (b) SMA-1 (c) SMA-2 properties in the matrix. The formulation is compared for dispersion from P (3, 6, 9, 12, 15, 30, 60, 90) in different volume fractions (7%, 10%, 15% and 20%) and AR $= (4, 1/4)$ at $\sigma = 300$MPa. The fitted functions with corresponding coefficients and goodness of fit R^2 are shown in each plot.

If $\hat{D}^2_{E_{zz}}(P)$ versus $\hat{D}^2_{\varepsilon_{zz}}$ is plotted in Figure 4.6 for a fixed P= 3 and different volume fractions (7%, 10%, 15% and 20%) independently for the aspect ratio 4 (a)-(c) and 1/4 (d)-(e), a better correlation with goodness of fit $R^2 \approx 1$ is obtained. This good correlation can be seen as the near perfect

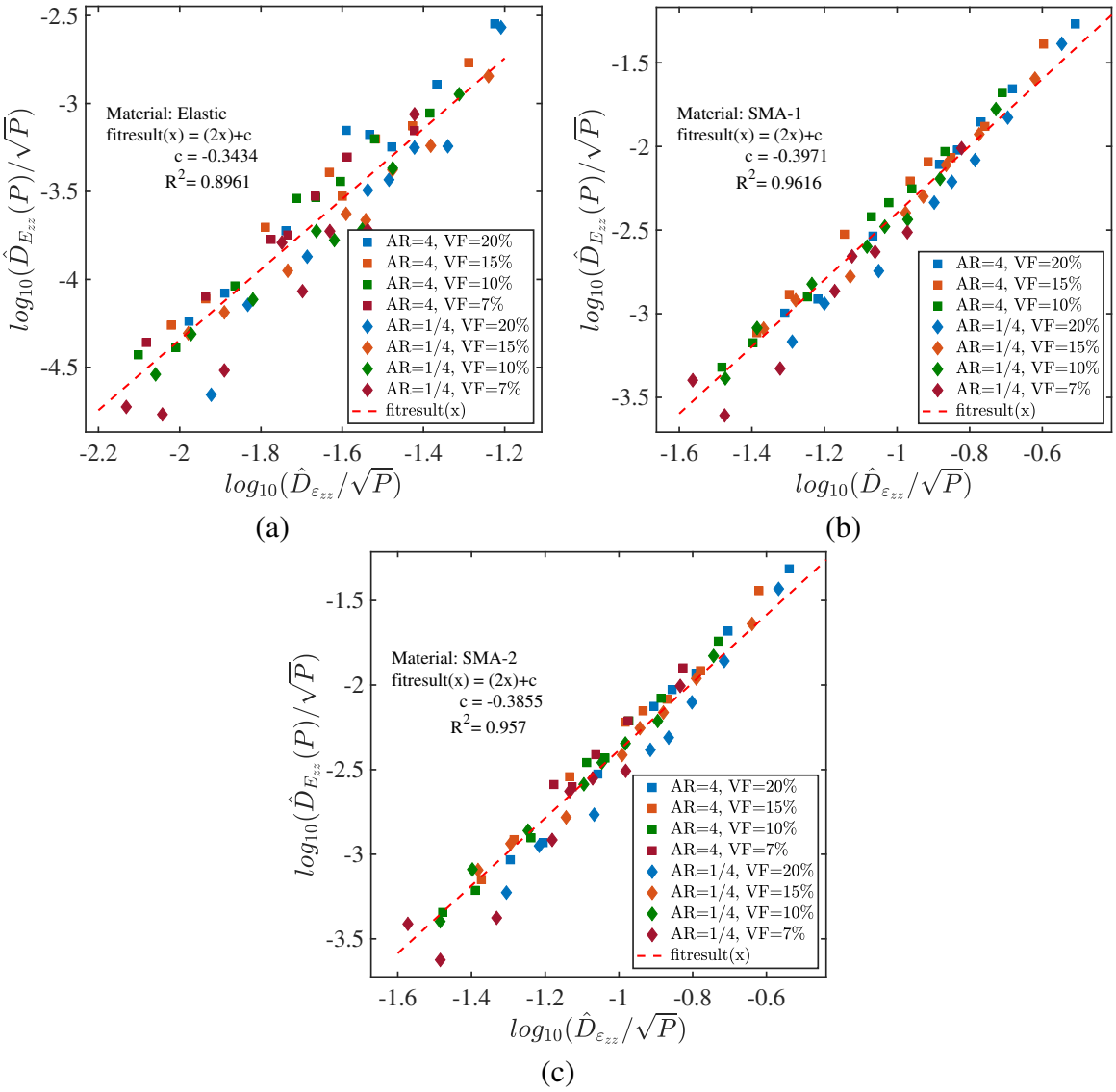

Figure 4.5: Quantifying the strain variation in the SMA response using 2nd order formulation [Case 1: $\hat{D}^2_{E_{zz}}(P) = (B\hat{D}^4_{\varepsilon_{zz}})/P$] for (a) Elastic (b) SMA-1 (c) SMA-2 properties in the matrix. The formulation is compared for dispersion from P (3, 6, 9, 12, 15, 30, 60, 90) in different volume fractions (7%, 10%, 15% and 20%) and AR $= (4, 1/4)$ at $\sigma = 300$MPa. The fitted functions with corresponding coefficients and goodness of fit R^2 are shown in each plot.

accuracy of second order approximations for capturing the influence of the volume fraction in the RVE size. The corresponding fitting using the simplified 2nd order formulation for the different RVE sizes is shown in Figure 4.7. A drastic improvement in the specific 'Elastic' case compared to the previous analysis with different ARs taken together is shown. This can be explained by

analyzing the interaction between the particles in the 'Elastic' and phase transformation SMA-1 or SMA-2 responses.

Figure 4.8(a-c) shows the normalized strain distribution ($\varepsilon_{zz}/\overline{\varepsilon}_{zz}$) between the particles for the Elastic, SMA-1 and SMA-2 behavior in the matrix. In the Elastic case, the maximum strain is more localized between the particles in comparison to the SMA-1 and SMA-2 cases, where phase transformation is active (see between P1 and P2 in Figure 4.8). More localized strain distribution indicates higher particle interaction, as the changes in the particle boundary can significantly change the localized distribution and the overall response. This can be a reason for higher sensitivity of dispersion correlations to the AR in the case of Elastic matrix, while in the SMA case, the maximum strain is distributed over a broader region between the particles due to the softening effect from phase transformation, and indicates lesser particle boundary interaction. This was reflected as higher robustness of dispersion correlations in the SMA-1 and SMA-2 towards AR. Overall, the difference in the sensitivity to the aspect ratio between SMA and Elastic is the consequence of the phase transformation behavior being more dissipative than elastic behavior.

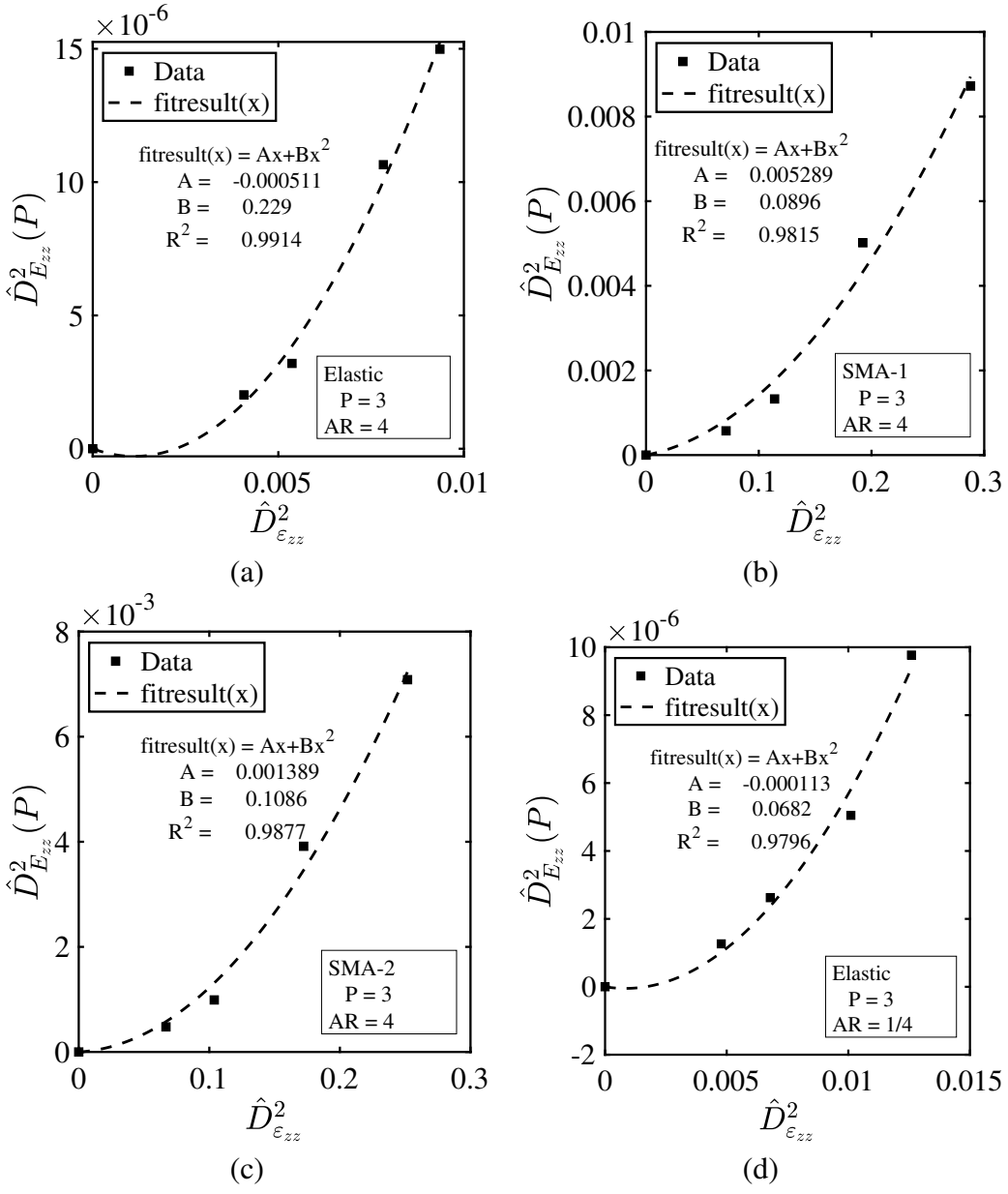

Figure 4.6: Variation of $\hat{D}^2_{E_{ij}}(P)$ verses $\hat{D}^2_{\varepsilon_{zz}}$ with $P = 3$ for different volume fractions (7%, 10%, 15% and 20%) considering aspect ratios separately. Variation for different material behavior was studied: Elastic with (a) AR$= 4$ and (d) AR$= 1/4$, SMA-1 with (b) AR$= 4$ and (e) AR$= 1/4$, and SMA-2 with (c) AR$= 4$ and (f) AR$= 1/4$.

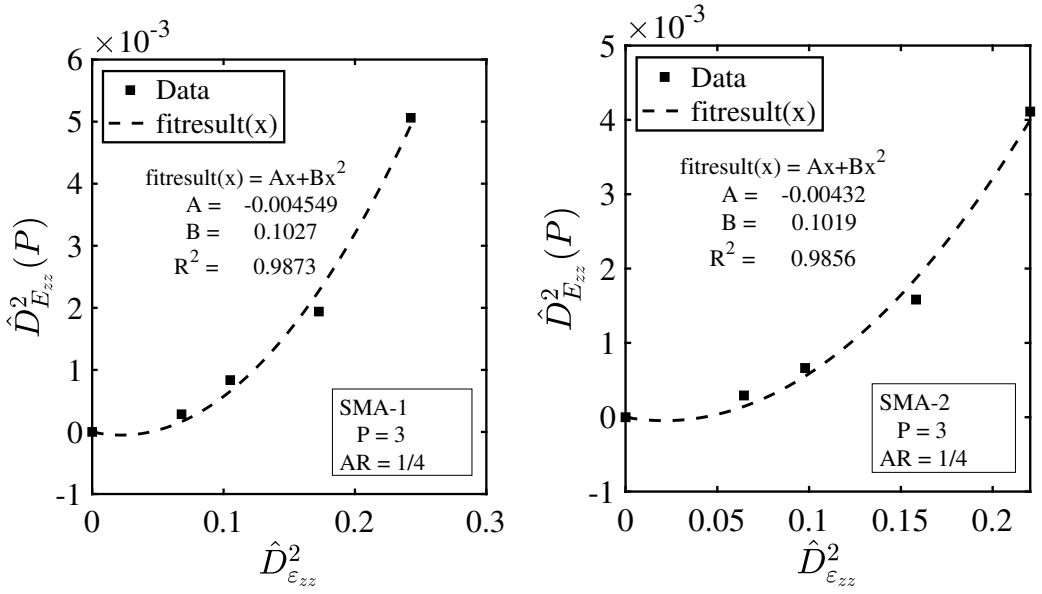

Figure 4.6: Continued

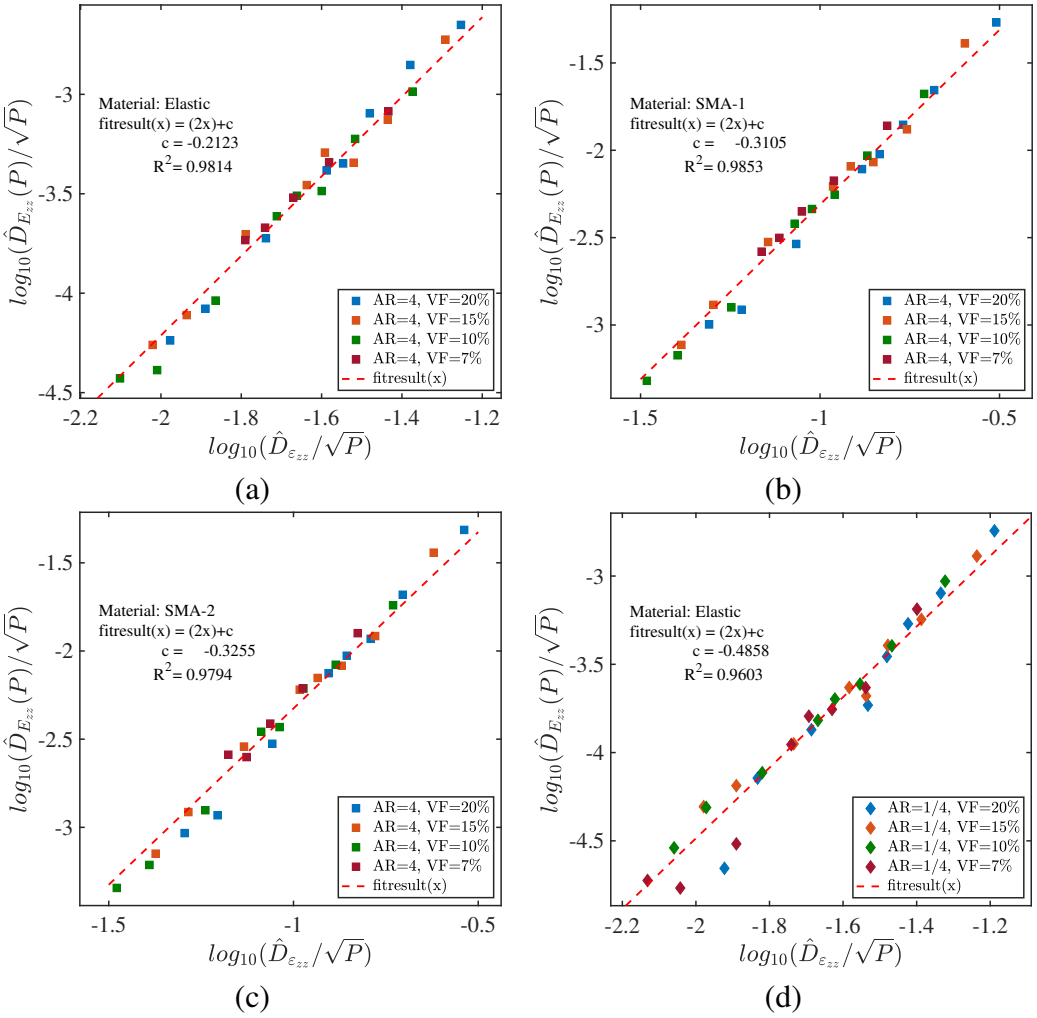

Figure 4.7: Quantifying the strain variation in the SMA response using 2nd order formulation [Case 1: $\hat{D}^2_{E_{zz}}(P) = (B\hat{D}^4_{\varepsilon_{zz}})/P$] when each AR is considered separately. AR$=4$ in (a)-(c) and AR$=1/4$ in (d)-(f). (a) & (d) have Elastic, (b) & (e) have SMA-1 and (c) & (f) have SMA-2 properties in the matrix. The formulation is compared for dispersion from P (3, 6, 9, 12, 15, 30, 60, 90) in different volume fractions (7%, 10%, 15% and 20%) at $\sigma = 300$MPa. The fitted functions with corresponding coefficients and R^2 are shown in each plot.

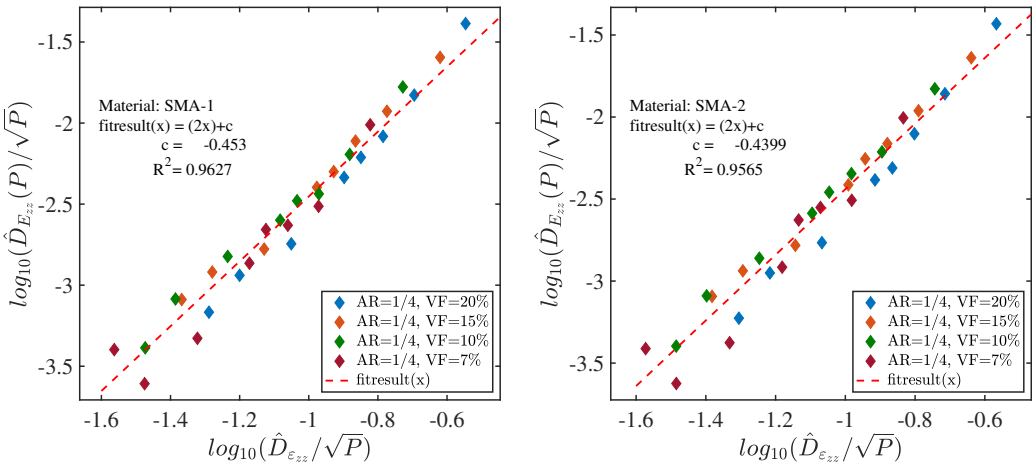

Figure 4.7: Continued

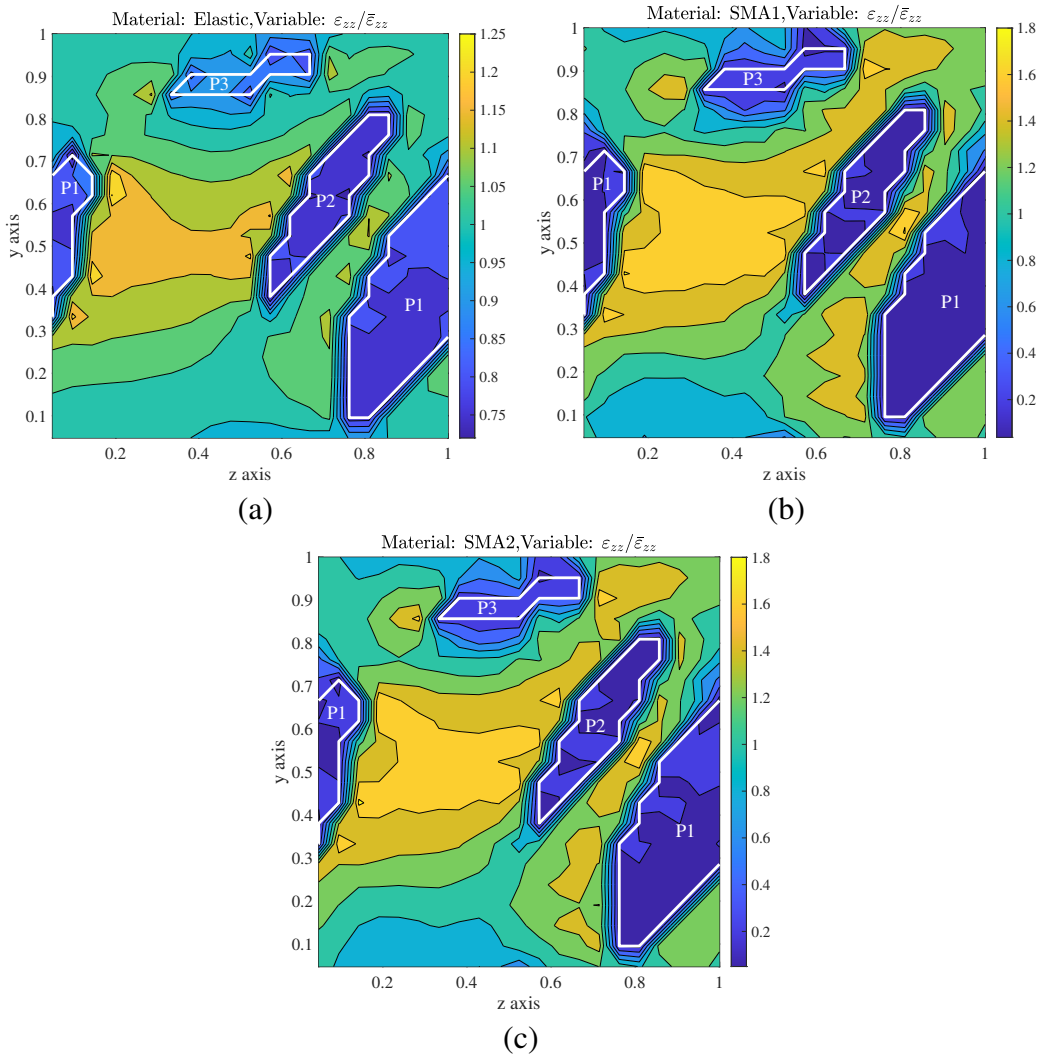

Figure 4.8: The local strain distribution showing the extend of dissipation between the particles in (a) Elastic (b) SMA-1 (c) SMA-2 properties in the matrix.

To have a better overview of the accuracy of 1st order versus 2nd order correlations, each model listed in Table 4.2 was used to build the strain dispersion correlation for the SMA-1. The parameters in the relations were estimated using fminsearch optimizer in MATLAB software [140, 90]. A comparison of their performance towards predicting the macroscopic response dispersion ($\hat{D}_{E_{zz}}(P)$) is made in Figure 4.9. The analysis was performed for combined ARs (Figure 4.9 (a)) and for single AR (Figure 4.9 (b)). It can be seen that the 2nd order correlations outperform the 1st order by an increase of 15%-30% in the goodness R^2. Furthermore, both 1st order and 2nd order cases with $1/P^{\alpha}$ type correlation proposed by Kanit *et al.* [7] seem to improve the accuracy of the model. The coefficients obtained for the different models shown in Figure 4.9 (b) are listed in Table 4.3. Note that the value of α is close for the $1/P^{\alpha}$ type correlations, although A and B change considerably in these cases.

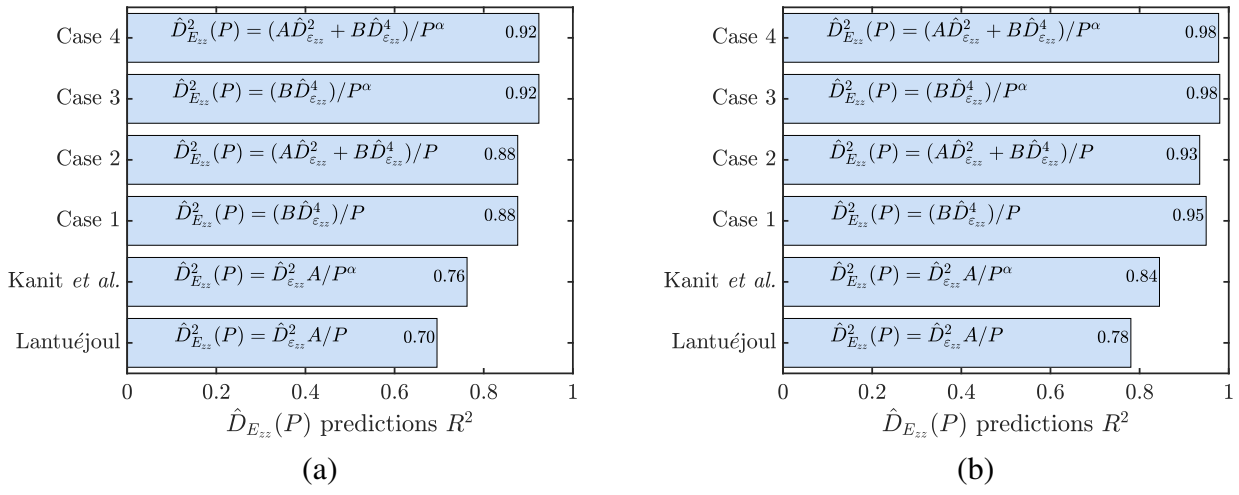

Figure 4.9: Comparison of methods with their goodness (R^2) towards predicting $\hat{D}_{E_{zz}}(P)$ in SMA1 RVEs response as (a) generalized in ARs $(= 4, 1/4)$ and single (b) AR $(= 4)$. The 2nd order correlations are seen to outperform the 1st order correlations with higher R^2 in predicting $\hat{D}_{E_{zz}}(P)$. Further, the correlations assuming $1/P^{\alpha}$ variation are seen to perform better than $1/P$ variation.

Table 4.3: Summary of estimated parameters for Figure 4.9 (b).

Case	A	B	α
Case 4	0.0084	0.3042	1.1624
Case 3	0	0.3748	1.1688
Case 2	0.0063	0.1910	1
Case 1	0	0.4892	1
Kanit *et al.*	0.0511	0	1.154
Lantuéjoul	0.0340	0	1

If we further analyze the general Eq. (4.23), it is necessary to obtain the correlation between the components A_{ij} and B_{ij} for the different strain components. To this end, Figure 4.10 (a) shows the dispersion of the three normal components of strain (E_{xx}, E_{yy} and E_{zz}) for the different volume fractions and aspect ratio cases. The absolute value is considered here so that the negative (E_{xx} and E_{yy}) and the positive (E_{zz}) strain components can be compared in the same plot. Remarkably, the dispersion from the three different components can be fitted well using a single relation indicating the same correlation. Although the values of E_{xx}, E_{yy} and E_{zz} are much different, the $\hat{D}$ term normalizes the dispersion with respect to the mean value. This means that the coefficients are related in magnitude along the normal strain components A_{ii} and B_{ii}, which in this case is $B_{11} \approx B_{22} \approx B_{33} = B$. In material behaviors with anisotropy, these coefficients may not be correlated in the same manner.

Finally, we aim to show the simplicity and ability of the reduced 2$^{\text{nd}}$ order relation in Eq. (4.30), by fitting the model with one data point and comparing the fit against all the remaining data. For this purpose, the RVE with highest VF ($= 20\%$), AR ($= 4$), and a moderate size ($P = 15$) was used. Figure 4.11 (a) & (b) shows that the corresponding fit for SMA-1 and SMA-2 captures the variation of dispersion with good accuracy of ($R^2 > 0.94$) although only one point was used in the estimation. For comparison, all remaining data points are included in the figure.

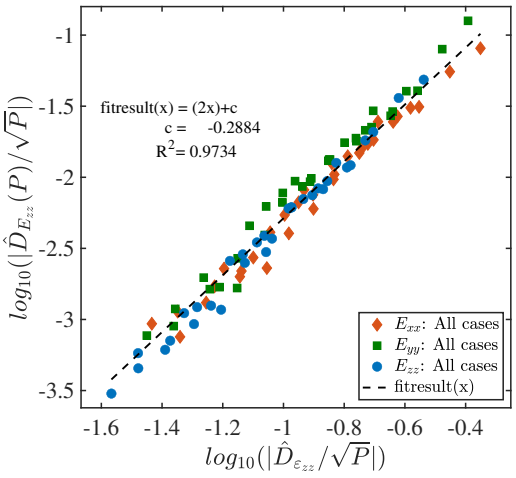

(a)

Figure 4.10: The variations of the strain terms (E_{xx}, E_{yy}, E_{zz}) in the SMA response for matrix: SMA-2, $\sigma_{zz} = 300MPa$ case. a) The $\hat{D}$ terms in E_{xx}, E_{yy} and E_{zz} from RVEs compared for varying P (3, 6, 9, 12, 15, 30, 60, 90), volume fraction (7%,10%,15% and 20%) and AR$= 4$. b) The data from (a) are fitted using Eq. (4.30); the coefficients and R^2 are shown.

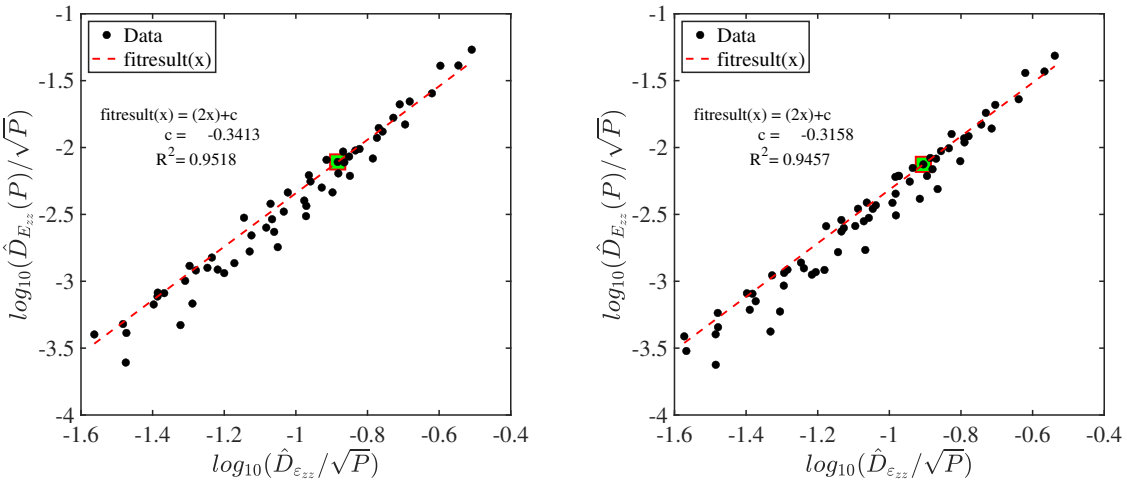

(a) (b)

Figure 4.11: Fit for (a) SMA-1 & (b) SMA-2 using only 1 point to calculate the coefficient c in Eq. (4.30) and compared against all the data. The 1 point used from the case (VF= 20%, AR$= 4$, $P = 15$) is marked with a green box.

An analysis on the P_{req} using the fit for SMA-1 property in Figure 4.11(a) was carried out.

Table 4.4: Size of RVE (P) calculated for $n = 1$, $\eta = 0.01$ for different VF.

VF (%)	$\hat{D}_{\varepsilon_{zz}}$	Size of RVE (P) $n = 1$,$\eta = 0.01$	η from 4 simulations for validation (95 % CI)
20	0.49	478	[0.0028, 0.0022, 0.0006, 0.0012]
15	0.41	234	[0.0002, 0.0032, 0.0010, 0.0025]
10	0.33	98	[0.0069, 0.0062, 0.0021, 0.0013]
7	0.27	44	[0.0001, 0.0038, 0.0017, 0.0020]

For 95% confidence interval ($z_s = 2$), the estimations of RVE size 'P_{req}' for specified accuracy ($\eta = 0.01$) and number of iteration $n = 1$ for different volume fractions from Eq. (4.27) are shown in Table 4.4. The results were verified with 4 simulations of the calculated RVE size and the individual error values were obtained, and compared with the mean value. The relative errors for all the 4 simulations shown in Table 4.4 are within the specified error range of $\delta = 0.01$ and validate the prediction of the RVE sizes.

4.5 Conclusions

A new analytical approach for quantifying the statistics of effective strain dispersion in the RVEs was developed. In the new formulation, the individual RVE behaviors were described in terms of the average behavior and possible perturbations from the average. The expression for effective strain dispersion were derived following the properties of perturbations, and further simplified in terms of the local strain distribution. The developed relations were found to be of 2nd order with respect to the point variance of strain. The new relation captured higher order effects which the previous methods could not as they were considering only linear correlations.

By quantifying the dispersion of effective SMA behaviors in the precipitated microstructure RVEs with the new formulation, the proposed 2nd order effects were validated. The statistics in the SMA responses with changing volume fraction, aspect ratio and number of precipitates were analyzed. With the new formulation, the effects from changing microstructure and number of precipitates were shown to be captured in the same relations. The higher sensitivity of correlations observed in elastic behavior towards changes in precipitate shape was associated with its higher

particle interaction. As there was less particle interaction in SMAs due to their dissipating behavior, the 2nd order relations built were robust towards the aspect ratio changes in the microstructure. The ability of the reduced 2nd order relation to predict the variation using only one RVE case in the case of SMAs demonstrates the potential of the developed formulation. The developed relation was used for predicting the RVE size at a prescribed accuracy in the responses, and the predictions were validated.

5. MACHINE LEARNING MODEL FOR PREDICTING THE SHAPE MEMORY ALLOY RESPONSE FROM MICROSTRUCTURES

5.1 Introduction

Shape Memory Alloys (SMAs) are a class of materials that undergo large recoverable shape changes in a range of temperatures and stresses as a result of reversible martensitic transformations. Among these, High Temperature SMAs (HTSMAs) have attracted significant interest due to their potential use as high-temperature solid-state actuators, especially with the recent discovery of nano-precipitation hardened NiTiHf HTSMAs, which exhibit an exceptionally stable cyclic actuation response. However, to facilitate efficient designing of these alloys, faster and accurate micromechanics based process-structure linkage models are required. This can be achieved successfully by relying on recently developed data science and machine learning tools.

With the growing interest in more rapid discovery of new materials with better performance, there is a need for development of faster and more accurate multiscale micromechanical models. While, traditional methods offer accurate solutions through high power Finite Element (FE) techniques such as FE^2, the high computational cost of these numerical methods significantly limits their broader adoption and utilization. However, recent developments in statistical continuum theories and machine learning (ML) offer highly promising methodologies for faster and more efficient multiscale modeling [63, 60]. These data science approaches using spatial statistics representation techniques for microstructures have made possible building lower-order accurate models to predict micromechanical behavior from representative volume elements (RVEs) of the microstructures. Data science approaches such as Materials Knowledge Systems (MKS) are based on this idea for building lower order structure-property linkage[61, 141, 62].

A key aspect in the efficacy of any data based model is how the input and the targets are described. In the present scenario, microstructures will be described using the recently developed spatial statistical technique of 2-point correlations, which have been successfully used to describe

microstructures of different size and morphology in some recent works [60, 61, 62, 63]. The advantage in using 2-point spatial statistical representation is the ability to represent microstructures of different size and morphology in the same data structure, carrying identical statistical information on respective grids in the representation [64]. The availability of large computational resources provides the means to perform many small level micromechanics simulations to generate a database covering the design space, in order to build robust ML models for all possible microstructures. The open source tool 'PyMKS' [65] in Python enable the micromechanics community to use some of these statistical methodologies. With PyMKS, the RVEs of SMA microstructures can be represented in terms of 2-point correlation. Further, through dimensionality reduction via Principal Component Analysis (PCA) of the statistical representations, low-dimensional data based ML models for the microstructure-property linkages are then possible. With PCA, the dimensionality of the model can be truncated efficiently according to the accuracy required, making the ML model feasible with fewer expensive simulations.

In recent years, advancements in the field of machine learning have provided promising tools for understanding and predicting material behaviors. However, to the best knowledge of the author, there have been no such attempts to capture multiscale modeling incorporating the effects of precipitation in the SMA modeling and characterization. The proposed 2-point spatial statistical techniques together with higher computational ability offer a fertile environment for machine learning tools to be trained on multiscale modeling. These tools will aid in the development of new prediction capabilities that learn directly from the microstructure descriptions. Although the focus here is on SMAs, the methodology can be extended to any material with similar mechanics.

5.2 Micromechanical modeling of SMA responses

Secondary heat treatments in NiTi SMAs create non transforming Ni_4Ti_3 precipitates. The formation of these precipitates changes the actuation behavior in SMAs. More on actuation behavior in SMAs can be read in Chapter 1. The new actuation behavior is the result of many underlying micromechanical interactions in the material due to the new precipitate phase. Details of different mechanisms in precipitated SMAs can be found in Chapter 2 and Chapter 3.

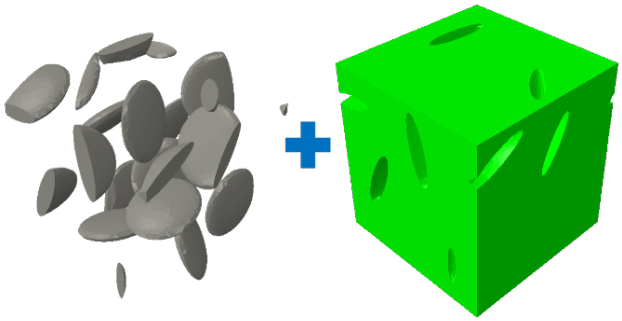

Figure 5.1: Figure showing the RVE based model used for training data based model. RVE shown with the precipitate and matrix phases.

A micromechanical model with RVEs of the precipitated SMAs can capture the modified effective behavior. Figure 5.1 shows a summary of the micromechanical model considered in the current work. The RVEs are modeled as non-transforming ellipsoidal precipitates embedded in a phase transforming matrix. The constitutive response of the SMA matrix is captured with the constitutive model for SMAs developed by Lagoudas *et al.*[38], and the precipitates are modeled with linear elastic and isotropic behavior. The effective actuation response of the heat treated material is predicted from the RVEs, applying corresponding thermo-mechanical loading conditions. Details of the micromechanical model can be found in Chapter 3. The micromechanical modeling framework developed using Fast Fourier Transform (FFT) based homogenization in Chapter 3 was used for solving the effective actuation response.

Properties of NiTi SMA used in the current study were obtained from experimental results reported in the work of Cox *et al.* [6] following calibration with the SMA constitutive model of Lagoudas *et al.* [38]. Ellipsoid precipitates with an aspect ratio of 4, with linear isotropic behavior, are considered. The SMA properties and elastic material properties used in the current study are summarized in table 5.1.

The RVE model is first solved for a loading step with an axial stress of Σ_{zz} =(200 MPa) at a constant nominal temperature of T =350 K. The behavior in the loading step is elastic. Further, the RVE is solved for the thermal path cooled to T =220 K and heated to T =350 K. The SMA

Table 5.1: SMA matrix and precipitate properties used in the micromechanical modeling [6].

SMA Matrix		**Precipitate**	
Parameter	Value	Parameter	Value
E_A	68 GPa	E	107 GPa
E_M	43 GPa	v	0.3
$v^A = v^M$	0.33		
H^{max}	0.055		
$k[MPa^{-1}]$	0.0206		
C_A	6.4 MPa/K		
C_M	21.7 MPa/K		
$n_1 = n... = n_4$	1		
M_s^0, M_f^0, A_s^0, A_f^0	280 K,266 K,290 K,307 K		

is initially in the austenite state (at T =350 K) and transforms to martensite while cooling to 220 K. With heating to 350 K, the material transforms back to its initial austenite configuration. Because of the constant stress 200 MPa, the RVE produces considerable transformation strain in the direction of applied loading. Through this thermo-mechanical loading path, the actuation behavior of the precipitated SMA at $\Sigma_{zz} = 200$ MPa is simulated in the RVE. More details of the actuation response and loading path can be read in Chapter 1.

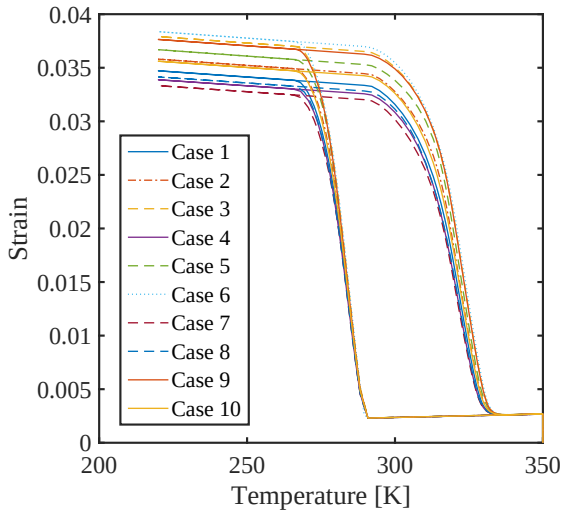

Figure 5.2: The actuation response from different RVE realizations for VF $= 20\%$ and fixed RVE size P $= 15$.

The developed micromechanical model and the FFT homogenization framework were used to generate data for training the machine learning model. Actuation responses were solved for volume fraction (VF) 7%, 10%, 15% and 20% of precipitates using RVEs of varying number of precipitates P $= (3, 6, 9, 12, 15, 30)$. For each RVE case, 10 RVE realizations were solved. In total, 240 RVEs and their effective responses were obtained and used for building the data based model.

For fixed VF, the different RVE realizations created slightly different microstructures due to the differences in particle position and alignment. Figure 5.2 shows the different responses from different realizations for a fixed volume fraction (VF $= 20$ %) and number of particles (P $= 15$). The different responses in the RVE realizations were captured from their microstructure differences. Increasing the number of RVE realizations solved helps the data based ML model to better differentiate between the microstructure variations in the RVEs.

5.3 ML model for SMA responses

The objective in the current data based ML model is to build a microstructure-response linkage for predicting effective heterogeneous responses. Since the shape memory alloy behavior is

nonlinear and has complex hysteresis behavior, the ML model should capture the evolution of the whole response with changes in the microstructure. In the current ML framework, the focus is only on building a microstructure-response linkage. Other factors such as changing material properties and loading conditions are not considered in the current modeling. Hence, the training responses for the model do not include changing material properties and changing boundary condition cases.

The ML model should be built on key features extracted from the RVEs which can differentiate their microstructures. Because considering the full spatial information in the whole RVE is not an efficient method to build a data based model, two-point correlation technique is used to extract only the key statistics from the RVEs. Another advantages in using 2-point correlation representation is that it can account for periodicity of particles in the RVEs in the present work. First, the 2-point correlations of the RVEs were obtained, which are matrices of the same size as the RVEs containing statistical information and must be truncated. To extract only the key features out of the 2-point representation, Principal Component Analysis (PCA) was performed and the dimensionality of the representation were reduced. After the PCA on the RVEs, each RVE can be represented with a vector containing the most important features differentiating the RVEs. As the Principal Components (PCs) in the PCA are obtained in order of decreasing relevance, the representation in the PCs can be truncated to a smaller size in the order of relevance. In the present study, the 2-point correlations were calculated using 'PyMKS' in Python [65]. In the following sections, a basic introduction to 2-point statistics and PCA is presented.

5.3.1 2-point statistics of microstructures

The microstructures can be described using the spatial statistical technique of 2-point correlations. A microstructure function is given by $m(\boldsymbol{x}, n)$, which denotes the probability of local state n at position $\boldsymbol{x}$. Assuming that the microstructure information is represented by a regular grid in the 3-D space, where each grid is enumerated by 's,' representing a position in the gird. Then the microstructure function can be represented as: m_s^n, where n represents material state and s denotes

position. Since m_s^n represents probability, the following constraint is expected:

$$\sum_{n=1}^{N} m_s^n = 1, \quad m_s^n \geq 0. \tag{5.1}$$

The 1-point statistics for the discretized microstructure is given as:

$$f^n = \frac{1}{S} \sum_{s=0}^{S-1} m_s^n. \tag{5.2}$$

Following similar logic, the discretized 2-point statistics for the microstructure are given as:

$$f_t^{nn'} = \frac{1}{S} \sum_{s=0}^{S-1} m_s^n m_{s+t}^{n'}, \tag{5.3}$$

where the superscripts n and n' represent local states, t enumerates the vectors that can be placed in the discretized microstructure and $s + t$ denotes the grid point that is reached by adding the vector corresponding to t to the grid point s. The book by Kalidindi *et al.* [62] provides more details on 2-point statistical representation. In the current work, the 'PyMKS' toolbox in Python developed from Georgia Tech [65] is used to calculate the 2-point statistics of the RVEs. Figure 5.3 shows an example RVE and cross-section of corresponding 2-point statistics.

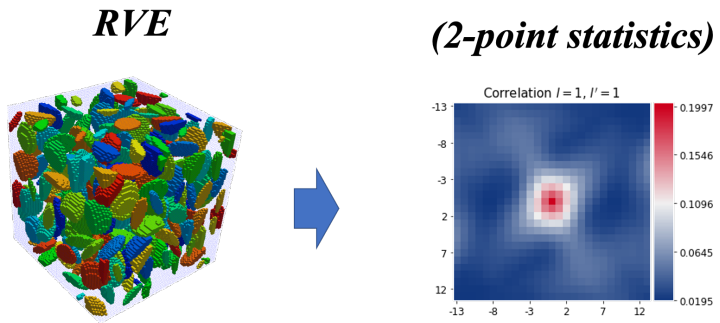

Figure 5.3: RVE and cross-section of corresponding 2-point statistics representation.

5.3.2 Principal component analysis for RVEs

In principal component analysis (PCA), we perform a linear, distance preserving transformation of the data from its original reference frame to a new orthogonal reference. The axes of the new reference are chosen along the directions of the maximum variance between the data points. This is schematically depicted in figure 5.4 in a two-dimensional (2-D) illustration. The axes for the data are chosen such that they capture the variance within the data in the order of decreasing relevance. The representation of the data in the new axes are captured in the principal components (PCs). So if only the first PC in the PCA is kept, it can still retain the variance within the data that can be captured using one variable. More on the PCA can be found in the references [142, 143, 144]

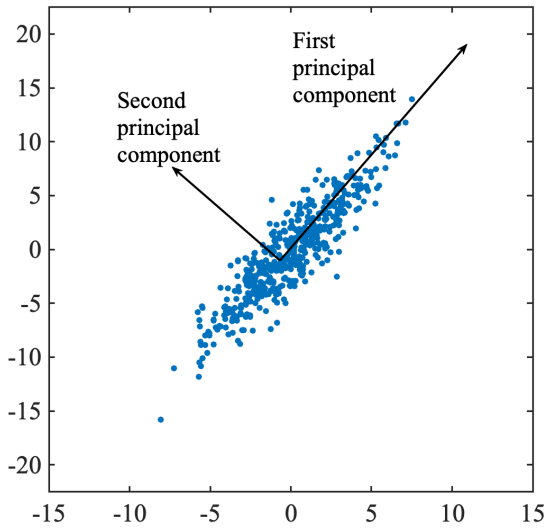

Figure 5.4: Schematic of principal component analysis in 2-D. The two axes show the first and second principal components.

PCA is very useful for building low-dimensional models for microstructure-property relations [62]. The advantage of PCA for the current model is that it reduces the high dimensional 2-

point correlation representations of the RVEs into low dimensional vectors, with PCs capturing the variance between the RVEs. Figure 5.5 shows the representation of the 240 RVEs studied here in their first three PCs. Using the three PCs, the differences between the RVEs are represented in 3-D. The VF $= 7\%$ RVEs are closer to each other, indicating less difference between the realizations. In the higher volume fraction RVEs (VF $= 20\%$) the scatter of points is higher, indicating larger difference between the realizations. This is expected since at higher volume fraction, the changing particle orientation can modify the microstructure more.

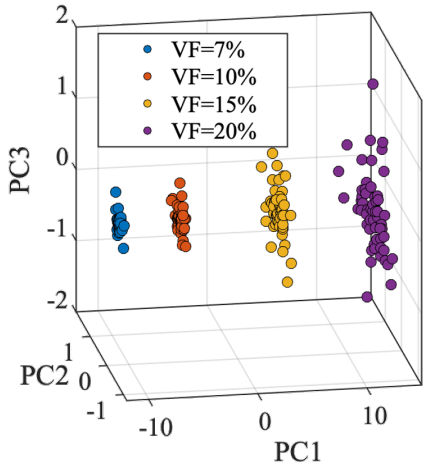

Figure 5.5: First 3 PCs of the 240 RVEs considered in the framework.

5.3.3 Steps in the Machine learning model

A data based machine learning model to capture microstructure-response linkage is presented. Figure 6.3 summarizes the steps involved in the process. Each of these steps is described in detail below.

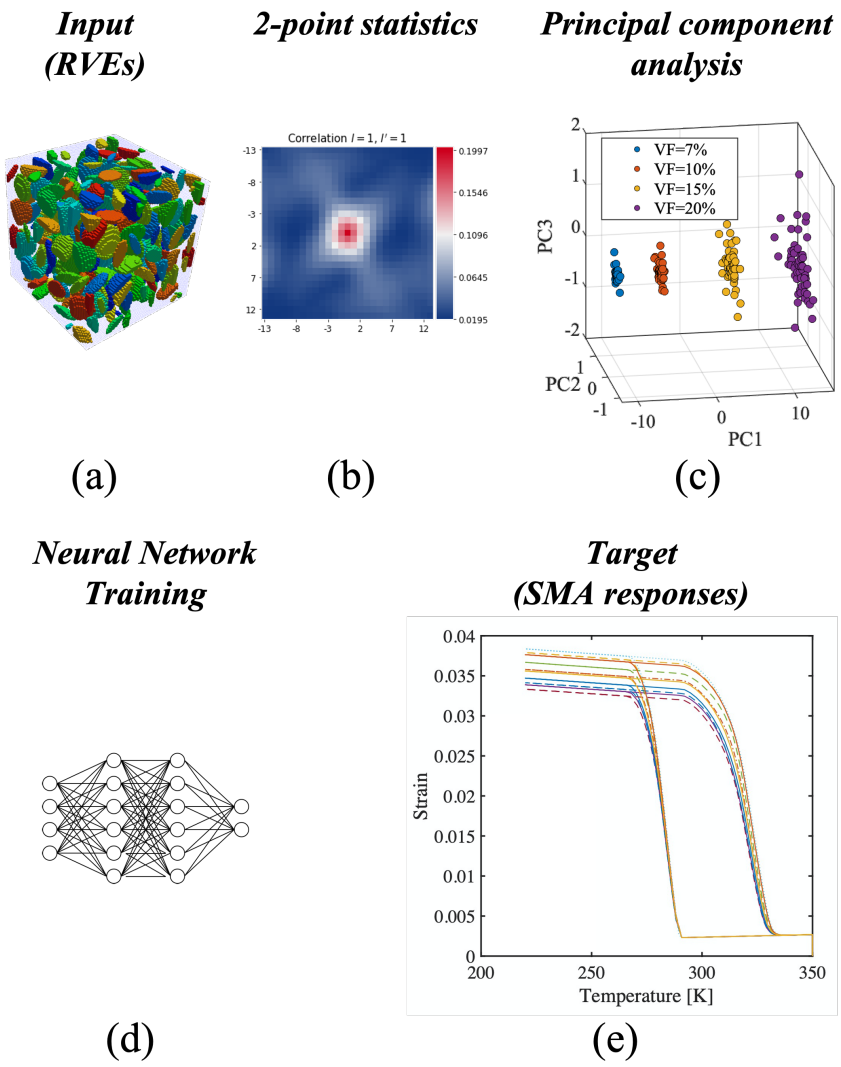

Figure 5.6: ML framework for predicting the SMA response contains (a) Considering all RVEs (b) 2-point correlations of the RVEs (c) principal component analysis on the RVEs (d) neural network model to capture the response and (e) target response for training.

1. First, the RVEs of different size and volume fraction are represented using 2-point statistics. An RVE is shown in figure 6.3(a) and the corresponding 2-point statistics representation in 6.3(b).

2. Next, the 2-point correlation representations are trimmed into the same data size. Larger RVEs, meaning those with higher number of particles, will have larger sized representation. The different sized RVEs are trimmed to $11 \times 11 \times 11$ size around the center region of the 3D 2-point correlation representation. This way they all maintain the same information from all RVEs of different size [60]. The size for trimming is chosen from the lowest sized RVE.

3. PCA is performed on the trimmed representations to find the Principal Components (PCs) of the RVEs. Each RVE is represented as a vector with the first 10 PCs from the PCA and used as input in the ML model.

4. The neural network is trained using material response as the target. The PCs and the material parameters are the input for training. The effective responses from the RVEs is the target for training.

The developed ML framework can be used to capture elastic response at the end of loading and the full actuation response. In the case of modeling the elastic response, the ML model is built to predict a single value corresponding to the elastic strain value. In the model of the whole actuation response, the suggested approach is to use a recurring neural network that can predict the successive strain values with the temperature loading path. The next sections present details on the these modeling approaches.

5.3.4 Modeling elastic response

The strain at the end of loading in the actuation response can be predicted using an ML model. The elastic strain values are correlated with the corresponding RVE microstructure. With only a single value modeled for changing microstructure, the main capabilities of the ML model can be analyzed. The obtained model will be used as the initial condition in the modeling of full actuation

response.

For modeling the elastic strain, the parameters describing the microstructure are sufficient for the input. This is because the material properties and loading conditions are the same for the RVE simulations compared. The ML model for elastic strain can be summarized in the equation (5.4). Here, the input parameters taken in the ML model $\hat{F}$ are the principal components of the RVEs. The target value from the ML model is the loading strain.

$$E_{zz} = \hat{F}\,[parameters] \tag{5.4}$$

A neural network model with three layers [10,4,2] is used for the ML model. The three layer model was chosen so that it can capture the complexity of microstructural variations sufficiently. The summary of input and target for the ML model is summarized in Table 5.2. The model was trained once and predictions were made.

Table 5.2: Input and output in the ML model for simulating the elastic loading step.

Parameter	Description
Input	
PC_{1-10}	First 10 PCs from PCA of RVEs
Target	
E_{zz}	Elastic Strain at the end of loading step

5.3.5 Modeling actuation response

An ML model was developed to capture the microstructure-response linkage for the actuation response. Since these responses are complex behaviors with hysteresis in the heating and cooling cycling, the ML model was modified significantly compared to the elastic ML model. A recurring ML model that can predict the strain in sequence of thermal step should be suitable for capturing the full response. The ML model for actuation response can be represented using the equation (5.5), where the effective strain $E_{zz}(T + \Delta T)$ at temperature $(T + \Delta T)$ is related to the effective strain

$E_{zz}(T)$, temperature change ΔT along with other material parameters and RVE inputs. Table 6.1 shows the detailed description of input parameters and target parameter in the ML model. The output from the loading strain model is the initial condition for the recurring ML model for actuation response.

$$E_{zz}(T + \Delta T) = \hat{F}\left[parameters, E_{zz}(T), \Delta T\right] \tag{5.5}$$

Table 5.3: Input and output for the ML model for simulating the full response.

Parameter	Description
Input	
PC_{1-10}	First 10 PCs from PCA of RVEs
$M_f^\sigma - T$	Difference of TTs and current temperature
$M_s^\sigma - T$	
$A_s^\sigma - T$	
$A_f^\sigma - T$	
$H(\sigma)$	Maximum transformation strain at stress σ
α_A	Thermal expansion coefficient at austenite phase
α_M	Thermal expansion coefficient at martensite phase
$T - T_0$	Difference of current temperature and starting temperature
$E_{zz}(T)$	Strain value at T
ΔT	Temperature change
Target	
$E_{zz}(T + \Delta T)$	Strain value at $T + \Delta T$

In the ML model for actuation response, transformation temperatures, temperature change and thermal coefficients are included in the input. The transformation temperatures are taken as input for defining the transformation range. The sign of the temperature change differentiates between heating and cooling, so the positive temperature change indicates heating and negative change indicates cooling.

A three layer neural network [16, 10, 5] was used to capture the strain evolution. The coefficients in the neural network were obtained through training with the RVE simulation responses. Multiple training using the same data was performed to capture the uncertainties in the training of

neural networks. The average response, along with the Confidence Intervals (CIs) compared with target RVE responses, can validate the performance of the model.

The actuation response may be modeled using different configurations of inputs and format, and these changes may improve the abilities of the ML model. With the current work, few capabilities of the machine learning approach relevant for the micromechanical modeling of materials are demonstrated. Examples of other ML configurations that can be used are presented in the other chapters of this thesis, where the different configurations bring different predictive capabilities. In Chapter 6, the ML model configuration used enables the prediction of partial cycle responses. Further, in Chapter 7, the different configuration helped with capturing anisotropy in single crystal SMA responses.

5.3.6 Training of ML models

The training data of the ML models were selected to demonstrate two capabilities in the current ML model. These are: 1) the ability to predict higher RVE responses from lower RVE responses, and 2) the ability to predict new microstructure response from available microstructure responses. To demonstrate the first ability, the ML models were trained using lower RVE sizes (P $= 3, 6, 9, 12, 15$) and responses in higher sized RVEs (P $= 30$) were predicted. For the second ability, the training was performed using responses from RVEs of the volume fractions (VF $= 7, 15, 20\%$) and the new volume fraction (VF $= 10\%$) responses were predicted. More on these predictions is presented in section 5.4, Results and discussion.

5.4 Results and discussion

The predictive capability of the ML framework was demonstrated in (a) the ML model for elastic behavior and (b) the ML model for full actuation response. The training of the models was performed for two different set of data, discussed in section 5.3.6. With the two comparison scenarios, the ability of the model to predict higher sized RVE responses and new volume fraction RVE responses was demonstrated. First the prediction capability of elastic ML model is discussed and further the predictive performance for full actuation response is discussed.

5.4.1 Elastic response prediction

The elastic strain values at the end of loading were simulated using the data based ML model discussed in section 5.3.4. Figure 5.7 shows the machine learning model predictions for RVE size of P $= 30$, using the responses from RVE sizes with lower number of particles P $= (3, 6, 9, 12, 15)$. Figure 5.7 (a) shows the comparison of the predictions to the actual data. Here, the cases used for training and cases predicted are compared with the target values. The ML model output in both training and prediction sets lie close to the target values marked by the dotted line.

The predictions for RVE size P $= 30$ (marked by red dots) show less dispersion compared to the training set of lower RVE sizes. This was expected since the higher sized RVEs are more representative, produce less dispersion between the predictions. A detailed discussion of this aspect can be found in Chapter 4. The ML model is able to predict this decreasing dispersion behavior, which indicates an ability to differentiate between larger RVEs and smaller RVEs. A zoomed in comparison considering VF $= 20\%$ is shown in Figure 5.7 (b), where this observation can be seen in detail.

Further, the variation of R^2 with the RVE size (P) is shown in Figure 5.7(c), where the extent of dispersion from ML prediction as function of P is seen. A gradual increase of R^2 value with RVE size (P) shows the convergence of responses with increasing P. More interestingly, the prediction RVEs with the largest size (P $= 30$) have the highest R^2 value, indicating their higher convergence of responses with larger RVE size. These comparisons demonstrate the ability of the ML model to make predictions for higher sized RVEs using the computationally less costly lower sized RVE simulations.

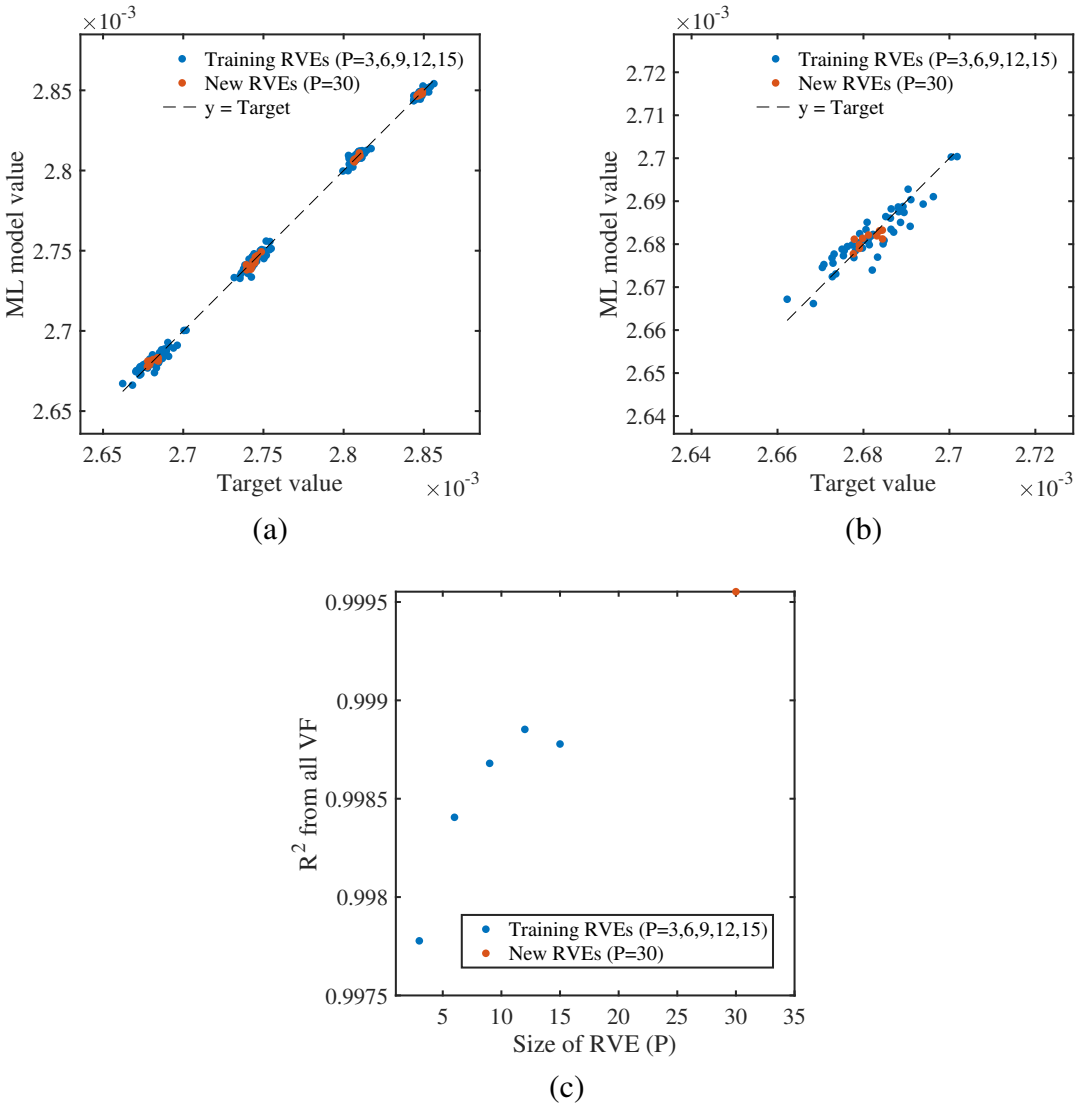

Figure 5.7: Elastic strain prediction for new RVE size of P $= 30$ using lower RVE sized simulations (P $= 3, 6, 9, 12, 15$). (a) Comparison of ML prediction values to target values for training set and new RVEs. (b) Comparison for prediction to target zoomed in for VF $= 20\%$. (c) Variation of R^2 for prediction to real values compared with RVE size (P)

The second capability of the ML model is to predict the responses for new microstructures with different volume fractions. In Figure 5.8, the ML model is trained using the responses from RVEs of three volume fractions (VF $= 7, 15, 20\%$), and responses in new volume fraction RVEs (VF $= 10\%$) are predicted. Figure 5.8(a) shows the comparison of strain values predicted by the ML model in comparison with the target values. The ML model predicts values close to the target value (represented by the dotted line) for both the training set and new RVEs. This demonstrates the ability of the current ML model to interpolate the behavior for the intermediate microstructure using the responses from other RVEs.

The zoomed in view of the comparison for the new RVEs for VF (VF = 10%) is shown in Figure 5.8(b), where the dispersion of the values from the target is seen. Although the RVEs compared here are for the same VF, there is considerable variation in the target behavior due to the microstructure differences in the RVE realizations. This is mainly due to the smaller RVEs that are not converged in terms of microstructure representation. The ML model captures this RVE realization variation to some extent, with scattered values around the target line. The R^2 values taking individual volume fraction separately (shown in Figure 5.8(c)) show that both training and the new cases (VF $= 10\%$) show moderate values. This demonstrates that the ML model captures the variation between realizations in the same microstructure with only moderate accuracy. Nevertheless, the tool proves to be very useful as it can make reasonable predictions of behaviors for any new RVE.

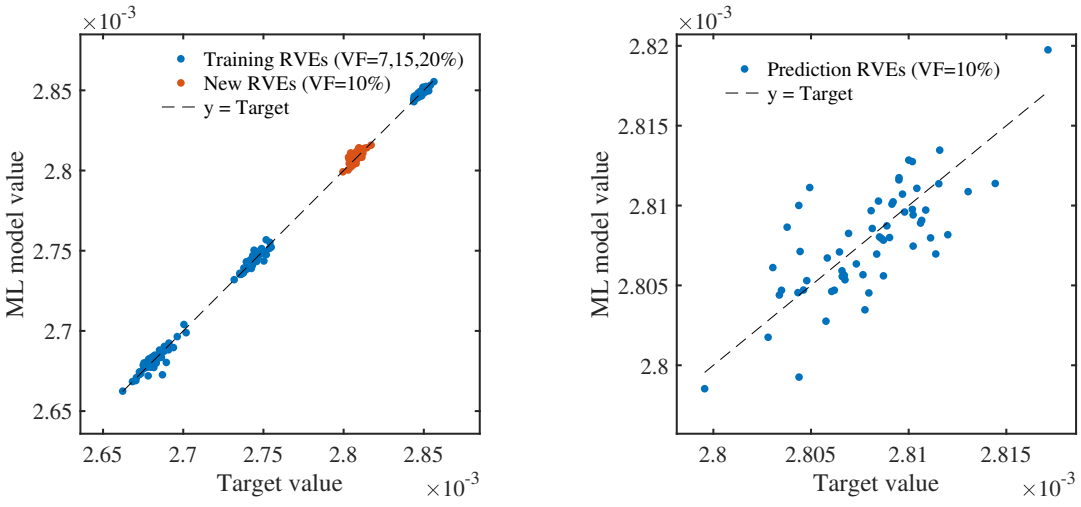

(a)

(b)

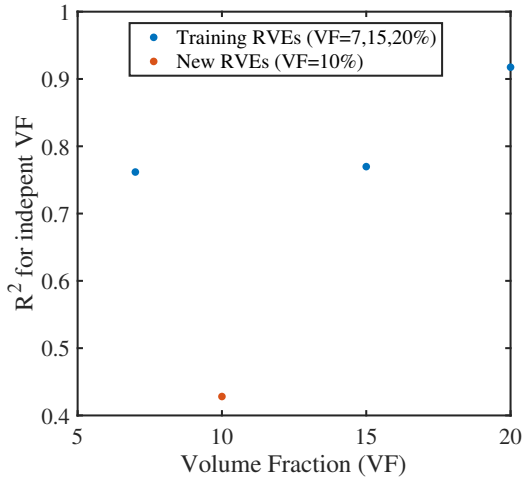

(c)

Figure 5.8: Elastic strain prediction for new VF $= 10\%$ using other VF simulations ($= 7, 15, 20\%$). (a) Comparison of ML prediction values to target values for training set and new VF. (b) Comparison for prediction to target zoomed in for VF $= 10\%$. (c) Variation of R^2 for prediction to real values compared with VF.

5.4.2 Actuation response predictions

The capabilities of the ML framework for modeling simple elastic responses were demonstrated. Next, for complex SMA actuation responses, the ability of the actuation ML model (described in section 5.3.5) to make predictions for higher RVE sizes and different microstructures was tested.

The ML model was used to predict the actuation responses for higher RVE size (P $= 30$) using the lower RVE size (P $= 3, 6, 9, 12, 15$) responses. Figure 5.9 compares the prediction of the ML model to actual response in four random RVEs with size (P $= 30$) taken from different volume fractions (VF $= 7, 10, 15, 20\%$). With each training of the ML model, different coefficients were obtained for the neural network. This is reflected as slightly different predictions for the target response. The Confidence Interval (CI) region indicates the scatter in the predicted responses from different training sessions. The average response from the ML model, which can be assumed to be the most accurate prediction, matches very closely with the target response.

The performance of the ML model for all RVEs was carried out by comparing the maximum strain in the full response. As the maximum strain is where the predictions may have the highest error, their comparison successfully reflects the accuracy of the overall response prediction. Since the maximum strain is only one value, it can be used to make a performance study similar to that carried out for the elastic ML model.

Figure 5.10 compares the maximum strain in the ML model predictions to the target values for all RVEs. The results are similar in comparison to the one obtained in the elastic ML model analysis. The training RVEs and new RVEs give close predictions to the target values shown with the dotted line. Also, the different RVE realizations for P $= 30$ give less dispersion in Figure 5.10 (a) and (b). The predictions for P $= 30$ lie around the center of the scattered training RVE values. A similar effect is apparent in the comparison of R^2 versus P variation shown in Figure 5.10 (c). This is because of the better statistical convergence of P $= 30$ compared to the lower sized RVEs used for training. The ML framework successfully predicts this higher convergence of the P $= 30$ RVEs even though it was trained using lower sized RVEs.

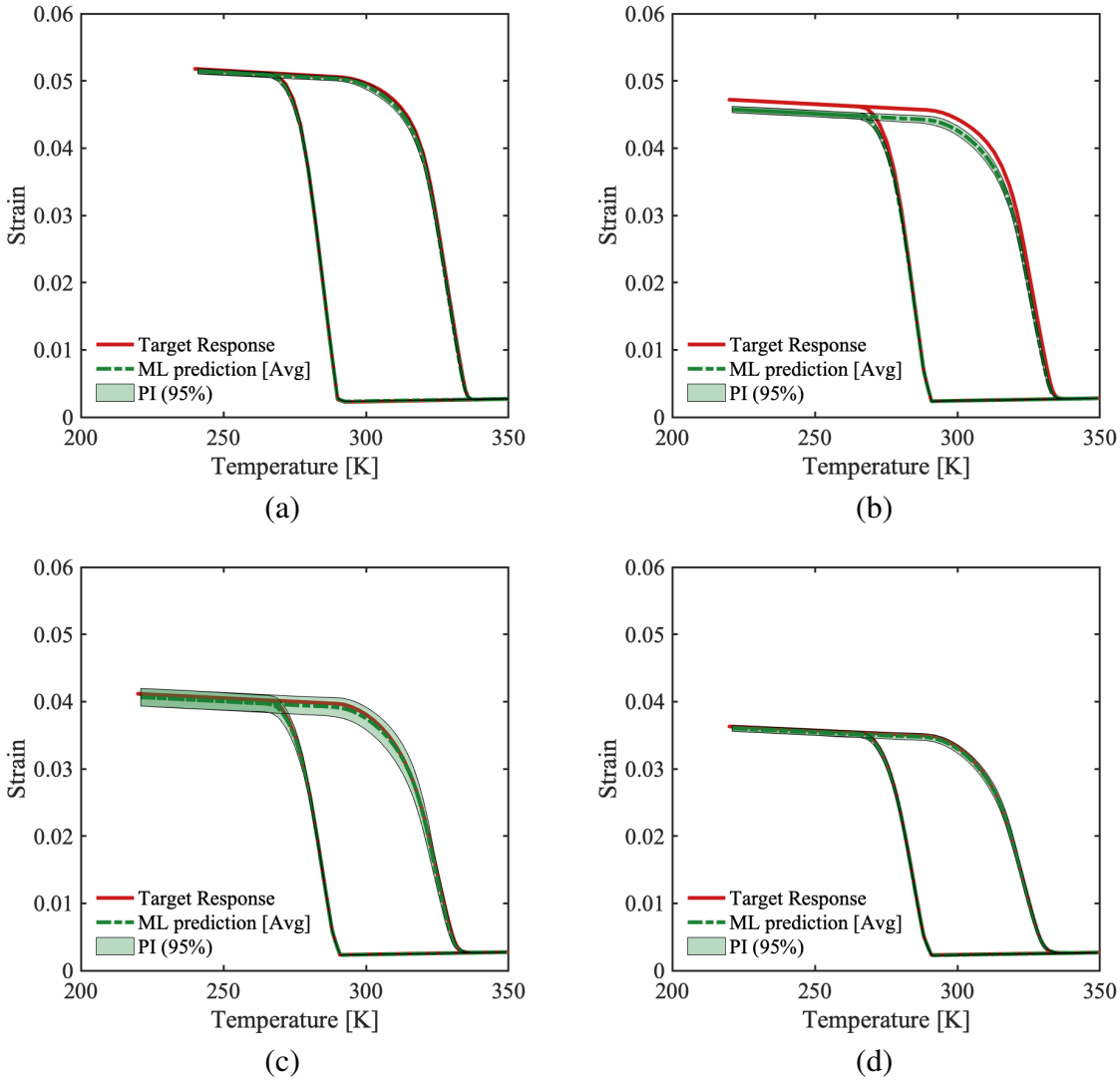

Figure 5.9: SMA full strain response prediction for new RVE size P $= 30$ using lower RVE sized simulations (P $= 3, 6, 9, 12, 15$).The target response, ensemble average and confidence of prediction are compared in a random realization for (a) VF $= 7\%$, (b) VF $= 10\%$, (c) VF $= 15\%$ and (c) VF $= 20\%$.

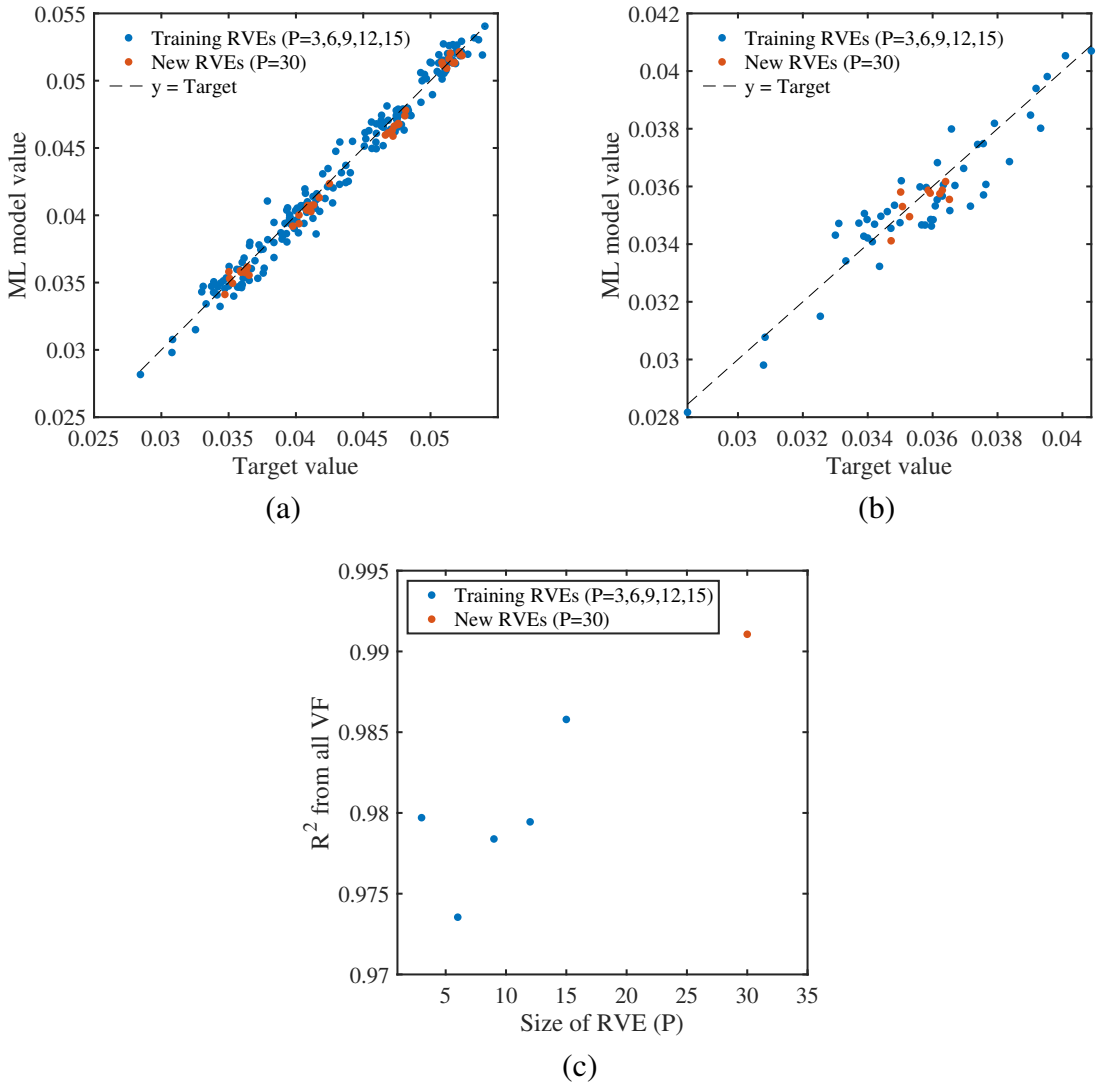

Figure 5.10: Maximum strain values (end of cooling) extracted from the full responses' prediction. (a) Comparison of ML prediction values to target values for training set (P $= 3, 6, 9, 12, 15$) and new RVEs (P $= 30$). (b) Comparison for prediction to target zoomed in for VF $= 20\%$. (c) Variation of R^2 for prediction to real values compared with RVE size (P)

The ability of the ML model to make predictions for new microstructures was tested in the SMA responses. For this, the ML model was trained using RVE responses of VF $= (7, 15, 20)\%$ and the response of VF $= 10\%$ was predicted. Figure 5.11 shows the comparison of full response predictions to the actual response in four different RVE sizes for random realizations. As indicated earlier, the confidence interval in these cases was generated from multiple trainings of the ML model. The average response in these predictions is in good agreement with the target response.

Similar to the study in the previous training, an analysis using the maximum strain from all RVEs was performed. Figure 5.12 show comparisons for maximum strain, analyzing the predictive capability of the ML model. The ML model predicts strain values in multiple realizations close to the target line, as seen in Figure 5.12 (a). The R^2 values for different VF, calculated separately, is compared against VF. The training set and prediction set have moderate values of R^2 (> 0.4). This shows that the current ML framework captures the differences between different RVE realizations with only moderate accuracy. This limitation may be improved by increasing training data with more microstructures or by improving the ML model with increased number of PCs to better differentiate between the RVEs. Nevertheless, the current model proves to give satisfactory estimation for new microstructures and to differentiate between realizations.

Figure 5.13 show the predictions in the new VF ($= 10\%$) compared with the responses in the training VF (7%, 15% and 20%) RVEs. In each VF, a particular RVE response is chosen for comparing. The solid line shows the target response from the simulations, and the CI region is obtained from predictions from a 10 training iteration of the ML model. Clearly, target responses are within the 95% interval predicted using the ML model. The predictions for (VF = 7, 15, 20%) shows the effectiveness of the ML model training to reproduce the training RVE case. Good prediction for the untrained microstructures (10%) shows very promising scope for machine learning in SMA micromechanics.

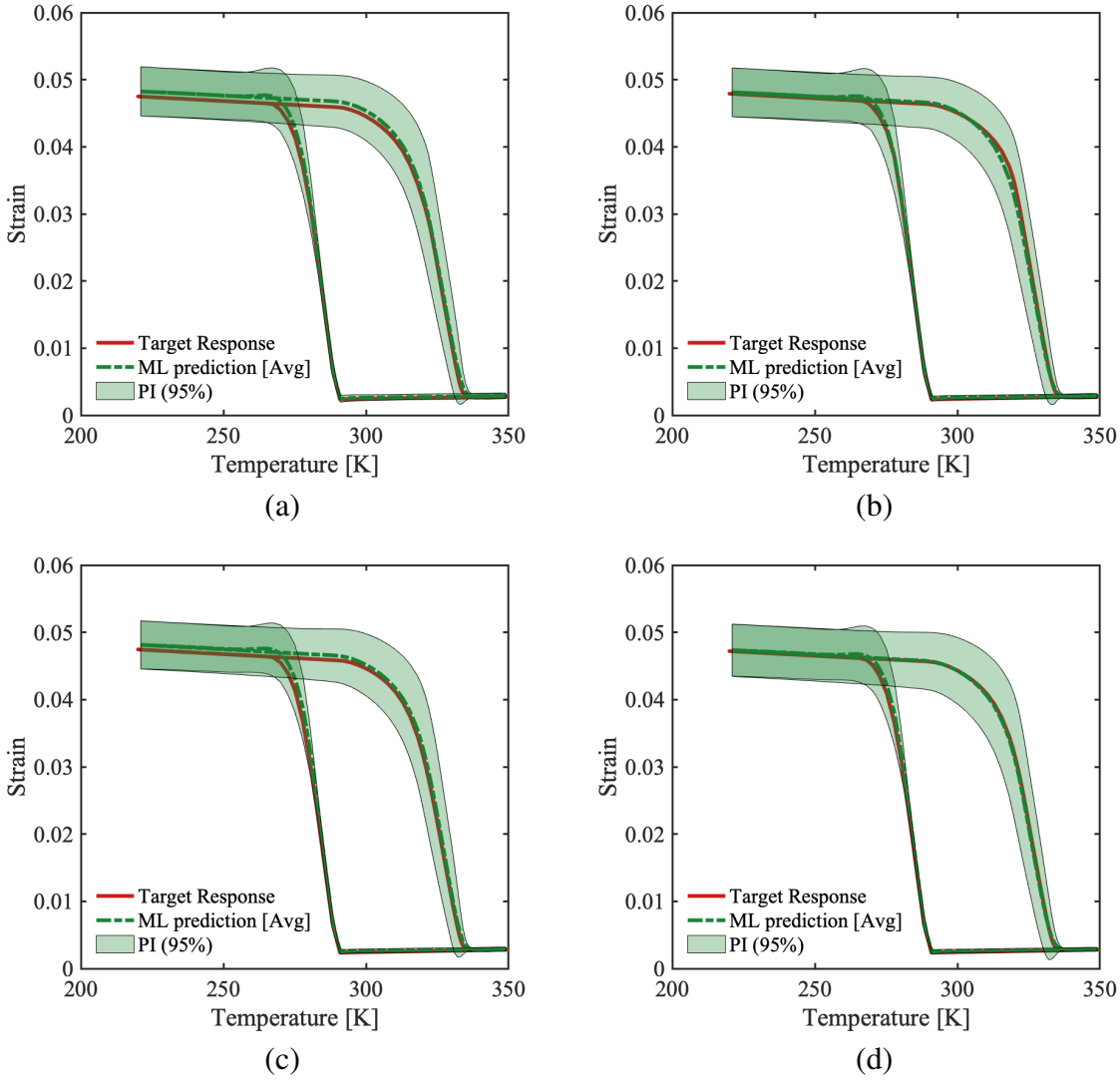

Figure 5.11: SMA full strain response prediction for new VF $= 10\%$ using other VF simulations (VF $= 7, 15, 20\%$).The target response, ensemble average and confidence of prediction are compared in a random realization for RVE sizes (a) P $= 3$, (b) P $= 6$, (c) P $= 15$ and (d) P $= 30$.

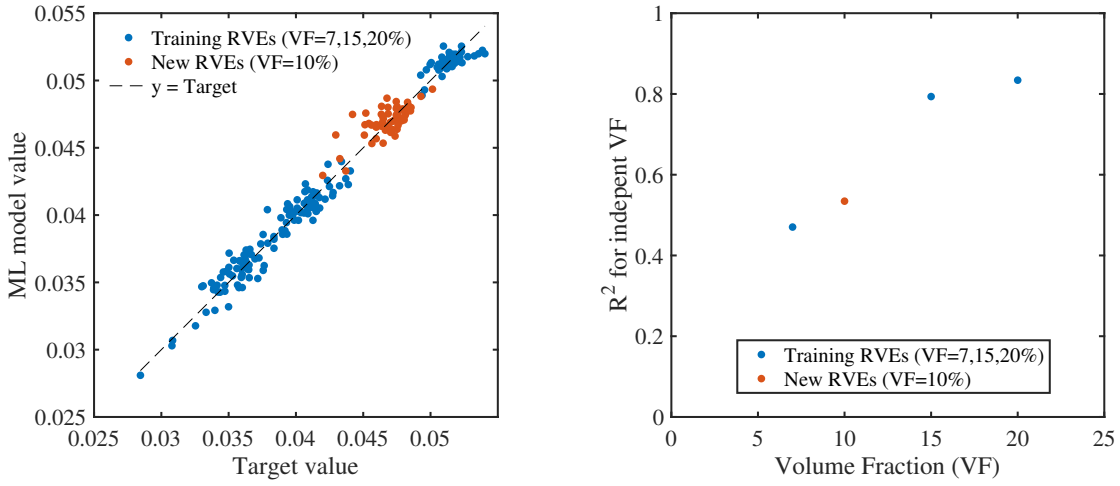

Figure 5.12: Maximum strain values (end of cooling) extracted from the full responses' prediction. (a) Comparison of ML prediction values to target values for training set (VF $= 7, 15, 20\%$) and new RVEs (VF $= 10\%$). (b) Variation of R^2 for prediction to real values compared with VF.

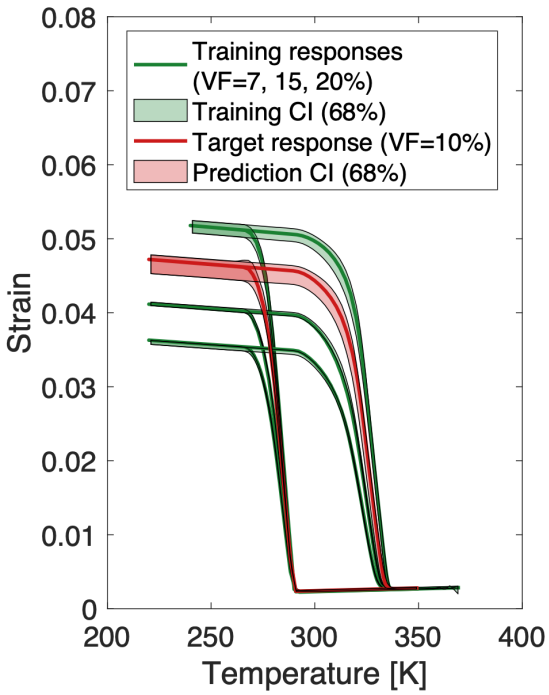

Figure 5.13: Results showing predictions using ML model for a particular RVE from (VF 7%, 10%, 15%, 20%) realizations. (VF = 7%, 15%, 20%) RVE cases were used for training and a VF 10% RVE case is predicted.

5.5 Conclusions

A machine learning (ML) model which can predict precipitation hardened behavior from RVEs in SMAs is presented. The ML model is trained using SMA thermo-mechanical responses from many RVEs of different volume fraction and number of precipitates. The RVEs are represented through 2-point correlation, and applying Principal Component Analysis (PCA) reduction to low dimensional representations is used as input in the ML model. The ML model is developed with Principal Components (PCs) of the RVEs and material parameters as input and the effective response from the micromechanical model as target. A neural network based model is used to predict the strain response of the SMA. The model was demonstrated to have two capabilities: 1) it predicted the response of larger RVEs trained using the simulations of smaller RVEs, and 2) it predicted the responses of new volume fraction RVEs trained using responses from different volume fraction RVEs. The predictions in both of these scenarios matched well with the target response, with good Confidence Interval (CI). The study shows promising scope for data based machine learning tool in SMA micromechanics.

6. MACHINE LEARNING MODEL FOR PREDICTING SHAPE MEMORY ALLOY ACTUATION RESPONSE

6.1 Introduction

Shape Memory Alloys (SMAs) are a special class of metals with many applications due to their ability to recover from high strains through solid-solid phase transformation between austenite and martensite phases. In the austenite phase, the lattice is cubic with a high symmetry structure and is stable at high temperatures, while in the martensite phase, which is stable at lower temperatures, both the twinned state (higher symmetry) and detwinned state (lower symmetry) can be present. The phase transformation between austenite and martensite phases can be induced by applying mechanical, thermal or combined thermo-mechanical loads [8] on the material. The transformation between austenite and detwinned martensite results in the generation/recovery of recoverable inelastic strain, called transformation strain. When the material is constrained, the recovery of the transformations strain can generate high forces, which allows SMA to produce higher work output compared to other active materials, and making it effective for use as compact, lightweight, solid-state actuators [9, 10]. Because of its unique properties, SMA is used in varying applications in fields such as biomedical, aerospace, industrial and wind energy [19, 20, 21, 22, 23, 11, 12, 13, 14, 15].

SMAs can exhibit complex behaviors based on the thermo-mechanical loading path the material undergoes [8]. A Shape Memory Effect (SME) is observed when the SMA in the twinned martensitic phase is deformed, unloaded and then heated above austenite finish temperature to recover its original shape by transforming back into its parent austenitic phase. Pseudoelastic behavior in SMAs is observed with stress-induced transformation at high temperatures where austenite is stable, and upon unloading the transformation strain is recovered. An actuation response is produced when SMAs are taken through cyclic cooling and heating between austenite and martensite phases while loaded under stress. Modeling the actuation response under constant stress responses

is important in the designing of SMA based actuators, in order to predict the extent of actuation displacement. For the current study, the focus is on modeling of actuation responses in NiTiHf SMAs.

SMA actuation response includes both partial transformation and full transformation behaviors based on the temperature range of cycling [15]. A complete transformation is obtained when the material is cooled below martensitic finish temperature or heated above austenitic finish temperature in the forward and reverse phase transformation, respectively. Heating or cooling beyond these finish temperatures ensure there is enough thermal driving force to complete transformation. Where complete transformation occurs through heating and cooling, it is referred to as a major cycle actuation response, while where heating and cooling are not sufficient, the resulting partial transformation is referred to as a minor cycle actuation response. Minor cyclic responses are of considerable relevance in the case of aerospace, wind turbine and controls applications where the SMA actuator can undergo partial phase transformation response.

In designing SMA actuators and developing control algorithms, faster and more accurate modeling of SMA behavior incorporating partial phase transformation is required [15]. There has been efforts in the area of phenomenological modeling of SMA actuation behaviors. The constitutive model developed by Lagoudas *et al.* [38] has successfully captured with good accuracy the major cyclic responses in the SMA polycrystals. Other modeling attempts referenced in the works in [66, 67, 68, 37] have also modeled the minor cycle responses in SMAs. The physics based models are successful in creating better understanding of the material behavior, whereas they cannot be determinate because of the limitations in a complete understanding of the material behavior and the assumptions imposed in the modeling, which can make their predictions less accurate.

With the use of data driven machine learning models such as neural networks, faster and more accurate models which can train directly from the experimental responses can be developed. Neural networks are capable of modeling complex variations and make faster predictions with less computational cost. Moreover, they can capture the hidden features specific to the experimental data, which may not be fully captured in phenomenological modeling. The downside of depending

on data driven techniques is that they may not give new understanding, and as these models are data specific, their broader application is limited. Neural network based modeling has been successfully implemented in medical, material science, agriculture and finance fields to make predictions in real-time scenarios [69]. More related applications in material modeling include modeling Young's modulus [70] and strain responses [71]. But for SMA responses, there have been few works using neural network based model for modeling SMA cyclic responses [72] and SMA wire actuation [73].

In the current work, neural network based modeling was implemented to predict the actuation transformation responses of a NiTiHf material. A neural network model was trained on the major cycle responses of the material at different stress levels. Predictions were made for major cycle responses at new stress levels and minor cycle responses in new temperature ranges. Comparisons showed that the presented approach captured major cycle responses and minor cycle responses that are close to the experimental cases that were available. Many complex minor cyclic responses were modeled for new loading paths using the trained neural network model. Although the predictions for these new paths appear to have a reasonable basis, the accuracy of the predictions was not verified as experimental data for behaviors was not available. To the best of the author's knowledge, this is the first attempt to use data based modeling to capture the partial transformation cycling in SMAs.

The chapter is structured as follows. In section 6.2, a brief theory on SMA actuation behavior explaining the major and minor cycle responses is presented. In section 6.3, the experimental responses of the studied NiTiHf SMA with key observations are presented. In section 6.4, a summary of the data based model used in the study is presented. In section 6.5, the discussion of predictions using the developed model is presented. In section 6.6, the key conclusions from the works are presented.

6.2 SMA actuation behavior

The cyclic heating and cooling of SMA in the phase transformation range produces actuation response in the SMAs. Depending on the extent of heating and cooling applied, the SMA can

undergo full transformation and partial transformation. If the heating and cooling is sufficient to produce full phase transformation in both directions, the response produced is a major cycle response. Actuation responses with partial transformation produces minor cycle responses. In the following discussion, the minor cycle behavior is explained in the context of actuation response. Details about major cycle behavior can be read in section 1.1.1 of the Introduction.

6.2.1 Minor cycle actuation response in SMAs

Minor cycle actuation response is resulted from partial phase transformation due to incomplete heating or cooling. Referring to the loading path in Figure 1.1 (b) (see section 1.1.1), the end state of heating ('A'), cooling ('B') or both will lie between the start and finish of transformation, resulting in partially transformed end states. Figure 6.1 summarizes representative minor cycle responses with respect to major cycle responses. In Figure 6.1 (a), the upper response represents the case where only the end of heating ('A_U') is within a partial transformation (between A_s^σ and A_f^σ). The lower response represents the case where only the end of cooling ('B_L') is within the partial transformation (between M_s^σ and M_f^σ). The case where both 'A' and 'B' are within the partial transformation range is shown in Figure 6.1 (b). Here the whole response is contained within the major cycle response.

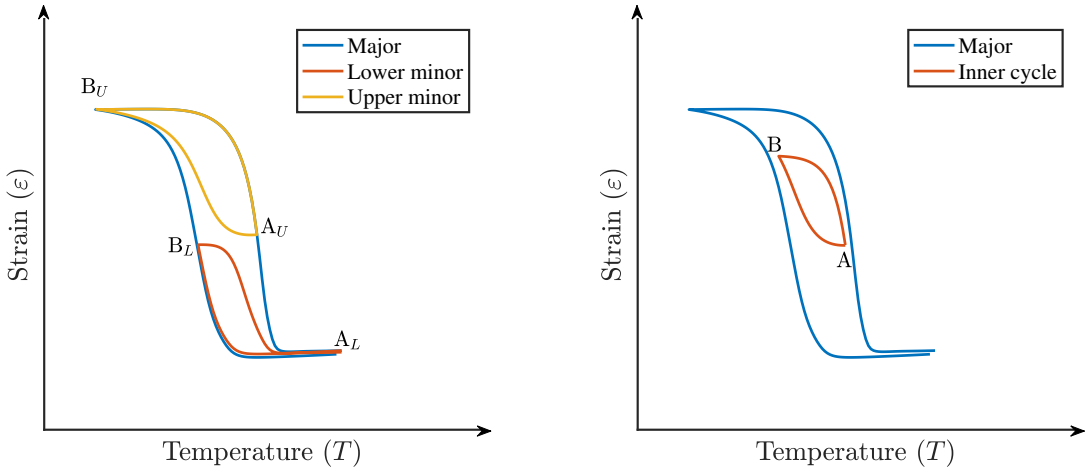

Figure 6.1: Schematic of minor cycle responses showing (a) major cycle, upper minor cycle and lower minor cycles, and (b) inner minor cycle.

6.3 Experimental investigation

To train and validate the machine learning model, a complete material characterization test series along with additional test cases was considered for a HTSMA material. Dog-bone shaped specimens were cut from a $Ni_{50.3}Ti_{29.7}Hf_{20}$ sheet using Electric Discharge Machining (EDM). Thermal cycles were applied to the material to induce complete phase transformation under various constant stress levels. The experiments were conducted using an MTS Insight testing machine equipped with an MTS load cell with 30 kN load capacity. The strain measurements were carried out using a high temperature Epsilon extensometer of 1-inch gauge length attached to the specimen. The temperature measurements were made using two K type thermocouples attached to the specimen. The specimen along with the grips were enclosed inside an insulated Thermcraft thermal chamber. The heating of the specimen was done by heating the air inside the chamber, and cooling was performed by passing cold liquid nitrogen through the chamber.

The major thermal cycling responses were obtained at 6 stress levels (43 MPa, 93 MPa, 144 MPa, 192 MPa, 294 MPa, 393 MPa) with heating and cooling between 80°C and 200°C. Figure

6.2 (a) shows the experimental responses obtained at different stress levels. The upper and lower minor cyclic responses were obtained at stress level 395 MPa, and for the minor cyclic responses, first the major cycling responses were obtained followed by 5 minor cycles. Figure 6.2 (b) shows the upper cyclic responses obtained between the temperature range 100°C and 175°C. A shifting with increasing strain in the response can be seen with number of cycles, which could be an effect of Transformation Induced Plasticity (TRIP). In Figure 6.2 (c), the lower cyclic responses were obtained in the temperature range 154°C and 200°C. Here, with increasing number of cycles, only a slight increase of strain is observed.

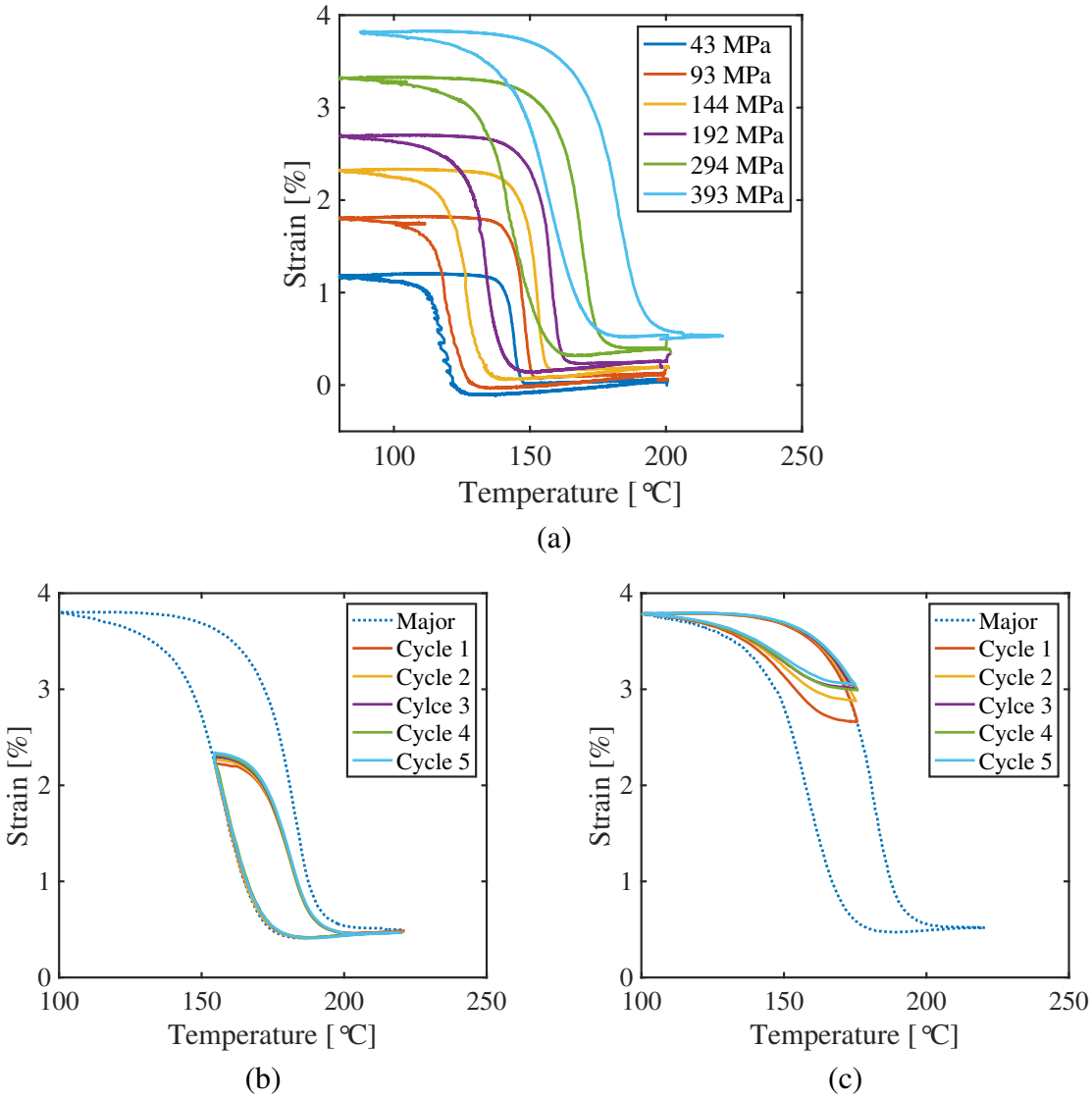

Figure 6.2: Experimental responses of actuation responses in NiTiHf SMAs. (a) Major actuation cycles at different stress levels, and (b) lower minor cycle responses and (c) upper minor cycle responses at 395 MPa.

6.4 Data based machine learning model for actuation response

Machine learning methods can be classified as supervised learning and unsupervised learning. In supervised learning, the task is to construct a function that maps the input and target pairs provided from training. In the unsupervised learning, the targets are not identified a priori and the model should self discover the naturally occurring patterns in the training data. A common example would be the clustering of data, where the algorithm group the training data into categories based on similarity. For modeling the response of the shape memory alloys, the task is to create a model to fit the available experimental behavior and then further extend it to predict for new loading conditions. In this scenario, supervised learning methods are used with a set of training data. The neural network modeling was selected for use because it is better suited to capture complex behaviors and work with large experimental data. In neural networks, the complexity of the model can also be controlled by choosing the number of layers, which allows for much more freedom to choose a model that works best for SMA responses.

A Machine Learning (ML) model capable of predicting major cycle response and minor cycle response is targeted, and the experimental response described in section 6.3 was used for training. To achieve this goal, an ML model was formulated to fit the slope ($\frac{d\varepsilon}{dT}$) in these curves in terms of the heating or cooling loading path. With the slopes known, at each heating or cooling step, the next value of strain (ε) could then be calculated in terms of the strain in the current state. By targeting for slope, the same model will be applicable irrespective of the thermal loading path that is for major cycle or minor cycle paths.

A neural network based model was built on the experimental response of $\mathrm{Ni_{50.3}Ti_{29.7}Hf_{20}}$. Figure 6.3 show a summary of the model trained for the derivative of strain with respect to temperature ($\frac{d\varepsilon}{dT}$) for each heating/cooling step with inputs (σ, ε, T, Sign(ΔT)) defining the state of the next thermal step. The model was trained using $\mathrm{Ni_{50.3}Ti_{29.7}Hf_{20}}$ experimental responses and predictions were made.

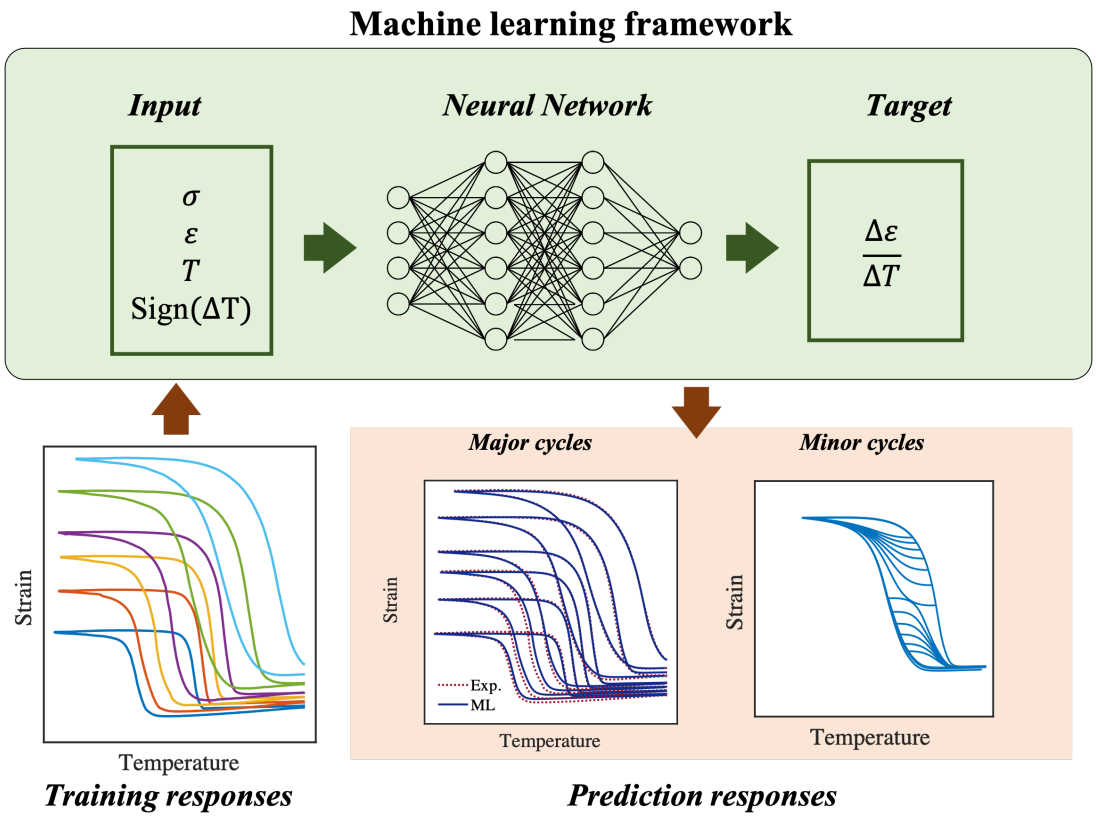

Figure 6.3: Machine learning framework for predicting the SMA response with input, output and training.

6.4.1 Description of the machine learning model

The ML model developed can be represented using the following equation 6.1, where the function $\mathbb{F}_{ML}$ relates temperature derivative of strain($\frac{d\varepsilon_{zz}(T,\sigma_{zz})}{dT}$)) in terms of the constant applied stress σ_{zz}, value of strain $\varepsilon_{zz}(T)$, temperature T and the sign of temperature change for the next step (Sign(ΔT). Table 6.1 summarizes the detailed description of input parameters and target parameter in the ML model.

$$exp\left(a\,\frac{d\varepsilon_{zz}(T,\sigma_{zz})}{dT}\right) = \mathbb{F}_{ML}\left[\sigma_{zz},\ \varepsilon_{zz}(T),\ T,\ \text{Sign}(\Delta T)\right], \tag{6.1}$$

where 'exp' is the natural exponential function and a is constant taken to be 10 in the present case. The target strain rate ($\frac{d\varepsilon_{zz}(T,\sigma_{zz})}{dT}$)) is expressed as an exponent to reduce the ratio maximum to minimum value, and this has improved the performance of the ML model.

Table 6.1: Input and output in the ML model for capturing the actuation response.

Parameter	Description
Input	
σ_{zz}	current stress value
$\varepsilon_{zz}(T)$	Strain value at current time step
T	Temperature at current time step
Sign(ΔT)	Sign of temperature change to next time step
Target	
$\frac{d\varepsilon_{zz}(T,\sigma_{zz})}{dT}$	Derivative of strain variation

For a given state of the material, the next value of strain is calculated using the tangent derivative in equation 6.1 and the following equation with corresponding temperature change ΔT.

$$\varepsilon_{zz}(T + \Delta T, \sigma_{zz}) = \varepsilon_{zz}(T, \sigma_{zz}) + \frac{d\varepsilon_{zz}(T, \sigma_{zz})}{dT}\Delta T \tag{6.2}$$

6.4.2 Constraints on strain rate while reversing thermal loading

As the SMAs exhibit hysteresis behavior, when the thermal loading is reversed, the material exhibits a different rate of reverse phase transformation with temperature. With respect to the presented ML model description, this will mean a different value of strain rate ($\frac{d\varepsilon_{zz}(T,\sigma_{zz})}{dT}$) in heating and cooling. In the major cycle responses of $\mathrm{Ni_{50.3}Ti_{29.7}Hf_{20}}$, for a given strain and temperatures the direction of thermal loading is unidirectional, that is, either heating or cooling, which gives only one value of strain rate. To predict the minor cycle responses, a strain rate for both heating and cooling is required. In the present ML model, this issue is resolved by training additional values for strain rate for the reversing of thermal load. For each point in the cooling of the major cycle response, the strain rate for heating is specified. Similarly, for the points of heating response,

the strain rate for cooling is specified. The strain rate at the reversing of thermal load is chosen to be equal to a fixed thermal expansion coefficient of the material (i.e. $= 0.00024°C^{-1}$). This concept is summarized in Figure 6.4 on an isobaric response. By providing this additional data, we are making sure that the values of strain rate for heating and cooling are specified for all the points in the major cycle hysteresis response. The implication of this would be that the strain rate interpolated by the ML model inside the hysteresis region will be bounded within the values at the boundary. As a result, the minor cycle responses will be predicted to be inside the major cycle. For this reason, the additional data added could be interpreted as constraints imposed on the responses from the ML model.

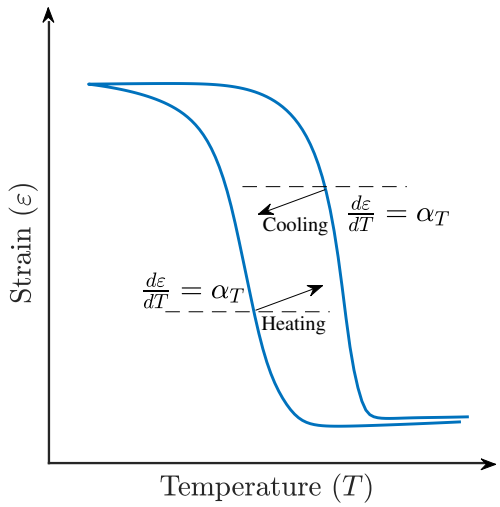

Figure 6.4: Figure describing extra constraints in the case of reverse thermal loading.

6.4.3 Initial condition for the response

The initial condition for the simulation of responses was considered to be the end of loading in austenite phase (point A in Figure 1.1 (a)). In the present simulations, the starting point was considered to be 195°C. The strain values at this state as a function of applied loading were fitted

using a linear function assuming elasticity. For any arbitrary stress value, the initial strain value was calculated using the fit shown in Figure 6.5.

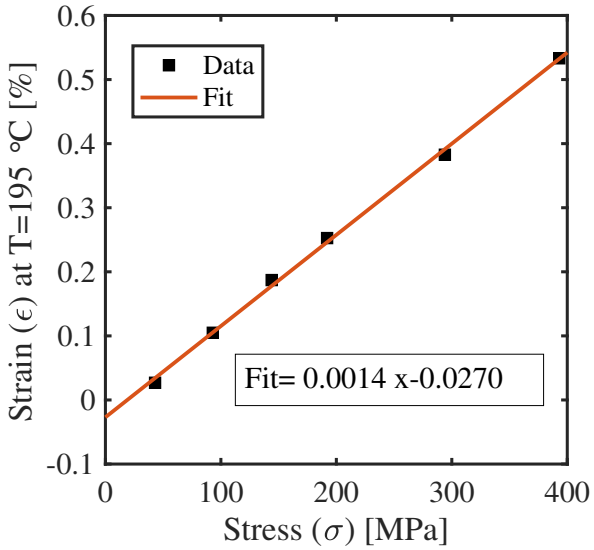

Figure 6.5: Figure showing the data and fit for the elastic strain at $T = 195°$C

6.4.4 Neural network architecture and training

The neural network architecture used for capturing the SMA response is shown in Figure 6.6. Four hidden layers with a size of 6 nodes were chosen, which used hyperbolic tangent sigmoid transfer functions. In the output layer, linear transfer function was used. More details on the equations and matrix representation of the layers are presented in E.1. Only the major cycle responses of NiTiHf at stress levels 43 MPa, 93 MPa, 144 MPa, 192 MPa, 294 MPa, 393 MPa with heating and cooling between 80°C and 200°C were used for training the model. Before using for training, the experimental data was processed using the 'smoothdata' function in MATLAB [90] software with Gaussian weighted moving average filter. The filtering was done separately for heating and cooling portions of the response to get accurate average values at the end points of cooling. The smoothing process helped to remove the unwanted noise in the data, and smooth responses were

obtained. In addition, the data was sampled at temperature steps of 1 °C to remove additional irregularities. The weights and biases in the neural network model were trained in MATLAB software using 'trainlm' which use a Levenberg-Marquardt backpropagation algorithm [145]. The values of the weights and biases obtained through training are described in detail in E.1.

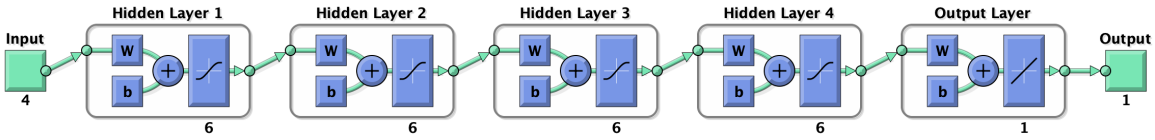

Figure 6.6: Neural network architecture used for modeling actuation responses.

6.5 Results and discussion

The trained neural network model was used to reproduce the major cycle responses in NiTiHf SMA. The starting values of strains, at the end of loading for 195°C for each stress value, were obtained from the fit described in section 6.4.3. The cooling and heating temperature limits were taken directly from the experimental responses for each stress level. Figure 6.7 shows the major cycle responses used for training and the comparison with the responses obtained from the neural network model. As seen in Figure 6.7 (b) the neural network model predictions are close to the experiments for all the stress levels.

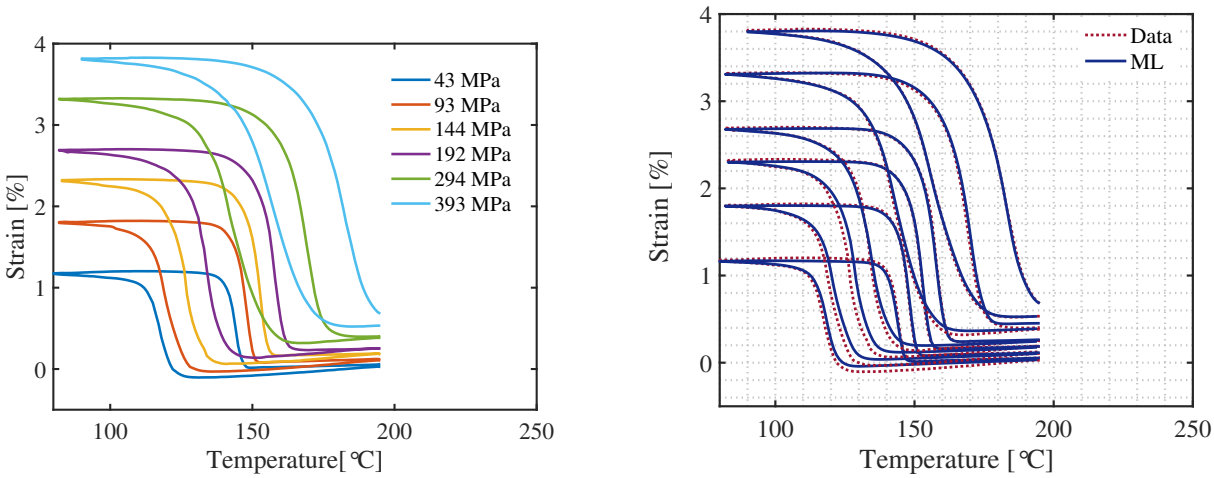

Figure 6.7: Major cycle responses (shown in (a)) and comparison with training results (shown in (b)) from machine learning model.

Minor cycle responses were simulated using the neural network model and compared with the experimental measurements. Figure 6.8 shows the comparison at stress level 395 MPa for major cycle and minor cycle responses. Details of these experiments are described in section 6.3. The temperature paths used to simulate the responses are also shown above each case. In Figure 6.8 (a), the prediction of 1st minor cycle response in the upper region is compared with the experimental observation, it is evident that the predictions of the minor cycle and that portion of the major cycle match well. However, this model could not capture the effects of plastic behavior with a higher number of cycles, as seen in section 6.3, where the minor cycle produced higher strain with increasing cycles.

Figure 6.8 (b) shows a comparison of the predictions for the minor cycle response in the lower region and the corresponding major cycle with those of the experiments. Here the predicted response is very similar to that of the experiments, with a small shift in the lower region for both the major cycle and minor cycle responses. It should be noted that the experimental major cycle response shown in (a) and (b) are different, as the hysteresis loading history in both the cases were different. The major cycle data used in the training had a different history of loading which

produced a higher strain in the lower region, which was reflected in the prediction of the lower minor cyclic response. Also, as the training of the model was done using experimental data with temperatures below 195°C, it could not capture the closing of the hysteresis curve in this case, as the data used did not include the closing response. However, the neural network model captures the nature of the behavior very well, as the predicted response in the minor cycle is very similar to that of the experiment, as shown.

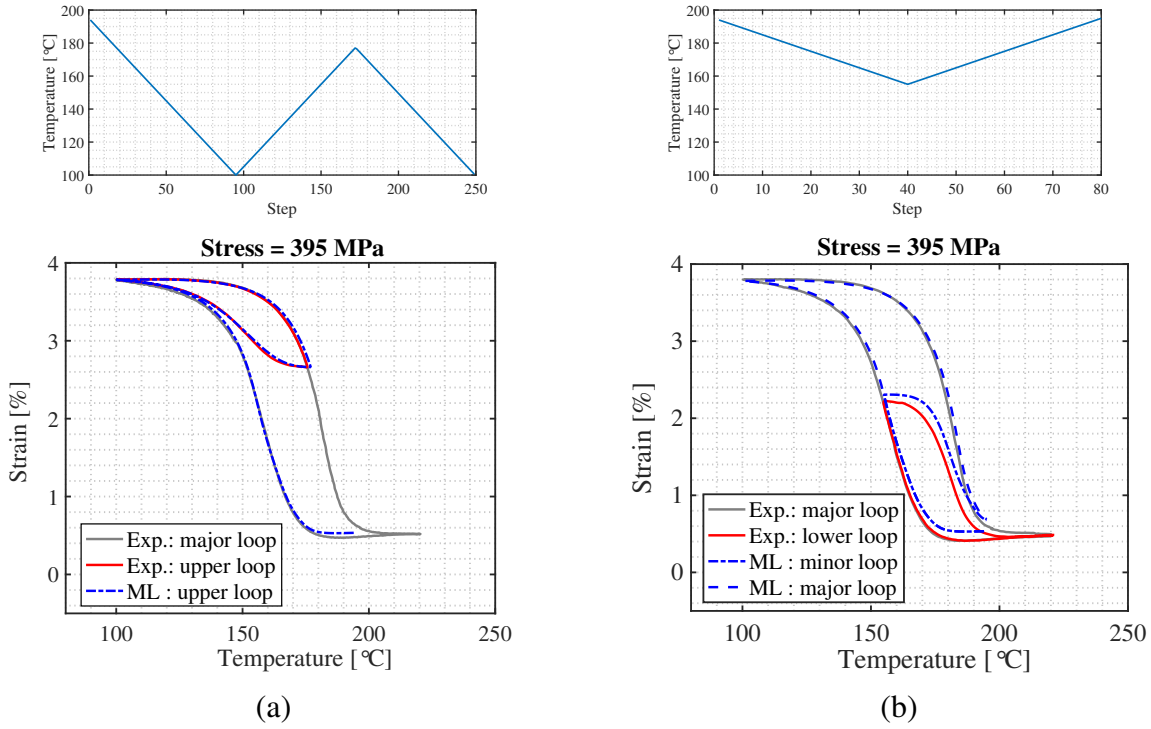

Figure 6.8: The experimentally measured major cycle and minor cycle responses at 395 MPa are compared with predictions from neural network model. (a) Upper minor cycle with the thermal loading path and (b) lower minor cycle with corresponding thermal loading path.

Figure 6.9 shows predictions of upper and lower minor cycles with varying temperature ranges for stress levels 250 MPa and 300 MPa, which are compared to the corresponding simulated major cycle response. The major cycle response was simulated first, and then the lower minor cycles and upper minor cycles were simulated. The temperature paths simulated at these stress levels

are shown at the top of the figure, where the minor cycles were simulated upon reducing the temperature range by 2 °C in adjacent cycles. The ML model is able to predict the responses for varying range of thermal loading paths both in the lower and upper cycle responses. It can be seen that in all the cases shown, the minor cycle responses are confined within the major cycle response. The additional imposed constraints described in section 6.4.2 ensure that the responses lie within the major cycle. Without these constraints, the minor cycle predictions might cross through the major cycle response and give unreliable responses.

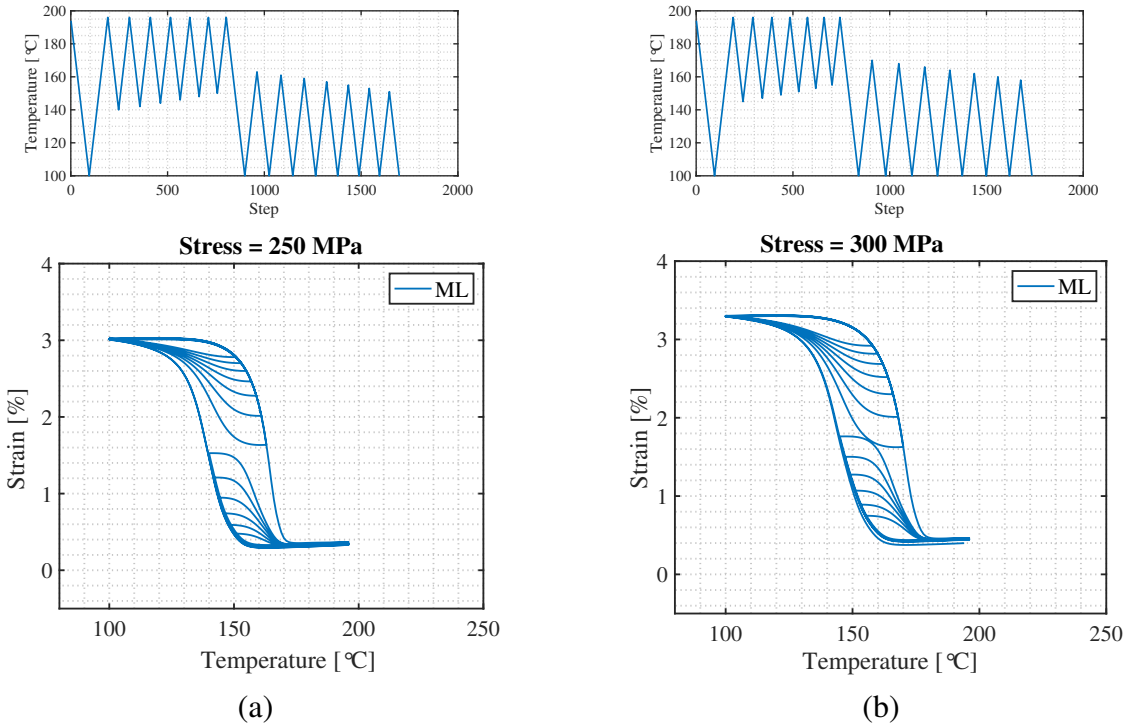

Figure 6.9: Predictions using the neural network Machine Learning (ML) model at different stress levels. Major cycle and minor cycle responses at (a) 250 MPa and (b) 300 MPa are shown. The respective thermal loading path is shown above.

Figure 6.10 shows the responses of repeated lower minor cycles in three different temperature ranges, creating cycles of large, medium and small sizes at 300 MPa. In each of these cases, the minor cycles were repeated 7 times. Here, the responses of the minor cycles cross through the

initial cyclic response and reach a steady response in the later cycles. Figure 6.10 (a) shows a repeated cycle with a large cycle. It can be seen that the response becomes steady after the first cycle and there is no significant difference compared to the first cycle response. Figure 6.10 (b) shows the response of a cycle in medium temperature range, where it can be seen that the response rises higher with additional cycles and reaches a steady response. The same is observed in Figure 6.10 (c), where a minor cycle in a smaller temperature range is shown.

Figure 6.11 shows the upper minor cyclic responses simulated from the neural network model for repeated cycling in large, medium and small ranges of temperatures at 300 MPa. For each case, 7 repeated minor cycles were simulated. In all the cases, the responses reach to a steady response within a few cycles, Which indicates the ability of the neural network model to simulate actual behavior from training with the experimental data.

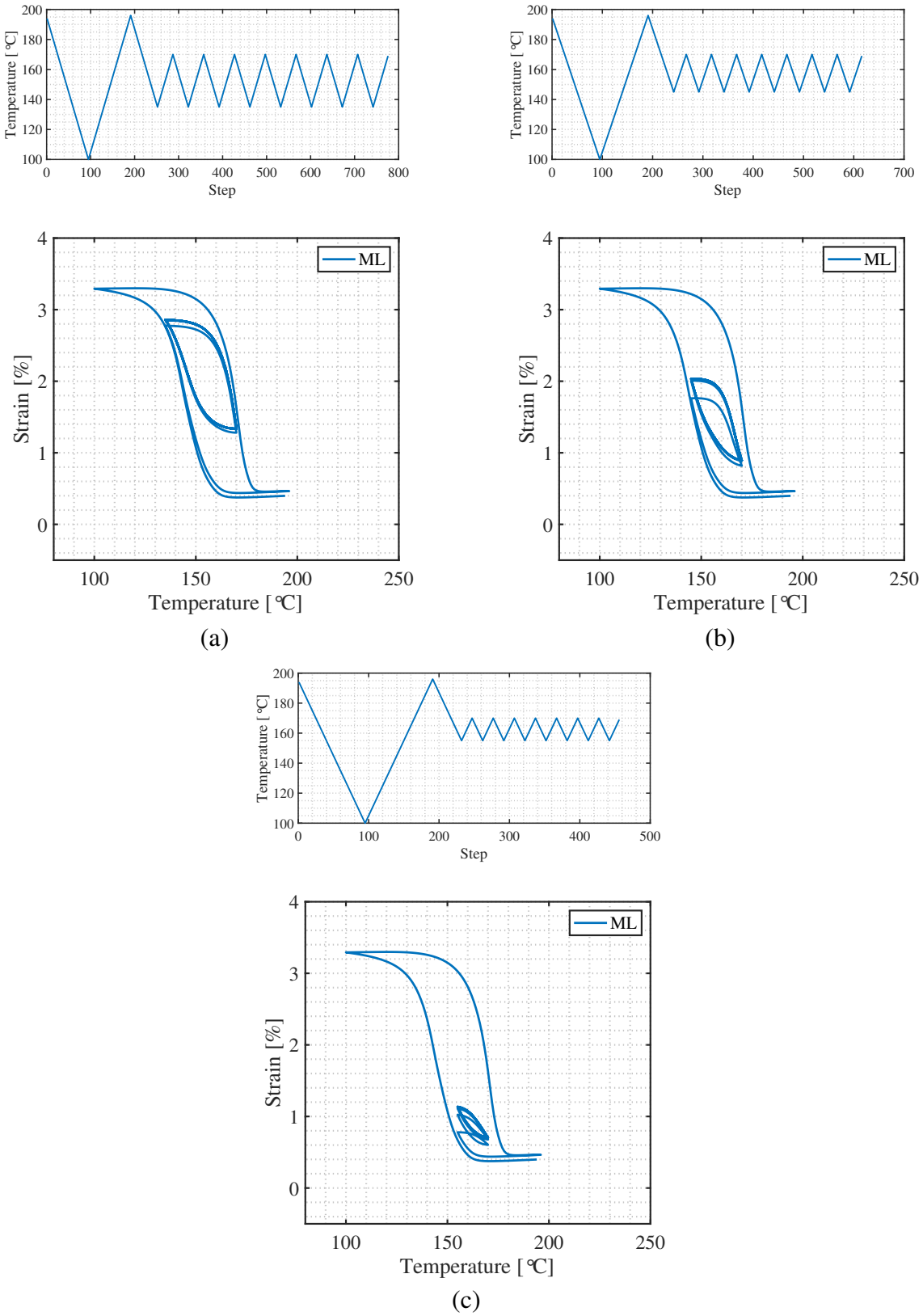

Figure 6.10: Repeated lower minor cycle responses predictions using the neural network model at 300 MPa. The temperature paths simulated are shown on top of each response.

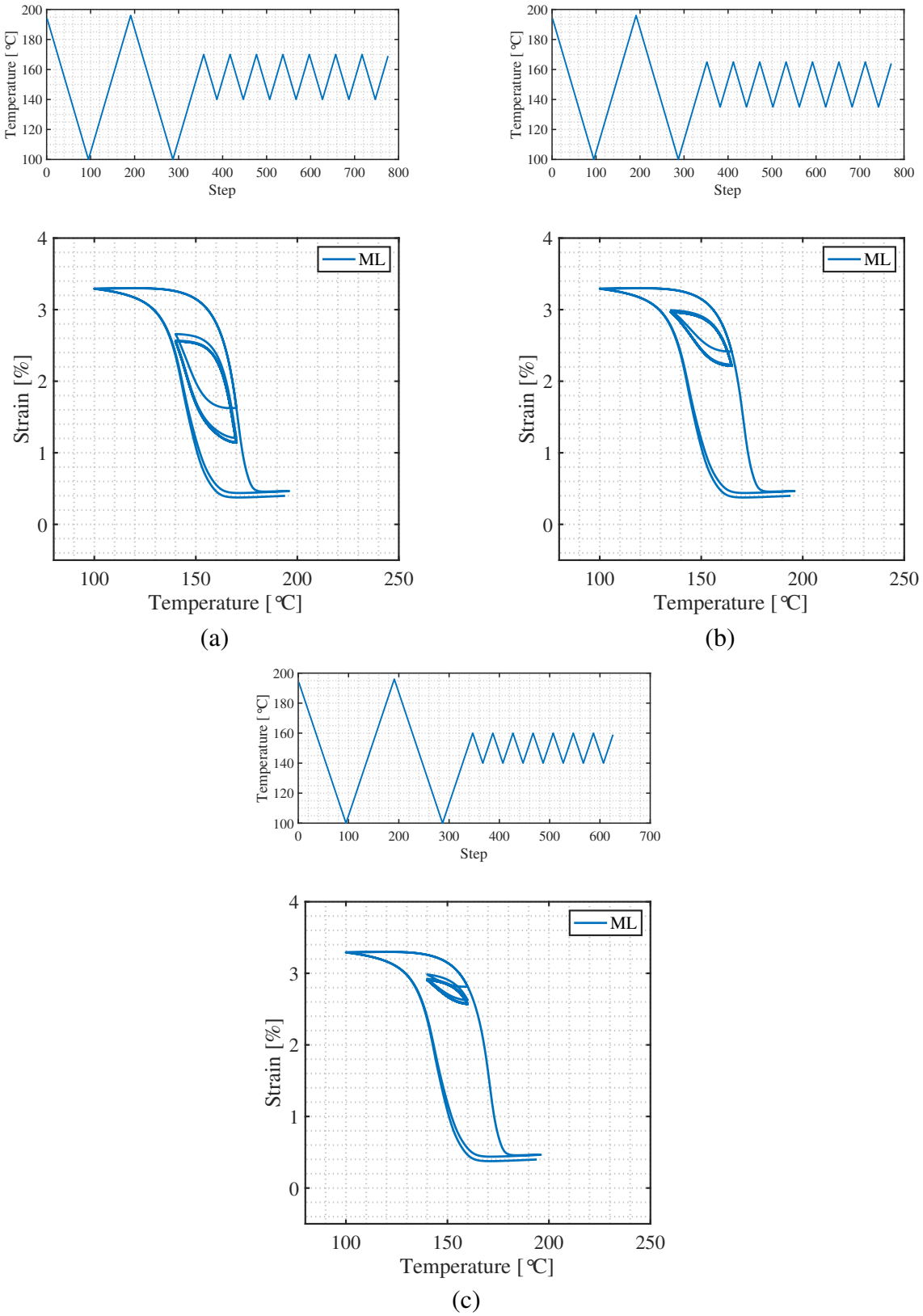

Figure 6.11: Repeated upper minor cycle responses predictions using the neural network model at 300 MPa. The temperature paths simulated are shown on top of each response.

6.5.1 Ensemble average and confidence interval

There can be variability amongst the many trainings of the neural network model, with different because of the different weights and biases obtained in each training. Taking the ensemble average of many trained model response is one technique to address this variability. In the present case, 50 realizations of the network training were performed to study the ensemble variability. For a targeted response, the mean response from the ensemble of neural networks can be calculated, and the standard deviation is an estimate of the confidence of prediction. In Figure 6.12, we show the ensemble average estimation corresponding to the two experimental cycles. In addition, the Confidence Interval (CI) with 1 standard deviation is created based on the variability from the 50 training performed. The CI presented gives an indication of the variability of responses from different training in the present model. The CI has smaller range in the major cycle regions and wider range in the minor cycle regions. This indicates that the model reproduces the major cycle responses used in the training with better confidence. The minor cycle regions have higher uncertainty because they include the prediction beyond the training region. The average response from the ensemble matches exactly with the upper minor cycle (Figure 6.12 (a)) and captures a similar response in the case of the lower minor cycle (Figure 6.12 (b)) as well. Moreover, in comparison with the predictions in Figure 6.8, it can be concluded that the particular neural network training presented is very close to the average ensemble response, as both give close estimations.

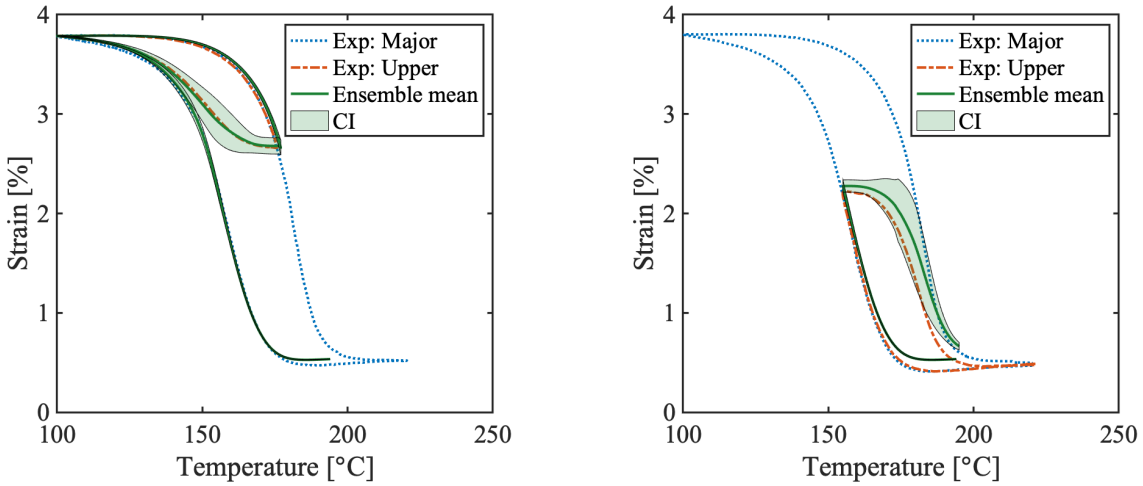

Figure 6.12: The experimentally measured major cycle and minor cycle responses at 395 MPa are compared with ensemble average predictions from 50 training of the neural network model. The confidence interval (CI) show 1 standard deviation from the average.

6.6 Conclusions

In this chapter, a data based Machine Learning (ML) framework to predict the experimentally observed nonlinear actuation responses of Shape Memory Alloys (SMAs) is presented. A NiTiHf High Temperature SMA (HTSMA) was selected for investigation and evaluation of the tool. The developed framework contains a neural network fitting method that fits the evolution of the nonlinear behavior of the SMA during thermally induced transformation under different constant stress levels. The output of the trained model presents good correlation with the experimentally observed behavior and seems to be able to account for different underlying effects at great accuracy. To demonstrate the predictive capabilities of the proposed ML model, the formation of partial transformation cycles was investigated at different locations inside the major hysteresis loop. When compared with experimentally obtained data, the model was able to capture the evolution of partial transformation branches initiated from the major heating and the major cooling branch.

The change in strain rate at the reversal of thermal loading was imposed through additional data from prior observation, and this helped in predicting the partial transformation branches. For

this, the strain gradient for the reversal of transformation at the major heating and the major cooling branches were assumed to be the thermal expansion coefficient based on experimental observation. This addition allowed the model to make meaningful predictions of partial transformation and made them bound within the major hysteresis cycle. Further, the model was used to predict inner cyclic responses for the material. Although these predictions of inner cycles seemed reasonable, they may be less reliable as the model is extrapolating too far for these loading paths. More developments using experiments on inner responses will be needed to ensure a comprehensive data based ML model that can predict all complex paths of actuation.

7. MACHINE LEARNING MODEL FOR ANISOTROPIC SINGLE CRYSTAL SHAPE MEMORY ALLOY RESPONSE

7.1 Introduction

In recent years, advancements in Machine Learning (ML) have provided promising tools for understanding and predicting material behaviors. In this chapter, the building of a ML framework that can learn the anisotropic variation in single crystal Shape Memory Alloy (SMA) responses is discussed. The data used for ML training were generated using a finite-element crystal plasticity framework. In this framework, the slip and transformation systems were taken into account to predict the plastic behavior in both the austenite and martensite phases and during phase transformation.

The Crystal-Plasticity (CP) framework was developed based on the constitutive model developed by Chaugule *et al*. [146]. It simulates the anisotropic, at the microscale, and isotropic, at the macroscale, responses of a NiTiHf HTSMA. This CP model can account for plastic slip, which is rate independent, and viscoplastic slip, which is rate dependent, in a HTSMA. The model can also account for phase transformation and its associated irrecoverable mechanisms, i.e., Transformation Induced Plasticity (TRIP) and retained martensite, through the formation of martensite variants at the microscale. In addition, the coupling between phase transformation and viscoplasticity, as observed experimentally in[147] is also accounted by the dislocation density generated from plastic and viscoplastic slip.

To date, there has been no case in the literature on any HTSMA system in which anisotropic data was used to train a ML model. The present study addresses this gap by formulating a ML model and presenting the approach taken to train it, building on the concepts and knowledge presented in the previously described ML studies on strain responses [71], SMA cyclic responses [72] and SMA wire actuation [73]. Numerous anisotropic responses were generated from randomly oriented single crystals, and relevant phase transformation strains and properties were extracted from

the responses. Using the CP model to generate results is beneficial as the effects of texture and random orientations can be leveraged to generate large amount of data for training the ML model. A ML framework was developed to fit the viscoplasticity and phase transformation interactions, across multiscale, from a Crystal-Plasticity Finite-Element (CP-FE) model. The developed ML framework provides reasonable predictions for different crystal orientations and stress conditions.

The chapter is organized as follows. In section 7.2 the theoretical frameworks and main constitutive equations for the crystal plasticity model and ML model are presented. For the detailed set of constitutive equations, refer to Chaugule *et al.* [146]. In section 7.3, details of the ML framework used in the study are presented. In section 7.4, a demonstration of training the ML model using the results of the CP model from the thermo-mechanical tests on single crystals is presented. Applications and limitations of the study and conclusions are presented in section 7.5 and section 7.6.

7.2 Crystal plasticity model

This section gives a summary of the constitutive model for single crystal SMA [146] used in the current study. The total strain in the single crystal SMA response is a cumulative effect of thermal, elastic, phase transformation, TRIP and viscoplastic deformations of the material. This is summarized in Eq. (7.1), where the total strain $\boldsymbol{\varepsilon}_{tot}$ is written as the sum of thermal strain $(\boldsymbol{\varepsilon}_{th})$, elastic strain $(\boldsymbol{\varepsilon}_{e})$, transformation strain $(\boldsymbol{\varepsilon}_{tr})$, TRIP strain $(\boldsymbol{\varepsilon}_{tr})$ and viscoplastic strain $(\boldsymbol{\varepsilon}_{vp})$.

$$\boldsymbol{\varepsilon}_{tot} = \underbrace{\boldsymbol{\varepsilon}_{th} + \boldsymbol{\varepsilon}_{e}}_{elastic} + \underbrace{\boldsymbol{\varepsilon}_{tr} + \boldsymbol{\varepsilon}_{TRIP} + \boldsymbol{\varepsilon}_{vp}}_{inelastic} \tag{7.1}$$

The thermal strain $\boldsymbol{\varepsilon}_{th}$ is modeled in Eq. (7.3) in terms of current temperature T, reference temperature T_{ref}, thermal expansion coefficients of austenite $\boldsymbol{\alpha}^A$ and martensite $\boldsymbol{\alpha}^M$ and martensitic volume fraction ξ. The effective thermal expansion is obtained using the rule of mixtures from $\boldsymbol{\alpha}^A$ and martensite $\boldsymbol{\alpha}^M$ using ξ.

$$\boldsymbol{\varepsilon}_{th} = \boldsymbol{\alpha}(\xi)(T - T_{ref}), \;\; \boldsymbol{\alpha}(\xi) = \boldsymbol{\alpha}^A + \xi\left(\boldsymbol{\alpha}^M - \boldsymbol{\alpha}^A\right) \tag{7.2}$$

The elastic strain is modeled in Eq. (7.3), where $\boldsymbol{\sigma}$ is the stress applied, and $\boldsymbol{S}^A$ and $\boldsymbol{S}^M$ are austenite and martensite compliance matrices. The effective compliance is evaluated using the rule of mixtures from $\boldsymbol{S}^A$ and $\boldsymbol{S}^M$ for martensitic volume fraction ξ.

$$\boldsymbol{\varepsilon}_e = \boldsymbol{S}(\xi).\boldsymbol{\sigma}, \;\; \boldsymbol{S}(\xi) = \boldsymbol{S}^A + \xi\left(\boldsymbol{S}^M - \boldsymbol{S}^A\right) \tag{7.3}$$

The transformation strain is modeled in Eq. (7.4), where the total transformation strain $\boldsymbol{\varepsilon}_{tr}$ is written as the summation of contributions from N_v martensitic variants. The direction of transformation for different variants $\mathbf{P}^{\alpha}_{tr}$ is found using their corresponding habit plane of transformation $\mathbf{b}^{\alpha}$ and habit direction of transformation $\mathbf{m}^{\alpha}$ using the dyadic product $\otimes$, and g_{tr} is a variable governing the rate.

$$\boldsymbol{\varepsilon}_{tr} = \sum_{\alpha=1}^{N_v} \xi^{\alpha} g_{tr} \mathbf{P}^{\alpha}_{tr}, \;\; \xi = \sum_{\alpha=1}^{N_v} \xi^{\alpha}, \;\; \mathbf{P}^{\alpha}_{tr} = \frac{1}{2}(\mathbf{b}^{\alpha} \otimes \mathbf{m}^{\alpha} + \mathbf{m}^{\alpha} \otimes \mathbf{b}^{\alpha}) \tag{7.4}$$

The effective TRIP strain $\boldsymbol{\varepsilon}_{TRIP}$ is estimated as a summation of the contributions from all variants as modeled in Eq. (7.5). The magnitude along individual variants is proportional to the corresponding variant transformation strain.

$$\boldsymbol{\varepsilon}_{TRIP} = \sum_{\alpha=1}^{N_v} \gamma^{\alpha} \mathbf{P}^{\alpha}_{tr}, \;\; \gamma^{\alpha} \propto \xi^{\alpha} \tag{7.5}$$

The viscoplastic strain rate $\boldsymbol{\varepsilon}_{vp}$ is modeled using Eq. (7.6). The effective viscoplastic change is modeled as a summation of contributions from all martensitic variants. The $\boldsymbol{\varepsilon}_{vp}$ is related to slip planes $\mathbf{n}^s$ and slip directions $\mathbf{l}^s$, and γ^s is a variable controlling the magnitude.

$$\begin{aligned} \boldsymbol{\varepsilon}_{vp} &= \sum_{s=1}^{N_s} \gamma^s \mathbf{T}^s \\ \mathbf{T}^s &= \frac{1}{2}(\mathbf{n}^s \otimes \mathbf{l}^s + \mathbf{l}^s \otimes \mathbf{n}^s) \end{aligned} \tag{7.6}$$

A comparison of equations between the polycrystal model for SMAs and the single crystal

model for SMA is presented in Table 7.1. The two models have different modeling approaches for the inelastic components of strain (transformation, TRIP, viscoplastic).

The Lagoudas *et al.* [38] model was developed within the framework of continuum thermodynamics and uses the classical rate-independent small-strain flow theory for the evolution equations of transformation strains. Here, the phase transformation direction is defined using the tensor $\mathbf{\Lambda}$. During forward transformation, the transformation strain is oriented by the direction of the deviatoric stress. This is reflected in the selected J_2 form of the direction tensor. While transformation is happening, the stress tensor components should remain on the transformation surface. The transformation surfaces are defined through relationships between thermodynamic driving force and the critical value of the thermodynamic force that determines transformation initiation and sustaining the transformation. The TRIP and viscoplastic modeling follows the same approach as that for transformation strain. The model has a phenomenological approach designed to capture the overall polycrystal behavior rather than the individual variant level.

The crystal plasticity modeling focuses on modeling behavior at the individual martensitic variation level. Each of the inelastic strain components are modeled as a cumulative contribution from all the individual variants. The variant level contributions are formulated in terms of the habit plane, habit direction, slip planes and slip directions.

Table 7.1: Comparison of polycrystal and single crystal SMA constitutive model.

Component of strain	Polycrystal SMA model (Lagoudas *et al.* [38, 148])	Crystal plasticity model (Chaugule *et al.* [146])
Elastic	$\boldsymbol{\varepsilon}_e = \boldsymbol{S}(\xi).\boldsymbol{\sigma}$ $\boldsymbol{S}(\xi) = \boldsymbol{S}^A + \xi\left(\boldsymbol{S}^M - \boldsymbol{S}^A\right)$	$\boldsymbol{\varepsilon}_e = \boldsymbol{S}(\xi).\boldsymbol{\sigma}$ $\boldsymbol{S}(\xi) = \boldsymbol{S}^A + \xi\left(\boldsymbol{S}^M - \boldsymbol{S}^A\right)$
Thermal	$\boldsymbol{\varepsilon}_{th} = \boldsymbol{\alpha}(\xi)(T - T_{ref})$ $\boldsymbol{\alpha}(\xi) = \boldsymbol{\alpha}^A + \xi\left(\boldsymbol{\alpha}^M - \boldsymbol{\alpha}^A\right)$	$\boldsymbol{\varepsilon}_{th} = \boldsymbol{\alpha}(\xi)(T - T_{ref})$ $\boldsymbol{\alpha}(\xi) = \boldsymbol{\alpha}^A + \xi\left(\boldsymbol{\alpha}^M - \boldsymbol{\alpha}^A\right)$
Transformation	$\dot{\boldsymbol{\varepsilon}}_{tr} = \boldsymbol{\Lambda}\dot{\xi}$ $\boldsymbol{\Lambda} = \begin{cases} \boldsymbol{\Lambda}^{fwd} & \text{if } \dot{\xi} > 0 \\ \boldsymbol{\Lambda}^{rev} & \text{if } \dot{\xi} < 0 \end{cases}$	$\boldsymbol{\varepsilon}_{tr} = \sum_{\alpha=1}^{N_v} \xi^\alpha g_{tr} \mathbf{P}_{tr}^\alpha,\ \xi = \sum_{\alpha=1}^{N_v} \xi^\alpha$ $\mathbf{P}_{tr}^\alpha = \frac{1}{2}(\mathbf{b}^\alpha \otimes \mathbf{m}^\alpha + \mathbf{m}^\alpha \otimes \mathbf{b}^\alpha)$
TRIP	$\dot{\boldsymbol{\varepsilon}}_{TRIP} = \boldsymbol{\Lambda}_{tp}\dot{\xi}$ $\boldsymbol{\Lambda}_{tp} = \begin{cases} \boldsymbol{\Lambda}_{tp}^{fwd} & \text{if } \dot{\xi} > 0 \\ \boldsymbol{\Lambda}_{tp}^{rev} & \text{if } \dot{\xi} < 0 \end{cases}$	$\boldsymbol{\varepsilon}_{TRIP} = \sum_{\alpha=1}^{N_v} \gamma^\alpha \mathbf{P}_{tr}^\alpha$ $\gamma^\alpha \propto \xi^\alpha$
viscoplastic	$\dot{\boldsymbol{\varepsilon}}_{vp} = \boldsymbol{\Lambda}_{vp}\dot{p}$ $\boldsymbol{\Lambda}_{vp} = \frac{3}{2}\frac{\boldsymbol{\sigma}'}{\overline{\sigma}}$	$\boldsymbol{\varepsilon}_{vp} = \sum_{s=1}^{N_s} \gamma^s \mathbf{T}^s$ $\mathbf{T}^s = \frac{1}{2}(\mathbf{n}^s \otimes \mathbf{l}^s + \mathbf{l}^s \otimes \mathbf{n}^s)$

7.2.1 Single crystal response with orientation

In order to simulate the anisotropic behavior of the single crystal NiTiHf SMA, the effective responses of the alloy along random orientations were simulated using the model. Figure 7.1(a) shows the schematics of the problem, where the material is loaded along one direction and the actuation response of the material is solved applying thermal cycling. The random loading direction was defined in a spherical coordinate system using polar angle (θ) azimuthal angle (φ), where the values were generated by $\theta = \arccos(2R_1 - 1)$ and $\varphi = R_2 * 2\pi$ for random variables R_1 and R_2 in [0 1] bound. Figure 7.1(b) shows the distribution of 500 random orientations in a spherical coordinate system. The schematic shows that the orientations are randomly distributed in the 3D sphere. Figure 7.1 (c) shows the distribution of the actuation responses solved for the 500 random orientations. The solution gives a range of strain values in the actuation response, showing a highly anisotropic behavior in the single crystal alloy.

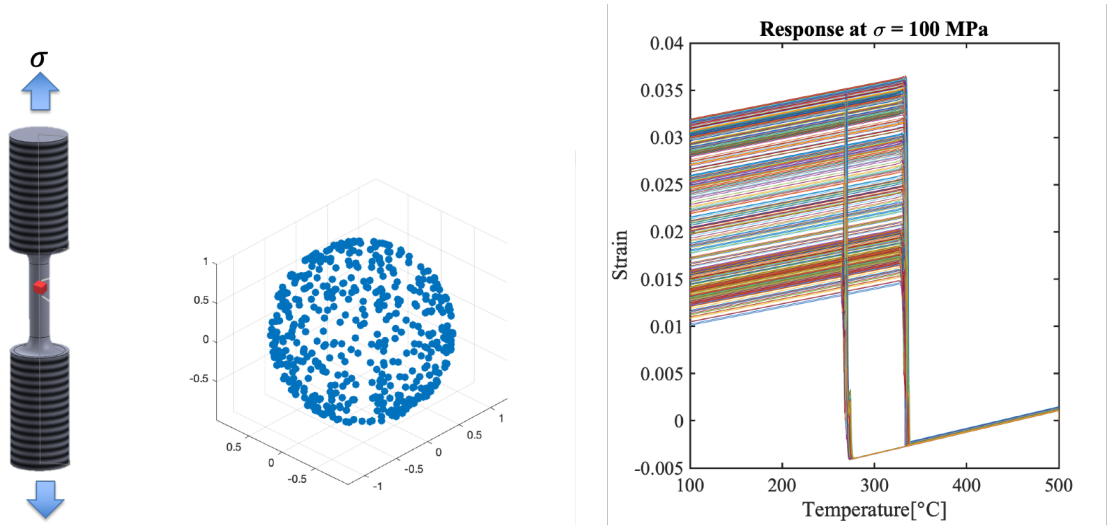

(a) (b) (c)

Figure 7.1: Single crystal response: (a) schematics of loading and material (b) random orientations (c) responses in random orientations

7.3 Machine Learning (ML) model

The developed ML framework consisted of: (a) representing responses using reduced order functions, (b) finding variation of functional features with orientation, (c) training the ML model for variation in orientation and (d) reproducing the full responses from functional features.

7.3.1 Extracting features from responses

To represent the variation of single crystal SMA responses in terms of functional features, a reduced order functional fitting shown in Eq. (7.7) was used. The strain value $\varepsilon(T)$ at temperature T is related as:

$$\varepsilon(T) = \varepsilon_0 + \varepsilon_t * H(T - T_s, b) + \Big(\alpha_A + (\alpha_M - \alpha_A) * H(T - T_s, b)\Big)T, \tag{7.7}$$

where, ε_0 is the initial elastic strain, ε_t is the strain jump at the transformation site, $H(T - T_s, b)$ is the Heaviside step function capturing the jump at transformation temperature T_s, b defines the smoothness in the Heaviside function, α_A is the thermal expansion coefficient at austenite phase

and α_M the thermal expansion coefficient at martensite phase. The Heaviside step function is defined by Eq. (7.8), where e refers to the natural exponent function.

$$H(T_0 - T, b) = \frac{1}{1 + e^{(b(T - T_s))}} \tag{7.8}$$

Figure 7.2 shows the effectiveness of the chosen function in fitting the single crystal responses. In Fig. 7.2 (a), the fit is used to capture the cooling behavior in the single crystal response. The function captures the phase transformation behavior in the cooling well. By using two fits, one for cooling and one for heating, the whole cyclic response is captured as shown in Fig. 7.2 (b). The behavior created by the two fits matches closely with the target response.

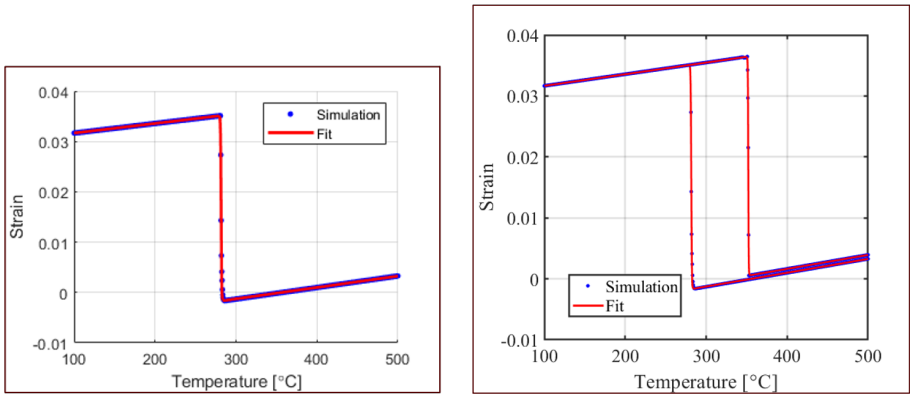

(a) (b)

Figure 7.2: Fitting of responses: (a) fit for half cycle (b) fit in the full cycle

Eq. (7.9) and Eq. (7.10) describes the fits for the forward and reverse phase transformation, respectively.

$$\varepsilon^f(T) = \varepsilon_0^f + \varepsilon_t^f * H(T - T_s^f,\ b^f) + \Big(\alpha_A + (\alpha_M - \alpha_A) * H(T - T_s^f,\ b^f)\Big)T \tag{7.9}$$

$$\varepsilon^r(T) = \varepsilon_0^r + \varepsilon_t^r * H(T - T_s^r,\ b^r) + \Big(\alpha_A + (\alpha_M - \alpha_A) * H(T - T_s^r,\ b^r)\Big)T \tag{7.10}$$

Different superscripts ('f' and 'r') are used to denote the different values of the fitting parameters in the forward and reverse transformation responses. The thermal expansion coefficients α_M and α_A corresponding to the martensitic and austenitic phases are taken to be fixed in the two equations based on the physics of the material. The values of thermal expansion coefficients α_M and α_A are estimated to be the average value of the forward and reverse transformation fits.

Additional constraints between the coefficients are derived based on the continuity of strain values between cooling and heating. The two equation should produce the same value of strain at the lowest temperature in the thermal cycle, which is 100 °C for the responses considered. From Eq. (7.9) and Eq. (7.10), this gives $\varepsilon^f(100) = \varepsilon^r(100)$. At $T = 100$ °C, the Heaviside function determines that $H(T_s^f - 100, b^f) = 1$ and $H(T_s^r - 100, b^r) = 1$ as $b^f >> 0$ and $b^r >> 0$ for the responses considered. Substituting in Eq. (7.9) and Eq. (7.10) and simplifying yields:

$$\varepsilon_0^f + \varepsilon_t^f = \varepsilon_0^r + \varepsilon_t^r = C_{100}, \tag{7.11}$$

where C_{100} is a constant estimated by taking the average value from the fits for forward and reverse transformation.

The fitting methodology described was used to fit the 500 orientations simulated using the crystal plasticity model. The orientation variation of features such as transformation temperature (T_S) and transformation strain (ε_t) were extracted from the responses. Figure 7.3 shows the variation of transformation temperature in cooling (M_s) and transformation strain (ε_t) with orientation angles. A substantial variation of the T_S and ε_t with the orientation parameters can be seen for these variables. The transformation temperatures in these cases have gradual variation with orientations, while the transformation strain shows faster variation in the values with changing orientations. The ML framework was targeted to model the anisotropic variation of the properties and capture their complex variation with changing orientation.

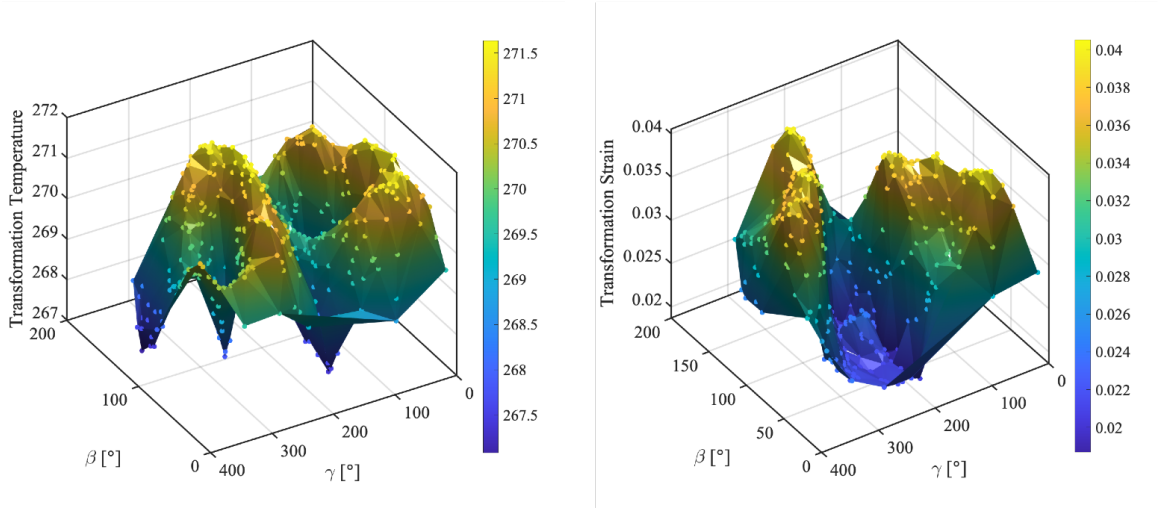

(a) (b)

Figure 7.3: 3D scatter+surface plots of (a) transformation temperature M_s (b) transformation strain for $\sigma = 100$ MPa in cooling.

7.3.2 Details of machine learning model

A machine learning (ML) model to capture the anisotropy in the single crystal behavior was developed, targeted to model the anisotropic variation of different features in the behavior obtained using the aforementioned fitting methodology. The inputs for the ML model were variables representing the changes in the orientation and loading conditions. For this ML model, trigonometric functions of the orientation angles were used to differentiate the orientations. In addition, the loading stress of the actuation response was also provided to differentiate responses based on the applied stress.

Table 7.2 summarizes the summary of parameters in the ML model. The estimation techniques for different parameters from the fit methodology are also summarized in Table 7.2. Each target parameters were fitted using a separate ML model. Once the ML model captured the variations of these parameters, they were predicted for any new orientation using the ML model. Once the set of target parameters was obtained, the whole response of the single crystal could then be reproduced. The parameters C_{100}, α_A, α_M, ε_0^f, ε_0^r, T_s^f, T_s^r, b^f and b^r were fitted using the ML model, while

the parameters ε_t^f and ε_t^r required in the fit were estimated from the ML target parameters from relations summarized in Table 7.2.

A schematic summary of the ML model used is shown in Fig. 7.4. The target from the ML model here is one of fitting parameter or feature. Instead of using choosing a multi-output framework, each feature was fitted separately using a single-output ML model. This improved the ability to predict the parameters accurately. The ML model used can be any of the typical techniques such as Gaussian Process Regression (GPR) or a neural network based model.

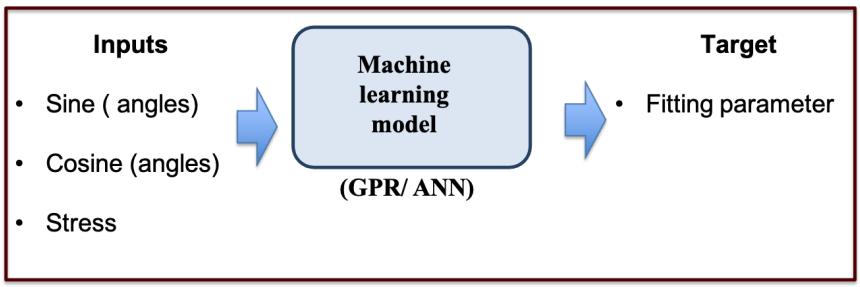

Figure 7.4: Schematics of the ML model for capturing anisotropic SMA response.

For the current modeling, a GPR based ML models was used. The GPR based model showed better fitting ability, considering the complex variations in the SMA single crystal model. The GPR models were implemented in MATLAB software[90]. For training, the GPR model 'linear' basis functions were used.

7.3.3 Training ML model

The responses from the crystal plasticity model in different orientations and different stress levels were used to train the ML model. The ability of the ML model was tested against two different scenarios through controlling the data used for training the model. In the first scenario, responses at a single stress level in different orientations were used in the training. The target of this training was to capture the anisotropy of the responses, but not the variation with changing

Table 7.2: Target parameters and related parameters for fitting using ML models.

Parameter	Estimation technique
Target parameters in the ML models	
$C_{100} = \varepsilon_0^f + \varepsilon_t^f$	Average from the forward and reverse response
α_A	Average from forward and reverse response
α_M	Average from forward and reverse response
ε_0^f	Estimated from forward response
ε_0^r	Estimated from reverse response
T_s^f	Estimated from forward response
T_s^r	Estimated from reverse response
b^f	Estimated from forward response
b^r	Estimated from reverse response
Estimation of related parameters	
ε_t^f	$C_{100} - \varepsilon_0^f$
ε_t^r	$C_{100} - \varepsilon_0^r$

stress levels. In the second scenario, the training of the ML model used data from different stress levels and orientations. Here, the ML model was targeted to capture the variation of behavior in different orientations and at different stress levels. The abilities of the ML model in the two scenarios were evaluated by comparing the predictions in the new orientations against the crystal plasticity model simulations. More on the performance of the developed ML model is discussed in the results and discussions.

7.4 Results and discussion

The responses from NiTiHf single crystal SMA in 500 random orientations were simulated at 50 MPa, 100 MPa, 150 MPa, 200 MPa, 250 MPa and 300 MPa using the crystal plasticity model in section 7.2. The steps described in the ML framework in section 7.3 were followed to extract key features and train the model. The abilities of the ML model in the two training scenarios (section 7.3.3) were analyzed.

The ML model was tested for the ability to capture the anisotropic behavior at a single stress level. The training was performed using the responses at 300 MPa. First, a convergence study was performed to determine the size of the training test. The ML model was used to model the

variation of transformation strain using different training size. The performance of the ML model was evaluated against the same 50 new, random orientation responses which were not used in the training. Figure 7.5 shows the variation of the goodness in prediction (R^2) for transformation strain with increasing number of training data size. The R^2 of predictions increased significantly with size at smaller data size, and achieved almost a plateau after 200. For further calculations, a training size of 450 was used to achieve maximum accuracy for capturing the anisotropic variation. The convergence analysis showed that the data size 450 is adequate to have convergence in the ML model.

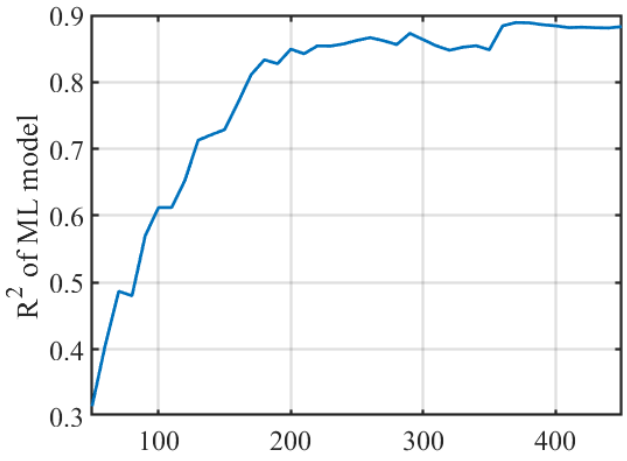

Figure 7.5: The performance of the ML model with increasing training size. Here, the goodness of prediction (R^2) in 50 testing orientation is compared against increasing size of training set.

Figure 7.6 (a) and (b) summarizes the performance of the ML models toward predicting the forward transformation temperature M_s and transformation strain in the cooling ϵ_t^f, respectively. Out of the 500 orientations, values from 450 orientations were used to train the ML model and the remaining 50 were used for testing predictions. In Fig. 7.6, the predictions from the ML models for the training and testing set are shown in different colors, and are compared against the target value in the line $y = x$. The comparisons show that the predictions from the ML models for the

training set and target set for the temperatures and strain are close to the target values. Similar performance was observed for all the features extracted from the full response.

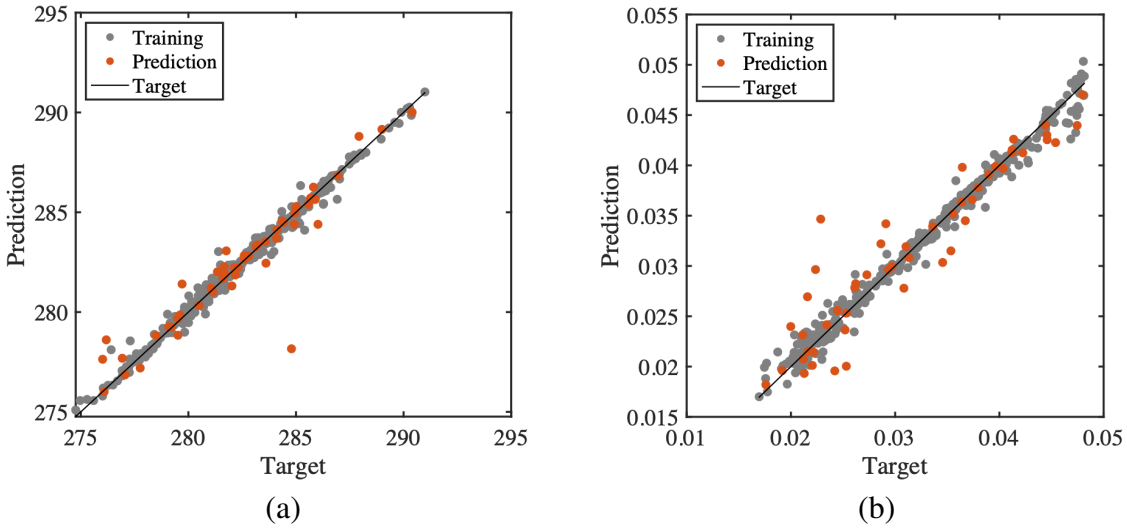

Figure 7.6: The performance of the ML models at 300 MPa. The outcomes from the ML models are compared for (a) transformation temperature M_s and (b) transformation strain ϵ_t^f to the target.

Using the prediction values of all fitting parameters from the ML models, the whole SMA response can be reproduced using Eq. (7.9) and Eq. (7.10). Figure 7.7 (a-d) shows responses generated using the ML framework for four random orientations taken from the training set. The predictions are compared with the target responses from the crystal plasticity model. Here the responses from the ML model match very well with the target responses. Similarly, Fig. 7.8 (a-d) shows the comparison of responses from ML model along four orientations from the testing set. The predictions from the ML model match well with the target response, indicating the ability of the ML model to predict the behavior along new orientations. With the performance of the ML framework for individual parameters and producing the whole responses, it can be concluded that the anisotropic behavior is captured successfully in the ML model at fixed stress levels.

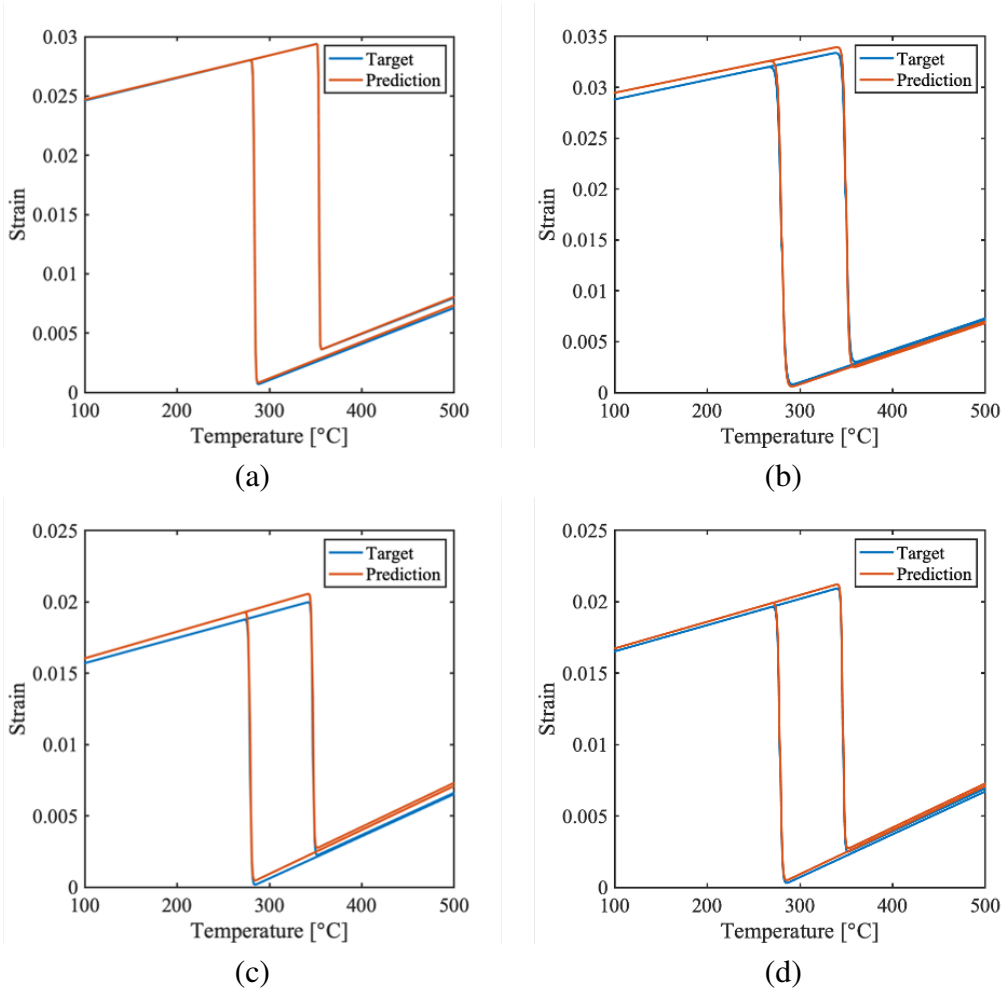

Figure 7.7: Four cases in the training set reproduced using the trained ML framework. The target responses are compared with the predictions.

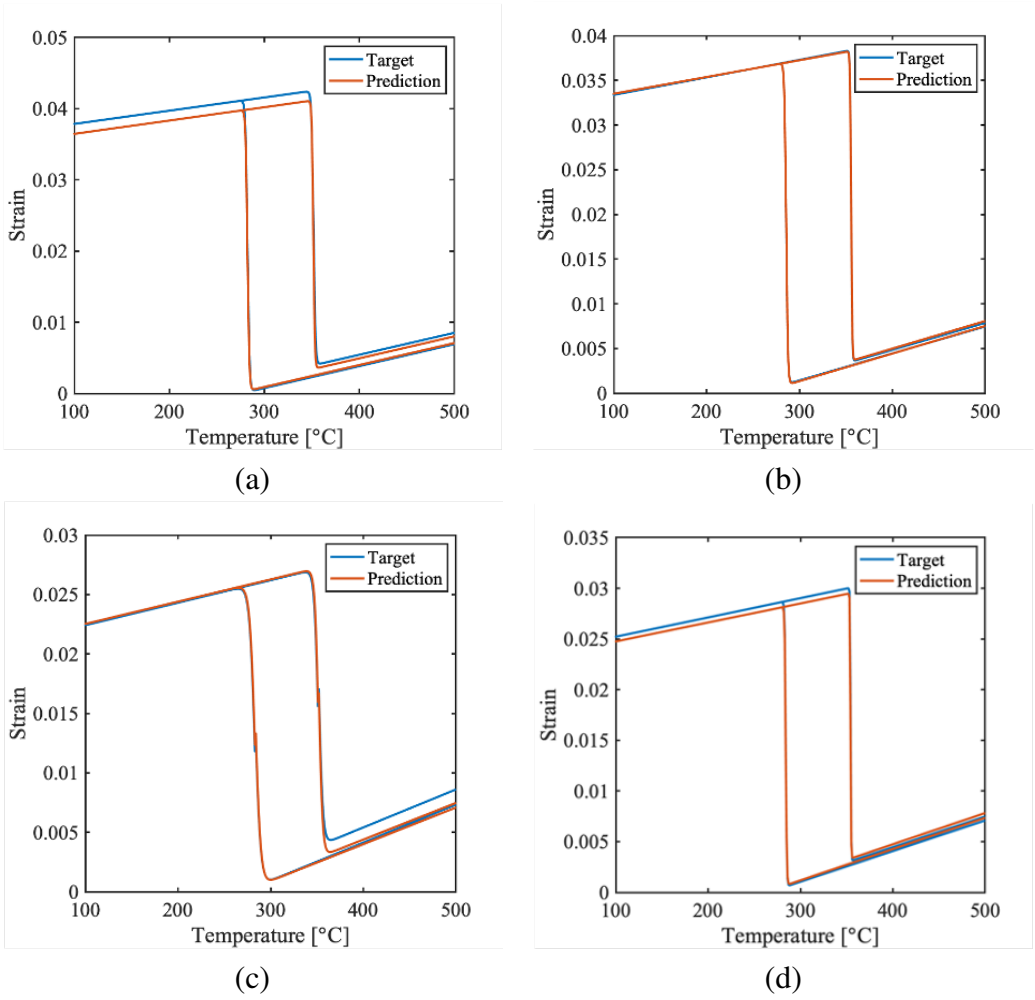

Figure 7.8: Four cases in the new orientation predicted using the trained ML framework. The predictions are compared with the target response.

Next, the ML framework was targeted to include the complexities of varying stress loading conditions in addition to the effect of orientation. For this, the training of the ML framework was done by including the responses from multiple stress levels. The responses from stress levels 50 MPa, 100 MPa, 150 MPa, 200 MPa and 300 MPa were used for training. The responses for stress level 250 MPa were simulated and compared with the ML framework predictions. At each stress level, responses in 450 orientations were included in the training and the remaining 50 were used for testing at the training stress level.

Figure 7.9(a-b) shows the transformation temperature and transformation strain predictions considering all stress levels. The data used for training in the training stress levels are shown with respective stress levels. The ML framework reproduces the training stress level data close to the 'Target' line. Further, the Target (σ =training) compares the prediction of the ML framework for the 50 new orientations that were not used for training from the training stress levels. These new orientations are predicted well, as they can be seen to match with the target values.

The Target ($\sigma = 250$ MPa) in Fig. 7.9 shows the predictions of the ML framework in the new stress level that was not used in the training. For the new stress level, the transformation temperature predictions from the ML model are slightly lower than the Target values, as seen in Fig. 7.9 (a). However, the transformation strain variations with stress and orientation are not captured well as seen in Fig. 7.9 (b), and the performance is poor when considering the transformation temperatures. One reason for this could be that the transformation temperature experiences gradual variation with changing orientation, compared to transformation strain, which has more discrete variation. Gradual variations are more easily captured in the ML framework, and the transformation temperatures are captured better.

Using the predictions of all parameters with the ML framework, the full responses were simulated. Figure 7.10 shows the full response prediction in a random orientation for the training stress levels 50 MPa, 100 MPa, 150 MPa and 200 MPa. The ML framework was able to reproduce the responses with sufficient accuracy for the training stress levels. This is due to good performance of the ML framework in training stress levels for capturing individual parameters. In Fig. 7.11,

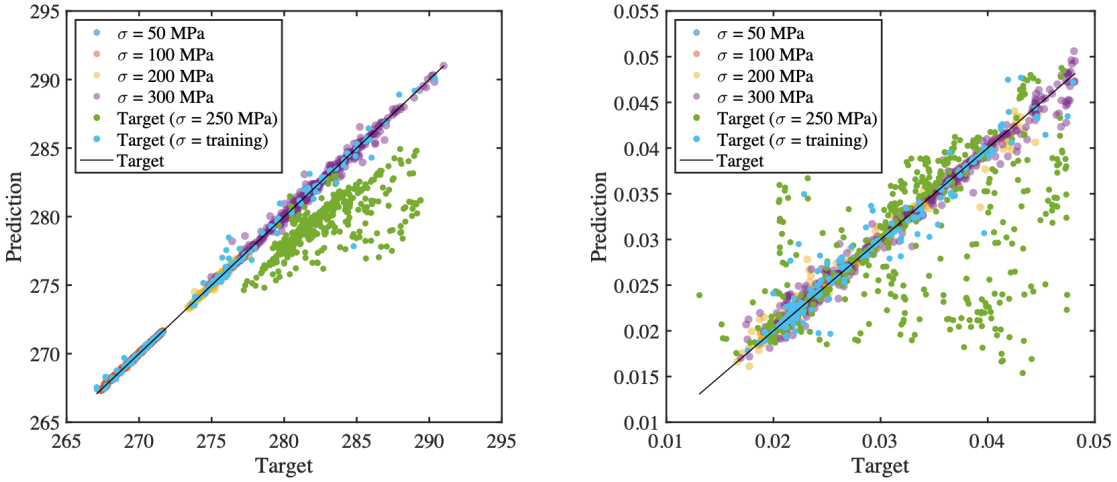

Figure 7.9: Comparison of prediction at different stress levels for (a)transformation temperature M_s (b) transformation strain.

the comparison of the full response predictions for the new stress level of 250 MPa to the target responses is shown. It can be seen that the ML framework makes poor predictions of the full response, as indicated by their poor performance in Fig. 7.9 for new stress levels.

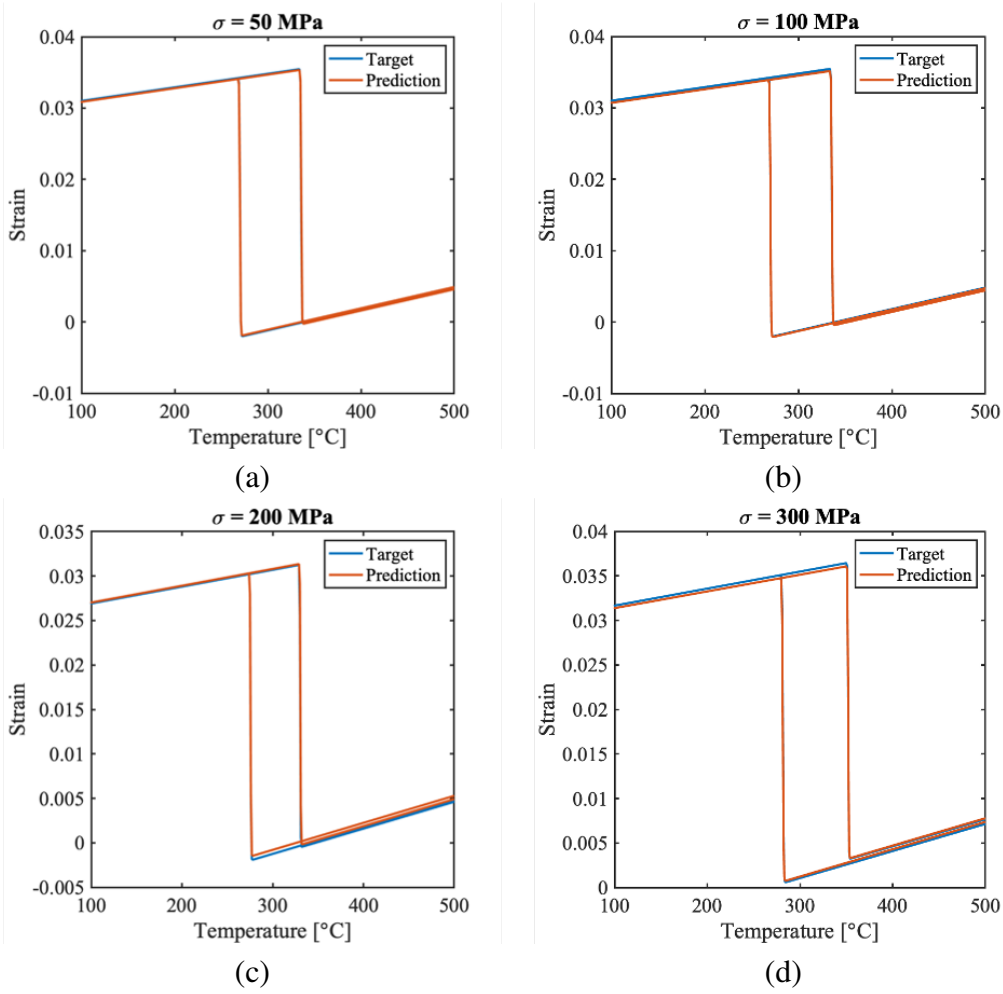

Figure 7.10: Prediction of whole responses in a random orientation for the training stress levels.

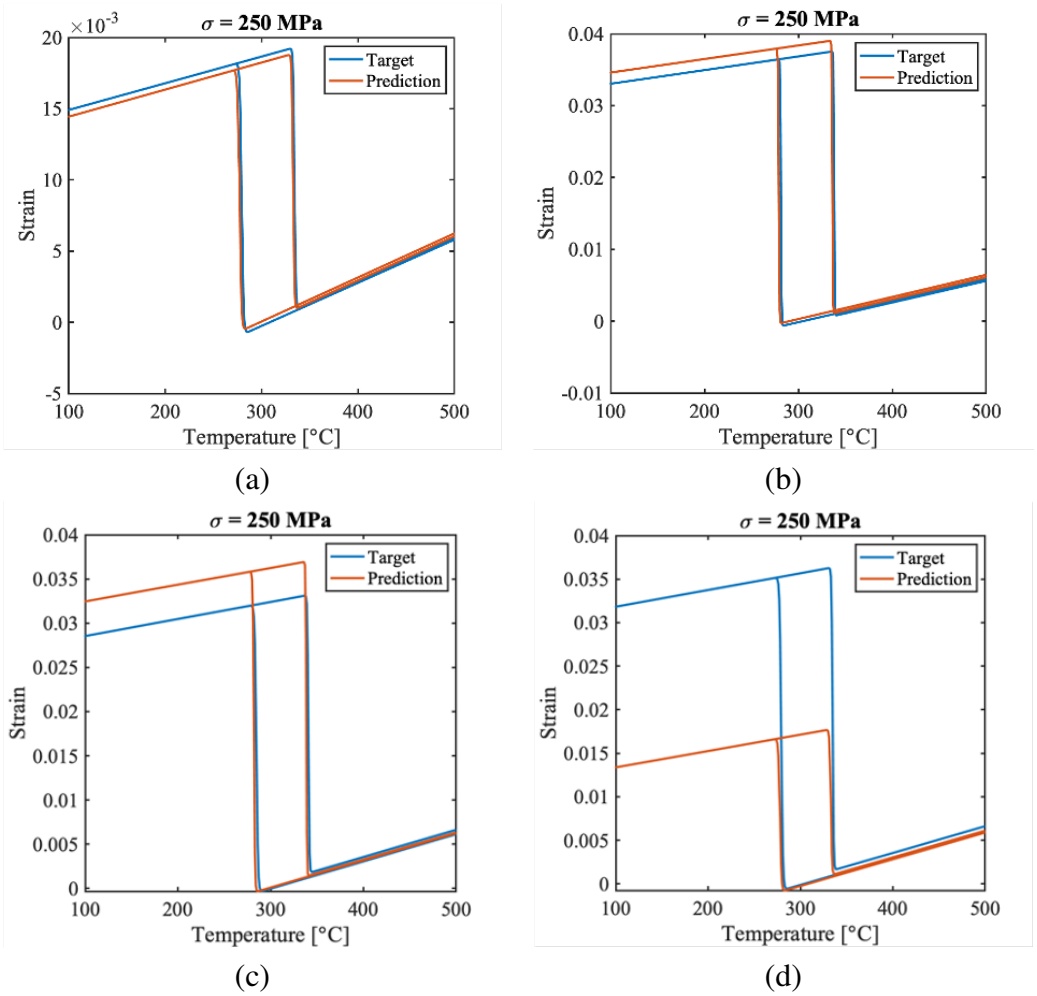

Figure 7.11: Prediction of whole responses in four different orientations for the new stress level 250 MPa.

7.5 Present study's applications, limitations and future directions

The developed Machine Learning (ML) framework has been demonstrated to successfully for its ability to model the anisotropic variations in phase transformation for single crystal SMAs. The model is thus useful for multiscale modeling of SMAs through up-scaling the interactions starting with the single crystal responses. A future work along these lines is to model the polycrystal behavior of SMAs through multiscale modeling using the developed ML modeling incorporating the grain level interactions. Another direction of interest is the modeling of the effects of precipitation on single crystal behavior and incorporating them in the ML model environment. With these two proposed developments, the modeling effort can be targeted to predict the polycrystal SMA behavior directly from the crystallography and precipitate microstructure using data based ML tools. An improvement in the current ML framework to accurately capture the stress effects is desired for future efforts in multiscale modeling.

7.6 Conclusions

A data based Machine Learning (ML) framework to fit anisotropic responses in single crystal SMA was developed. The training of the model was performed using a crystal plasticity model that captured viscoplasticity and phase transformation interactions. The key features in the responses were extracted using a fit that captured the stress-temperature responses from the crystal plasticity model. Further, the ML framework was built based on Gaussian Process Regression (GPR) models capturing the variation of the features with orientations. The ML framework successfully predicted the anisotropic variation of the features along new orientations and reproduced the full stress-temperature SMA response. Further, the modeling was tested for its ability to capture stress effects in addition to the anisotropic variation by including data from different stress levels. The model captured the training data with good accuracy, while it did not predict well the responses for new stress level. Future works will be focusing on better capturing the stress effects and furthering multiscale modeling towards predicting polycrystal behaviors.

8. SUMMARY AND FUTURE WORK

8.1 Conclusions and Summary

Aging heat treatments in NiTiHf SMAs produce nano-sized precipitates, which significantly modifies their phase transformation behavior. The change in behavior is attributable to underlying microstructural modification of the material. These modifications include but are not limited to compositional changes during diffusion, creation of new phases, mechanical effects of precipitates on phase transformation, coherency between phases, modification of material properties and change in the crystallography. Micromechanics is the study of mechanics at the micro-level and is relevant in the context of NiTiHf SMAs in understanding the effect of microstructural changes on such modified phase transformation behavior. Through micromechanical modeling, the desired microstructures in NiTiHf can be identified, and specific heat treatments required in order to determine a specific phase transformation behavior. An understanding of the microstructure and the mechanisms affecting material behavior are necessary for micromechanical modeling. For NiTiHf, this involves a process of investigating, discovering, understanding and modeling the micro-level mechanisms that determine the new behavior.

The presented work showed the development of a micromechanical modeling framework (Chapter 2) for precipitation hardened NiTiHf SMAs. Experimental investigation of the material behavior and micrographs of the microstructure were instrumental in understanding the mechanisms and development of the modeling framework. 3D tomographic representations were used for a better description of the precipitate morphology, and new methods of estimating the volume fraction of precipitates from externally measurable transformation temperature properties were developed. A new phenomenon of composition effect on phase transformation strain was identified. The identified mechanisms were then incorporated in the model and the actuation behavior of different precipitated SMAs were simulated.

Within the modeling framework, the research questions of finding faster solution techniques

and estimating statistics of representative volume elements were of interest. The Fast Fourier Transform (FFT) based solver gave the advantage of reduced computational cost. Further, solutions involving larger RVEs and the responses in different RVE realizations were explored. This helped in evaluating statistical effectiveness of RVEs in predicting the effective response. These investigations led to the development of higher order statistical relationships for RVEs for quantifying the dispersion in the effective response. The enormous amount of data generated using FFT solution methodology helped further the development of data-based tools for micromechanics, and a Machine Learning (ML) framework that uses 2-point statistical representation for RVEs was developed.

While the focus of these tasks was capturing the actuation behavior with complete phase transformation cycles (major cycles), predicting more complex partial cycle behaviors is of critical importance for the actuation designing process and development of control algorithms for actuation. This challenge was addressed by developing a data-based ML modeling framework. The developed ML tool was implemented on NiTiHf experimental responses. Further, a preliminary work in progressing multiscale modeling with modeling of anisotropic single crystal SMA responses using data-based techniques was attempted.

As shown in the previous chapters of this dissertation, tools were developed that can assist the prediction of actuation behaviors in NiTiHf SMAs. The work successfully explored new horizons such as the statistics of RVEs, uncertainty quantification and data-based modeling techniques, and incorporated these in the micromechanical modeling. Detailed descriptions of the findings and key insights from different chapters are listed below.

8.1.1 Micromechanical modeling of NiTiHf SMA actuation

The phase transformation behavior of precipitation-hardened NiTiHf SMAs was investigated with the developed micromechanical modeling framework. After precipitation, the aged NiTiHf SMAs were found to produce higher transformation strain. This was unexpected because, intuitively, the non-transforming precipitates should reduce the transformation strain as they restrain phase transformation. Further investigation of NiTiHf SMA responses with various compositions

revealed that this observed increase in transformation strain might occur because of a composition dependency of transformation strain at the micro-level. By accounting for the phenomenon in the micromechanical modeling, the predictions of the micromechanical modeling were improved. RVEs of the microstructure were generated using two different methods: 1) ellipsoidal RVEs and 2) RVEs based on TEM reconstructions of aged SMAs. In the ellipsoidal RVEs, the volume fractions were estimated from transformation temperatures of the aged SMA measured using DSC techniques. In TEM RVEs, the precipitate microstructure morphology were extracted directly from 3D reconstructions from many TEM images generated using a tilting experiment. With these methodologies, the behavior of different NiTiHf SMAs was investigated. Key results from the study are the following:

1. The volume fraction of precipitation was found to be the primary parameter deciding the new phase-transformation response.

2. By accounting for the composition dependency of transformation strain at the micro-level, the increasing of transformation strain with precipitation in NiTiHf SMAs was explained.

3. In comparing the predictions from two RVE generation methodologies (ellipsoidal shaped RVEs and 3D TEM RVEs), they were qualitatively close to the experimental responses. As the ellipsoidal RVEs were less expensive to generate, they proved to be useful for future predictions and optimization purposes.

4. The developed micromechanical model accounting for the microstructural and composition effects was used to study the responses in NiTiHf SMAs that had undergone two processing histories: hot forging and hot extrusion. By calibrating the modeling framework in the alloys from the two processing, new heat treatment responses were predicted.

The developed micromechanical framework proved valuable for the optimization of heat treatment processes to achieve desired microstructures. Next, Fast Fourier Transform (FFT) based solution methodology was introduced in the micromechanical framework for solving the RVE

boundary problem with less computational cost and thereby making analyzing of larger RVEs computationally less costly.

8.1.2 Fast Fourier transform (FFT) based solution for SMA micromechanics

The recently developed FFT methodology in SMA micromechanics uses a Fourier transform based formulation to simplify integrals in the discretized weak form of boundary value problems. The trigonometric shape functions used in FFT methodology cover the whole RVE region, and the periodic boundary conditions at the faces are inherently accounted for in the formulation. One disadvantage of the FFT methodology is that the formulation is currently restricted to using voxel mesh discretization. Therefore, the performance of FFT and Finite Element Analysis (FEA) method using conforming mesh types for solving the same RVE behavior was of interest. A comparative study on the convergence of FFT voxel with FEA linear (C3D4), FEA quadratic modified (C3D10M) and FEA (voxel) was performed in solving the homogenized response in the SMA micromechanical model. Results were analyzed using three different convergence criteria: two area criteria that analyzed the convergence of the overall response and one particular strain value criterion that analyzed the convergence of maximum strain value in the responses. The analysis using the two average convergence criteria showed that the three methods FFT (voxel), FEA (C3D4) and FEA (C3D10M) have closer convergence and much higher accuracy compared to the FEA (voxel) method. The convergence and accuracy for the maximum strain value in the study gave FEA (C3D4)$>$ FFT (voxel) $>$ FEA (C3D10M) $>$ FEA (voxel). As the FFT (voxel) and FEA (C3D4) exhibited performance in the same order, their CPU solving times were compared. This time comparison showed that the FFT (voxel) method solves at least four times faster than the FEA (C3D4). One key difference between the two was FFT used an iterative solver and FEA used a direct solver. Future studies should clarify these comparisons by using the same type of solver.

The FFT method was then used for investigating RVE size convergence in the SMA micromechanical model. The effective response dispersion was estimated from many realizations of RVEs at different volume fractions and number of precipitates (equivalent to their size). Smaller RVEs produced higher dispersion in the prediction, which can be attributed to the fluctuating local strain

distribution with fewer precipitates modeled in the RVEs. With an increasing number of precipitates in the RVE, the dispersion of the effective response was reduced. The effectiveness of the RVE size was analyzed using the relation built on the evolution of dispersion with number of precipitates modeled. Based on the analysis, larger RVEs are needed to capture the responses more accurately at higher volume fractions. Results showed that dispersion versus RVE size can be correlated with simple relations for a given microstructure and volume fraction. The existing relations to quantify the statistics of dispersion in the RVEs were found to be sensitive to changing volume fraction and microstructure.

The study highlighted the need for a robust methodology to capture RVE dispersion, which can be generalized between the microstructures and volume fraction. Therefore, a new methodology was developed to capture the RVE dispersion across changing microstructure and volume fraction, to further aid in estimating converged RVE size and reducing the uncertainty in the predictions.

8.1.3 Statistics of representative volume in micromechanics

In micromechanical homogenization modeling, determining the converged RVEs is important for more precise predictions. A new analytical approach for quantifying the statistics of effective strain dispersion was developed. The formulation was built on the idea of describing individual RVE behavior through perturbations from the ensemble average behavior. The expression for effective strain dispersion was simplified in terms of average behavior and standard deviation of perturbations. Further, assuming relations between the perturbations and local strain distribution, the effective strain dispersion was related only in terms of local strain distribution. The developed relations were found to be of the 2^{nd} order on point variance of strain. The new relation was able to capture higher order effects and found to be robust compared to previous methods that considered only linear correlations. The proposed 2^{nd} order effects in the new formulation were validated by quantifying the dispersion of effective SMA behaviors in the precipitated microstructure RVEs. With changing volume fraction, aspect ratio, and number of precipitates, the statistics in the SMA responses were examined. The effects of changing microstructure and number of precipitates were shown to be captured in the 2^{nd} order formulations. Hence, the developed 2^{nd} order relations were

more robust towards changes in the microstructure compared to the previous relations, which had volume fraction dependency.

Next, an extension to data-based approaches was made, because of the large amount of data generated in the statistical study. With the goal of faster micromechanical model estimations for new RVEs, the capabilities of data-based machine learning tools were explored.

8.1.4 Data-based techniques for micromechanics

A Machine Learning (ML) model (refer Chapter 5) to predict precipitation hardened phase transformation behaviors taking RVEs as inputs was developed. The SMA thermo-mechanical responses from many RVEs of different volume fractions and number of precipitates were used to train the ML model. The RVEs were represented using 2-point correlation and then reduced to low-dimensional representations using Principal Component Analysis (PCA). The Principal Components (PC) of the RVEs and material parameters were used as inputs in the ML model, and the effective response from the micromechanical model was then targeted.

A recurrent neural network based model is used to predict the effective strain change with temperature change. The model demonstrated two capabilities: 1) it predicted the response of larger RVEs training on the simulations of smaller RVEs, and 2) it predicted the responses of new volume fraction RVEs by training from other volume fraction RVEs. The predictions in both of these scenarios were qualitatively close to the target response. The study showed promising scope for the use of a data-based ML tool in SMA micromechanics.

Next, a similar approach of data-based modeling was explored for predicting partial phase transformation responses by training on full transformation actuation cycles. A similar recurrent neural network based modeling approach was also used to predict the phase transformation response.

8.1.5 Data-based techniques for modeling SMA response with partial transformation

A data-based Machine Learning (ML) framework (refer Chapter 6) to predict the experimentally observed non-linear actuation responses of Shape Memory Alloys (SMAs) was developed,

using a recurrent neural network based method. When actuation responses in the NiTiHf High Temperature SMA (HTSMA) were trained in the developed ML framework, the trained model successfully reproduced the actuation behaviors. To demonstrate the predictive capabilities of the model, many partial transformation cycles inside the major hysteresis loop were predicted. When compared with experimental measurements, the model captured the evolution of partial transformation branches. This indicates the developed framework will be useful for predicting partial transformation in applications and will aid in creating control algorithms for SMAs.

Next, the performance of a ML based framework for capturing anisotropic single crystal SMA responses was explored.

8.1.6 Data-based techniques for anisotropic SMA response

Data-driven Machine Learning (ML) tools were developed to capture the anisotropy of single crystal SMA responses. To train the model, a crystal plasticity model which modeled viscoplasticity and phase transformation interactions was used. The developed ML framework used Gaussian Process regression (GPR) models to capture feature variations in the responses with changing orientation. In fixed stress responses, the ML framework accurately captured the variation of anisotropy with changing orientations and accurately predicted the full stress-temperature SMA response. With data at new stress levels, the ML framework was extended to capture stress effects together with anisotropy. The model accurately captured the training data, but did not accurately predict the variations at new stress levels. Future research will concentrate on capturing stress effects and the further up-scaling of interactions in order to predict polycrystal responses.

8.2 Recommended future research

Some areas of potential future research related to the presented work were identified:

- A compositional dependency of transformation strain in NiTiHf SMAs was observed (Chapter 2). Currently, few experiments are available to calibrate this phenomenon. An experimental investigation of these effects with a focus on different NiTiHf compositions is needed for better understanding the composition effect.

- Different processing was shown to affect the transformation strain in NiTiHf polycrystals due to differences in crystallography (Chapter 2). Further investigation of the effects of the crystallographic distribution on phase transformation strain in NiTiHf SMAs is needed.

- The presented comparison of computation time in Chapter 3 used an iterative solver for FFT and a direct solver for FEA. A study with iterative solvers in both FEA and FFT would be beneficial.

- In the presented work, a new statistical relation was validated for isotropic SMA responses (Chapter 4). Future investigation into validation of the formulation with anisotropic non-linear material modeling would be of interest.

- Some potential benefits of data-based modeling in micromechanics of SMAs (Chapter 5) were presented. Incorporating minor loop behavior in micromechanical modeling would advance this work further.

- The application of data based modeling in actuation responses of SMAs for the prediction of minor cycles was presented (Chapter 6). However, the predictions of inner cycle responses could not be validated with experiments. A future investigation with predictions for inner cycles with experimental validation is needed.

- Some basic tools for multiscale modeling using data-based techniques for the anisotropic single crystal behavior were developed (Chapter 7). Further progress in this direction to capture the polycrystal behavior with up-scaling of phenomenons from the crystal level would be beneficial.

REFERENCES

[1] A. Solomou, G. Zhao, S. Boluki, J. K. Joy, X. Qian, I. Karaman, R. Arróyave, and D. C. Lagoudas, "Multi-objective bayesian materials discovery: Application on the discovery of precipitation strengthened niti shape memory alloys through micromechanical modeling," *Materials & Design*, vol. 160, pp. 810–827, 2018.

[2] J. Frenzel, E. P. George, A. Dlouhy, C. Somsen, M.-X. Wagner, and G. Eggeler, "Influence of ni on martensitic phase transformations in niti shape memory alloys," *Acta Materialia*, vol. 58, no. 9, pp. 3444–3458, 2010.

[3] T. Umale, D. Salas, B. Tomes, R. Arroyave, and I. Karaman, "The effects of wide range of compositional changes on the martensitic transformation characteristics of nitihf shape memory alloys," *Scripta Materialia*, vol. 161, pp. 78–83, 2019.

[4] A. Evirgen, *Microstructural characterization and shape memory response of Ni-rich NiTiHf and NiTiZr high temperature shape memory alloys*. PhD thesis, 2014.

[5] D. Lagoudas, D. Hartl, Y. Chemisky, L. MacHado, and P. Popov, "Constitutive model for the numerical analysis of phase transformation in polycrystalline shape memory alloys," *International Journal of Plasticity*, vol. 32-33, pp. 155–183, 2012.

[6] A. Cox, B. Franco, S. Wang, T. Baxevanis, I. Karaman, and D. C. Lagoudas, "Predictive Modeling of the Constitutive Response of Precipitation Hardened Ni-Rich NiTi," *Shape Memory and Superelasticity*, vol. 3, no. 1, pp. 9–23, 2017.

[7] T. Kanit, S. Forest, I. Galliet, V. Mounoury, and D. Jeulin, "Determination of the size of the representative volume element for random composites: statistical and numerical approach," *International Journal of solids and structures*, vol. 40, no. 13-14, pp. 3647–3679, 2003.

[8] D. C. Lagoudas, *Shape memory alloys: modeling and engineering applications*. Springer, 2008.

[9] O. Benafan, J. Brown, F. Calkins, P. Kumar, A. Stebner, T. Turner, R. Vaidyanathan, J. Webster, and M. Young, "Shape memory alloy actuator design: Casmart collaborative best practices and case studies," *International Journal of Mechanics and Materials in Design*, vol. 10, no. 1, pp. 1–42, 2014.

[10] J. M. Jani, M. Leary, A. Subic, and M. A. Gibson, "A review of shape memory alloy research, applications and opportunities," *Materials & Design (1980-2015)*, vol. 56, pp. 1078–1113, 2014.

[11] D. J. Hartl and D. C. Lagoudas, "Aerospace applications of shape memory alloys," *Proceedings of the Institution of Mechanical Engineers, Part G: Journal of Aerospace Engineering*, vol. 221, no. 4, pp. 535–552, 2007.

[12] F. T. Calkins and J. H. Mabe, "Shape memory alloy based morphing aerostructures," *Journal of Mechanical Design*, vol. 132, no. 11, 2010.

[13] E. A. P. Hernandez, D. J. Hartl, and D. C. Lagoudas, *Active Origami: modeling, design, and applications*. Springer, 2018.

[14] H. Stroud and D. J. Hartl, "Shape memory alloy torsional actuators: a review of applications, experimental investigations, modeling, and design," *Smart Materials and Structures*, 2020.

[15] A. A. Karakalas, T. T. Machairas, D. C. Lagoudas, and D. A. Saravanos, "Design of morphing strips using sma actuators under partial phase transformation operation," in *Smart Materials, Adaptive Structures and Intelligent Systems*, vol. 84027, p. V001T04A021, American Society of Mechanical Engineers, 2020.

[16] O. Ozbulut, S. Hurlebaus, and R. Desroches, "Seismic response control using shape memory alloys: a review," *Journal of Intelligent Material Systems and Structures*, vol. 22, no. 14, pp. 1531–1549, 2011.

[17] G. Song, N. Ma, and H.-N. Li, "Applications of shape memory alloys in civil structures," *Engineering structures*, vol. 28, no. 9, pp. 1266–1274, 2006.

[18] J. Dong, C. Cai, and A. M. Okeil, "Overview of potential and existing applications of shape memory alloys in bridges," *Journal of Bridge Engineering*, vol. 16, no. 2, pp. 305–315, 2011.

[19] T. Duerig, A. Pelton, and D. Stöckel, "An overview of nitinol medical applications," *Materials Science and Engineering: A*, vol. 273, pp. 149–160, 1999.

[20] N. Morgan, "Medical shape memory alloy applications—the market and its products," *Materials Science and Engineering: A*, vol. 378, no. 1-2, pp. 16–23, 2004.

[21] L. Machado and M. Savi, "Medical applications of shape memory alloys," *Brazilian journal of medical and biological research*, vol. 36, no. 6, pp. 683–691, 2003.

[22] A. Bansiddhi, T. Sargeant, S. I. Stupp, and D. Dunand, "Porous niti for bone implants: a review," *Acta biomaterialia*, vol. 4, no. 4, pp. 773–782, 2008.

[23] M. H. Elahinia, M. Hashemi, M. Tabesh, and S. B. Bhaduri, "Manufacturing and processing of niti implants: A review," *Progress in materials science*, vol. 57, no. 5, pp. 911–946, 2012.

[24] J. Ma, I. Karaman, and R. Noebe, "High temperature shape memory alloys," *International Materials Reviews*, vol. 55, no. 5, pp. 257–315, 2010.

[25] O. Benafan, G. Bigelow, and D. Scheiman, "Transformation behavior in niti-20hf shape memory alloys–transformation temperatures and hardness," *Scripta Materialia*, vol. 146, pp. 251–254, 2018.

[26] J. Ma, I. Karaman, and R. D. Noebe, "High temperature shape memory alloys," *International Materials Reviews*, vol. 55, no. 5, pp. 257–315, 2010.

[27] H. Karaca, E. Acar, H. Tobe, and S. Saghaian, "Nitihf-based shape memory alloys," *Materials Science and Technology*, vol. 30, no. 13, pp. 1530–1544, 2014.

[28] S. Besseghini, E. Villa, and A. Tuissi, "Ni□ ti□ hf shape memory alloy: effect of aging and thermal cycling," *Materials Science and Engineering: A*, vol. 273, pp. 390–394, 1999.

[29] I. D. N. AbuJudom, P. E. Thoma, M.-Y. Kao, and D. R. Angst, "High transformation temperature shape memory alloy," May 19 1992. US Patent 5,114,504.

[30] H. E. Karaca, S. M. Saghaian, G. Ded, H. Tobe, B. Basaran, H. J. Maier, R. D. Noebe, and Y. I. Chumlyakov, "Effects of nanoprecipitation on the shape memory and material properties of an Ni-rich NiTiHf high temperature shape memory alloy," *Acta Materialia*, vol. 61, no. 19, pp. 7422–7431, 2013.

[31] A. A. Karakalas and D. C. Lagoudas, "Preliminary design and numerical investigation of sma torsion tubes for the actuation of articulated adaptive panels," in *AIAA Scitech 2021 Forum*, p. 1318, 2021.

[32] J. H. Mabe, D. J. Hartl, N. Tichenor, M. Zackery, E. Blades, and M. Nucci, "Fluid-structure interaction modeling of a shape-memory alloy actuated supersonic wind tunnel model alloy," in *AIAA Scitech 2019 Forum*, p. 0602, 2019.

[33] J. Mabe, S. Frederes, D. Hartl, and F. Carpenter, "A direct comparison of shape memory alloy and electromechanical actuation for wing twist applications," in *Behavior and Mechanics of Multifunctional Materials IX*, vol. 11377, p. 113770L, International Society for Optics and Photonics, 2020.

[34] A. Evirgen, I. Karaman, R. Santamarta, J. Pons, and R. D. Noebe, "Microstructural characterization and shape memory characteristics of the Ni50.3Ti34.7Hf15 shape memory alloy," *Acta Materialia*, vol. 83, pp. 48–60, 2015.

[35] O. Karakoc, C. Hayrettin, A. Evirgen, R. Santamarta, D. Canadinc, R. Wheeler, S. Wang, D. Lagoudas, and I. Karaman, "Role of microstructure on the actuation fatigue performance of ni-rich nitihf high temperature shape memory alloys," *Acta Materialia*, vol. 175, pp. 107–120, 2019.

[36] J. G. Boyd and D. C. Lagoudas, "A thermodynamical constitutive model for shape memory materials. part i. the monolithic shape memory alloy," *International Journal of Plasticity*, vol. 12, no. 6, pp. 805–842, 1996.

[37] D. C. Lagoudas, Z. Bo, and M. A. Qidwai, "A unified thermodynamic constitutive model for sma and finite element analysis of active metal matrix composites," *Mechanics of composite materials and structures*, vol. 3, no. 2, pp. 153–179, 1996.

[38] D. Lagoudas, D. Hartl, Y. Chemisky, L. Machado, and P. Popov, "Constitutive model for the numerical analysis of phase transformation in polycrystalline shape memory alloys," *International Journal of Plasticity*, vol. 32, pp. 155–183, 2012.

[39] M. Qidwai and D. Lagoudas, "Numerical implementation of a shape memory alloy thermomechanical constitutive model using return mapping algorithms," *International Journal for Numerical Methods in Engineering*, vol. 47, no. 6, pp. 1123–1168, 2000.

[40] J. D. Eshelby, "The determination of the elastic field of an ellipsoidal inclusion, and related problems," *Proceedings of the royal society of London. Series A. Mathematical and physical sciences*, vol. 241, no. 1226, pp. 376–396, 1957.

[41] T. Mori and K. Tanaka, "Average stress in matrix and average elastic energy of materials with misfitting inclusions," *Acta metallurgica*, vol. 21, no. 5, pp. 571–574, 1973.

[42] T. Mura, *Micromechanics of defects in solids*. Springer Science & Business Media, 2013.

[43] S. Nemat-Nasser and M. Hori, *Micromechanics: overall properties of heterogeneous materials*. Elsevier, 2013.

[44] D. Krajcinovic, *Damage mechanics*. Elsevier, 1996.

[45] F. Roters, P. Eisenlohr, L. Hantcherli, D. Tjahjanto, T. Bieler, and D. Raabe, "Overview of constitutive laws, kinematics, homogenization and multiscale methods in crystal plasticity finite-element modeling: Theory, experiments, applications," *Acta Materialia*, vol. 58, no. 4, pp. 1152 – 1211, 2010.

[46] A. Cruzado, B. Gan, M. Jiménez, D. Barba, K. Ostolaza, A. Linaza, J. Molina-Aldareguia, J. Llorca, and J. Segurado, "Multiscale modeling of the mechanical behavior of IN718 superalloy based on micropillar compression and computational homogenization," *Acta Materialia*, vol. 98, pp. 242 – 253, 2015.

[47] E. J. Pineda, B. A. Bednarcyk, A. M. Waas, and S. M. Arnold, "Progressive failure of a unidirectional fiber-reinforced composite using the method of cells: Discretization objective computational results," *International Journal of Solids and Structures*, vol. 50, pp. 1203 – 1216, 2013.

[48] A. Cruzado, S. Lucarini, J. LLorca, and J. Segurado, "Microstructure-based fatigue life model of metallic alloys with bilinear coffin-manson behavior," *International Journal of Fatigue*, vol. 107, no. Supplement C, pp. 40 – 48, 2018.

[49] T. Baxevanis, A. Solomou, I. Karaman, and D. C. Lagoudas, *Full-Field Micromechanics of Precipitated Shape Memory Alloys*, pp. 225–255. Cham: Springer International Publishing, 2018.

[50] H. Moulinec and P. Suquet, "A fast numerical method for computing the linear and nonlinear properties of composites," *Comptes rendus de l'Académie des sciences Paris II*, vol. 318, pp. 1417 – 1423, 1994.

[51] R. A. Lebensohn, A. D. Rollett, and P. Suquet, "Fast fourier transform-based modeling for the determination of micromechanical fields in polycrystals," *Jom*, vol. 63, no. 3, pp. 13–18, 2011.

[52] A. Richards, R. Lebensohn, and K. Bhattacharya, "Interplay of martensitic phase transformation and plastic slip in polycrystals," *Acta Materialia*, vol. 61, no. 12, pp. 4384 – 4397, 2013.

[53] M. Kabel, T. Böhlke, and M. Schneider, "Efficient fixed point and newton–krylov solvers for fft-based homogenization of elasticity at large deformations," *Computational Mechanics*, vol. 54, pp. 1497–1514, Dec 2014.

[54] J. Zeman, T. W. de Geus, J. Vondřejc, R. H. Peerlings, and M. G. Geers, "A finite element perspective on nonlinear fft-based micromechanical simulations," *International Journal for Numerical Methods in Engineering*, vol. 111, no. 10, pp. 903–926, 2017.

[55] S. Lucarini and J. Segurado, "On the accuracy of spectral solvers for micromechanics based fatigue modeling," *Computational Mechanics*, vol. 63, pp. 365 – 382, 2019.

[56] R. Hill, "Elastic properties of reinforced solids: some theoretical principles," *Journal of the Mechanics and Physics of Solids*, vol. 11, no. 5, pp. 357–372, 1963.

[57] T. Yu, Y. Gao, L. Casalena, P. Anderson, M. Mills, and Y. Wang, "H-phase precipitation and its effects on martensitic transformation in niti-hf high-temperature shape memory alloys," *Acta Materialia*, vol. 208, p. 116651, 2021.

[58] T. Baxevanis, A. Cox, and D. C. Lagoudas, "Micromechanics of precipitated near-equiatomic Ni-rich NiTi shape memory alloys," *Acta Mechanica*, vol. 225, pp. 1167–1185, 2014.

[59] J. Joy, A. Solomou, T. Baxevanis, and D. Lagoudas, "Predicting the constitutive response of precipitation hardened NiTiHf," *Proceedings of SPIE - The International Society for Optical Engineering*, vol. 10165, p. 101650F, 2017.

[60] A. Cecen, H. Dai, Y. C. Yabansu, S. R. Kalidindi, and L. Song, "Material structure-property linkages using three-dimensional convolutional neural networks," *Acta Materialia*, vol. 146, pp. 76–84, 2018.

[61] M. I. Latypov and S. R. Kalidindi, "Data-driven reduced order models for effective yield strength and partitioning of strain in multiphase materials," *Journal of Computational Physics*, vol. 346, pp. 242–261, 2017.

[62] S. R. Kalidindi, *Hierarchical materials informatics: novel analytics for materials data*. Elsevier, 2015.

[63] M. Pathan, S. Ponnusami, J. Pathan, R. Pitisongsawat, B. Erice, N. Petrinic, and V. Tagarielli, "Predictions of the mechanical properties of unidirectional fibre composites by supervised machine learning," *Scientific Reports*, vol. 9, no. 1, pp. 1–10, 2019.

[64] F. E. Bock, R. C. Aydin, C. J. Cyron, N. Huber, S. R. Kalidindi, and B. Klusemann, "A review of the application of machine learning and data mining approaches in continuum materials mechanics," *Frontiers in Materials*, vol. 6, p. 110, 2019.

[65] D. Wheeler, D. Brough, T. Fast, S. Kalidindi, and A. Reid, "PyMKS: Materials Knowledge System in Python," 5 2014.

[66] A. A. Karakalas, T. T. Machairas, and D. A. Saravanos, "Effect of shape memory alloys partial transformation on the response of morphing structures encompassing shape memory alloy wire actuators," *Journal of Intelligent Material Systems and Structures*, vol. 30, no. 11, pp. 1682–1698, 2019.

[67] A. A. Karakalas and D. C. Lagoudas, "Effect of tension-compression asymmetry and partial transformation on the response of shape memory alloy beam structures," in *Behavior and Mechanics of Multifunctional Materials IX*, vol. 11377, p. 1137715, International Society for Optics and Photonics, 2020.

[68] G. Scalet, A. Karakalas, L. Xu, and D. Lagoudas, "Finite strain constitutive modelling of shape memory alloys considering partial phase transformation with transformation-induced plasticity," *Shape Memory and Superelasticity*, pp. 1–16, 2021.

[69] W. Zhang, *Computational ecology: artificial neural networks and their applications*. World Scientific, 2010.

[70] S. Elkatatny, Z. Tariq, M. Mahmoud, A. Abdulraheem, and I. Mohamed, "An integrated approach for estimating static young's modulus using artificial intelligence tools," *Neural Computing and Applications*, vol. 31, no. 8, pp. 4123–4135, 2019.

[71] M. L. du Bos, F. Balabdaoui, and J. N. Heidenreich, "Modeling stress-strain curves with neural networks: a scalable alternative to the return mapping algorithm," *Computational Materials Science*, vol. 178, p. 109629, 2020.

[72] J. Owusu-Danquah, A. Bseiso, and S. Allena, "Artificial neural network models to predict the response of 55niti shape memory alloy under stress and thermal cycles," *Neural Computing and Applications*, pp. 1–14, 2021.

[73] G. Song, V. Chaudhry, and C. Batur, "A neural network inverse model for a shape memory alloy wire actuator," *Journal of intelligent material systems and structures*, vol. 14, no. 6, pp. 371–377, 2003.

[74] J. K. Joy, T. Umale, D. Zhao, A. Solomou, K. Xie, I. Karaman, and D. C. Lagoudas, "Effects of microstructure and composition on constitutive response of high temperature shape memory alloys: micromechanical modeling using 3-d reconstructions with experimental validation," *Acta Materialia*, p. 117929, 2022.

[75] Z. Lu and G. Weng, "Martensitic transformation and stress-strain relations of shape-memory alloys," *Journal of the Mechanics and Physics of Solids*, vol. 45, no. 11-12, pp. 1905–1928, 1997.

[76] Z. Lu and G. Weng, "A self-consistent model for the stress–strain behavior of shape-memory alloy polycrystals," *Acta Materialia*, vol. 46, no. 15, pp. 5423–5433, 1998.

[77] C. Collard and T. Ben Zineb, "Simulation of the effect of elastic precipitates in SMA materials based on a micromechanical model," *Composites Part B: Engineering*, vol. 43, no. 6, pp. 2560–2576, 2012.

[78] C. Collard, T. Ben Zineb, E. Patoor, and M. O. Ben Salah, "Micromechanical analysis of precipitate effects on shape memory alloys behaviour," *Materials Science and Engineering A*, vol. 481-482, no. 1-2 C, pp. 366–370, 2008.

[79] J. G. Boyd and D. C. Lagoudas, "Thermomechanical Response of Shape Memory Composites," *Journal of Intelligent Material Systems and Structures*, vol. 5, no. May, pp. 333–346, 1994.

[80] J. G. Boyd and D. C. Lagoudas, "A thermodynamical constitutive model for shape memory materials. part ii. the sma composite material," *International Journal of Plasticity*, vol. 12, no. 7, pp. 843–873, 1996.

[81] V. Birman, "Properties and response of composite material with spheroidal superelastic shape memory alloy inclusions subject to three-dimensional stress state," *J. Phys. D: Appl. Phys.*, vol. 43, no. 22, pp. 225402–(5pp), 2010.

[82] A. Cox, B. Franco, S. Wang, T. Baxevanis, I. Karaman, and D. Lagoudas, "Predictive modeling of the constitutive response of precipitation hardened ni-rich niti," *Shape Memory and Superelasticity*, vol. 3, no. 1, pp. 9–23, 2017.

[83] F. Yang, D. R. Coughlin, P. J. Phillips, L. Yang, A. Devaraj, L. Kovarik, R. D. Noebe, and M. J. Mills, "Structure analysis of a precipitate phase in an Ni-rich high-temperature NiTiHf shape memory alloy," *Acta Materialia*, vol. 61, no. 9, pp. 3335–3346, 2013.

[84] L. Casalena, J. Sosa, D. Coughlin, F. Yang, X. Chen, H. Paranjape, Y. Gao, R. Noebe, G. Bigelow, D. Gaydosh, *et al.*, "Revealing transformation and deformation mechanisms in nitihf and nitiau high temperature shape memory alloys through microstructural investigations," *Microscopy and Microanalysis*, vol. 22, no. S3, pp. 1954–1955, 2016.

[85] *Tomviz software for tomographic visualization of 3D scientific data*. http://www.tomviz.org/.

[86] B. D. Levin, Y. Jiang, E. Padgett, S. Waldon, C. Quammen, C. Harris, U. Ayachit, M. Hanwell, P. Ercius, D. A. Muller, *et al.*, "Tutorial on the visualization of volumetric data using tomviz," *Microscopy Today*, vol. 26, no. 1, pp. 12–17, 2018.

[87] J. Ahrens, B. Geveci, and C. Law, "Paraview: An end-user tool for large data visualization," *The visualization handbook*, vol. 717, 2005.

[88] S. Cao, M. Nishida, and D. Schryvers, "Quantitative three-dimensional analysis of ni4ti3 precipitate morphology and distribution in polycrystalline ni–ti," *Acta Materialia*, vol. 59, no. 4, pp. 1780–1789, 2011.

[89] R. Santamarta, R. Arróyave, J. Pons, A. Evirgen, I. Karaman, H. E. Karaca, and R. D. Noebe, "TEM study of structural and microstructural characteristics of a precipitate phase in Ni-rich Ni-Ti-Hf and Ni-Ti-Zr shape memory alloys," *Acta Materialia*, vol. 61, no. 16, pp. 6191–6206, 2013.

[90] MATLAB, *version (R2019a)*. Natick, Massachusetts: The MathWorks Inc., 2019.

[91] G. S. Bigelow, A. Garg, S. A. Padula, D. J. Gaydosh, and R. D. Noebe, "Load-biased shape-memory and superelastic properties of a precipitation strengthened high-temperature Ni 50.3Ti 29.7Hf 20 alloy," *Scripta Materialia*, vol. 64, no. 8, pp. 725–728, 2011.

[92] B. C. Hornbuckle, T. T. Sasaki, G. S. Bigelow, R. D. Noebe, M. L. Weaver, and G. B. Thompson, "Structure-property relationships in a precipitation strengthened Ni-29.7Ti-20Hf (at%) shape memory alloy," *Materials Science and Engineering A*, vol. 637, pp. 63–69, 2015.

[93] A. Evirgen, F. Basner, I. Karaman, R. D. Noebe, J. Pons, and R. Santamarta, "Effect of aging on the martensitic transformation characteristics of a ni-rich nitihf high temperature shape memory alloy," *Functional Materials Letters*, vol. 5, no. 04, p. 1250038, 2012.

[94] D. Stroz, J. Kwarciak, and H. Morawiec, "Effect of ageing on martensitic transformation in niti shape memory alloy," *Journal of materials science*, vol. 23, no. 11, pp. 4127–4131, 1988.

[95] I. Kaya, H. Karaca, M. Nagasako, and R. Kainuma, "Effects of aging temperature and aging time on the mechanism of martensitic transformation in nickel-rich niti shape memory alloys," *Materials Characterization*, vol. 159, p. 110034, 2020.

[96] J. Kim and S. Miyazaki, "Effect of nano-scaled precipitates on shape memory behavior of ti-50.9 at.% ni alloy," *Acta Materialia*, vol. 53, no. 17, pp. 4545–4554, 2005.

[97] R. Hamilton, H. Sehitoglu, Y. Chumlyakov, and H. Maier, "Stress dependence of the hysteresis in single crystal niti alloys," *Acta Materialia*, vol. 52, no. 11, pp. 3383–3402, 2004.

[98] Y. Tong, F. Chen, B. Tian, L. Li, and Y. Zheng, "Microstructure and martensitic transformation of Ti49Ni51 - xHfx high temperature shape memory alloys," *Materials Letters*, vol. 63, no. 21, pp. 1869–1871, 2009.

[99] L. Bataillard, J.-E. Bidaux, and R. Gotthardt, "Interaction between microstructure and multiple-step transformation in binary NiTi alloys using in-situ transmission electron microscopy observations," *Philosophical Magazine A*, vol. 78, no. 2, pp. 327–344, 1998.

[100] E. Hornbogen, "The effect of variables on martensitic transformation temperatures," *Acta Metallurgica*, vol. 33, no. 4, pp. 595–601, 1985.

[101] M. Smith, *ABAQUS/Standard User's Manual, Version 6.9*. United States: Dassault Systèmes Simulia Corp, 2009.

[102] N. Zhou, C. Shen, M.-X. Wagner, G. Eggeler, M. Mills, and Y. Wang, "Effect of ni4ti3 precipitation on martensitic transformation in ti–ni," *Acta Materialia*, vol. 58, no. 20, pp. 6685–6694, 2010.

[103] O. Gal, *fit_ellipse*. MATLAB Central File Exchange, 2021.

[104] J. Michutta, M. Carroll, A. Yawny, C. Somsen, K. Neuking, and G. Eggeler, "Martensitic phase transformation in ni-rich niti single crystals with one family of ni4ti3 precipitates," *Materials Science and Engineering: A*, vol. 378, no. 1-2, pp. 152–156, 2004.

[105] J. Michutta, C. Somsen, A. Yawny, A. Dlouhy, and G. Eggeler, "Elementary martensitic transformation processes in ni-rich niti single crystals with ni4ti3 precipitates," *Acta materialia*, vol. 54, no. 13, pp. 3525–3542, 2006.

[106] O. Benafan, G. Bigelow, A. Garg, R. Noebe, D. Gaydosh, and R. Rogers, "Processing and scalability of nitihf high-temperature shape memory alloys," *Shape Memory and Superelasticity*, vol. 7, no. 1, pp. 109–165, 2021.

[107] H. Sehitoglu, Y. Wu, L. Patriarca, G. Li, A. Ojha, S. Zhang, Y. Chumlyakov, and M. Nishida, "Superelasticity and shape memory behavior of nitihf alloys," *Shape Memory and Superelasticity*, vol. 3, no. 2, pp. 168–187, 2017.

[108] P. Honarmandi, A. Solomou, R. Arroyave, and D. Lagoudas, "Uncertainty quantification of the parameters and predictions of a phenomenological constitutive model for thermally induced phase transformation in ni–ti shape memory alloys," *Modelling and Simulation in Materials Science and Engineering*, vol. 27, no. 3, p. 034001, 2019.

[109] D. C. Lagoudas, ed., *Shape memory alloys modeling and engineering applications*, vol. 1. New York, London: Springer, 2008.

[110] B. Haghgouyan, C. Hayrettin, T. Baxevanis, I. Karaman, and D. C. Lagoudas, "Fracture toughness of niti–towards establishing standard test methods for phase transforming materials," *Acta Materialia*, vol. 162, pp. 226–238, 2019.

[111] B. Haghgouyan, C. Hayrettin, T. Baxevanis, I. Karaman, and D. C. Lagoudas, "On the experimental evaluation of the fracture toughness of shape memory alloys," in *TMS Annual Meeting & Exhibition*, pp. 565–573, Springer, 2018.

[112] L. Xu, T. Baxevanis, and D. Lagoudas, "A finite strain constitutive model considering transformation induced plasticity for shape memory alloys under cyclic loading," *arXiv preprint arXiv:1812.05695*, 2018.

[113] M. Zarinejad, Y. Liu, and Y. Tong, "Transformation temperature changes due to second phase precipitation in NiTi-based shape memory alloys," *Intermetallics*, vol. 17, no. 11, pp. 914–919, 2009.

[114] J. Michutta, C. Somsen, A. Yawny, A. Dlouhy, and G. Eggeler, "Elementary martensitic transformation processes in Ni-rich NiTi single crystals with Ni4Ti3 precipitates," *Acta Materialia*, vol. 54, no. 13, pp. 3525–3542, 2006.

[115] K. Otsuka and X. Ren, "Physical metallurgy of Ti-Ni-based shape memory alloys," *Progress in Materials Science*, vol. 50, no. 5, pp. 511–678, 2005.

[116] A. Cruzado, J. Segurado, D. Hartl, and A. A. Benzerga, "A variational fast fourier transform method for phase-transforming materials," *Modelling and Simulation in Materials Science and Engineering*, vol. 29, no. 4, p. 045001, 2021.

[117] H. Karaca, S. Saghaian, G. Ded, H. Tobe, B. Basaran, H. Maier, R. Noebe, and Y. Chumlyakov, "Effects of nanoprecipitation on the shape memory and material properties of an ni-rich nitihf high temperature shape memory alloy," *Acta Materialia*, vol. 61, no. 19, pp. 7422–7431, 2013.

[118] M. Zarinejad, Y. Liu, and Y. Tong, "Transformation temperature changes due to second phase precipitation in niti-based shape memory alloys," *Intermetallics*, vol. 17, no. 11, pp. 914–919, 2009.

[119] J. K. Allafi, X. Ren, and G. Eggeler, "The mechanism of multistage martensitic transformations in aged ni-rich niti shape memory alloys," *Acta Materialia*, vol. 50, no. 4, pp. 793–803, 2002.

[120] J. Vondřejc, J. Zeman, and I. Marek, "An FFT-based Galerkin method for homogenization of periodic media," *Computers and Mathematics with Applications*, vol. 68, no. 3, pp. 156–173, 2014.

[121] G. W. Milton and R. V. Kohn, "Variational bounds on the effective moduli of anisotropic composites," *Journal of the Mechanics and Physics of Solids*, vol. 36, no. 6, pp. 597 – 629, 1988.

[122] A. Cruzado, J. LLorca, and J. Segurado, "Modeling cyclic deformation of inconel 718 superalloy by means of crystal plasticity and computational homogenization," *International Journal of Solids and Structures*, vol. 122-123, no. Supplement C, pp. 148 – 161, 2017.

[123] R. Hill, "Elastic properties of reinforced solids: Some theoretical principles," *Journal of the Mechanics and Physics of Solids*, vol. 11, no. 5, pp. 357 – 372, 1963.

[124] M. Stroeven, H. Askes, and L. Sluys, "Numerical determination of representative volumes for granular materials," *Computer Methods in Applied Mechanics and Engineering*, vol. 193, no. 30, pp. 3221 – 3238, 2004. Computational Failure Mechanics.

[125] M. Shenoy, J. Zhang, and D. McDowell, "Estimating fatigue sensitivity to polycrystalline ni-base superalloy microstructures using a computational approach," *Fatigue and Fracture of Engineering Materials and Structures*, vol. 30, no. 10, pp. 889–904, 2007.

[126] A. Salahouelhadj and H. Haddadi, "Estimation of the size of the rve for isotropic copper polycrystals by using elastic–plastic finite element homogenisation," *Computational Materials Science*, vol. 48, no. 3, pp. 447 – 455, 2010.

[127] C. Sweeney, B. O'Brien, F. Dunne, P. McHugh, and S. Leen, "Micro-scale testing and micromechanical modelling for high cycle fatigue of cocr stent material," *Journal of the Mechanical Behavior of Biomedical Materials*, vol. 46, pp. 244 – 260, 2015.

[128] M. Bouchedjra, T. Kanit, C. Boulemia, A. Amrouche, and M. E. A. Belouchrani, "Determination of the rve size for polycrystal metals to predict monotonic and cyclic elastoplastic behavior: Statistical and numerical approach with new criteria," *European Journal of Mechanics - A/Solids*, vol. 72, pp. 1 – 15, 2018.

[129] B. Koohbor, S. Ravindran, and A. Kidane, "Experimental determination of representative volume element (rve) size in woven composites," *Optics and Lasers in Engineering*, vol. 90, pp. 59 – 71, 2017.

[130] I. Gitman, H. Askes, and L. Sluys, "Representative volume: Existence and size determination," *Engineering Fracture Mechanics*, vol. 74, no. 16, pp. 2518 – 2534, 2007.

[131] S. Mirkhalaf, F. Andrade Pires, and R. Simoes, "Determination of the size of the representative volume element (rve) for the simulation of heterogeneous polymers at finite strains," *Finite Elements in Analysis and Design*, vol. 119, pp. 30 – 44, 2016.

[132] D. Trias, J. Costa, A. Turon, and J. Hurtado, "Determination of the critical size of a statistical representative volume element (srve) for carbon reinforced polymers," *Acta Materialia*, vol. 54, no. 13, pp. 3471 – 3484, 2006.

[133] J. Dirrenberger, S. Forest, and D. Jeulin, "Towards gigantic rve sizes for 3d stochastic fibrous networks," *International Journal of Solids and Structures*, vol. 51, no. 2, pp. 359 – 376, 2014.

[134] S. Yang, J. Dirrenberger, E. Monteiro, and N. Ranc, "Representative volume element size determination for viscoplastic properties in polycrystalline materials," *International Journal of Solids and Structures*, vol. 158, pp. 210 – 219, 2019.

[135] C. Pelissou, J. Baccou, Y. Monerie, and F. Perales, "Determination of the size of the representative volume element for random quasi-brittle composites," *International Journal of Solids and Structures*, vol. 46, no. 14, pp. 2842 – 2855, 2009.

[136] B. Abdallah, F. Willot, and D. Jeulin, "Stokes flow through a boolean model of spheres: Representative volume element," *Transp Porous Med*, vol. 109, pp. 711 – 726, 2015.

[137] F. Bignonnet, "Efficient fft-based upscaling of the permeability of porous media discretized on uniform grids with estimation of rve size," *Computer Methods in Applied Mechanics and Engineering*, vol. 369, p. 113237, 2020.

[138] D. Savvas, G. Stefanou, and M. Papadrakakis, "Determination of rve size for random composites with local volume fraction variation," *Computer Methods in Applied Mechanics and Engineering*, vol. 305, pp. 340 – 358, 2016.

[139] C. Lantuejoul, "Ergodicity and integral range," *Journal of microscopy*, vol. 161, no. 3, pp. 387–403, 1991.

[140] J. C. Lagarias, J. A. Reeds, M. H. Wright, and P. E. Wright, "Convergence properties of the nelder–mead simplex method in low dimensions," *SIAM Journal on optimization*, vol. 9, no. 1, pp. 112–147, 1998.

[141] Z. Yang, Y. C. Yabansu, R. Al-Bahrani, W.-k. Liao, A. N. Choudhary, S. R. Kalidindi, and A. Agrawal, "Deep learning approaches for mining structure-property linkages in high contrast composites from simulation datasets," *Computational Materials Science*, vol. 151, pp. 278–287, 2018.

[142] N. Halko, P.-G. Martinsson, Y. Shkolnisky, and M. Tygert, "An algorithm for the principal component analysis of large data sets," *SIAM Journal on Scientific computing*, vol. 33, no. 5, pp. 2580–2594, 2011.

[143] V. Rokhlin, A. Szlam, and M. Tygert, "A randomized algorithm for principal component analysis," *SIAM Journal on Matrix Analysis and Applications*, vol. 31, no. 3, pp. 1100–1124, 2010.

[144] I. T. Jolliffe, "Principal components in regression analysis," in *Principal component analysis*, pp. 129–155, Springer, 1986.

[145] M. T. Hagan and M. B. Menhaj, "Training feedforward networks with the marquardt algorithm," *IEEE transactions on Neural Networks*, vol. 5, no. 6, pp. 989–993, 1994.

[146] P. S. Chaugule and J. B. le Graverend, "Crystal-plasticity modeling of phase transformation-viscoplasticity coupling in high-temperature shape memory alloys," *International Journal of Plasticityl*, vol. (Under rev, 2022.

[147] P. S. Chaugule, O. Benafan, and J.-B. l. Graverend, "Phase transformation and viscoplasticity coupling in polycrystalline nickel-titanium-hafnium high-temperature shape memory alloys," *Acta Materialia*, vol. 221, p. 117381, 2021.

[148] Y. Chemisky, G. Chatzigeorgiou, P. Kumar, and D. C. Lagoudas, "A constitutive model for cyclic actuation of high-temperature shape memory alloys," *Mechanics of Materials*, vol. 68, pp. 120–136, 2014.

[149] A. Cruzado, J. Segurado, D. J. Hartl, and A. A. Benzerga, "A variational fast fourier transform method for phase-transforming materials," *Modelling and Simulation in Materials Science and Engineering*, 2021.

APPENDIX A

COMPARISON CALCULATIONS IN MICROMECHANICAL MODELING OF POLYCRYSTALS WITH PRECIPITATES[1]

A.1 Comparison of stiffness calculation in a polycrystal from two methodologies

In this analysis, the effective stiffness of a precipitated polycrystal was calculated with two methodologies and the results were compared. Figure A.1 summarizes the two methodologies with respective RVEs used. In the Case 1 methodology, the effective stiffness matrix was calculated through a multiscale upscaling with two level calculations: within a grain using a unit cell with precipitates, and further up-scaling using an RVE of the polycrystal containing many grains. The effective stiffness matrix of the grain was calculated from the unit cell shown in Figure A.1 (a), where the precipitate was chosen to be in a single orientation to simulated preferred orientations of the precipitates within a grain [104, 105]. The chosen unit cell simulate an anisotropy that can be caused because of the preferred orientation of the precipitates. A polycrystal RVE with 200 grains was created using open-source DREAM3D software and is shown in Figure A.1 (a). The effective stiffness of the polycrystal was calculated from the polycrystal RVE, with the effective stiffness of the unit cell as an input with random rotation in each grain. In the Case 2 methodology, the effective stiffness matrix was solved from a single RVE with many precipitates in random positions and orientations, which is shown in Figure A.1 (b).

Isotropic stiffness properties were assumed in both cases for the matrix and the precipitates. The values for the stiffness properties were chosen such that the analysis represents an upper bound for the tangent stiffness calculation in the phase transformation response. Periodic boundary conditions were used at the boundary of the RVEs. The estimation from the two cases showed that the stiffness calculated from the two methodologies are close within an error bound of 5%. The

[1]Reprinted with permission from "Effects of microstructure and composition on constitutive response of high temperature shape memory alloys: micromechanical modeling using 3-D reconstructions with experimental validation.", Acta Materialia (2022): 117929 by Joy, Jobin K., Tejas Umale, Dexin Zhao, Alexandros Solomou, Kelvin Xie, Ibrahim Karaman, and Dimitris C. Lagoudas. [74].

details of the calculation are presented in the following discussion.

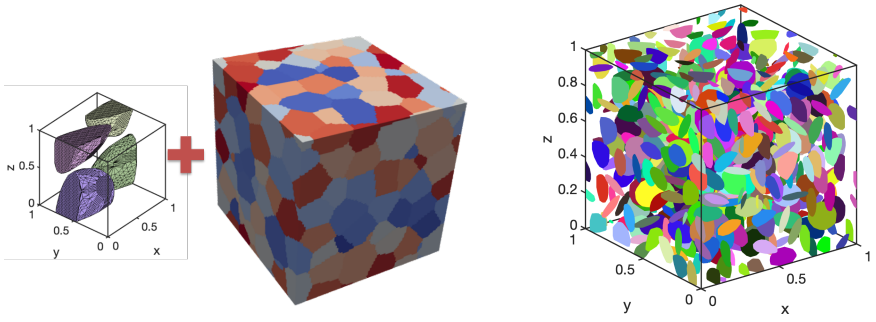

(a) Case 1: Multiscale modeling with 2 RVEs (b) Case 2: RVE with random precipitates

Figure A.1: RVEs used for effective stiffness calculation in the two methodologies. RVEs were constructed with a volume fraction of 20% disc shaped precipitates with an aspect ratio of 4.

A.1.1 Stiffness properties of matrix and precipitate

The stiffness property of the matrix in the RVEs were chosen such that they are in the order of softness in the SMA matrix during phase transformation. Considering an upper bound of 0.2 transformation strain at 200 MPa for the SMA matrix, the tangent stiffness in the SMA matrix during phase transformation will be less than 1 GPa. The matrix in these calculations was assumed to be isotropic linear elastic with Young's modulus of 1 GPa and Poisson's ratio of 0.4. The precipitate stiffness property was assumed to be in the order of stiffness value of the precipitates in the SMAs. The precipitates were assumed to be isotropic linear elastic with Young's modulus of 100 GPa and Poisson's ratio of 0.4.

A.1.2 Case 1: Multiscale modeling with two-scale calculation

First, the effective stiffness matrix for the grain was solved from the unit cell with precipitates. The calculation was carried out by applying unit load along normal and shear directions, and the terms in the stiffness matrix were calculated from the resulting strain produced. The solution was

performed using the Fast Fourier Transform (FFT) algorithm described in the work of Cruzado *et al.* [149]. The effective stiffness of the unit cell ($C_{eff}^{\text{unit cell}}$) was obtained as the following:

$$\left[C_{eff}^{\text{unit cell}}\right] \approx \begin{bmatrix} 3.76 & 1.84 & 1.82 & 0.01 & -0.04 & -0.13 \\ 1.84 & 2.73 & 1.82 & -0.01 & 0.03 & -0.02 \\ 1.82 & 1.82 & 4.27 & -0.1 & -0.05 & 0 \\ 0.01 & -0.01 & -0.1 & 0.51 & -0.07 & 0.01 \\ -0.04 & 0.03 & -0.05 & -0.07 & 0.91 & -0.04 \\ -0.1 & 0 & 0 & 0 & 0 & 0.5 \end{bmatrix} \text{ GPa}$$

The effective macroscopic stiffness matrix of the polycrystal was obtained using the polycrystal RVE. The stiffness matrix for each grain was calculated by rotating the effective stiffness matrix of the unit cell in the orientation of the grain. The orientation of the grains were defined randomly. The effective macroscopic stiffness matrix (C_{eff}) was solved applying unit loads along normal and shear directions.

$$\left[C_{eff}\right] \approx \begin{bmatrix} 3.43 & 1.9 & 1.89 & -0.01 & 0.01 & -0.01 \\ 1.9 & 3.39 & 1.89 & -0.01 & 0 & -0.02 \\ 1.89 & 1.89 & 3.16 & 0 & 0 & 0.02 \\ -0.01 & -0.01 & 0 & 0.76 & -0.01 & 0 \\ 0.01 & 0 & 0 & -0.01 & 0.65 & -0.01 \\ -0.01 & -0.02 & 0.02 & 0 & -0.01 & 0.64 \end{bmatrix} \text{ GPa}$$

$$\approx C[E = 1.93 \text{ GPa}, \nu = 0.36]$$

The stiffness matrix is close to isotropic because of the cumulative effect from the grains in random orientations. The isotropic stiffness and Poisson's ratio were approximated from the stiffness matrix and are shown.

A.1.3 Case 2: Methodology using RVE of many particles

In this methodology, the effective stiffness was calculated using the RVE with 400 precipitates in random orientation. The effective stiffness matrix was calculated by applying a unit load in the

RVE along the normal or shear directions. The obtained stiffness matrix is the following:

$$\left[C_{eff}\right] \approx \begin{bmatrix} 3.06 & 1.88 & 1.88 & 0 & 0 & 0 \\ 1.88 & 3.34 & 1.89 & 0 & 0 & 0.01 \\ 1.88 & 1.89 & 3.33 & 0 & 0 & 0 \\ 0 & 0 & 0 & 0.73 & 0 & 0 \\ 0 & 0 & 0 & 0 & 0.64 & 0 \\ 0 & 0.01 & 0 & 0 & 0 & 0.65 \end{bmatrix} \text{GPa}$$

$$\approx C[E = 1.85 \text{ GPa}, \nu = 0.37]$$

The stiffness matrix is close to isotropic from the cumulative effect of many random precipitates. The isotropic stiffness and Poisson's ratio were approximated from the stiffness matrix and are shown.

A.1.4 Summary

The effective stiffness value from the case 1 and case 2 methodologies were calculated as 1.93 GPa and 1.85 GPa respectively. The values are within 5% absolute error. The close prediction from both the analyses indicate the methodology with many random precipitates and isotropic matrix around may simulate the effective polycrystal SMA response with the precipitates within an accepted error.

APPENDIX B

DIFFUSION EQUATIONS FOR NITIHF ALLOYS

B.1 Derivation of diffusion equations for a ternary alloy

The diffusion equations for a ternary alloy are derived from the flux in the lattice plane. The different elements in the alloy are denoted by: A, B and C.

Diffusion relative to the lattice plane gives the following equations:

$$\mathbf{J}_A = -D_A \frac{\partial C_A}{\partial \mathbf{x}} \tag{B.1}$$

$$\mathbf{J}_B = -D_B \frac{\partial C_B}{\partial \mathbf{x}} \tag{B.2}$$

$$\mathbf{J}_C = -D_C \frac{\partial C_C}{\partial \mathbf{x}} \tag{B.3}$$

Total number of atoms per unit volume is a constant C_0.

$$C_A + C_B + C_C = C_0 \tag{B.4}$$

Taking the derivative gives:

$$\frac{\partial C_A}{\partial \mathbf{x}} + \frac{\partial C_B}{\partial \mathbf{x}} + \frac{\partial C_C}{\partial \mathbf{x}} = 0 \tag{B.5}$$

In this context, the flux equation is modified as:

$$\mathbf{J}_C = D_C \left(\frac{\partial C_A}{\partial \mathbf{x}} + \frac{\partial C_B}{\partial \mathbf{x}} \right) \tag{B.6}$$

Net flux of vacancies ($\mathbf{J}_v$) is given as:

$$\mathbf{J}_v = -\mathbf{J}_A - \mathbf{J}_B - \mathbf{J}_C. \tag{B.7}$$

$$\mathbf{J}_v = D_A \frac{\partial C_A}{\partial \mathbf{x}} + D_B \frac{\partial C_B}{\partial \mathbf{x}} - D_C \left(\frac{\partial C_A}{\partial \mathbf{x}} + \frac{\partial C_B}{\partial \mathbf{x}} \right) \tag{B.8}$$

Simplifying,

$$\mathbf{J}_v = (D_A - D_C) \frac{\partial C_A}{\partial \mathbf{x}} + (D_B - D_C) \frac{\partial C_B}{\partial \mathbf{x}} \tag{B.9}$$

In terms of the velocity (v) of lattice planes,

$$\mathbf{J}_v = C_0 v. \tag{B.10}$$

Substituting gives v in terms of concentration fraction as:

$$v = (D_A - D_C) \frac{\partial X_A}{\partial \mathbf{x}} + (D_B - D_C) \frac{\partial X_B}{\partial \mathbf{x}}. \tag{B.11}$$

To derive Fick's second law, we consider a thin plane with $\mathbf{J}'$ flux entering from one side, where $\mathbf{J}'$ is the flux defined in terms of the lab reference.

$$\frac{\partial C_A}{\partial t} = -\frac{\mathbf{J}'_A}{\partial \mathbf{x}} \tag{B.12}$$

$$\frac{\partial C_B}{\partial t} = -\frac{\mathbf{J}'_B}{\partial \mathbf{x}} \tag{B.13}$$

Also,

$$\mathbf{J}'_A = -D_A \frac{\partial C_A}{\partial \mathbf{x}} + v.C_A \tag{B.14}$$

$$\mathbf{J}'_B = -D_B \frac{\partial C_B}{\partial \mathbf{x}} + v.C_B \tag{B.15}$$

Substituting for v gives:

$$\mathbf{J}'_A = -D_A \frac{\partial C_A}{\partial \mathbf{x}} + \left[(D_A - D_C) \frac{\partial X_A}{\partial \mathbf{x}} + (D_B - D_C) \frac{\partial X_B}{\partial \mathbf{x}} \right] .C_A \tag{B.16}$$

$$\mathbf{J}'_B = -D_B \frac{\partial C_A}{\partial \mathbf{x}} + \left[(D_A - D_C) \frac{\partial X_A}{\partial \mathbf{x}} + (D_B - D_C) \frac{\partial X_B}{\partial \mathbf{x}} \right] .C_B \tag{B.17}$$

Simplifying $\mathbf{J}'_A$ gives:

$$\mathbf{J}'_A = -D_A \frac{\partial C_A}{\partial \mathbf{x}} + X_A (D_A - D_C) \frac{\partial C_A}{\partial \mathbf{x}} + X_A (D_B - D_C) \frac{\partial C_B}{\partial \mathbf{x}} \tag{B.18}$$

$$\mathbf{J}'_A = -(1 - X_A) \frac{\partial C_A}{\partial \mathbf{x}} + X_A (-D_C) \frac{\partial C_A}{\partial \mathbf{x}} + X_A (D_B - D_C) \frac{\partial C_B}{\partial \mathbf{x}} \tag{B.19}$$

$$\mathbf{J}'_A = -(X_B + X_C) D_A \frac{\partial C_A}{\partial \mathbf{x}} + X_A (-D_C) \frac{\partial C_A}{\partial \mathbf{x}} + X_A (D_B - D_C) \frac{\partial C_B}{\partial \mathbf{x}} \tag{B.20}$$

$$\mathbf{J}'_A = -\left[(X_B + X_C) D_A + X_A D_C \right] \frac{\partial C_A}{\partial \mathbf{x}} + X_A (D_B - D_C) \frac{\partial C_B}{\partial \mathbf{x}} \tag{B.21}$$

Similarly,

$$\mathbf{J}'_B = -\left[(X_A + X_C) D_B + X_B D_C \right] \frac{\partial C_B}{\partial \mathbf{x}} + X_B (D_A - D_C) \frac{\partial C_A}{\partial \mathbf{x}} \tag{B.22}$$

The final diffusion equation is obtained by substituting the expression of $\mathbf{J}'_A$ and $\mathbf{J}'_B$ in the rate equation.

$$\frac{\partial C_A}{\partial t} = \frac{\partial}{\partial \mathbf{x}} \left(\left[(X_B + X_C) D_A + X_A D_C \right] \frac{\partial C_A}{\partial \mathbf{x}} \right) - \frac{\partial}{\partial \mathbf{x}} \left(X_A (D_B - D_C) \frac{\partial C_B}{\partial \mathbf{x}} \right) \tag{B.23}$$

$$\frac{\partial C_B}{\partial t} = \frac{\partial}{\partial \mathbf{x}} \left(\left[(X_A + X_C) D_B + X_B D_C \right] \frac{\partial C_B}{\partial \mathbf{x}} \right) - \frac{\partial}{\partial \mathbf{x}} \left(X_B (D_A - D_C) \frac{\partial C_A}{\partial \mathbf{x}} \right) \tag{B.24}$$

Equation in mole fraction is obtained by dividing with C_0.

$$\frac{\partial X_A}{\partial t} = \frac{\partial}{\partial \mathbf{x}} \left([(X_B + X_C)D_A + X_A D_C] \frac{\partial X_A}{\partial \mathbf{x}} \right) - \frac{\partial}{\partial \mathbf{x}} \left(X_A (D_B - D_C) \frac{\partial X_B}{\partial \mathbf{x}} \right) \tag{B.25}$$

$$\frac{\partial X_B}{\partial t} = \frac{\partial}{\partial \mathbf{x}} \left([(X_A + X_C)D_B + X_B D_C] \frac{\partial X_B}{\partial \mathbf{x}} \right) - \frac{\partial}{\partial \mathbf{x}} \left(X_B (D_A - D_C) \frac{\partial X_A}{\partial \mathbf{x}} \right) \tag{B.26}$$

B.1.1 Case 1: Binary case

(For problem A-Ni, B-Hf, C-Ti)

If $C_0 = 0 \implies X_B = 0$, then

$$\frac{\partial X_A}{\partial t} = \frac{\partial}{\partial \mathbf{x}} \left([(0 + X_C)D_A + X_A D_C] \frac{\partial X_A}{\partial \mathbf{x}} \right) - 0 \tag{B.27}$$

Simplifying gives:

$$\frac{\partial X_A}{\partial t} = \frac{\partial}{\partial \mathbf{x}} \left([X_C D_A + X_A D_C] \frac{\partial X_A}{\partial \mathbf{x}} \right) \tag{B.28}$$

$$\frac{\partial X_A}{\partial t} = \frac{\partial}{\partial \mathbf{x}} \left(\tilde{D} \frac{\partial X_A}{\partial \mathbf{x}} \right); \tilde{D} = [X_C D_A + X_A D_C] \tag{B.29}$$

If $D_A = D_C$, then:

$$[X_C D_A + X_A D_C] = D_A [X_C + X_A] = D_A. \tag{B.30}$$

$$\frac{\partial X_A}{\partial t} = D_A \frac{\partial}{\partial \mathbf{x}} \left(\frac{\partial X_A}{\partial \mathbf{x}} \right) \tag{B.31}$$

B.1.2 Case 2: Ternary case simplified

(For problem A-Ni, B-Hf, C-Ti)

If $D_B = 0$, $D_C = D_A$:

$$\frac{\partial X_A}{\partial t} = \frac{\partial}{\partial \mathbf{x}} \left([(X_B + X_C)D_A + X_A D_C] \frac{\partial X_A}{\partial \mathbf{x}} \right) - \frac{\partial}{\partial \mathbf{x}} \left(X_A(0 - D_C) \frac{\partial X_B}{\partial \mathbf{x}} \right) \tag{B.32}$$

$$\frac{\partial X_B}{\partial t} = \frac{\partial}{\partial \mathbf{x}} \left([0 + X_B D_C] \frac{\partial X_B}{\partial \mathbf{x}} \right) - \frac{\partial}{\partial \mathbf{x}} \left(X_B(D_A - D_C) \frac{\partial X_A}{\partial \mathbf{x}} \right) \tag{B.33}$$

If we make the approximation $D_C = D_A$:

$$\frac{\partial X_A}{\partial t} = D_A \frac{\partial}{\partial \mathbf{x}} \left([(X_B + X_C) + X_A] \frac{\partial X_A}{\partial \mathbf{x}} \right) + D_A \frac{\partial}{\partial \mathbf{x}} \left(X_A \frac{\partial X_B}{\partial \mathbf{x}} \right) \tag{B.34}$$

$$\frac{\partial X_B}{\partial t} = \frac{\partial}{\partial \mathbf{x}} \left([X_B D_A] \frac{\partial X_B}{\partial \mathbf{x}} \right) - 0 \tag{B.35}$$

Simplifying,

$$\frac{\partial X_A}{\partial t} = D_A \frac{\partial}{\partial \mathbf{x}} \left(1 * \frac{\partial X_A}{\partial \mathbf{x}} \right) + D_A \frac{\partial}{\partial \mathbf{x}} \left(X_A \frac{\partial X_B}{\partial \mathbf{x}} \right) \tag{B.36}$$

$$\frac{\partial X_B}{\partial t} = D_A \frac{\partial}{\partial \mathbf{x}} \left(X_B \frac{\partial X_B}{\partial \mathbf{x}} \right) \tag{B.37}$$

B.1.3 Case 3: Simplifications in Ternary diffusion

(For problem A-Ni, B-Hf, C-Ti)

If C_B is assumed to be constant, $\implies$ X_B is constant, then:

$$\frac{\partial X_A}{\partial t} = \frac{\partial}{\partial \mathbf{x}} \left([(X_B + X_C)D_A + X_A D_C] \frac{\partial X_A}{\partial \mathbf{x}} \right) \tag{B.38}$$

$$0 = 0 - \frac{\partial}{\partial \mathbf{x}} \left(X_B(D_A - D_C) \frac{\partial X_A}{\partial \mathbf{x}} \right) \implies \frac{\partial^2 X_A}{\partial \mathbf{x}^2} = 0 \tag{B.39}$$

Simplifying both equations:

$$\frac{\partial X_A}{\partial t} = \frac{\partial}{\partial \mathbf{x}} \left([(X_C) D_A + X_A D_C] \frac{\partial X_A}{\partial \mathbf{x}} \right) \tag{B.40}$$

Again, simplifying:

$$\frac{\partial X_A}{\partial t} = \frac{\partial}{\partial \mathbf{x}} \left(\tilde{D} \frac{\partial X_A}{\partial \mathbf{x}} \right) ; \tilde{D} = [(X_C) D_A + X_A D_C] \tag{B.41}$$

This is the simplified diffusion equation for ternary alloys with A=Hf, C=Ti and B-Ni.

APPENDIX C

ESTIMATION OF PRECIPITATE STIFFNESS THROUGH UNCERTAINTY ANALYSIS

C.1 Introduction

It is a common difficulty in micromechanics that the material properties at the micro-level are an unknown. In the micromechanical modeling of NiTiHf SMAs, this includes the material parameters of the matrix and precipitates. However, after making the assumption that the matrix is behaving with similar properties to the solutionized SMA, most of the properties in the matrix were resolved. Other than the composition dependent properties such as transformation temperatures and strain, properties such as stiffness and phase diagram slopes were obtained with this assumption. Nevertheless, for the precipitate which is assumed to behave as elastic, the stiffness properties must still be determined. In this section, the stiffness property of the precipitate were determined from austenite stiffness of the precipitated material through micromechanics evaluations. The methodology also accounting for the uncertainty from the experimental measurements. A detailed discussion for the stiffness estimation summarized in section 2.6.3 is presented.

C.2 Effective stiffness estimation accounting for uncertainty

The micromechanical model presented in Chapter 4 can be used to model the effective austenite stiffness of the material. At high temperatures, the material can be modeled as an elastic composite, since the matrix will be austenite everywhere. The stiffness of the precipitate phase can be calculated through an inverse calculation comparing the micromechanical model with the effective stiffness measurements. In order for this inverse estimation to be accurate, accounting for the measurement errors, this should be carried out with uncertainty propagation.

In figure C.1, a schematic representation of the problem is described with a schematic of the RVE loaded with involved parameters. Details of the uncertainty in each of the parameters are discussed here. The matrix stiffness is assumed to be the same as the solutionized material (E_{SHT}), which has measurement uncertainty from sample-sample variation. Hence, the matrix stiffness

(E_{SHT}) is described with a Gaussian distribution with mean and standard deviation from the measurements. As the precipitate stiffness is an unknown, it is varied for the estimation. The effective stiffness to which the micromechanical model is compared also has associated uncertainty from sample-sample variation. A Gaussian distribution is used to describe the effective stiffness, with mean and standard deviation estimated from the measurements. Table C.1 summarizes the measurement uncertainty in the values of solutionized stiffness, and the three heat treated material stiffness values.

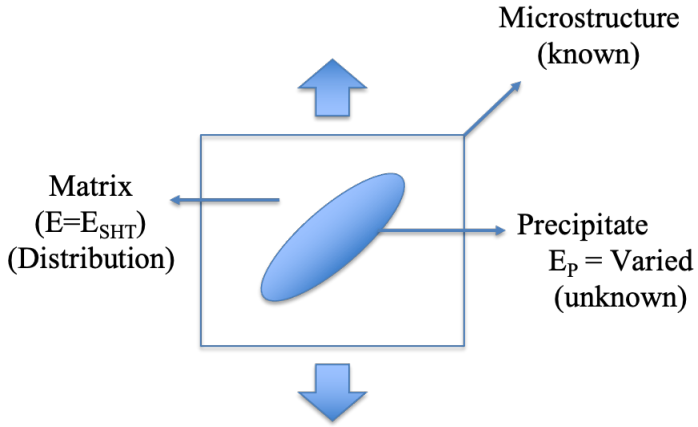

Figure C.1: The schematics showing the RVE problem with respective parameters. The sample-sample variation is accounted for, assuming likelihood distribution for the value. The unknown precipitate stiffness is varied in the model.

Table C.1: Austenite phase stiffness values for different heat treatments in $Ni_{50.3}Ti_{29.7}Hf_{20}$[A] and their estimated values from the finite element micromechanical model.

Material aging	**Experimental Young's modulus (GPa)**	**Value from E_P estimation (GPa)**
Solutionized	79.6 ± 2.4	-
550°C for 10 h	80.8 ± 1.8	80.6 ± 2.1
600°C for 10 h	82.2 ± 2.7	80.8 ± 2.1
650°C for 10 h	84.4 ± 4.1	81.3 ± 2.0

In summarizing the uncertainties to be accounted for in the estimation of the precipitate stiffness, they are the following.

- The uncertainty in the matrix stiffness and its propagation in the modeling.
- The uncertainty in the effective stiffness reflected by the precipitate stiffness.

The likelihood of the precipitate stiffness is the combined effect of the two factors described above.

First, the effect of propagation of uncertainty from matrix stiffness on the precipitate stiffness is examined. Figure C.2 shows the uncertainty in the predictions from the micromechanical model for varying values of precipitate stiffness (E_P), if the matrix stiffness is taken as a likelihood distribution. Here the sample $\mathrm{Ni}_{50.3}\mathrm{Ti}_{29.7}\mathrm{Hf}_{20}$[A] heat treated at $550°$C for 10 h is considered for study and the effective stiffness is denoted as E_{550}. It can be seen that the prediction from the model has a mean value with a likelihood distribution along the y-axis. Now, if the likelihood of E_P for a fixed effective stiffness (for instance, $= 80$ GPa) is estimated, it will generate a likelihood distribution with maximum probability at the mean value (denoted as: $\mathcal{L}(E_P|E_{550})$).

From the second factor, the measured effective stiffness E_{550} is not a fixed value, but a likelihood distribution ((E_{Ag})) accounting for measurement error and sample to sample variation. The effect of E_{550} distribution is accounted for by weighted integration of $\mathcal{L}\left(E_P|E_{Ag}\right)$ with weights equal to (E_{Ag}), which is summarized as follows:

$$\mathcal{L}\left(E_P|Ag\right) = \int_{-\infty}^{\infty} \mathcal{L}\left(E_P|E_{Ag}\right) \mathcal{L}\left(E_{Ag}\right) dE_{Ag}, \tag{C.1}$$

where, E_{Ag} represents the specific heating treatment and $\mathcal{L}\left(E_{Ag}\right)$ is the likelihood of the E_{Ag} from multiple experiments and samples.

In the current modeling, the precipitate stiffness is assumed to be constant with heat treatment. In that case, the effective stiffness should be estimated as a cumulative effect from different heat treatments. Thus, the estimation should follow the following steps:

- The likelihood distribution of precipitate stiffness is obtained for individual heat treatment.

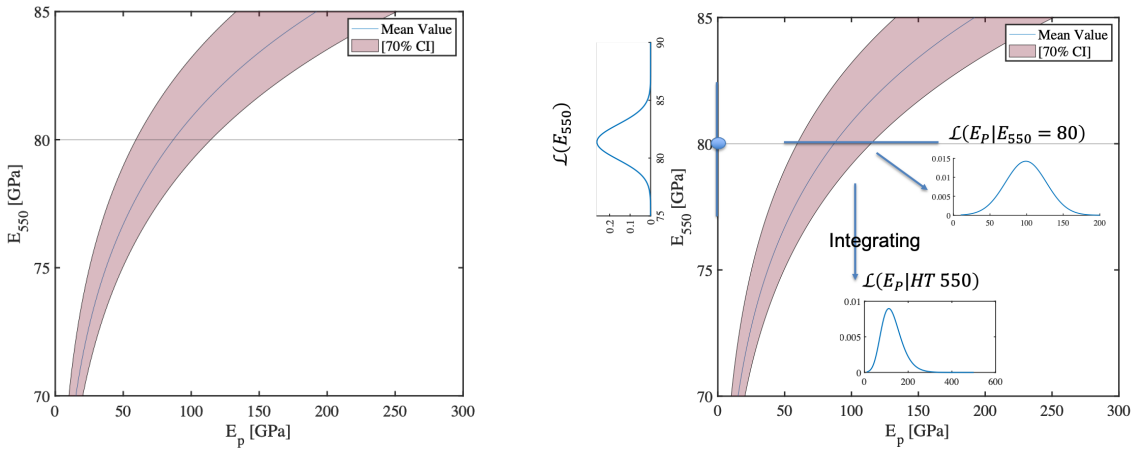

Figure C.2: Figures showing the uncertainty propagation in the micromechanical model for effective stiffness solution: (a) shows the likelihood of precipitate stiffness for fixed effective value and (b) shows the estimation of precipitate stiffness considering the likelihood of effective stiffness with uncertainty.

- The overall likelihood of the precipitate stiffness is obtained from the heat treatment cases, taking the product of the likelihood distributions.

With the likelihood of precipitate stiffness from the individual aging conditions, the effective likelihood function $\mathcal{L}(E_P)$ is determined to be the product of likelihood functions. This is summarized in the following equation:

$$\mathcal{L}(E_P) = \prod_{Ag=1,2,3} \mathcal{L}\left(E_P|Ag\right), \tag{C.2}$$

where $Ag = 1, 2, 3$ represents the three aging conditions corresponding to $550°$C, $600°$C and $650°$C respectively, and E_{Ag} corresponds to the austenite stiffness of the aged SMA. The analysis gives E_P to be 95 ± 26 GPa based on the maximum likelihood estimation (MLE). Table C.1 also compares the estimations from MLE with the experimental measurements.

Studying figure C.2 (a), several observations can be made about the uncertainty in the precipitate stiffness. It is apparent that the confidence interval in the precipitate stiffness for fixed value of E_{550} increases along the y-axis from 75 GPa to 85 GPa. This follows from the micromechanics

in the effective stiffness. If the effective stiffness is less than that of matrix stiffness ($\approx$ 80 GPa), it would mean softer stiffness in the precipitates. The bound for the stiffness in the precipitate would then be [0 $\approx$80) GPa, where the lower value corresponds to the void stiffness and the upper value corresponds to the matrix stiffness. However, if the effective stiffness is higher than that of matrix stiffness, this would mean a stiffer precipitate phase. In that case the bound for the stiffness would be ($\approx$80 ∞) GPa, where the lower value corresponds to the matrix stiffness and the upper value is ∞ as any value higher than the matrix stiffness can make the material stiffer. The difference in the ranges is reflected in the uncertainty in the estimations for larger value and higher stiffness. Corresponding to the tight limit, whenever the effective stiffness is lower than the matrix, the precipitate stiffness can be estimated with tight confidence intervals. In higher effective stiffness, the precipitate stiffness estimation will have higher uncertainty, as a result of the large range.

APPENDIX D

DESCRIPTION OF STRAIN DISTRIBUTION IN RVE REALIZATIONS

In order to derive the strain response statistics from Representative Volume Elements (RVEs), the individual RVE responses were described with respect to their ensemble average behavior. In this section, details on the reasoning for describing the particular RVE behavior through perturbations from the ensemble average behavior are presented, using the micromechanics problem of RVEs with precipitates. Although the images used in this section are based on 2D, the reasoning is the same as in the case of 3D RVEs. The current work focuses on the effective strain behavior from the RVEs. However, the process should be similar for any other behavior modeled using RVEs.

Fig.D.1(a) shows the schematic of a precipitated RVE loaded with uni-axial tension. When this RVE models only a finite number of randomly oriented particles, the behavior of the material described in the RVE is not isotropic but anisotropic. When this RVE is solved in different orientations, the resultant strain produced can be different. In Fig.D.1(b), a polar plot is used to represent the normalized strain this RVE may produce for the loading along different 2D orientations. The radius along a specific orientation represents the magnitude along that orientation.

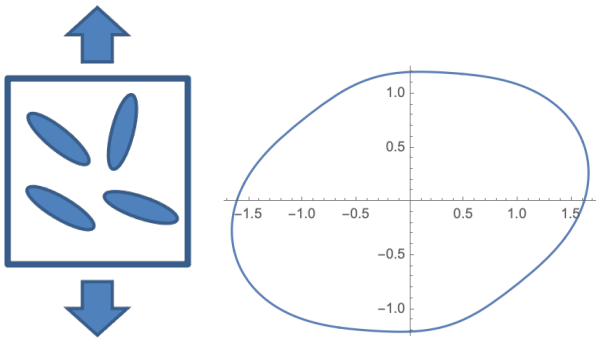

(a) (b)

Figure D.1: Schematics showing the problem of single RVE with uniaxial loading. (a) the RVE with loading (b) polar plot showing the normalized effective strain.

Next, the ensemble average behavior of these RVEs is examined. As the precipitates are chosen randomly, there are no preferred orientations in these RVEs. Hence, the ensemble average behavior can be assumed to be isotropic, with the same magnitude of effective strain for loading in any direction. Fig.D.2 shows a schematic of the isotropic ensemble average behavior of the RVEs, which is a circle or sphere with equal magnitude in all orientations. Taking the average behavior as the reference for describing the individual RVE behavior, the individual RVE strain magnitudes are described as a ratio to the average value.

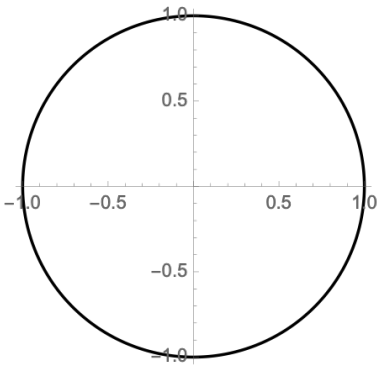

Figure D.2: Schematics showing the ensemble average behavior of RVEs in a polar plot.

All the perturbations that can happen to the average behavior to simulate the individual RVE should be considered. This might include an increase/decrease of magnitude equally along all orientations, which can be referred to as an isotropic perturbation. Fig.D.3 (a) shows a schematic of the isotropic perturbation from the average behavior. The change due to isotropic perturbation can be quantified as magnitude multiplied by $(1 + \delta)$, where δ is a distribution with mean of zero. The isotropic perturbation captures the uniform increase of magnitude along all orientations.

The isotropic perturbation alone is not sufficient, as the anisotropy in the RVE has not been captured. Hence, an anisotropic perturbation from the average isotropic behavior is introduced. Fig.D.3(b) compares the modified effective behavior with an anisotropic perturbation. Here, only the perturbation in 11-direction is considered. Anisotropic perturbation in the effective strain can

be modeled by multiplying with a factor of $(1 + z_{ij})$ on the compliance matrix of the RVE, where z_{ij} are perturbations with mean equals zero.

In addition to the anisotropic perturbation, a rotation may also be needed to capture the orientation differences between the coordinates. The material coordinates might be oriented differently compared to coordinates in the anisotropic perturbations. Thus, through a rotation, the random orientation of anisotropy in the RVE can be captured. In Fig. D.3(c), the rotation on the perturbed behavior is shown. This rotation enables to include all RVEs with the same anisotropy but different orientations in the statistics analysis. It should be noted that if the principal strain matrix is perturbed by multiplying with $(1 + z_{ij})$, the shear components will not be captured, as they are zero. However, the rotation of the principal strain matrix will capture the shear.

Using the two types of perturbations and rotations together, the individual RVE behavior can be assumed to be captured. This concept is summarized in Fig. D.4. In Fig. D.5, two individual RVE behaviors obtained through the three-step process are compared to the isotropic average response. The two cases shown have smaller and higher radial magnitude compared to the average response. Also, they have differences in their anisotropy and are rotated in different directions. These comparisons show the extent of behaviors that can be described in the presented perturbation theory.

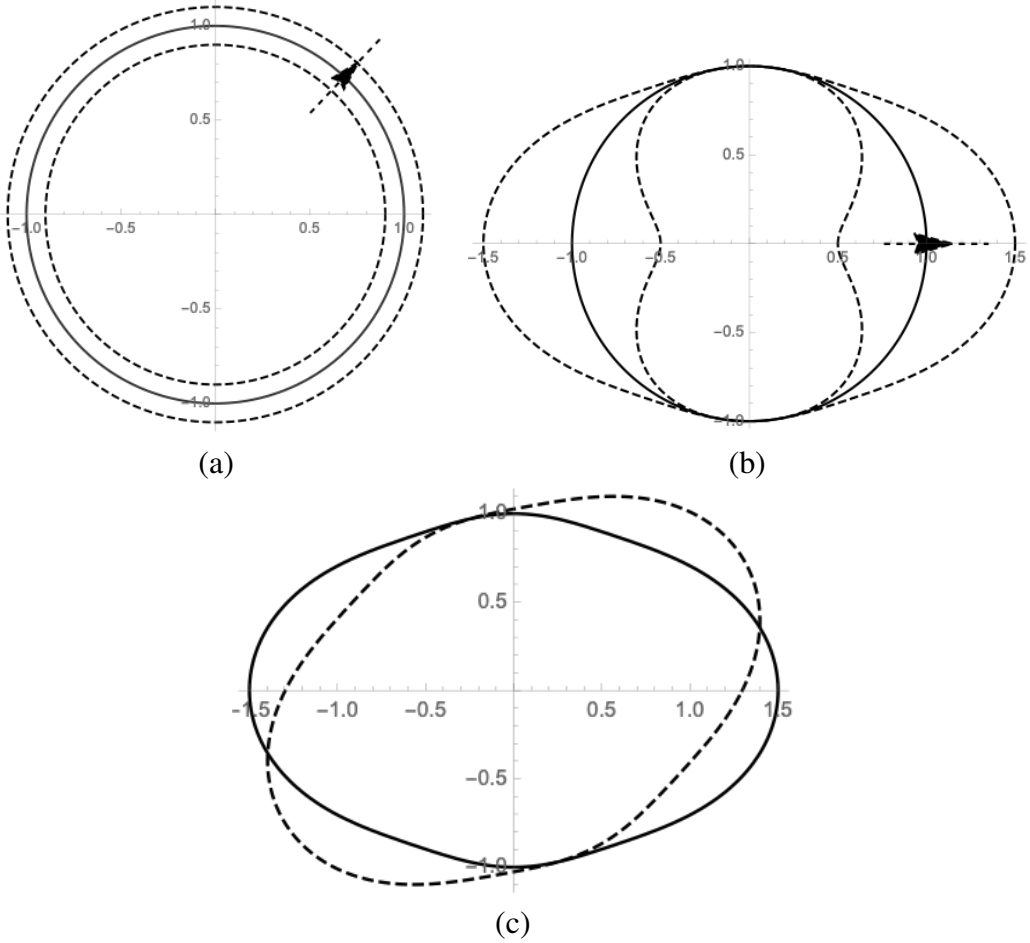

Figure D.3: Schematics showing (a) isotropic perturbation, (b) anisotropic perturbation and (c) rotation of the perturbed behavior with respect to the average behavior. The solid line is used for the behavior before perturbation, and the dotted line for the behavior after the perturbation.

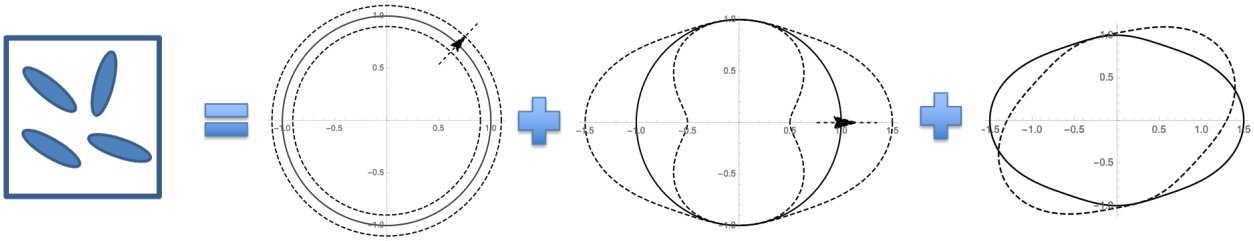

Figure D.4: Schematics showing the two perturbations and rotation defining the behavior of the individual RVE.

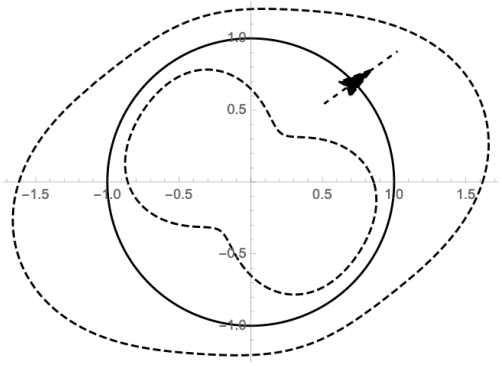

Figure D.5: Schematics of individual RVE behaviors compared to the isotropic average behavior. The individual RVE behaviors are shown with dotted lines.

APPENDIX E

DETAILS OF ARTIFICIAL NEURAL NETWORK MODEL FOR SMA RESPONSE

E.1 Weights and biases in the neural network model

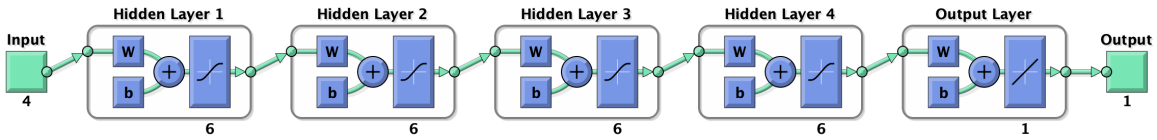

Figure E.1: Neural network architecture for modeling SMA actuation response.

Input and output normalization

The inputs and the outputs in the neural network model are normalized by mapping minimum and maximum values to [-1 1]. The normalization function is given by the following equation:

$$y = \frac{(y_{max} - y_{min})(x - x_{min})}{(x_{max} - x_{min})} + y_{min}, \tag{E.1}$$

where, x is the input variable and y is the normalized value, x_{max} and x_{min} are the maximum and minimum values of the data used in the training, and y_{max} and y_{min} are the target maximum and minimum values, which in this case are taken to be 1 and -1 respectively. The following table summarizes the minimum and maximum value for the input and target. The input to the neural network is a column matrix following the same order shown in the table. In order to get the actual value from the normalized value, a reverse transformation is performed, which is given by the inverse equation of equation E.1 given as the following:

$$x = \frac{(y - y_{min})(x_{max} - x_{min})}{(y_{max} - y_{min})} + x_{min}. \tag{E.2}$$

Table E.1: Input and output for the ML model

Parameter	x_{min}	x_{max}
Input		
σ_{zz}	43.0000	393.0000
$\varepsilon_{zz}(T)$	-0.1043	3.8275
T	80.0000	195.0000
Sign(ΔT)	-1.0000	1.0000
Target		
$exp(10 * \frac{d\varepsilon_{zz}(T,\sigma_{zz})}{dT})$	0.0413	1.0650

Hidden Layer 1 parameters

The equation of the Hidden Layer 1 is the following:

$$\mathrm{H}_1 = \text{tansig}\left([w] * \text{Input} + [b]\right), \tag{E.3}$$

where the tansig is a hyperbolic tangent sigmoid transfer function or hyperbolic tangent function given by the following equation (equation E.4):

$$\text{tansig}(x) = \frac{2}{(1 + exp(-2x))} - 1 \tag{E.4}$$

The weights $[w]$ and biases $[b]$ in equation E.3 are defined by the following matrices:

$$\Big[w\Big] = \begin{bmatrix} -0.2021 & 1.5268 & 0.6701 & 0.1691 \\ 0.5578 & 0.3051 & -1.1083 & -0.0071 \\ 0.1194 & -1.2973 & 0.2836 & -0.4568 \\ -0.7240 & 0.6657 & -1.6536 & -0.0321 \\ -0.6550 & 1.8522 & 0.6516 & 2.2017 \\ 1.0144 & 0.2214 & 1.3141 & 0.7210 \end{bmatrix} \quad \Big[b\Big] = \begin{bmatrix} -1.0815 \\ 0.7229 \\ -0.3915 \\ -0.6939 \\ 1.6228 \\ 2.2853 \end{bmatrix}$$

Hidden Layer 2 parameters

The equation of the Hidden Layer 2 follows:

$$\mathrm{H}_2 = \text{tansig}\left([w] * \mathrm{H}_1 + [b]\right), \tag{E.5}$$

where the tansig follows equation E.4, and weights $[w]$ and biases $[b]$ given in the following matrices:

$$\Big[w\Big] = \begin{bmatrix} 0.0844 & 0.7067 & -0.3732 & -0.8597 & -1.1867 & -0.8299 \\ 0.1463 & -1.6497 & -2.2026 & -1.1570 & -0.7605 & 1.5479 \\ -0.2723 & 1.6385 & -1.4868 & 2.3816 & -1.2083 & 1.1984 \\ 0.1212 & 1.1463 & -0.9947 & 0.1601 & -1.1288 & -1.7626 \\ -1.1706 & -1.3779 & 3.3846 & -0.8548 & -0.0335 & -1.5071 \\ -0.5717 & 1.9129 & -0.0364 & -1.1046 & -1.8124 & 0.9991 \end{bmatrix} \quad \Big[b\Big] = \begin{bmatrix} -1.8227 \\ -1.5151 \\ 0.3379 \\ -0.6379 \\ -2.0530 \\ -1.9297 \end{bmatrix}$$

Hidden Layer 3 parameters

The equation of the Hidden Layer 3 follows:

$$\mathrm{H}_3 = \text{tansig}\left([w] * \mathrm{H}_2 + [b]\right), \tag{E.6}$$

where the tansig follows equation E.4, and weights $[w]$ and biases $[b]$ given in the following matrices:

$$\Big[w\Big] = \begin{bmatrix} -0.2829 & 0.9268 & 1.0115 & -0.8684 & 0.4009 & -0.6485 \\ 0.5884 & -1.1177 & 0.8139 & -1.1498 & -1.7354 & 1.0300 \\ 0.9664 & -0.3711 & -0.5597 & 1.0517 & -0.1145 & 0.8905 \\ 1.0864 & 0.1691 & 0.0475 & -1.0652 & -1.2324 & -0.3705 \\ -0.9072 & -1.4208 & -1.9061 & 0.8620 & 1.8428 & -0.6094 \\ 0.6215 & -0.1965 & 2.2827 & 0.8882 & 1.5640 & 2.9501 \end{bmatrix} \quad \Big[b\Big] = \begin{bmatrix} 1.8301 \\ -1.1650 \\ -0.3231 \\ -0.2385 \\ -1.9373 \\ -2.3321 \end{bmatrix}$$

Hidden Layer 4 parameters

The equation of the Hidden Layer 4 follows:

$$\mathrm{H}_4 = \text{tansig}\left([w] * \mathrm{H}_3 + [b]\right), \tag{E.7}$$

where the tansig follows equation E.4, and weights $[w]$ and biases $[b]$ given in the following matrices:

$$\left[w\right] = \begin{bmatrix} 0.9888 & -1.4559 & 0.1577 & 1.5692 & -2.2115 & 0.5138 \\ 0.1378 & 1.8843 & 0.9027 & 1.0502 & -0.3496 & -0.6959 \\ 0.1677 & 1.0720 & 0.6189 & -1.6078 & 2.2571 & -1.4248 \\ -0.8514 & 0.8315 & 0.6170 & 0.9836 & -0.3636 & 1.2126 \\ -0.0236 & 1.4341 & 0.0302 & -1.4513 & 1.0824 & -1.3539 \\ -1.0606 & -0.9529 & 1.0411 & 0.1185 & 0.4651 & 0.7543 \end{bmatrix} \quad \left[b\right] = \begin{bmatrix} -1.6158 \\ -1.6710 \\ 0.5499 \\ -0.4499 \\ 1.1102 \\ -2.0891 \end{bmatrix}$$

Output Layer parameters

The equation of the Output Layer follows:

$$\text{Output} = \left([w] * \mathrm{H}_4 + [b]\right), \tag{E.8}$$

where weights $[w]$ and biases $[b]$ given in the following matrices:

$$\left[w\right] = \begin{bmatrix} 0.5475 & 0.0839 & 0.4659 & -0.8835 & 1.1739 & 1.1398 \end{bmatrix} \quad \left[b\right] = \begin{bmatrix} 0.1437 \end{bmatrix}$$